

**OPTO-ELECTROMECHANICAL DEVICES  
FOR LOW-NOISE DETECTION OF RADIO WAVES**

by

Tolga Bağcı



PhD Thesis

Danish National Research Foundation Center for Quantum Optics (QUANTOP)

Niels Bohr Institute

This thesis has been submitted to the PhD School of the Faculty of Science,

University of Copenhagen

February, 2014

Supervisor: Prof. Eugene Simon Polzik



## ABSTRACT

There is currently an increasing interest in developing hybrid devices that unite the desirable features of different systems. Opto-electromechanics has emerged as one of these promising hybrid fields, where the functionality of conventional electrical circuits can be combined with the salient features of optical systems for various technological and sensing applications. Nanomechanical resonators stand as promising candidates in terms of linking the two systems, primarily thanks to their versatility in coupling to various physical systems, together with their excellent mechanical quality factors. For example, a hybrid system like this, would enable the use of well-established shot-noise limited optical sensing technologies for detecting weak radio-frequency (rf) signals, rf-to-optical photon conversion and transmission of information in low-loss fiber-optic links over long distances.

Driven mainly by potential sensing applications, we started an experimental project with the goal of realizing a hybrid opto-electromechanical device operating at room temperature. The device consists of an LC electrical circuit coupled to a metal-coated high-quality nanomechanical membrane, the vibrations of which are monitored as phase fluctuations via optical interferometry. At the first stage of the experiment, we have tested several bare, metal (aluminum)-coated and graphene-coated SiN (silicon nitride) membranes in terms of their capacitive interaction strength. Our findings support the expectation that metal and graphene coated membranes show similar performance that is significantly better than bare SiN membranes and single layer graphene does not alter the mechanical quality and mass. Later on, we have incorporated an inductor to the system in order to achieve coupling between an aluminum coated membrane and an LC circuit (at  $\approx 0.7$  MHz). We have characterized the electromechanical coupling by both optical and electrical means, along with the observation of mechanically induced transparency and normal mode splitting due to strong coupling. Finally, we have analyzed the noise performance of our device for optical detection of radio waves. We demonstrate an actual Johnson noise-limited voltage sensitivity of  $\approx 800$  pV/ $\sqrt{\text{Hz}}$  and beyond that, we infer a sensitivity of 60 pV/ $\sqrt{\text{Hz}}$  both for the thermal noise of the membrane and shot noise (quantum) of the optical readout, at the optimal electromechanical cooperativity  $\mathcal{C}_{\text{em}} = 150$ . Our findings are supplemented by additional Y-factor noise temperature measurements. This performance competes with the current state of the art operational amplifiers at room temperature and our device's performance can be improved with further advances. For a specific set of parameters, we have achieved  $\mathcal{C}_{\text{em}} = 6800$  meaning that the membrane noise can be suppressed down to  $T_m/\mathcal{C}_{\text{em}} \approx 40$  mK. We believe our device will be of interest in sensing applications (NMR, radio astronomy etc.) where it is coupled to a cold signal input and the Johnson noise is strongly suppressed.



## RESUMÉ

Der har i nyere tid været en stigende interesse i at udvikle hybride enheder, der forener de ønskelige egenskaber af forskellige systemer. Opto-elektromekanik er opstået som en af disse hybrid teknikker, hvor funktionaliteten af konventionelle elektroniske kredsløb kan kombineres med de fremtrædende egenskaber af optiske systemer, til forskellige teknologiske anvendelser. Nanomekaniske resonatorer er en lovende kandidat til at forbinde optik med elektronik, takket være deres alsidige kobling til forskellige fysiske systemer sammen med fremragende mekanisk  $Q$ -faktor. For eksempel vil et hybrid-system som dette tillade brugen af etablerede optiske målemetoder, som kun er begrænset af kvantemekanisk målestøj, til at måle svage radio-frekvens (rf) signaler, rf-til-optisk foton konvertering og transmission af information i optiske fibre med lavt tab over lange distancer.

Vi startede på et eksperimentelt projekt med målet om at lave et hybridt opto-elektromekanisk element der virker ved stuetemperatur, hovedsageligt motivet af de potentielle anvendelser indenfor præcisionsmåling. Vores system, består af et LC elektrisk kredsløb koblet til en metal-belagt nanomekanisk membran med høj  $Q$ -faktor. Membranen giver et faseskift når den vibrerer, hvilket kan måles af et optisk interferometer. I starten af eksperimentet testede vi flere rene, samt metal (aluminum)- og grafen-belagte SiN membraner og fandt deres kapacitative interaktionsstyrke. Vores resultater understøtter forventningen om at metal- og grafen-belægning klarer sig nærmest identisk, men bedre end almindelige SiN membraner, og at et enkelt grafen lag ikke forringer den mekaniske  $Q$ -faktor. Senere har vi inkorporeret en induktor i systemet, for at opnå kobling mellem en aluminiums-belagt membran og et LC kredsløb ( $\approx 0.7$  MHz). Vi har karakteriseret den elektromekaniske kopling både optisk og elektronisk, samt observeret mekanisk induceret transparens og opdeling af egensvingningen på grund af den stærke kobling. Tilsidst har vi analyseret præstationen af vores enhed igennem dens støjniveau for optisk detektion af radiobølger. Vi demonstrerer en Johnson-støj begrænset spændingsfølsomhed af  $\approx 800$  pV/ $\sqrt{\text{Hz}}$  og vi udleder en sensitivitet på 60 pV/ $\sqrt{\text{Hz}}$  for membranens termiske samt den optiske støj ved en optimal elektromekaniske kooperativitet på  $\mathcal{C}_{\text{em}} = 150$ , hvilket er understøttet af supplerende  $Y$ -faktor målinger. Denne ydeevne kan konkurrere med moderne avancerede operationsforstærkere ved stuetemperatur og præstationen af vores produkt kan forbedres med yderligere udviklinger. For et givet sæt parametre har vi opnået  $\mathcal{C}_{\text{em}} = 6800$  hvilket vil sige at membranens støjbidrag kan undertrykkes til  $T_m/\mathcal{C}_{\text{em}} \approx 40$  mK. Vi tror på, at vores produkt vil have potentielle anvendelsesmuligheder indenfor præcisionsmålinger (NMR, radio astronomi, etc.), hvor det kobles til en kold signal input så den Johnson støj er stærkt undertrykt.



## ACKNOWLEDGMENTS

Within the timespan of this PhD project, I have had the opportunity of being a member of the QUANTOP Labs at the historic Niels Bohr Institute. I am grateful to my supervisor, Eugene Polzik, for giving me the chance to work here and for his illuminating guidance and support in these three years. I feel privileged to have known him and benefited from his knowledge.

The opto-electromechanics project commenced with our collaboration with the Nanoprobes group at DTU Nanotech. I would like to thank Silvan Schmid for our very fruitful work together, for his supervision and efforts in the design/fabrication of the capacitors and membranes as well as his assistance with the vibrometer measurements at DTU. I would also like to thank Anja Boisen for our collaboration at DTU and L. Guillermo Villanueva for his involvement in the fabrication of aluminum coated membranes.

Around the end of 2012, we started to see the interesting physics of membrane-LC circuit coupling. In the beginning of 2013, Albert Schliesser joined our group. I am grateful to him for his substantial contributions to the project. His expertise in experimental optomechanics and his theoretical knowledge was a great source for the membrane team. Both Eugene and Albert have had a big impact on pushing the limits of our experiment with their supervision. I would like to thank Anders Simonsen, with whom I shared the long hours of measurements. I am grateful to him for his persistent efforts, ideas and input to improve the measurements. I would like to thank Jürgen Appel for his crucial contributions in electronics/circuit design and for his energy and willingness to help in general. Thanks to Jacob Taylor, our collaborator, for his ideas and theoretical work which inspired the membrane team; Emil Zeuthen and Anders Sørensen for their theoretical contributions to our experiments and discussions at NBI. I would like to thank Maja Cassidy and Patrick Herring who produced the graphene membranes and Charles Marcus-the head of the group. The Michelson interferometer has been set up at NBI and optimized during the course of time. I am grateful to Andreas Barg, Andreas Næsby and Anders Simonsen for their diligent work on developing it. I also thank Dalziel Wilson, who visited our group for a while and shared his experimental knowledge; Henrik Bertelsen and Axel Boisen who helped with electronics and Louise Jørgensen who took part in the cleanroom processes.

Within the first year of my PhD project, I had the chance of being involved in the GaAs experiment. I thank Koji Usami for driving this work towards a novel regime; Andreas Næsby for his experimental efforts (who has always been willing to help me in general) and Lodahl group - Jin Liu, Søren Stobbe and Peter Lodahl for fabricating the magic GaAs membranes.

I would like to thank all the individuals of the Quantop family for contributing to the collective spirit and for making this place such a warm, cosy and friendly environment. I shall, in particular, express my gratitude to Jörg Helge Müller, who has always been willing to share his deep scientific knowledge (also for our specific project) and help with practical issues in the lab. Thanks to Jean-Baptiste Béguin for our mostly optimistic and rapidly

diverging conversations here. Apart from being at NBI, I also spent quite some time for the measurements at DTU. I thank İzzet Yıldız and Haldun Sevinçli for our discussions there and for our good times in Copenhagen. In these three years of my PhD lifetime, I have had the chance of meeting many nice people here. I am grateful to all those friends who made life easier amidst the chaotic matrix of a PhD adventure in Copenhagen, in particular to Matteo Cataneo and Verdiana Steccanella. Special thanks to my friends and colleagues, Mustafa Gündoğan and Kutun Gürel for our experiences and motivating conversations accumulated over many years. Finally, I would like to thank my family for showing their support in my career path even though they were physically far away.

The experimental projects covered as parts of this PhD work have been financially supported by several funding programs. I would like to acknowledge DARPA, QUANTOP, EU and ERC grants.

# Contents

<b>Table of Contents</b>	<b>ix</b>
<b>1 Introduction</b>	<b>1</b>
1.1 Background and motivation . . . . .	1
1.2 Publications and conferences . . . . .	2
1.3 Chapter structure . . . . .	4
<b>2 Theory</b>	<b>7</b>
2.1 Vibrations of a thin membrane . . . . .	7
2.2 Mechanical resonator-capacitor coupling . . . . .	12
2.3 Langevin equations of motion for the electromechanical system (Membrane-LC)	14
2.4 Voltage sensitivity and noise . . . . .	18
2.5 Alternative derivation of the coupling rate . . . . .	21
2.6 Instability due to the pull-in voltage . . . . .	23
2.7 RF to optical photon conversion . . . . .	25
2.8 Inductive coupling for ac drive . . . . .	26
<b>3 Capacitive coupling with metal and graphene coated SiN membranes</b>	<b>29</b>
3.1 Mechanism behind capacitive coupling . . . . .	30
3.2 Experimental Setup . . . . .	32
3.2.1 Doppler Vibrometer . . . . .	33
3.2.2 Capacitor chips and membranes . . . . .	37
3.3 Preliminary tests . . . . .	41
3.3.1 AC force as a function of the dc bias and rf modulation . . . . .	41
3.3.2 Static displacement of the membrane . . . . .	43
3.3.3 Frequency shift of the membrane . . . . .	44
3.3.4 Charging and hysteresis effects in bare SiN membranes . . . . .	46
3.4 Results/Analysis . . . . .	47
3.4.1 Electrostatic interaction strength with different types of membranes	47
3.4.2 Theoretical force constant for four-segment electrodes and effects of the graphene layer . . . . .	50
3.4.3 Overlap factor as a correction to the force constant . . . . .	51
3.4.4 Mechanical Q-factor comparison . . . . .	52
3.5 Conclusive remarks . . . . .	53

<b>4</b>	<b>Optical/Electrical readout of electromechanical coupling</b>	<b>55</b>
4.1	Experimental Setup . . . . .	55
4.2	LC circuit . . . . .	57
4.2.1	LC Circuit diagram and the PCB . . . . .	58
4.2.2	Inductor-The antenna . . . . .	59
4.2.3	Membrane-Capacitor chip . . . . .	62
4.2.4	Loss of the equivalent circuit . . . . .	62
4.3	Experimental Methods . . . . .	64
4.3.1	Optical Interferometry I- Doppler Vibrometer . . . . .	64
4.3.2	Optical Interferometry II- Michelson Interferometer . . . . .	65
4.3.3	Calibration of the mechanical amplitude . . . . .	68
4.3.4	Electrical characterization . . . . .	71
4.4	Data analysis and results . . . . .	72
4.4.1	Mechanically induced transparency regime . . . . .	73
4.4.2	Extraction of the coupling parameter ( $G$ ) in different ways . . . . .	78
4.4.3	Strong coupling regime . . . . .	81
4.5	Conclusive remarks . . . . .	86
<b>5</b>	<b>An opto-electromechanical sensor for detection of rf waves</b>	<b>87</b>
5.1	Voltage sensitivity under ambient rf noise . . . . .	87
5.1.1	First noise tests with the Michelson interferometer . . . . .	87
5.1.2	Experimental noise performance, model fits and discussion . . . . .	90
5.2	Johnson noise-limited performance with shielded inductors . . . . .	93
5.2.1	Reducing the noise . . . . .	93
5.2.2	Adjusting the optimum cooperativity . . . . .	96
5.3	Noise measurements with a cold resistor . . . . .	99
5.3.1	Noise temperature and the Y-factor method . . . . .	99
5.3.2	Preliminary measurements with liquid nitrogen . . . . .	100
5.3.3	Sub-300 K transducer noise temperature without excess noise . . . . .	107
5.4	Performance comparison . . . . .	108
5.5	Limitations of the setup . . . . .	109
5.5.1	Gap distance . . . . .	109
5.5.2	Mechanical damping . . . . .	110
5.5.3	Sensitivity limit due to instability . . . . .	110
5.6	RF to optical photon conversion in practice . . . . .	111
5.7	Conclusive remarks . . . . .	111
5.8	Future prospects and outlook . . . . .	112
<b>6</b>	<b>Optical cavity cooling with GaAs membranes</b>	<b>115</b>
6.1	GaAs membranes - Fabrication and characterization . . . . .	115
6.2	Setup for characterization and cooling of GaAs membranes . . . . .	118
6.3	Cooling mechanism . . . . .	119
6.4	Vibrational cooling results . . . . .	121
6.5	Investigation of the cooling mechanism . . . . .	124
6.6	Conclusive remarks and outlook . . . . .	125

---

<b>7</b>	<b>Summary and conclusion</b>	<b>127</b>
<b>A</b>	<b>Detailed schematics for the electrical circuit</b>	<b>129</b>
<b>B</b>	<b>FET Op-amp for the electrical measurements</b>	<b>131</b>
<b>C</b>	<b>Mechanical endurance of the membranes</b>	<b>133</b>
<b>D</b>	<b>Ultra-high precision resistors for the Y-factor measurement</b>	<b>135</b>
<b>E</b>	<b>Shot noise limited optical detection</b>	<b>137</b>
<b>F</b>	<b>Effective mass</b>	<b>139</b>



# Chapter 1

## Introduction

### 1.1 Background and motivation

Optomechanics and electromechanics have gained a large momentum in the last decade. Along with the advances in fabricating high-quality mechanical resonators [1, 2], a promising toolbox of physics has emerged together with the utilization of optical cavities and microwave resonator circuits. On the one side, optomechanical systems have shown progress with recent experimental demonstrations such as strong coupling of radiation pressure to mechanics [10], ground state cooling of a mechanical resonator [8] and quantum coherent coupling between optical and mechanical states [9]. On the other side, microwave fields in an electrical resonator circuit have been coupled to mechanical resonators [21] and ground-state cooling [11] as well as coherent state transfer [22] have also been achieved with these systems. Besides microwave and optical manipulation, high-quality mechanical resonators have found extensive use in various sensing applications such as highly sensitive displacement detection [3], temperature sensing [26], mass detection [27], magnetic resonance imaging of single electrons [23] and force detection at zeptonewton level [24]. Due to their ease of coupling to different degrees of freedom, it has been proposed to use mechanical resonators as transducers between charge and spin [25].

Given all these expeditious advances in optomechanical and electromechanical systems, the idea of combining the desirable features of the two in a hybrid opto-electromechanical setup has evoked a rapidly rising interest. A high-quality mechanical interface coupled to both optical and electrical systems can be utilized for efficient and faithful transfer of quantum microwave and optical states [12, 13]. A crucial advantage of converting an rf or microwave signal to optical domain is that quantum-limited signal detection can be routinely achieved with current laser technology, whereas in the microwave domain it becomes a tedious task even with expensive cryogenic amplifiers such as HEMT (high electron mobility transistor) [81] and JPA (Josephson parametric amplifier) [82]. Another advantage of optical systems appears in the transmission of signals over long distances, as fiber optic-links offer low-loss transfer whereas microwave channels are typically lossy and detrimental for fragile states [12].

In a theoretical work performed in collaboration with our group, a scheme has been proposed where a nanomembrane is coupled capacitively to an LC electrical resonator and to an optical resonator simultaneously in a hybrid setup (J. Taylor *et al* [19]). In this setup,

the membrane displacement changes the capacitance, thereby the LC resonance frequency - generating the electromechanical coupling. Since the membrane-LC circuit is placed in an optical cavity, a laser beam can be used to achieve considerable optomechanical coupling as well. It has been shown that the laser beam can be used to monitor the coupled electromechanical system by probing the cavity output and furthermore radiation-pressure cooling can be applied to the electrical circuit via the mechanical interface. Therefore, the envisioned setup enables both optical detection and cooling of rf resonators.

Inspired by the proposal in [19], the Quantum Membrane group at NBI (Niels Bohr Institute) - QUANTOP Labs (under the supervision of Prof. Eugene Polzik) started an experimental project in close collaboration with DTU Nanotech - Technical University of Denmark (Silvan Schmid and Anja Boisen). The main motivation of the experiment - within the timescale of this PhD study - was to realize an opto-electromechanical device for low-noise detection of weak radio waves at room temperature. Throughout the project, we have characterized the voltage sensitivity performance of our device thoroughly and demonstrated low-noise optical detection of rf signals. Although we have so far worked in the classical domain at room-temperature, extension of our setup to the quantum domain at cryogenic temperatures together with superconducting circuitry is a possible direction of research. We note that around the same time, relevant experimental works resulted in demonstration of coupling between microwave and optical photons in a piezoelectric nanomechanical material [84] and efficient rf to optical photon transfer in a cryogenic opto-electromechanical configuration [85].

## 1.2 Publications and conferences

### Journal papers

[P1] Optical detection of radio waves through a nanomechanical transducer  
T. Bagci, A. Simonsen, S. Schmid, L. G. Villanueva, E. Zeuthen, J. Appel, J. M. Taylor, A. Sørensen, K. Usami, A. Schliesser, E. S. Polzik.  
Accepted to *Nature* (2014).  
(preliminary version on arXiv:1307.3467).

[P2] Single-layer graphene on silicon nitride micromembrane resonators  
S. Schmid, T. Bagci, E. Zeuthen, J. M. Taylor, P. K. Herring, M. C. Cassidy, C. M. Marcus, L. G. Villanueva, B. Amato, A. Boisen, Y. C. Shin, J. Kong, A. Sørensen, K. Usami, E. S. Polzik.  
*Journal of Applied Physics* 115, 054513 (2014).

[P3] Optical cavity cooling of mechanical modes of a semiconductor nanomembrane  
K. Usami, A. Naesby, T. Bagci, B. M. Nielsen, J. Liu, S. Stobbe, P. Lodahl, E. S. Polzik.  
*Nature Physics* 8, 168-172 (2012).

[P4] High-Q optomechanical GaAs nanomembranes  
J. Liu, K. Usami, A. Naesby, T. Bagci, E. S. Polzik, P. Lodahl and S. Stobbe.  
*Applied Physics Letters* 99, 243102 (2011).

### Conference contributions

[C1] Optical readout of coupling between a nanomembrane and an LC circuit at room temperature

T. Bagci, A. Simonsen, E. Zeuthen, J. M. Taylor, L.G.Villanueva, S. Schmid, A. Sørensen, A. Schliesser, K. Usami and E.S. Polzik.

CLEO Europe - IQEC, Conference on Laser and Electro-optics, Munich (2013).

[C2] Graphene on silicon nitride micromembranes for optoelectromechanical devices

S. Schmid, T. Bagci, A.N. Rasmussen, P. Herring, M. Cassidy, C.M. Marcus, J. Taylor, A.S. Sørensen, K. Usami and E.S. Polzik.

Carbonhagen 2012 : 3rd Symposium on graphene and carbon nanotubes. 2012. p. 12.

### Talks/Presentations

[T1] Invited Talk - Optical readout of coupling between a nanomembrane and an LC circuit at room temperature

CLEO Europe- IQEC, Conference on Laser and Electro-optics. Munich, Germany (2013).

[T2] Talk - Hybrid cavity opto-electromechanics

QNLO Summer School, Sønderborg, Denmark (2012).

[T3] Poster presentation - Optoelectronic cooling of a GaAs membrane

Quantum Optics of Microresonators (Conference), Monte Verita, Switzerland (2011).

### Contribution of the author

The project regarding the realization of an opto-electromechanical device is the main work of the author within this PhD study. In paper [P1] - the author's main contribution, the experimental work (except fabrication) and data collection have been carried out extensively by the author and Anders Simonsen, together with significant help and guidance from Albert Schliesser. The formal theoretical framework and modelling behind this paper is mostly worked out by Albert Schliesser, with contributions from the author for the data analysis. The author's contribution to the development of the manuscript was substantial. In paper [P2] - the author's contribution is second to Silvan Schmid, with significant amount of work on the measurements, data collection and analysis.

Before starting the main opto-electromechanics project, the author has also been involved in a separate experiment - optical cooling of a GaAs (Gallium Arsenide) membrane - which, timewise, coincided with the first year of the PhD study. In paper [P3] - the main work of Koji Usami and Andreas Næsby, the author has contributed to the initial setup for the experimental project, data collection for several measurements and discussions for the manuscript. In paper [P4] - Jin Liu's main work, the author's contribution was to help for some part of the data analysis/presentation and discussions for the manuscript.

### 1.3 Chapter structure

The focus of the experimental work performed for this PhD work lies on the realization of an opto-electromechanical system for highly-sensitive detection of radio waves. The structure of the thesis is arranged such that the main work of the author- the opto-electromechanical project- is treated in detail and systematically, while the GaAs membrane experiment (to which the author has contributed) is discussed in Chapter 6 in a compact way (This has been treated in detail in Andreas Næsby's PhD thesis). Chapter 2 covers the theory of the opto-electromechanical system. The experimental part of the opto-electromechanical project is divided into three consecutive parts that follow the logical flow and unity towards the main goal and fit the actual chronological order of the experimental work. This includes the systematic investigation of capacitive coupling with different membrane types (Chapter 3), optical/electrical characterization of the coupled membrane-LC circuit (Chapter 4) and the opto-electromechanical system used as an optical radio wave sensor (Chapter 5). In the following chapter (Chapter 6), the GaAs project is presented as an independent topic. In Chapter 7, we conclude by summarizing the outcome of the thesis. A more detailed account of what is presented is given below with a short description of each chapter.

**Chapter 2 :** In this chapter, the theory behind our opto-electromechanical device is worked out. We first start with the treatment of vibrational modes of a mechanical resonator and write down the equations of motion for a harmonic oscillator. Subsequently, capacitive coupling is introduced where a mechanical resonator modulates the capacitance of a capacitor due to its displacement. For an intuitive understanding, the equivalent RLC circuit model is introduced for the mechanical resonator. In the next section, we switch to a more formal treatment of the theory, starting with the system Hamiltonian and writing down the Langevin equations of a coupled membrane - LC circuit system. We derive expressions that are essential tools in the modelling and analysis for the characterization and determination of the final noise performance of our device (Chapter 4 and Chapter 5).

**Chapter 3 :** We start with the underlying mechanism behind capacitive coupling and present our first experimental results with a membrane coupled to a capacitor, only. This chapter covers all the measurements we have performed with the Doppler Vibrometer at DTU and the investigation of different membrane types - bare, aluminum-coated and graphene-coated SiN membranes in terms of their electrostatic force constants and mechanical qualities. This study has helped us in understanding the interaction between the membrane and the capacitor which is crucial for the next step of introducing an inductor and realizing membrane- LC circuit coupling. But apart from that, the study in this chapter has yielded independently meaningful comparative results. Aluminum and graphene coated membranes show similar electrostatic performance and they clearly outperform SiN membranes. In addition, the coating eliminates the unwanted charging effects of bare SiN membranes. We also report advantages of graphene- coated membranes such as undegraded Q-factors and unchanged mass.

**Chapter 4 :** This chapter deals with the systematic measurements and analysis we have carried out with the coupled membrane- LC circuit system. We have utilized both electrical and optical detection for the characterization of the electromechanical coupling. The

experimental results in the mechanically induced transparency and strong coupling regimes are analyzed separately based on our model introduced in Chapter 2. We discuss several ways of extracting the coupling parameter  $G$  which shows our corroborative understanding of the underlying physics behind our device. We report large normal mode splitting, which exhibits the strong electromechanical coupling we can achieve with this system.

**Chapter 5 :** In this chapter, we discuss our experiments performed in order to achieve very low-noise optical detection of radio waves with our opto-electromechanical system. This is carried out via optical interferometric monitoring of the membrane vibrations. We first analyze the results we have obtained with high ambient noise due to inductive pickup. Then we describe our efforts to reach Johnson noise-limited (LC circuit) sensitivity by trying several inductor types and report the actual noise, together with inferred membrane and optical readout contributions. Finally, we discuss our experiments where we couple the inductor to an external coolable resistor (77K) in order to perform the Y-factor noise temperature measurements. Based on our final results, we compare the performance of our device to state-of-the-art operational amplifiers. In the end, we discuss the possible improvements and future prospects for our device.

**Chapter 6 :** We discuss briefly an independent project in this chapter which deals with optical cavity cooling of a GaAs membrane. In this experiment, we have explored a novel cooling mechanism originating from electron-hole pair generation and subsequent thermal stress release in the membrane. A mode temperature of 4K is achieved for a specific mechanical mode. The main results are outlined in a compact manner.

**Chapter 7 :** We wrap up the milestones of the work performed within this PhD thesis and discuss the outlook.



# Chapter 2

## Theory

In this chapter, we will discuss the equations of motion that govern our electromechanical system consisting of an LC circuit and a nanomechanical resonator, the motion of which- in its most general sense- is monitored by optical interferometry. We will start with the mechanical component and study the equations of motion for a thin vibrating membrane. Next, we will deal with a simple depiction of a mechanical resonator-coupled to a capacitor- which is modeled as an RLC circuit for an intuitive understanding. This introduction will form the basis for the capacitive coupling tests we will show in Chapter 3. We will then continue with a generic opto-electromechanical device, incorporating a mechanical resonator coupled to an LC circuit. We will follow a formal treatment starting from the system Hamiltonian and derive the Langevin equations for a mathematical understanding of the system. This treatment will lead to the equations for the noise and sensitivity performance of our device which we experimentally test in the following chapters. Finally, we will briefly discuss the concept of rf to optical photon conversion and extension of the device to GHz frequency range.

### 2.1 Vibrations of a thin membrane

The mechanical resonator, which is a thin nanomembrane in our case, is a crucial component of our hybrid device. With its ability to couple to both a capacitor and a laser beam, it forms the bridge between the rf photons and optical photons as a transducer. In this section we will aim at understanding the dynamics and equations governing the vibrations of the mechanical resonator, which in the end can be tracked by optical interferometry.

We will begin our treatment by introducing the elastic wave equation and follow the approach in *Theory of Elasticity* by Landau and Lifshitz [5]. Afterwards, by making the proper assumptions for the specific case of an externally stretched thin membrane, we will simplify the wave equation and solve it to find the eigenmodes of a square membrane.

We start by restricting our investigation to thin deformed plates where the thickness of the plate is small compared to the other two dimensions.  $x$  and  $y$  refer to the coordinate axis in the direction of the lateral displacements, whereas the variable  $z$  refers to the displacements perpendicular to the x-y plane of the plate. The full derivation of the elastic wave equation is rather lengthy, so we will give the key steps in [5] briefly. Following the general treatment for large deformations of plates ( $dz$  is allowed to be on the order of the thickness,

but still small enough so as to keep Hooke's law valid - relating stress and strain), we have the following definition for the two-dimensional strain tensor

$$u_{\alpha\beta} = \frac{1}{2} \left( \frac{\partial u_\alpha}{\partial x_\beta} + \frac{\partial u_\beta}{\partial x_\alpha} \right) + \frac{1}{2} \frac{\partial z}{\partial x_\alpha} \frac{\partial z}{\partial x_\beta} \quad (2.1)$$

where  $u_x$  and  $u_y$  form the two-dimensional vector  $u$  for pure stretching. Here, the indices  $\alpha$  and  $\beta$  run over  $x$  and  $y$  and the Einstein summation convention is used. Using the strain tensor and the stress tensor  $\sigma_{\alpha\beta}$  stemming from the stretching of the plate, one can write the total free energy of the plate as

$$F = \int (\Psi_1(z) + \Psi_2(u_{\alpha\beta})) df \quad (2.2)$$

where  $\Psi_2 = \frac{1}{2} h u_{\alpha\beta} \sigma_{\alpha\beta}$  is the total stretching energy per unit area with  $h$  denoting the thickness of the plate,  $\Psi_1$  is the bending energy per unit area (function of the Young's modulus and partial derivatives of  $z$ ) and  $df = dx dy$  is the surface element. The potential energy  $U$  in this case is  $U = - \int P \delta z df$  where  $P$  is the external force per unit area. Imposing the condition of minimum energy  $\delta F + \delta U = 0$  and calculating the variations of the integrals, one finally reaches the key equation

$$D \Delta^2 z - h \frac{\partial}{\partial x_\beta} \left( \sigma_{\alpha\beta} \frac{\partial z}{\partial x_\alpha} \right) = P \quad (2.3)$$

where  $\Delta = \frac{\partial^2}{\partial x^2} + \frac{\partial^2}{\partial y^2}$  is the two-dimensional Laplace operator and  $D$  is the flexural rigidity. We may now treat the vibrations of a thin membrane as a particular case of this equation. The membrane - as a result of the fabrication process - is bounded with a solid frame and externally stretched. This stretching is typically very large compared to the bending of the membrane, therefore we can neglect the first term in equation 2.3 and other longitudinal stress components of the stress tensor and simply write for equilibrium

$$h \sigma_{\alpha\beta} \frac{\partial^2 z}{\partial x_\alpha \partial x_\beta} + P = 0 \quad (2.4)$$

By assuming an isotropic stretching of the membrane and letting  $T$  be the magnitude of the stretching per unit length, then we have  $h \sigma_{\alpha\beta} = T \delta_{\alpha\beta}$ . With this, we reach the equation of equilibrium in a simple form

$$T \Delta z + P = 0 \quad (2.5)$$

Alternatively, the equation can be written as

$$T \Delta z = \rho h \ddot{z} \quad (2.6)$$

where  $\rho$  is the density of the membrane and  $\ddot{z}$  refers to the second time derivative of the transverse displacement. In our case for a membrane with tensile stress  $\mathcal{T}$  (defined per unit area) and film mass density  $\rho$  the equation takes the form  $\mathcal{T} \Delta z = \rho \ddot{z}$ . This leads to the standard form of the wave equation

$$\frac{\partial^2 z}{\partial x^2} + \frac{\partial^2 z}{\partial y^2} = \frac{1}{c^2} \frac{\partial^2 z}{\partial t^2} \quad (2.7)$$

relating the spatial derivatives and the time derivative via the speed of wave propagation

$$c = \sqrt{\frac{\mathcal{T}}{\rho}} \quad (2.8)$$

In order to solve the differential equation for  $z(x, y, t)$ , we shall write it as multiplication of three separable solutions  $X(x), Y(y)$  and  $T(t)$  [6]

$$z(x, y, t) = X(x)Y(y)T(t) \quad (2.9)$$

Inserting this form into the elastic wave equation and solving for the derivatives, we reach the following expression

$$YT \frac{d^2 X}{dx^2} + XT \frac{d^2 Y}{dy^2} = \frac{1}{c^2} XY \frac{d^2 T}{dt^2} \quad (2.10)$$

Dividing all the terms by  $XYT$  and multiplying by  $c^2$ , we get

$$\frac{c^2}{X} \frac{d^2 X}{dx^2} + \frac{c^2}{Y} \frac{d^2 Y}{dy^2} = \frac{1}{T} \frac{d^2 T}{dt^2} \quad (2.11)$$

There is only one possibility for a solution being that both sides are equal to the same

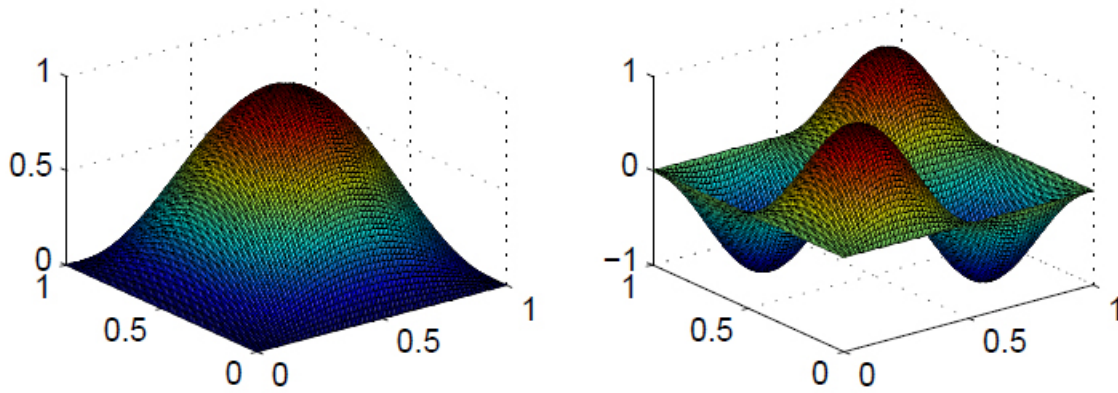


**Figure 2.1** Depiction of the vibrational eigenmodes of the membrane based on the solution of the elastic wave equation( (1,1) mode on the left and (2,2) mode on the right) .

constant yielding

$$\frac{1}{T} \frac{d^2 T}{dt^2} = -\Omega_m^2 \quad (2.12)$$

This is the well-known equation for a harmonic oscillator oscillating with frequency  $\Omega_m$ . Then  $T(t)$  becomes,

$$T(t) = A \cos(\Omega_m t) + B \sin(\Omega_m t) \quad (2.13)$$

Doing the same operation for the left hand side

$$\frac{c^2}{X} \frac{d^2 X}{dx^2} + \frac{c^2}{Y} \frac{d^2 Y}{dy^2} = -\Omega_m^2 \quad (2.14)$$

The equation can be re-written in a form as follows

$$\frac{1}{X} \frac{d^2 X}{dx^2} = -\frac{\Omega_m^2}{c^2} - \frac{1}{Y} \frac{d^2 Y}{dy^2} = -k_x^2 \quad (2.15)$$

by introducing the new constant  $k_x^2$ . The same procedure follows for the Y dependent terms leading to

$$\frac{1}{Y} \frac{d^2 Y}{dy^2} = k_x^2 - \frac{\Omega_m^2}{c^2} = -k_y^2 \quad (2.16)$$

imposing the new relationship for the constants

$$k_x^2 + k_y^2 = \frac{\Omega_m^2}{c^2} \quad (2.17)$$

The separate solutions for the  $x$  and  $y$  coordinates become

$$\begin{aligned} X &= C \cos(k_x x) + D \sin(k_x x) \\ Y &= E \cos(k_y y) + F \sin(k_y y) \end{aligned} \quad (2.18)$$

As the membrane is rigidly fixed from its ends, we can apply the boundary condition that the wave should vanish at the boundaries. Formally, these conditions imply that

$$z(0, y, t) = 0, \quad z(x, 0, t) = 0, \quad z(L_x, y, t) = 0, \quad z(x, L_y, t) = 0 \quad (2.19)$$

with the membrane dimensions  $L_x$  and  $L_y$ . The first two boundary conditions yield  $C=0$  and  $E=0$  and the other two yield  $\sin(k_x L_x) = 0$  and  $\sin(k_y L_y) = 0$ , thus the wave numbers  $k_x$  and  $k_y$  can be written as

$$k_x = \frac{i\pi}{L_x}, \quad k_y = \frac{j\pi}{L_y} \quad (2.20)$$

where  $i$  and  $j$  are integers.

The eigenfrequency of the mechanical oscillator  $\Omega_m$  can then be written as

$$\Omega_m = c\pi \sqrt{\left(\frac{i}{L_x}\right)^2 + \left(\frac{j}{L_y}\right)^2} \quad (2.21)$$

Here,  $i$  and  $j$  are integers referring to the specific vibrational modes. For the particular case of a square membrane with length  $L$  in each dimension, we have [1, 2]

$$\nu_m = \Omega_m/2\pi = \sqrt{\frac{\mathcal{T}}{4\rho L^2}} \sqrt{i^2 + j^2} \quad (2.22)$$

Finally, the most general form of a solution for the motion of a square membrane can be written as the sum of all vibrational modes

$$z(x, y, t) = \sum_{i=1}^{\infty} \sum_{j=1}^{\infty} [A_{ij} \cos(\Omega_{ij}t) + B_{ij} \sin(\Omega_{ij}t)] \sin\left(\frac{i\pi x}{d}\right) \sin\left(\frac{j\pi y}{d}\right) \quad (2.23)$$

where  $A_{ij}$  and  $B_{ij}$  are constants of motion depending on the initial conditions. At this point, it would be convenient to transform the problem of the transverse vibrations on the surface of a thin plate to a single point harmonic oscillator problem in one dimension. This can be done by introducing the so-called effective mass which accounts for the motion of different points in the plate, namely due to the spatial structure of the eigenmodes. Choosing a proper probing point (for example the antinode), one can assign a corresponding effective mass to the membrane (1/4 of the physical mass in case of a square membrane) [7] and then treat the membrane as a one-dimensional harmonic oscillator vibrating along the z-axis. The detailed discussion for the effective mass determination for a square membrane is given in Appendix F. Having made this transformation, we can write the equation of motion for our membrane as [14, 15]

$$mz(\ddot{t}) + m\Gamma_m \dot{z}(t) + kz(t) = F_{th}(t) \quad (2.24)$$

where  $m$  refers to the effective mass,  $\Gamma_m$  is the dissipation rate of the membrane to account for the phenomenologically inserted velocity-dependent damping term and  $k = m\Omega_m^2$  is the one-dimensional spring constant. The right-hand side of the equation has the force term  $F_{th}(t)$  which denotes the thermal Langevin force on the membrane. Following the approach in [14] and implementing a Laplace transform on the equation, we have the following equation in the frequency domain

$$-m\Omega^2 z_\Omega + i\Omega m\Gamma_m z_\Omega + kz_\Omega = F_{th}(\Omega) \quad (2.25)$$

Solving for  $z_\Omega$ , we find

$$z_\Omega = \frac{F_{th}(\Omega)}{m} \frac{1}{\Omega_m^2 - \Omega^2 - i\Omega\Gamma_m} \quad (2.26)$$

where  $|F_{th}(\Omega)|^2 = Sdf$  with  $S$  denoting the spectral density per bandwidth and  $\Omega_m$  is the natural resonance frequency of the mechanical oscillator. As the Langevin force, by using the fluctuation dissipation theorem, is given by (single-sided spectrum)

$$|F_{th}(\Omega)|^2 = 4k_B T m \Gamma_m \frac{d\Omega}{2\pi} \quad (2.27)$$

we end up with the power spectral density expression for the vibration amplitude in case of a thermally driven mechanical oscillator [14]

$$|z_\Omega|^2 = \frac{4k_B T \Gamma_m}{m} \frac{1}{(\Omega_m^2 - \Omega^2)^2 + (\Omega\Gamma_m)^2} \frac{d\Omega}{2\pi} \quad (2.28)$$

This is the expression - which is a Lorentzian- that governs the mechanical power in the frequency domain in case of only thermal noise. In a series of experiments, we monitor the membrane spectral shape by optical detection and fit the recorded data to this function in order to extract the intrinsic parameters like  $\Gamma_m$  and  $m$  of the membrane. However, the mechanical transfer function is strongly modified when coupled to an LC resonator and the detailed treatment of this is given in the section with Langevin equations.

## 2.2 Mechanical resonator-capacitor coupling

In this section, we will focus on the description of a vibrating mechanical resonator which is coupled to a capacitor. We will first write down the capacitive force on the resonator - typical for NEMS capacitive devices. The main idea is that the membrane acts as a capacitance modulating element due to its varying displacement and this can be interpreted as a current flowing through the circuit due to this modulated capacitance [17,18]. For this part, we will follow [16] and in its simplest form, the equivalent circuit can be represented by Fig. 2.2 below where the membrane is represented as a series RLC circuit in parallel to  $C_0$ .

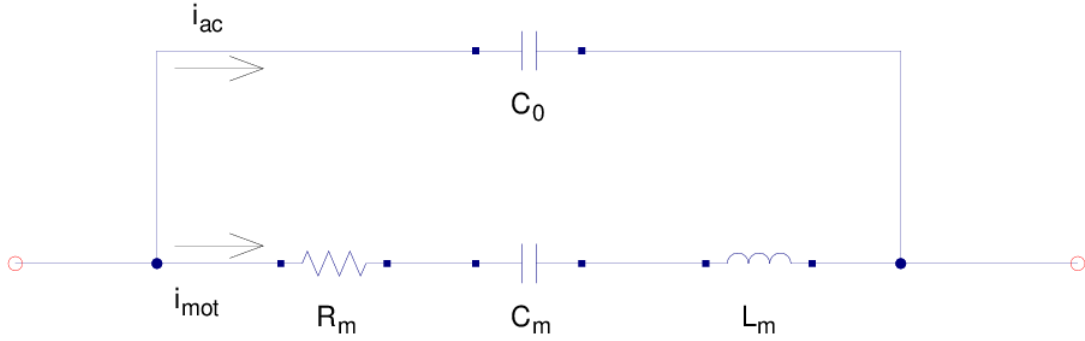


**Figure 2.2** Equivalent circuit picture of a mechanical resonator coupled to a capacitor.  $C_0$  is the unchanging capacitor with current  $i_{ac}$  flowing through that part. The membrane brings a modulated capacitance  $C_m$  which causes a motional current  $i_{mot}$  in a parallel branch to  $C_0$ .

We start by writing the electrical energy for a capacitive system where one of the end plate, which constitutes the mechanical resonator, is free to move and therefore brings a position dependent capacitance. For the general case of a dc bias voltage and rf voltage applied (at  $\Omega_m$ ) on the capacitor legs, we have

$$E = \frac{1}{2}C(V_{dc} + V_{rf})^2 = \frac{1}{2}C(V_{dc}^2 + 2V_{dc}V_{rf} + V_{rf}^2) \quad (2.29)$$

and concentrating on the response at the mechanical resonance,  $V_{rf}^2$  term that resonates at twice the resonance frequency and the static term  $V_{dc}^2$  drop out. Inserting the general expression for capacitance between two parallel plates  $C = \epsilon A/(d-x)$  where  $\epsilon$  is the permittivity,  $A$  is the area of the plate,  $d$  is the initial separation distance and  $x$  is the displacement of the mechanically movable part, we shall write the electrostatic force as the first derivative of the energy  $f = -\frac{\partial E}{\partial x}$  which yields for the magnitude of the force

$$f = (V_{dc}^2 + 2V_{dc}V_{rf} + V_{rf}^2)\epsilon \frac{A}{2(d-x)^2} \approx V_{dc}V_{rf}\epsilon \frac{A}{d^2} \quad (2.30)$$

where we have used two assumptions ( $x \ll d$  and  $V^2 \approx 2V_{dc}V_{rf}$ ). It would then be convenient to define the electrostatic transduction factor which converts a given  $V_{rf}$  to

an actuation force  $f$  as follows,

$$f = \eta V_{rf} \text{ with } \eta = V_{dc} \epsilon \frac{A}{d^2} \quad (2.31)$$

In case of a fixed voltage condition where we bias the capacitor with a dc voltage, the current through the capacitor is given by

$$i = \frac{dq}{dt} = \frac{\partial(CV)}{\partial t} = C \frac{\partial V}{\partial t} + V \frac{\partial C}{\partial t} \quad (2.32)$$

and by using the approximations we made before, one reaches

$$i = C_0 \frac{\partial V_{rf}}{\partial t} + \eta \frac{\partial x}{\partial t} = i_{rf} + i_{mot} \quad (2.33)$$

where  $C_0$  is the non-varying offset capacitance. The first term is the standard ac current that passes through the capacitor and the second term is the contribution from the vibrations of the membrane that results in a motional current through the capacitor.

In order to be able to represent the mechanical resonator with an equivalent RLC circuit, we first write the equations of motion for a damped harmonic oscillator in the time domain

$$m \frac{\partial^2 x}{\partial t^2} + \Gamma_m \frac{\partial x}{\partial t} + kx = f \quad (2.34)$$

We can replace  $\frac{\partial x}{\partial t}$  by  $\frac{i_{mot}}{\eta}$  to write the formula in terms of electrical parameters like current and also inserting  $f = \eta V_{rf}$ , we end up with the following equation

$$\frac{m}{\eta^2} \frac{\partial i_{mot}}{\partial t} + \frac{\Gamma_m}{\eta^2} i_{mot} + \frac{k}{\eta^2} \int i_{mot} dt = V_{rf} \quad (2.35)$$

The equation of motion for a series RLC circuit (with  $L_m, R_m$  and  $C_m$ ) is given by

$$L_m \frac{\partial i_{mot}}{\partial t} + R_m i_{mot} + \frac{1}{C_m} \int i_{mot} dt = V_{rf} \quad (2.36)$$

therefore we can rewrite equation 2.35 with the following transformation between electrical and mechanical parameters [16, 17]

$$\begin{aligned} R_m &= \frac{\Gamma_m}{\eta^2} = \sqrt{km}/Q\eta^2 \\ C_m &= \eta^2/k \\ L_m &= m/\eta^2 \end{aligned} \quad (2.37)$$

where  $Q$  is the mechanical quality factor. This shows that given the mechanical parameters of the mechanical resonator, we can represent it as a series RLC circuit with the electrical parameters as formulized above. The treatment so far gives an intuitive picture of the two-way coupling between the capacitor and the mechanical resonator. An actuation voltage applied to the capacitor electrodes drives the membrae via the capacitive force and conversely the mechanical vibrations create a modulated capacitance. This results in a motional current that can be modelled electrically on top of the electrical circuit it is coupled to.

### 2.3 Langevin equations of motion for the electromechanical system (Membrane-LC)

In this section, we will give a formal treatment of the equations of motion that govern an opto-electromechanical system where an LC circuit (now an inductor is introduced) is coupled to a nanomechanical resonator via capacitive coupling and the mechanical vibrations are read out via optical interferometry. For the sake of generality, we model the electrical circuit as a series RLC circuit and the mechanical resonator acts as a perturbation on the total capacitance of the circuit. Here, we will stick to the formalism that is worked out by A. Schliesser in the SI of our work [4] and we will use it to model and describe our experimental setup. The following data analysis in the subsequent chapters is to a large extent based on the equations of motion we derive in this section. We start by writing down the Hamiltonian [19] of our electromechanical system based on the simplified electrical circuit (Fig. 2.3) as follows (back-action of the optical readout is negligible in our case, therefore it acts a non-perturbative probe)

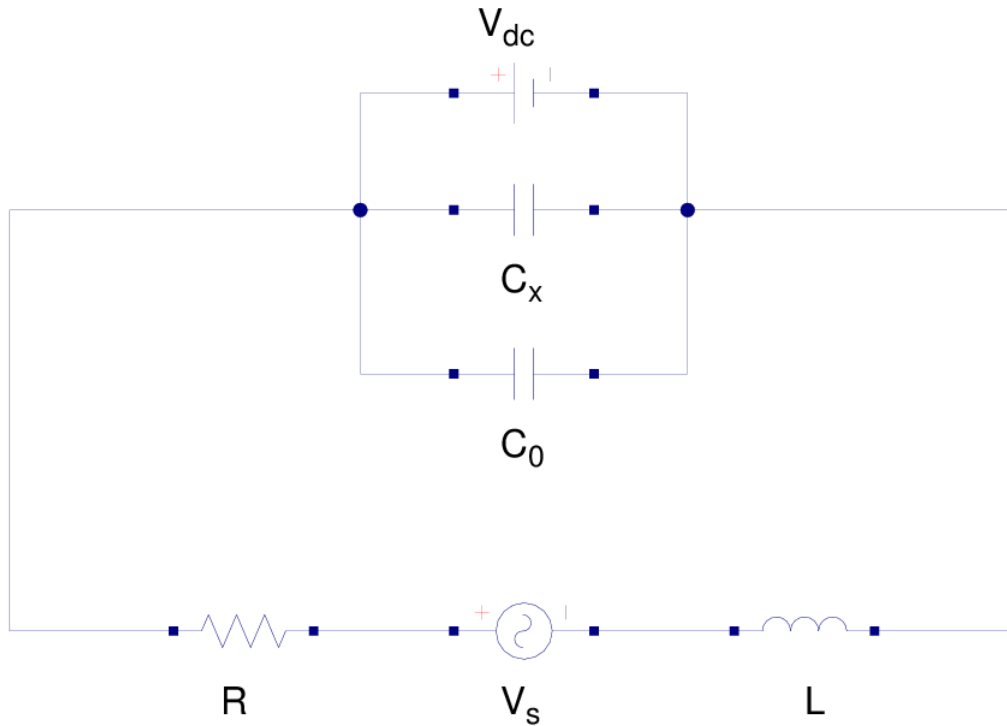


**Figure 2.3** Simplified circuit diagram for a generic LC resonator circuit with resistive loss  $R$  (assigned to the inductor),  $V_s$  (Johnson noise source) and a position dependent capacitance  $C_0 + C_x$  due to capacitive coupling to a mechanical resonator.  $V_{dc}$  is the bias voltage that is applied to the capacitor electrodes to enhance the coupling (A large capacitor in series to the inductor is used in the experiment in order to avoid short-circuiting of the dc bias which is not shown here).

$$H = \frac{\phi^2}{2L} + \frac{p^2}{2m} + \frac{m\Omega_m^2 x^2}{2} + \frac{q^2}{2C(x)} - qV \quad (2.38)$$

where  $\phi$  and  $q$  denote the flux of the inductor (with inductance  $L$ ) and the charge on the capacitors (with capacitance  $C(x)$ ) forming an LC resonator circuit with eigenfrequency  $\Omega_{LC} = \frac{1}{\sqrt{LC}}$ .  $x$  and  $p$  denote the displacement and momentum of the mechanical resonator, respectively. We note that we only deal with one vibrational mode of the mechanical resonator (square membrane in our case) which is the fundamental drum mode with effective mass  $m$  and eigenfrequency  $\Omega_m$ . The origin of the electromechanical coupling is encoded in the  $\frac{q^2}{2C(x)}$  term which refers to the displacement dependence capacitance of the circuit. Applying the Langevin approach on the Hamiltonian, we reach the following set of equations

$$\dot{x} = \frac{p}{m} \quad (2.39)$$

$$\dot{p} = -m\Omega_m^2 x - \frac{q^2}{2} \frac{\partial}{\partial x} \left( \frac{1}{C(x)} \right) - \Gamma_m p - \delta F_{th} \quad (2.40)$$

$$\dot{q} = \frac{\phi}{L} \quad (2.41)$$

$$\dot{\phi} = -\frac{q}{C(x)} - \Gamma_{LC} \phi + V \quad (2.42)$$

where  $\Gamma_m$  denotes the dissipation rate of the membrane and the electrical loss in the LC circuit  $\Gamma_{LC} = R/L$  is modeled as a resistive element ( $R$ ) attached in series to the coil. We also add a term  $F_{th}$  to account for the thermal Langevin force on the membrane and a driving voltage term  $V$  to refer to a voltage induced in the inductor.

From this point on, we will write the voltage  $V$  as the sum of a dc bias voltage  $V_{dc}$  and a small fluctuating term  $\delta V$  together with the total charge as

$$V(t) = V_{dc} + \delta V(t) \quad (2.43)$$

$$q(t) = \bar{q} + \delta q(t) \quad (2.44)$$

and we write the terms  $x$ ,  $p$  and  $\phi$  as the sum of their equilibrium values  $\bar{x}$ ,  $\bar{p}$  and  $\bar{\phi}$  plus small fluctuations around these values in order to be able to switch to the picture of linearized Langevin equations. We can then express the new form of the set of equations as follows (first order perturbations)

$$\dot{\delta x}(t) = \frac{\delta p(t)}{m} \quad (2.45)$$

$$\dot{\delta p}(t) = -m\Omega_m^2 \delta x(t) - \frac{\bar{q}^2}{2} \frac{\partial^2}{\partial x^2} \left( \frac{1}{C(x)} \right) \Big|_{x=\bar{x}} \delta x(t) - \Gamma_m p - \underbrace{\bar{q} \frac{\partial}{\partial x} \left( \frac{1}{C(x)} \right) \Big|_{x=\bar{x}}}_{G} \delta q(t) - \delta F_{th}(t) \quad (2.46)$$

$$\dot{\delta q}(t) = \frac{\delta \phi(t)}{L} \quad (2.47)$$

$$\dot{\delta \phi}(t) = -\frac{\delta q(t)}{C(\bar{x})} - \underbrace{\bar{q} \frac{\partial}{\partial x} \left( \frac{1}{C(x)} \right) \Big|_{x=\bar{x}}}_{G} \delta x(t) - \Gamma_{LC} \delta \phi(t) + \delta V(t) \quad (2.48)$$

where we have the conditions pertaining to the equilibrium state

$$m\Omega_m^2 \bar{x} = -\frac{\bar{q}^2}{2} \frac{\partial}{\partial x} \left( \frac{1}{C(x)} \right) \Big|_{x=\bar{x}} = \frac{\bar{q}^2}{2} \frac{C'(\bar{x})}{C(\bar{x})^2} \quad (2.49)$$

$$\bar{q} = V_{dc} C(\bar{x}) \quad (2.50)$$

$$\bar{p} = \bar{\phi} = 0 \quad (2.51)$$

Here, equation 2.49 gives the static displacement of the membrane due to the capacitive force on it, leading to a new equilibrium position and equation 2.50 gives the static charge on the capacitor due to the applied dc bias voltage. A crucial parameter for the system, named the coupling parameter  $G$ , is introduced here which is given by

$$G = \bar{q} \frac{\partial}{\partial x} \left( \frac{1}{C(x)} \right) \Big|_{x=\bar{x}} = -\bar{q} \frac{C'(\bar{x})}{C(\bar{x})^2} = -V_{dc} \frac{C'(\bar{x})}{C(\bar{x})} \quad (2.52)$$

The coupling parameter is linearly proportional to the applied dc voltage and the ratio of the modulated capacitance to the total capacitance. It also provides a convenient direct link between voltage fluctuations in the circuit and mechanical fluctuations of the membrane. An important feature of the electromechanical system - namely the frequency shift of the mechanical resonator due to the electrostatic force in addition to the intrinsic spring constant - has already been discussed in the previous chapters and here it appears related the second derivative of the  $q^2/2C(x)$  term which in the end looks like

$$\Delta\Omega_m = \frac{\bar{q}^2}{4m\Omega_m} \frac{\partial^2}{\partial x^2} \left( \frac{1}{C(x)} \right) \Big|_{x=\bar{x}} \quad (2.53)$$

We now transform the time-dependent set of equations of motion to frequency domain with a Fourier transform and also absorb the frequency shift into the redefined  $\Omega_m$ .

$$-i\Omega \delta x(\Omega) = \delta p(\Omega)/m \quad (2.54)$$

$$-i\Omega \delta p(\Omega) = -m\Omega_m^2 \delta x(\Omega) - \Gamma_m \delta p(\Omega) - G\delta q(\Omega) - \delta F_{th}(\Omega) \quad (2.55)$$

$$-i\Omega \delta q(\Omega) = \delta \phi(\Omega)/L \quad (2.56)$$

$$-i\Omega \delta \phi(\Omega) = -\delta q(\Omega)/C - \Gamma_{LC} \delta \phi(\Omega) - G\delta x(\Omega) - \delta V(\Omega) \quad (2.57)$$

At this point it would be convenient to introduce the bare susceptibilities for the mechanical resonator and the LC circuit as well as their modified forms due to the electromechanical coupling, namely the effective susceptibilities as follows

$$\chi_m(\Omega) = \frac{1}{m(\Omega_m^2 - \Omega^2 - i\Omega\Gamma_m)} \quad (2.58)$$

$$\chi_{LC}(\Omega) = \frac{1}{L(\Omega_{LC}^2 - \Omega^2 - i\Omega\Gamma_{LC})} \quad (2.59)$$

$$\chi_{m, \text{eff}}(\Omega) = \frac{1}{(\chi_m^{-1}(\Omega) - G^2 \chi_{LC}(\Omega))} \quad (2.60)$$

$$\chi_{LC, \text{eff}}(\Omega) = \frac{1}{(\chi_{LC}(\Omega)^{-1} - G^2 \chi_m(\Omega))} \quad (2.61)$$

Now we establish the link between the coupling parameter  $G$  and the electromechanical coupling rate  $g_{em}$  through the zero-point fluctuations of the membrane displacement  $x_{zpf}$  and capacitor charge  $q_{zpf}$

$$\hbar g_{em} = G x_{zpf} q_{zpf} = G \sqrt{\frac{\hbar}{2m\Omega_m}} \sqrt{\frac{\hbar}{2L\Omega_{LC}}}, \quad (2.62)$$

It is then possible to write down the electromechanical cooperativity [20, 21], a very crucial parameter for the system that relates the coupling rate to the individual dissipation rates of the mechanical resonator and the electrical circuit as follows

$$\mathcal{C}_{em} = \frac{4g_{em}^2}{\Gamma_m \Gamma_{LC}} \quad (2.63)$$

Having established the equations of motion and relations that govern our electromechanical system, we now look at the two experimentally feasible methods of probing the system. First, we concentrate on the **electrical** response of the system which can be probed non-perturbatively (in our experiment via an op amp) at the leads of the capacitor by measuring the voltage across the capacitor

$$V_c = \frac{q}{C(x)} = \bar{V}_c + \delta V_c = (\bar{q} + \delta q) \left( \frac{1}{C(\bar{x})} + \left. \frac{\partial}{\partial x} \frac{1}{C(x)} \right|_{x=\bar{x}} \delta x \right) \quad (2.64)$$

and neglecting the small nonlinear terms, we end up with

$$\delta V_c = \frac{\delta q}{C(\bar{x})} + G \delta x \quad (2.65)$$

By using the set of Langevin equations in the Fourier domain, we can write the voltage across the capacitor as follows

$$\begin{aligned} \delta V_c(\Omega) &= \left( \frac{1}{C(\bar{x})} - \chi_m(\Omega) G^2 \right) \delta q(\Omega) = \\ &= \left( \frac{1}{C(\bar{x})} - \chi_m(\Omega) G^2 \right) \underbrace{\left( \chi_{LC}(\Omega)^{-1} - G^2 \chi_m(\Omega) \right)^{-1}}_{\chi_{LC,eff}^{\text{eff}}(\Omega)} (-\delta V_s(\Omega)) \end{aligned} \quad (2.66)$$

where the circuit is driven via inductive coupling through the inductor port with a signal  $\delta V_s(\Omega)$ . The driving signal is supposed to be large with respect to the fluctuating terms. Equation 2.66 is one of the key equations describing the voltage dynamics in the circuit influenced by the presence of coupling to the mechanical resonator. The electrical response of the system is now altered due to the effective susceptibility  $\chi_{LC,eff}$  originating from the coupling dynamics. An obvious consequence of this coupled dynamics is the appearance of a mechanically induced transparency window within the LC resonance bandwidth stemming from the interference of the probe voltage and the back-coupled voltage due to the membrane fluctuations. Observation of this coupling physics has been realized in an optomechanical (OMIT- Optomechanically induced transparency [20]) and electromechanical (EMIT- Electromechanically induced transparency [21]) setup. This is one of the phenomena we will refer quite often in order to analyze our experimental results which will be discussed in

detail in the following chapters. We note that the appearance of the mechanically induced dip is a purely classical interference phenomenon that is encoded in the Langevin equations.

Next we turn to another way of extracting information regarding the electromechanical system which can be implemented via purely **optical** means. Just like the voltage fluctuations in the circuit, the displacement fluctuations of the membrane reveal the coupled nature of the electromechanical system. This becomes clear when the Langevin equations are arranged such that  $\delta x(\Omega)$  is written in terms of the total force acting on it and the modified mechanical susceptibility of the membrane as follows

$$(\chi_m^{-1}(\Omega) - G^2 \chi_{LC}(\Omega)) \delta x(\Omega) = -\delta F_{th}(\Omega) + G \chi_{LC}(\Omega) \delta V(\Omega) \quad (2.67)$$

or in a more compact form by using  $\chi_{m,\text{eff}}$

$$\delta x(\Omega) = \chi_{m,\text{eff}}(\Omega) (-\delta F_{th}(\Omega) + G \chi_{LC}(\Omega) \delta V(\Omega)) \quad (2.68)$$

Equation 2.68 shows that it is possible to extract electromechanical coupling parameters also by looking at the mechanical response around resonance. In terms of optical detection, it would show up in the phase fluctuations of light hitting the membrane, which is for the sake of generality, a part of an interferometric path. Following the well-known phase relation

$$\delta \varphi_{\text{mem}} = 2k \delta x \quad (2.69)$$

and replacing  $\delta x$  with 2.68, the measured optical phase shift becomes

$$\delta \varphi(\Omega) = 2k \chi_m^{\text{eff}}(\Omega) [-\delta F_{th}(\Omega) + G \chi_{LC}(\Omega) \delta V(\Omega)] + \delta \varphi_{\text{im}}(\Omega) \quad (2.70)$$

where  $\delta \varphi_{\text{im}}$  refers to the imprecision term coming from the optical readout. In our experiments, we probe the optical phase fluctuations due to the mechanical displacements via interferometric means (Doppler Vibrometry and Michelson Interferometry). An immediate consequence of electromechanical coupling acting on the membrane is the change in the mechanical susceptibility. This is manifest in the modification of the mechanical linewidth (broadening in case of  $Q_m \gg Q_{LC}$ ) which can be summarized in the following relation

$$\Gamma_{m,\text{eff}} = \Gamma_m (1 + \mathcal{C}_{\text{em}}) \quad (2.71)$$

As the cooperativity is increased, the membrane linewidth starts to broaden due to its coupling to a more lossy resonator. To sum up, the presence of electromechanical coupling manifests itself both in the electrical and optical readout, giving us two independent ways of quantifying the coupling parameters of the device. We note that the treatment here so far has dealt with the special case of dc drive. In the section discussing the alternative way of representing the coupling strength, we will write it as a general voltage term which can also be an ac driving voltage and make use of it for future goals related to the experiment.

## 2.4 Voltage sensitivity and noise

In this section, we will follow the equations we have derived in the previous section and use them to write down the voltage sensitivity of our opto-electromechanical system taking

into account the relevant noise sources. The motivation behind this treatment is to see how this opto-electromechanical device can be used as a very sensitive sensor by converting an rf input signal to an optical signal via nanomechanics. Focusing on optical detection, we can start by writing down the spectral density of phase fluctuations by taking the square of the expression in equation 2.70 and omitting the cross coupling terms since we assume uncorrelated inputs for  $\delta V$ ,  $\delta F_{\text{th}}$  and  $\delta\varphi_{\text{im}}$ . Thus the total phase noise becomes

$$S_{\phi\phi}^{\text{tot}}(\Omega) = (2k)^2 |\chi_{\text{m,eff}}(\Omega)|^2 \left( |G\chi_{LC}(\Omega)|^2 S_{VV}(\Omega) + S_{FF}^{\text{th}}(\Omega) \right) + S_{\phi\phi}^{\text{im}}(\Omega) \quad (2.72)$$

where  $S_{VV}(\Omega)$  and  $S_{FF}^{\text{th}}(\Omega)$  refer to the power spectral densities (double-sided) for the voltage fluctuations and thermal Brownian motion of the membrane, respectively. As can be seen, in order to be detected, a voltage signal has to be larger than the two noise contribution terms, namely the thermal fluctuations of the membrane and the optical readout noise. It is worth to note the situation for the case when the optical readout noise can be neglected. Then the thermal noise - limited voltage sensitivity becomes

$$S_{VV}^{\text{mem}}(\Omega) = \frac{S_{FF}^{\text{th}}(\Omega)}{|G\chi_{LC}(\Omega)|^2} = \left| \frac{\chi_{LC}(\Omega_{LC})}{\chi_{LC}(\Omega)} \right|^2 \cdot 2k_{\text{B}} \frac{T_{\text{m}}}{\mathcal{C}_{\text{em}}} R \quad (2.73)$$

On resonance ( $\Omega_m = \Omega_{LC}$ ), it further simplifies to

$$S_{VV}^{\text{mem}}(\Omega_m) = 2k_{\text{B}} \frac{T_{\text{m}}}{\mathcal{C}_{\text{em}}} R \quad (2.74)$$

The result is remarkable in the sense that due to the rich coupled nature of the system, the voltage sensitivity can be increased significantly since the thermal membrane fluctuations are suppressed by the cooperativity. Thus, as a fundamental limit, the individual membrane thermal noise contribution can be much lower than the physical temperature of the membrane ( $T_m$ -room temperature in our case).

Following the same treatment for the optical readout noise (which in principle is the quantum shot-noise of light), we find the voltage sensitivity as

$$S_{VV}^{\text{im}}(\Omega) = \frac{S_{\phi\phi}^{\text{im}}(\Omega)}{|2k\chi_{\text{m,eff}}(\Omega)G\chi_{LC}(\Omega)|^2}, \quad (2.75)$$

and again at resonance, this becomes

$$S_{VV}^{\text{im}}(\Omega_r) = \frac{2n^{\text{im}}\hbar\Omega_r \cdot R(1 + \mathcal{C}_{\text{em}})^2}{\mathcal{C}_{\text{em}}} \quad (2.76)$$

with

$$n^{\text{im}} = \frac{S_{xx}^{\text{im}}(\Omega_r)}{4x_{\text{zpf}}^2/\Gamma_m} \quad (2.77)$$

referring to the imprecision in terms of the number of quanta. Here  $S_{xx}^{\text{im}}$  is the optical readout imprecision expressed in terms of displacement noise. In Chapter 5, the relationship between the displacement imprecision and optical readout noise will become more clear within the discussion of optimal cooperativity.

## Noise Temperature

The spectral noise power densities we have dealt with in the previous section can for convenience be translated into effective noise temperatures. We can therefore assign a noise temperature to our transducer/amplifier by summing all the individual contributions - namely the thermal noise of the membrane, optical readout noise and Johnson noise of the circuit. We start by writing down the relationship between the total voltage noise and the total phase noise

$$S_{VV}^{\text{tot}}(\Omega) = S_{\phi\phi}^{\text{tot}}(\Omega)/|\chi^{\text{tot}}(\Omega)|^2 \quad (2.78)$$

where

$$\chi^{\text{tot}}(\Omega) = 2k\chi_{\text{m,eff}}(\Omega)G\chi_{LC}(\Omega) \quad (2.79)$$

is the transducer transfer function. Also including the Johnson noise of the LC circuit  $S_{VV}^J(\Omega) = 2k_B T_R R$ , we then have the total voltage noise

$$S_{VV}^{\text{tot}}(\Omega) = S_{VV}^J(\Omega) + S_{VV}^{\text{mem}}(\Omega) + S_{VV}^{\text{im}}(\Omega) \quad (2.80)$$

Writing down the individual contributions explicitly and imposing the resonance condition again, we reach

$$S_{VV}^{\text{tot}}(\Omega_r) = 2k_B T_R R + 2k_B \frac{T_m}{\mathcal{C}_{\text{em}}}(R + R_s) + \frac{2n^{\text{im}}\hbar\Omega_r \cdot (R + R_s)(1 + \mathcal{C}_{\text{em}})^2}{\mathcal{C}_{\text{em}}} \quad (2.81)$$

At this stage, we have introduced a series source resistance  $R_s$  that is connected to the input of the transducer. This is done in order to switch to the conventional language of electrical engineering where an amplifier noise is referred with respect to a source resistance at its input. The noise temperature of a receiver is defined as the temperature of a source resistor that would generate power equal to the noise power of the receiver [28]. As can be seen, the noise equation above takes into account the fact that the additional source resistance alters the cooperativity of the system due to increased electrical damping. By using equation 2.81, we can write the total noise temperature of the transducer referenced to the input resistance  $R_s$  as

$$T_n = \frac{R}{R_s} T_R + \frac{R + R_s}{R_s} \left( \frac{T_m}{\mathcal{C}_{\text{em}}} + \frac{(1 + \mathcal{C}_{\text{em}})^2}{\mathcal{C}_{\text{em}}} n^{\text{im}} \hbar \Omega_r \right) \quad (2.82)$$

By defining a loading factor  $\eta_e = \frac{R_s}{R_s + R}$  to account for the effect of the source resistance and the optical readout noise temperature  $T_L = n^{\text{im}} \hbar \Omega_r$ , we reach the following form for the noise of the transducer

$$T_n = \left( \frac{1}{\eta_e} - 1 \right) T_R + \frac{1}{\eta_e} \left( \frac{T_m}{\mathcal{C}_{\text{em}}} + \frac{(1 + \mathcal{C}_{\text{em}})^2}{\mathcal{C}_{\text{em}}} T_L \right) \quad (2.83)$$

Equation 2.83 is a crucial result describing the noise contributions due to different elements of our hybrid opto-electromechanical device as an effective noise temperature. This total output noise temperature of the transducer can experimentally be determined by implementing the so-called Y-factor method [29] which will be explained in Chapter 5. The source resistor temperature can be varied and the output noise of the amplifier at different

temperatures can be measured to extract the actual transducer noise in the presence of thermal LC noise. Decomposing the total noise into its constituents, the first term now appears as the Johnson noise of the LC circuit, however modified due to coupling to the source resistor which might be at a different physical temperature. The second term is the membrane noise contribution which is suppressed by the modified cooperativity due to the additional source resistance. The third term is the optical noise which also scales with the modified cooperativity. We will use this formula in order to analyze our data in chapter 5 regarding the noise measurements of our device with external loading and cooling.

## 2.5 Alternative derivation of the coupling rate

Our treatment has so far involved writing down the Hamiltonian and solving the Langevin equations of the coupled electromechanical system. It can be seen from the set of equations we have reached that the voltage fluctuations and mechanical displacement are coupled via the coupling parameter  $G$  and it can also be expressed through the electromechanical coupling rate  $g_{em}$ . It would be useful to reach the coupling rate in an alternative way, where it is expressed via the mean displacement of the membrane - namely by  $g_{em} = \sqrt{\Omega_m \Omega_{LC}} \sqrt{\frac{x_e - x_0}{2\zeta}}$  as formulated in the proposal by Taylor *et al* [19]. Thus in this section, we will attempt to reach the same expression by going through the intermediate steps. In the end, we will also mention the form of the coupling rate for the case of an ac drive. The Hamiltonian is the same as before so we begin by writing the interesting term that brings the coupling

$$H_{int} = \frac{q^2}{2C(x)} \quad (2.84)$$

Expanding  $C(x)$  around a large offset capacitance and assuming small changes in capacitance, we can write

$$H_{int} = \frac{q^2}{2(C_0 + C(x))} = \frac{q^2}{2(1 + \frac{C_x}{C_0})C_0} \approx \frac{q^2}{2C_0} \left(1 - \frac{C_x}{C_0}\right) \quad (2.85)$$

Dropping out the offset term ( $q^2/2C_0$ ) that is independent of  $C(x)$ , writing the total charge as a large classical value  $q_0$  plus a small fluctuating term  $\delta q$  as  $q = q_0 + \delta q$  and applying linearization (omitting  $q_0^2$  and  $\delta q^2$  and only keeping  $2q_0\delta q\delta x$ ), we end up with

$$H_{int} = -\frac{q_0}{C_0^2} \frac{\partial C}{\partial x} \delta q \delta x \quad (2.86)$$

and here we have replaced the position dependent capacitance (to first order approximation) with  $C(x) = \frac{\partial C}{\partial x} \delta x$ . Next we find the new equilibrium position due to the applied bias voltage  $V$ . This can be found by equating the derivative of the capacitive force to the spring force acting on the membrane.

$$-\frac{1}{2} \frac{\partial C}{\partial x} V^2 = -m\Omega_m^2 (x_0 - x_e) \quad (2.87)$$

where  $x_e$  is the equilibrium position at  $V = 0$  and  $x_0$  is the new equilibrium position with the applied voltage  $V$  (although in general it can be an ac voltage, it is assumed to be dc

in this case). We now write this equation in a slightly different manner with the convenient characteristic length  $\zeta^{-1} = -C^{-1}\partial C/\delta x_m|_{x_0}$  introduced in [19]

$$x_0 - x_e = -\frac{q_0^2}{C(x_0)} \frac{1}{\Omega_m} \frac{x_{\text{zpf}}^2}{\zeta} \quad (2.88)$$

and with  $\hbar = 1$ , we have defined the zero point fluctuations of charge and position as  $q_{\text{zpf}} = 1/\sqrt{2L\Omega_{LC}}$  and  $x_{\text{zpf}} = 1/\sqrt{2m\Omega_m}$  with the new equilibrium charge  $q_0 = C(x_0)V$ . By using 2.88 and reexpressing the equilibrium charge, we have

$$q_0 = \sqrt{(x_e - x_0)\Omega_m}\sqrt{2m\zeta C_0} \quad (2.89)$$

Here we use the sign convention such that  $(x_e - x_0)$  is positive and consequently  $\frac{\partial C}{\partial x}$  is negative. We have also replaced  $C(x_0)$  by  $C_0$ . Now by inserting this expression for  $q_0$  into the interaction Hamiltonian in 2.86, we get

$$H_{\text{int}} = \frac{\sqrt{(x_e - x_0)\Omega_m}\sqrt{2m\zeta C_0}}{C_0} \underbrace{\left(-\frac{1}{C_0} \frac{\partial C}{\partial x}\right)}_{\frac{1}{\zeta}} \delta q \delta x \quad (2.90)$$

By switching to the annihilation/creation operators for charge ( $a, a^\dagger$ ) and position ( $b, b^\dagger$ ) fluctuations as follows

$$\delta q = (a + a^\dagger) \frac{1}{\sqrt{2L\Omega_{LC}}} \quad (2.91)$$

$$\delta x = (b + b^\dagger) \frac{1}{\sqrt{2m\Omega_m}} \quad (2.92)$$

the expression for the interaction Hamiltonian becomes

$$H_{\text{int}} = \frac{\sqrt{(x_e - x_0)\Omega_m}\sqrt{2m\zeta C_0}}{C_0} \frac{1}{\zeta} (a + a^\dagger) \frac{1}{\sqrt{2L\Omega_{LC}}} (b + b^\dagger) \frac{1}{\sqrt{2m\Omega_m}} \quad (2.93)$$

and simplifies to

$$H_{\text{int}} = \sqrt{(x_e - x_0)\Omega_m\Omega_{LC}} \frac{1}{\sqrt{2\zeta}} (a + a^\dagger)(b + b^\dagger) = g_{em}(a + a^\dagger)(b + b^\dagger) \quad (2.94)$$

and consequently the operators for charge and displacement fluctuations become coupled through the electromechanical coupling rate  $g_{em}$  [19]

$$g_{em} = \sqrt{\Omega_m\Omega_{LC}} \sqrt{\frac{(x_e - x_0)}{2\zeta}} \quad (2.95)$$

This expression can be written in a more intuitive way if we use the assumption that the derivative of the capacitance  $\partial C/\delta x_m|_{x_0}$  is constant between  $x_e$  and  $x_0$ . This is a safe assumption as the static displacement caused by the applied bias voltage is typically small compared to the initial distance between the membrane and the capacitor electrodes. Therefore for small displacements we can write

$$\Delta C = \frac{\partial C}{\partial x_m}(x_0 - x_e) \quad (2.96)$$

where  $\Delta C$  is the change in capacitance (positive) due to the static displacement caused by the applied bias voltage and it is directly proportional to the derivative times the displacement from the initial membrane-electrode distance at  $V = 0$ . Then by rewriting  $x_e - x_0$  in terms of this capacitance change and plugging into 2.95, we end up with [19]

$$g_{em} = \sqrt{\Omega_m \Omega_{LC}} \sqrt{\frac{\Delta C}{2C_0}} \quad (2.97)$$

It is clear that any additional capacitance (parasitic elements for example) reduce the coupling since it is the ratio of the change in capacitance that matters for the coupling rate (for an  $\Omega_{LC}$  that is fixed by modifying the inductance for example). Furthermore, it is possible to link the capacitance change to more readily accessible experimental parameters like the static displacement and frequency shift by using the approximations to first order  $\Delta C/C_0 \approx \Delta x/x \approx \Delta \Omega_m/\Omega_m$ . For example, by just measuring the frequency shift of the mechanical resonator, one can estimate the coupling strength for a given bias voltage and LC circuit parameters.

It would also be important to write down the coupling rate for the case of **ac drive**, where the LC resonator frequency might be vastly larger than the mechanical frequency. A convenient way to derive such an expression (usually done in the context of opto or electromechanical systems) is to start from the frequency change of the LC resonator due to the motion of the membrane.  $g_{em}$  in this case is given by

$$g_{em} = \frac{d\Omega_{LC}}{dx} x_{zpf} \sqrt{n} = \left( \frac{d}{dx} \frac{1}{\sqrt{LC(x)}} \right) \sqrt{\frac{\hbar}{2m\Omega_m}} \sqrt{\frac{\frac{1}{2}CV_c^2}{\hbar\Omega_{LC}}} \quad (2.98)$$

where  $n$  is the number of charges circulating in the LC resonator,  $C$  is the capacitance and  $V_c$  is the rms voltage on the capacitor. The expression simplifies to

$$g_{em} = V_c \frac{\partial C}{\partial x} \sqrt{\frac{\Omega_{LC}}{4\Omega_m m C}} \quad (2.99)$$

The coupling rate for **ac drive** is linearly proportional to the derivative of the capacitance and the voltage on the capacitor which depends on the response function of the LC circuit to a given ac coupling voltage at a specific frequency. The coupling term arises out of the frequency shift of the LC resonator due to the mechanically modulated capacitance and the coupling rate is enhanced by the number of charges.

## 2.6 Instability due to the pull-in voltage

There is a certain instability limit for the bias voltage that can be used to increase the cooperativity. This voltage is known as the pull-in voltage [16, 30] for capacitive systems and it is therefore also relevant for our system. Writing the capacitance as  $C = \frac{A\epsilon}{(d-x)}$  we find for the force on the membrane (here we are interested in the static response under fixed bias voltage conditions)

$$F = -\frac{\partial E}{\partial x} = \frac{1}{2} \frac{A\epsilon}{(d-x)^2} V_{dc}^2 - k_0 x \quad (2.100)$$

where  $d$  is the initial membrane-chip gap distance,  $k_0$  is the intrinsic spring constant of the membrane and  $x$  is the displacement of the membrane towards the electrodes. From the equation above, we find the relation at equilibrium as

$$k_0 x = \frac{A\epsilon}{2(d-x)^2} V_{dc}^2 \quad (2.101)$$

By substituting the above equation in the expression for the spring constant  $\partial F/\partial x$  (derivative of the expression in 2.100, we reach for the spring constant at equilibrium [16]

$$\frac{\partial F}{\partial x} = \frac{2k_0 x}{(d-x)} - k_0 \quad (2.102)$$

The equation goes to zero at the condition  $x = d/3$  meaning that if the membrane is displaced by that amount due to the dc bias voltage, the spring constant will go to zero causing instability of the system. Practically, when this point is reached, the membrane will collapse and stick to the electrodes rendering the device useless.

We have observed this phenomenon during our tests with several membranes resulting in the eventual breaking of the membranes. Experimentally, a conventional way of keeping track of this instability regime is to monitor the frequency shift of the membrane. Making some reasonable assumptions, a direct mathematical link between the relative static displacement and the relative frequency shift of the membrane can be established. Assuming a homogeneous force and neglecting the deflection of the membrane (or treating the membrane as a slab moving straight down), one can find the direct link between the two as follows. For a coplanar electrode-membrane configuration, the capacitance and its first and second derivatives are related by

$$C = \frac{A\epsilon}{d} \quad C' = -\frac{A\epsilon}{d^2} \quad C'' = 2\frac{A\epsilon}{d^3} \quad (2.103)$$

The equilibrium distance is directly related to the first derivative of the capacitance yielding the expression below for the relative displacement

$$\frac{\Delta x}{d} = -\frac{1}{2d} \frac{C' V_{dc}^2}{m 4\pi^2 f^2} = \frac{1}{2} \frac{A\epsilon}{d^3} \frac{V_{dc}^2}{k_0} \quad (2.104)$$

whereas the frequency shift is related to the second derivative of the capacitance bringing

$$\frac{\Delta f}{f} \approx \frac{\frac{1}{2} C'' V_{dc}^2}{2k_0} = \frac{1}{2} \frac{A\epsilon}{d^3} \frac{V_{dc}^2}{k_0} \quad (2.105)$$

leading to the same expression. So within the limits of these assumptions, the measured frequency shift can be related to the relative displacement in order to estimate the maximum allowable dc voltage by empirical means through

$$\frac{\Delta f}{f} \approx \frac{\Delta x}{d} \quad (2.106)$$

## 2.7 RF to optical photon conversion

So far in the theory chapter, we have dealt with how a voltage signal is transferred to mechanical vibrations. Another interesting case would be to investigate how the number of rf photons is converted to optical photons. This is basically derived from the same Langevin equations, however the impedance matching conditions are different. The concept of rf to optical photon conversion is important in achieving faithful coherent transfer of photons from the rf domain to optical domain including practical applications like carrying otherwise fragile microwave states (quantum) via less lossy fiber-optic communication lines to long distances.

The fundamental equation that we use to derive the conversion efficiency is the total phase noise equation we have introduced before in our opto-electromechanical system

$$\delta\phi(\Omega) = 2k\chi_{m,\text{eff}}(\Omega) [-\delta F_{th}(\Omega) + G\chi_{LC}(\Omega)\delta V(\Omega)] + \delta\phi_{\text{im}}(\Omega) \quad (2.107)$$

For the special case of a sufficiently high rf input, we may neglect the thermal noise term for the membrane and the optical readout imprecision leaving us with

$$\delta\phi(\Omega) = 2k\chi_{m,\text{eff}}(\Omega) [G\chi_{LC}(\Omega)\delta V(\Omega)] \quad (2.108)$$

Furthermore, imposing the resonant drive condition ( $\Omega_R$ ), we end up with

$$\delta\phi(\Omega_R) = 2k\sqrt{\frac{C}{m\Gamma_{LC}\Gamma_m} \frac{\mathcal{C}_{\text{em}}}{(\mathcal{C}_{\text{em}} + 1)^2}} \delta V(\Omega_R) \quad (2.109)$$

One of the figure of merits for such an electro-optic modulator is the half-wave voltage  $V_\pi$  which is the voltage necessary to yield an optical phase shift of  $\pi$ . Using the optimum cooperativity  $\mathcal{C}_{\text{em}} = 1$  for the expression above,  $V_\pi$  becomes

$$V_\pi = \frac{\lambda}{2} \sqrt{mL\Gamma_{LC}\Gamma_m} \Omega_R \quad (2.110)$$

Next, we derive the explicit form of the conversion efficiency which is given by the ratio of output optical photons to the input rf photons

$$\eta_{\text{eo}} = \frac{P_{\text{sb}}/\hbar\Omega_{\text{opt}}}{P_{\text{RF}}/\hbar\Omega_R} \quad (2.111)$$

where the modulated sideband optical power  $P_{\text{sb}}$  with an optical input of  $P_{\text{in}}$  is given by

$$P_{\text{sb}} = P_{\text{in}} 2(\phi/2)^2 \quad (2.112)$$

and the electrical power in the circuit is

$$P_{\text{rf}} = \frac{V_s^2}{r_s(1 + \mathcal{C}_{\text{em}})} \quad (2.113)$$

with  $\phi = 2(2\pi/\lambda)x_{\text{rms}}$ . Going back to the conversion efficiency equation 2.111 and also writing the phase shift in terms of the  $V_\pi$ , one reaches

$$\eta_{\text{eo}} = \frac{4\mathcal{C}_{\text{em}}}{1 + \mathcal{C}_{\text{em}}} (kx_0)^2 \frac{\Phi_{\text{car}}}{\Gamma_m} \quad (2.114)$$

where  $\Phi_{\text{car}}$  is the flux for the carrier photons. The conversion efficiency does not have the same optimal condition of  $\mathcal{C}_{\text{em}} = 1$  for  $V_{\pi}$ . Since, in our opto-electromechanical system, the impedance increases with higher cooperativities, it means that less rf power is needed to make the same optical phase shift. So for  $\mathcal{C}_{\text{em}} \gg 1$ , the expression simplifies to [4]

$$\eta_{\text{eo}} = 4(kx_0)^2 \frac{\Phi_{\text{car}}}{\Gamma_m} \quad (2.115)$$

The conversion efficiency increases with the optical input (it can exceed one at the expense of added noise) and inversely proportional to the mechanical dissipation rate of the membrane.

## 2.8 Inductive coupling for ac drive

In this section, we theoretically investigate the case of an ac coupling voltage which is relevant for the extension of our device (at  $\approx$  MHz) to frequencies in the GHz range. Here, we derive an expression for the voltage on the membrane capacitor and also for the cooperativity at the optimal coupling condition between the drive circuit and the LC resonator. To begin with, we take the specific case of inductive drive where we transfer the rf coupling voltage through a primary transformer circuit to the tuned secondary circuit (LC resonator). Note that there are several other possible coupling schemes (tuned primary and secondary, capacitive etc) [31] which however may be practically more involved compared to this simple inductive drive case. The generic circuit for such a scenario is depicted in Fig. 2.4. The primary circuit (left) consists of an rf drive source  $V_d$  with a typical output

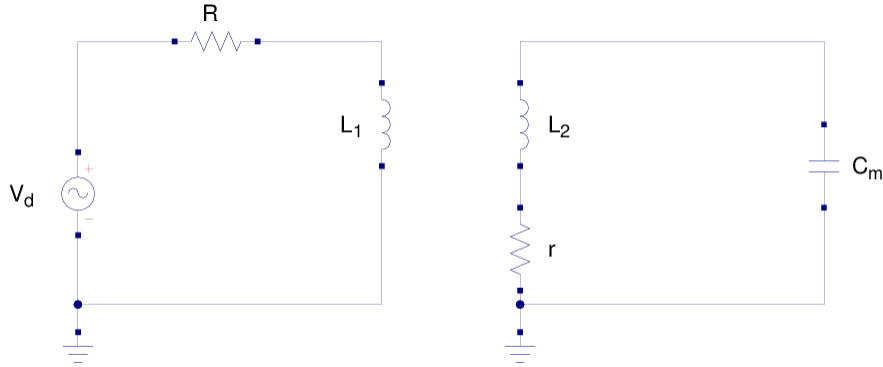


**Figure 2.4** The primary circuit is driven with an rf source and the voltage on  $L_1$  can be transferred to the second inductor  $L_2$  via inductive coupling. The secondary circuit is a resonant LC circuit where  $C_m$  is a capacitive element consisting of a metal coated membrane sitting on electrodes.

impedance of  $R$  and a small inductor  $L_1$ . The secondary circuit in the close vicinity (right) is inductively coupled through the mutual inductance  $M = k\sqrt{L_1 L_2}$  where  $k$  is the coupling factor and  $L_2$  is the inductance of the secondary resonant circuit. Here,  $C_m$  represents the membrane capacitance together with added parasitic elements (pcb etc) and  $r$  denotes the effective series resistance of the LC circuit which is set by the inductor  $L_2$ . Following

Kirchoff's rules for the two circuits, we have the equations for the primary and secondary circuit, respectively ( $i_1$  and  $i_2$  are the corresponding clockwise currents)

$$V_d = (R + j\Omega L_1)i_1 + j\Omega M i_2 \quad (2.116)$$

$$0 = i_2(r + j\Omega L_2 + \frac{1}{j\Omega C_m}) + j\Omega M i_1 \quad (2.117)$$

Solving for  $i_2$  and plugging into  $V_c = i_2 Z_c = i_2 \frac{1}{j\Omega C_m}$ , one reaches the expression for the voltage across the capacitor

$$V_c = \frac{V_d}{j\Omega C_m} \frac{1}{\left( \frac{(R+j\Omega L_1)(r+j\Omega L_2 + \frac{1}{j\Omega C_m})}{-j\Omega M} + j\Omega M \right)} \quad (2.118)$$

Imposing the resonance condition for the secondary circuit  $\Omega = \frac{1}{\sqrt{L_2 C_m}}$  and expressing  $M$

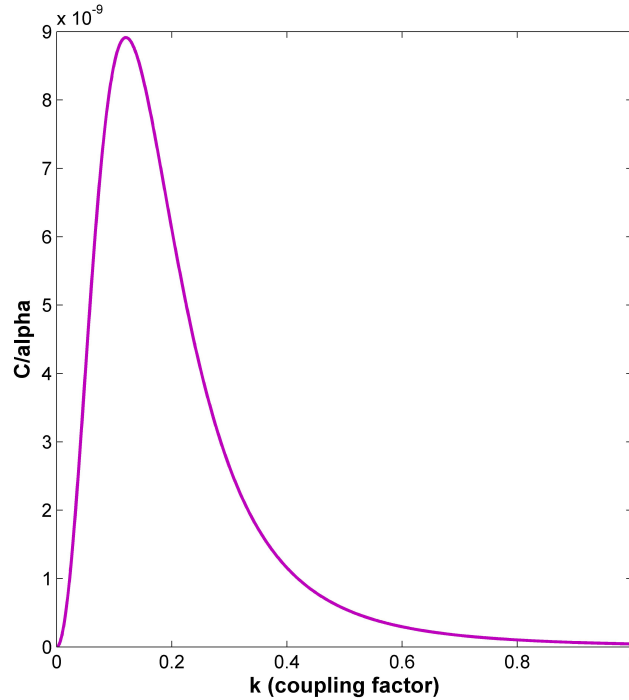


**Figure 2.5** Cooperativity divided by  $\alpha$  as a function of the coupling factor  $k$  between the primary and secondary circuit, reaching a maximum for  $k \approx 0.12$ . The parameters used for the circuit elements are  $V_d = 1$  V,  $L_1 = L_2 = 1$  nH,  $R = 50$   $\Omega$  and  $C_m = 3$  pF with a corresponding LC resonance frequency  $\Omega_{LC} = 2\pi \times 2.9$  GHz. The initial Q of the LC circuit is assumed to be 100 which is limited by the resistive part  $r$  assigned to the secondary coil. The mechanical decay rate is  $\Gamma_m = 2\pi \times 2$  Hz.

explicitly with the coupling factor  $k$ , one reaches the absolute value of the voltage across the capacitor as follows

$$|V_c| = \frac{V_d k \sqrt{L_1 L_2}}{\sqrt{(RrC_m + k^2 L_1)^2 + L_1^2 r^2 \frac{C_m}{L_2}}} \quad (2.119)$$

Using the general expression for the cooperativity,  $\mathcal{C}_{em} = \frac{4g_{em}^2}{\Gamma_m \Gamma_{LC}}$  and  $g_{em} = \alpha V_c$ , the cooperativity can be parametrized with the circuit elements and more importantly with the coupling factor  $k$  which needs to be optimized for reaching the maximum cooperativity (in case reaching a  $\mathcal{C}_{em}$  as high as possible is of interest). Here  $\alpha$  is a scaling factor establishing the link between the parametric ac drive coupling and the voltage across the capacitor. The scaling factor  $\alpha$  was worked out in section 2.5 and expressed through the relation  $g_{em} = V_c \frac{\partial \mathcal{C}}{\partial x} \sqrt{\frac{\Omega_{LC}}{4\Omega_{mm}C}}$ . Here, it also absorbs a linear correction factor due to the off-resonant drive ( $\Omega_{LC} - \Omega_m$  for the parametric coupling case), however for the optimization problem the explicit form of the scaling factor is irrelevant since it is independent of the coupling factor  $k$  and involves fixed parameters. Thus, we end up with an expression for  $\mathcal{C}_{em}$  as follows

$$\mathcal{C}_{em} = \frac{4\alpha V_d^2}{\Gamma_m \left( \Gamma_{LC} + \frac{k^2 L_1}{L_2 R C_m} \right)} \frac{k^2 L_1 L_2}{\left( (RrC_m + k^2 L_1)^2 + L_1^2 r^2 \frac{C_m}{L_2} \right)} \quad (2.120)$$

Here the expression  $\frac{k^2 L_1}{L_2 R C_m}$  can be interpreted as an additional dissipation rate on top of  $\Gamma_{LC}$  as the secondary circuit now sees a modified impedance given by  $r' = r + \frac{k^2 L_1 L_2 \Omega^2}{R}$  due to coupling to the primary circuit. By using equation 2.120,  $\mathcal{C}_{em}/\alpha$  can be maximized for the optimal coupling condition. Within the realistic set of parameters for our system (considering typical fabrication limitations), this optimal coupling factor  $k$  is found to be around 0.12 (Fig. 2.5). At this condition, the initial Q-factor of the LC which is taken to be 100 becomes  $Q_{loaded} = 66$  due to coupling to the primary and  $V_c$  on the capacitor is enhanced to 2.8 V (on resonance) for an input of  $V_d = 1$  V.

With this general treatment, one engineering problem - namely the coupling of the drive voltage to the capacitor - can be solved for the optimal condition with a given set of realistic parameters. Furthermore, with the explicit form of the ac coupling rate  $g_{em}$  which was found previously, the cooperativity can be estimated at the optimal coupling condition for a given bias voltage.

## Chapter 3

# Capacitive coupling with metal and graphene coated SiN membranes

In this chapter, we will discuss our first experimental attempts and results on the way to realizing an opto-electromechanical system. The physics behind capacitive force will be examined and the experimental system including the capacitor electrodes and various membrane types will be explored. At this stage, the inductor that forms the LC resonator is not yet introduced, therefore these measurements can be seen as preliminary steps for understanding and maximizing the electromechanical coupling, by investigating different capacitor-membrane configurations. Throughout these experimental runs, we have investigated several bare SiN, aluminum coated (SiN-Al) and graphene coated (SiN-G) membranes in order to compare their performances in terms of the electrostatic force constant. The main motivation behind metal-coated membranes is that the electrostatic force is expected to be larger than the bare dielectric SiN membranes as this has typically been the case with capacitive systems. The idea behind experimentation with graphene is, in a more general sense, based on its intriguing and exceptional electrical properties [45] and potential use for future opto-electromechanical experiments, as it also has exceptional mechanical properties such as extremely small thickness, low mass density and high Young's modulus [46]. These properties make graphene-NEMS devices ideal for mass, force and charge detection [46]. A few of the specific questions that have motivated us for the graphene project are: Would graphene coated membranes give similar results to a perfect conductor (aluminum for example) in terms of the electromechanical coupling strength? Is the mechanical Q-factor of the SiN membrane not affected since it is coated with only single layer of graphene? Are the mass and frequency of the membrane minimally affected? These questions are addressed in the results/analysis parts along with a comparison of different membranes.

During the timespan of this project, we have used the membranes and chips that have been fabricated by our collaborators. Fabrication of the capacitor chips and Al-coated membranes has been accomplished at DTU/Danchip facilities and production of the graphene-coated membranes has been mostly conducted at Harvard.

### 3.1 Mechanism behind capacitive coupling

Capacitive systems have long been in extensive use in our daily lives. The main idea behind such devices is to measure the change in the capacitance of the system which depends on certain geometric parameters. In that sense, utilizing the position dependence of the capacitance has appeared as a very conventional and highly sensitive method for various applications [34,38]. A simple conceptual model for capacitive coupling along with the circuit picture has already been given in Chapter 2. Here, we will outline the possible practical incarnations of such devices. The idea behind capacitive coupling can be summarized with the modification of the electric field lines between two charged plates which is a function of their relative distance. Several capacitive devices have been demonstrated over the last couple of decades based on this mechanism [37]. The use of capacitive MEMS (micro-electromechanical) devices in rf-based switches has shown significant advantages like low loss and low power consumption over power-hungry semiconductor switches [43,44]. Together with the improvements in fabrication and understanding of nano-mechanical resonators, the field of NEMS (nano-electromechanical sensors) has extended the concept of capacitive coupling to very versatile and sensitive nano-devices [38,39]. Starting from the capacitive energy stored between two plates as given below (under fixed voltage conditions)

$$E = \frac{1}{2}C(x)V^2 \quad (3.1)$$

where  $C(x)$  is the position dependent capacitance and  $V$  is the voltage difference between the two plates, the most generic form of a capacitive force can readily be shown to be

$$F_c = -\frac{1}{2} \frac{\partial C(x)}{\partial x} V^2 \quad (3.2)$$

by taking the first derivative of the energy. There are different ways of achieving capacitive coupling, depending on the method of charging the two metal electrodes (one of which is movable). One way is to make electrical connections to both plates and apply voltage. This, however, requires contacting the movable object as well which might be invasive in the context of keeping the nice properties of nanomechanical resonators. Apart from that, there are basically two non-contact ways where a position dependent electrostatic interaction can take place, which can be outlined [37] in Fig. 3.1. In the first case (a), an applied voltage  $V$  induces charges on the surface of a suspended metallic plate, which results in electric field lines directed perpendicular to the surface of the plate and attracts the suspended plate towards the electrodes. In the second case, where the suspended object is a dielectric material, the net force comes from dielectrophoresis [48], which is a phenomenon experienced by any polarizable object placed in an inhomogeneous electric field. The attractive force is essentially generated via the gradient of the electric field intensity (also known as the Kelvin polarization force) [42]. Since charges can not move freely as in a metal, but can only be polarized as depicted in Fig. 3.1, an inhomogeneous field is necessary to apply a net force and attract the object, which usually requires a strong gradient provided by the gap.

A detailed analytical and numerical analysis on the Kelvin polarization force for nanomechanical beams has been conducted by Schmid *et al* in [42]. Starting from the force on an infinitesimal dipole

$$f = p \cdot \nabla E \quad (3.3)$$

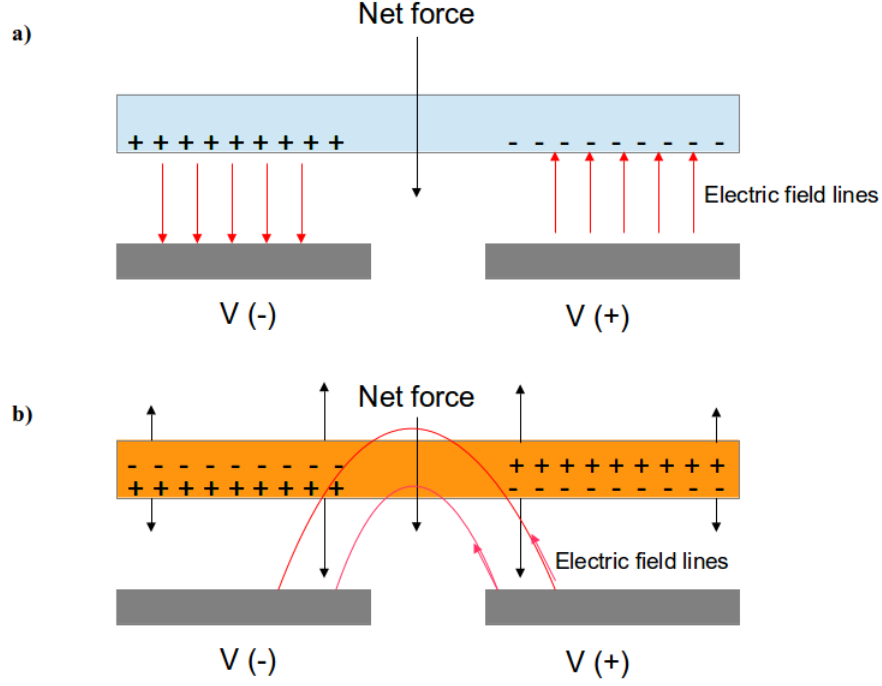


**Figure 3.1** a) Depiction of the electrostatic interaction between two oppositely charged electrodes (maintained with a bias voltage  $V$ ) and a suspended metallic plate. b) The suspended object in this case is a dielectric plate which is polarized when a bias voltage is applied to the electrodes. In both cases, the field lines are formed such that the suspended plate is attracted towards the electrodes [37].

one can calculate the corresponding Kelvin polarization force density and then integrate this force over the thickness of a nanomechanical beam of width  $w$ , length  $L$ , thickness  $h$  and distance to the electrodes  $d$ , in order to reach the distance dependent total force as follows

$$F(d) = -\frac{1}{2\pi}\epsilon_0(\epsilon_d - \epsilon_m)\alpha^2 L \frac{h}{d(d+h)} V^2 \quad (3.4)$$

where  $\epsilon_0$ ,  $\epsilon_d$  and  $\epsilon_m$  refer to the permittivity of vacuum and the relative dielectric constant of the beam and the surrounding medium, respectively. To get this simple form of dependence, a beam width that is large compared to the thickness of the beam and distance to the electrodes needs to be assumed.  $\alpha$  is a correction factor that accounts for the imperfection of the field inside the dielectric and the electric field is assumed to be concentric over the whole area [42]. This equation is very similar in nature to the force between two parallel-plate capacitors which reads as

$$F(d) = -\frac{1}{2}\epsilon_0\epsilon_m \frac{A}{d^2} V^2 \quad (3.5)$$

where  $A$  is the area of one of the plates. In our experiments, we have used capacitor samples with interdigitated design allowing for dielectric coupling and planar electrodes for metallic coupling and compared their performances with different types of membranes. As can be seen from the discussion above, the mathematical form of the capacitive force is the

same in nature and we will use a generic form of the capacitive force for convenience for the rest of the discussion in this chapter, given by

$$F_c = cAf(d)V^2 \quad (3.6)$$

where  $c$  is defined as the electrostatic force constant which absorbs all the geometric parameters as well the permittivity and  $f(d)$  refers to the distance dependence of the force which accounts for corrections to the general  $1/d^2$  scaling law.

### 3.2 Experimental Setup

The experiments performed in this section for the characterization of capacitive coupling and electrostatic force constants of different membranes, have been conducted at DTU with an integrated commercial Doppler Vibrometer MSA-500 from Polytec [49]. The interdigitated

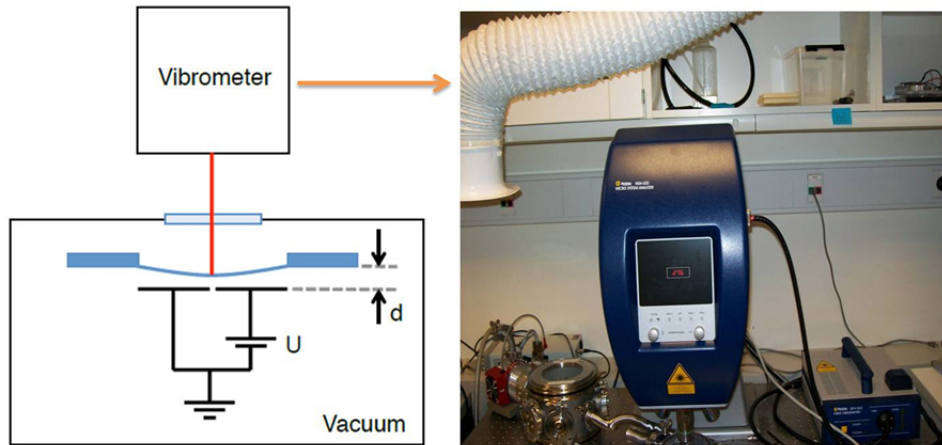


**Figure 3.2** Setup for the capacitive coupling experiments (reproduced from [41]) comprises a commercial vibrometer which utilizes optical interferometry and a vacuum chamber ( $10^{-5}$  mbar) in which the membrane- capacitor chip samples are placed. Samples are aligned by using the integrated camera/imaging system in the vibrometer head (in the middle of the photo). Light that is reflected back from the membrane goes through a fiber interferometer (box in the right) in which it interferes with the beam from the reference arm mirror. The thermal or driven amplitude of the mechanical vibrations are analyzed via the FFT software of the vibrometer and displayed in calibrated units. Capacitive excitation of the membrane is achieved via a dc bias and an rf signal. The electronic control unit of the vibrometer is not shown here.

and quarter-segment electrodes for the capacitor chips have been fabricated through several iterations at DTU/Danchip clean room facilities. Fig. 3.2 shows a wholistic picture of the setup. The samples are prepared manually before each experimental run and placed

inside a vacuum chamber. Sample preparation involves cleaning of the chip surface and membranes and then assembling the two to form a distance dependent capacitor, which will be discussed particularly in this chapter.

### 3.2.1 Doppler Vibrometer

The vibrometer is of type MSA-500 analyzer system with integrated laser scanning head, fiber interferometer and software for data acquisition. The principle behind detection of vibrational modes of the mechanical resonator is based on the Laser-Doppler Vibrometry [49] which is a powerful tool for several sensing applications. The basic idea is to interfere

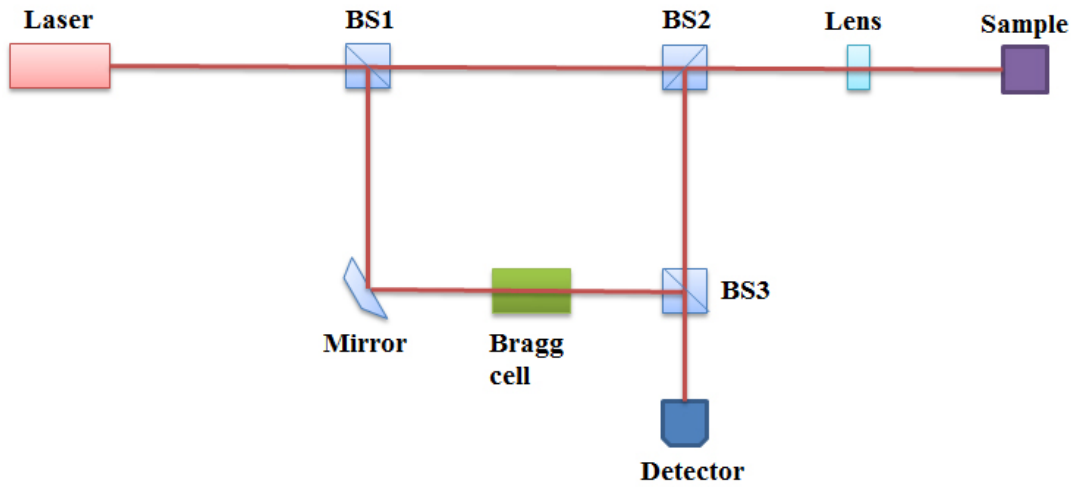


**Figure 3.3** Depiction of the Laser-Doppler Vibrometry scheme utilized by the Polytec Vibrometer. The beam from the reference arm and the sample arm interfere at the detector and the frequency shift from the moving object is deduced from the demodulation of the interference signal. The Bragg cell is an additional element in the reference arm used to infer the direction of the moving object.

light coming from a reference arm and a moving object in order to deduce the Doppler shifted frequency of the beam as this will generate a phase modulation at the output. The frequency shift of a beam reflected from a moving object is given by [49]

$$\Delta f = 2 \frac{v}{\lambda} \quad (3.7)$$

where  $\lambda$  is the fixed wavelength of the laser beam and  $v$  is the velocity of the moving object. If two coherent beams having intensities  $I_1$  and  $I_2$  and path lengths  $r_1$  and  $r_2$  are overlapped, the resultant intensity profile exhibits the well-know interference signal

$$I = I_1 + I_2 + 2\sqrt{I_1 I_2} \cos(2\pi(r_1 - r_2)/\lambda) \quad (3.8)$$

As one of the arms (reference arm) is fixed and the sample arm has a time dependent optical path due to its motion, it is possible to see fringes. In this case, the modulation frequency of the interference pattern is directly linked to the velocity of the moving object. Thus the

frequency modulation can be used to infer the velocity of the object and its displacement by time-integration of the acquired data. For the specific device we use (Fig. 3.3), the beam from a He-Ne laser first passes through beam splitter 1. One arm goes to a Bragg cell unit (Acousto-optic modulator) which shifts the frequency by 40 MHz. The purpose of the Bragg cell is to be able to distinguish the direction of the object since two different directions give shifts either below or above this 40 MHz extra shift. The beam that by-passes the Bragg cell goes to beam splitter 2 where some portion of the light impinges on the sample and is reflected back on to beam splitter 2, finally interfering with the reference arm beam on the detector. The detector then sees the beat note between the shifted frequency of the reference beam (due to the Bragg cell) and the Doppler shifted beam from the sample. The vibrometer has electronic units which allow detection up to 25 MHz. The FFT (fast Fourier transform) spectrum analyzer has a resolution limit of 1 Hz which is good enough to resolve the narrow mechanical peaks (typically 2-3 Hz) we are interested in. The output power of the He-Ne laser can be adjusted in discrete steps up to  $250 \mu\text{W}$ . Fig. 3.4 shows an example of a SiN membrane on an interdigitated capacitor that is excited via an rf signal (in this case a periodic chirp sent from the vibrometer electronic unit) applied through the capacitor electrodes together with a dc bias voltage. Several mechanical modes can be

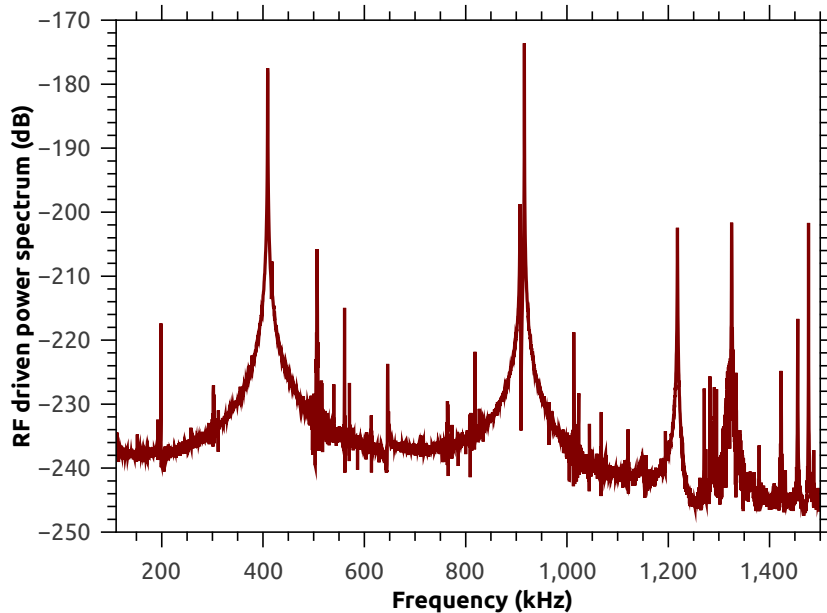


**Figure 3.4** With a dc bias=10 V and an rf signal amplitude=6 V, several mechanical modes of a SiN membrane are excited via the Kelvin polarization force. The fundamental mode of this membrane is clearly seen at the expected eigenfrequency around 410 kHz which is the typical value for a 1 mm square membrane.

excited and tracked at the same time and these preliminary measurements constitute the first indication that our capacitive coupling mechanism actually works. We have also used the scanning function of the vibrometer which generates a clear picture (in Fig. 3.5) of the vibrating modes of the membrane. In the scan mode, the membranes are capacitively excited

and the vibrometer automatically scans the laser beam position (beam size of a couple of microns) along the sample area and then shows the vibrating mode in an animation. The

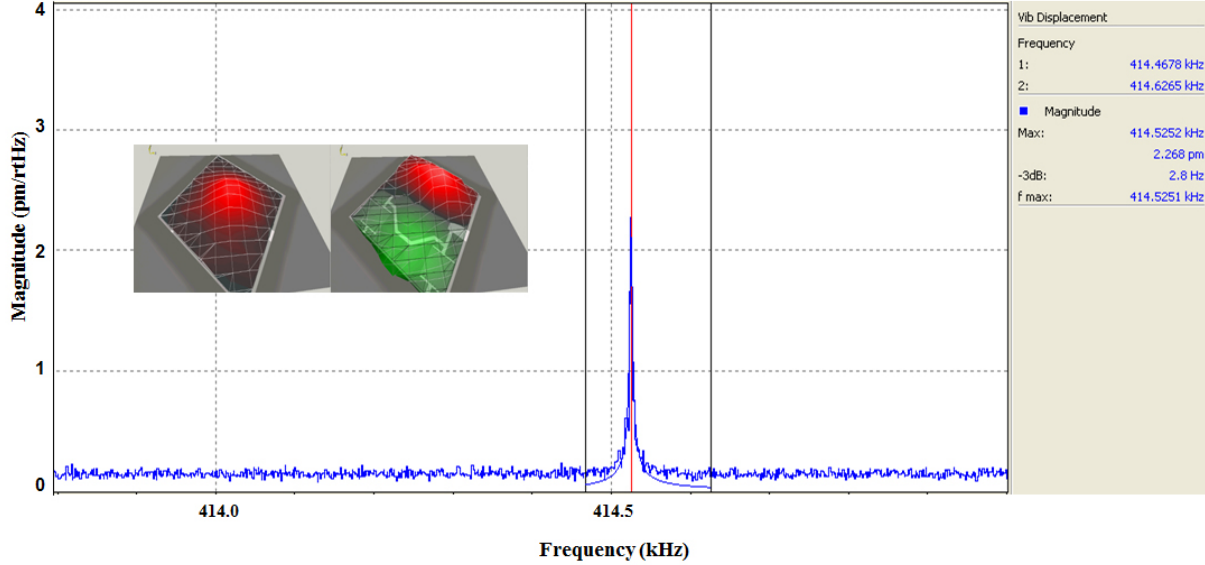


**Figure 3.5** A snapshot from the FFT analyzer of the vibrometer revealing the spectrum of membrane vibrations. A thermally excited membrane peak which corresponds to the fundamental drum mode is easily discernible. Attached on the spectrum is a snapshot from the animations recorded with the scanning mode of the vibrometer. The membrane is capacitively excited to have high signal to noise ratio for the quality of the scan picture.

thermal noise of the membrane due to the Brownian motion at room temperature can also be readily resolved with the FFT of the vibrometer. This is shown with a sample snapshot from the analyzer of the vibrometer in Fig. 3.5. The mechanical peak amplitude is tracked with the red line. A lorentzian fit can then be fitted to the spectrum after a few seconds of averaging in order to deduce the peak amplitude and the mechanical linewidth (which is 2.8 Hz in the example).

The distance between the membrane and the capacitor electrodes is a crucial parameter in our electromechanical setup that determines the strength of coupling together with the dc bias voltage. Therefore, for each sample we have tested at DTU throughout this project, we have checked this distance after the assembly of our samples, since we have had several problems in reaching the pre-determined values set by the pillar heights (600 nm and 1  $\mu\text{m}$ ). This issue will be addressed in the assembly process in this chapter and in section 5.5 while dealing with the limitations of the setup. Before starting the measurements with our membranes in the vacuum chamber, white light interferometry setting of the Doppler vibrometer (no vacuum) is utilized to infer the distance. The white light measurement is performed with a broadband light source (green laser beam from the vibrometer) which is split to the reference arm and the sample arm (in our case membrane placed on the chip). As the piezo attached to the reference mirror is scanned, the interference signal from the sample surface is recorded. This signal reaches a maximum when the path length of the

beam reflected from the sample equals the reference arm path length. In this way, one can map out the surface profile of a sample that needs to be investigated. The plot shown

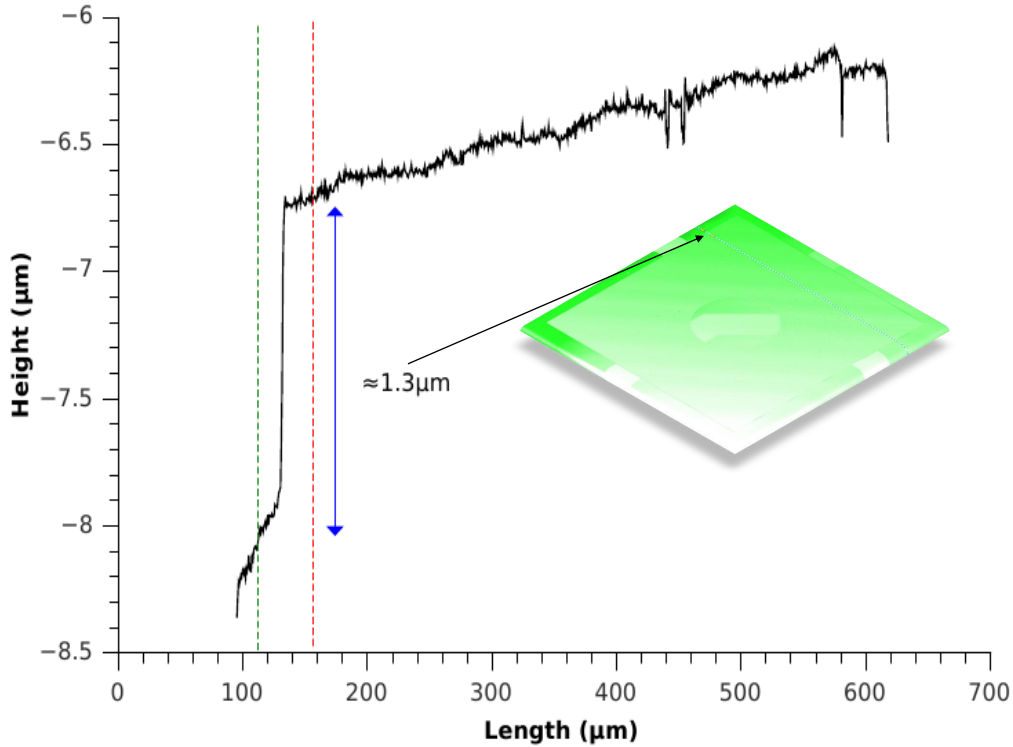


**Figure 3.6** White Light Interferometry setting of the vibrometer. The initial distance between the membrane and the chip, which is crucial for the strength of the electromechanical coupling, is determined via a white light interferometric measurement. The outcome is a profile picture deduced from the analysis of the reflected beam coming from different layers—the membrane and the electrodes underneath (reproduced from [4]).

in Fig. 3.6 depicts the surface height variation along the corresponding line-cut of the membrane placed on the chip. In our case, we deduce the distance between the membrane and the electrode underneath in the following way. We get a strong reflection from the Al-coated part which is converted to a certain distance (around  $-6.5 \mu\text{m}$  in this case) which is denoted by the red dashed line. However, for example the edges of the membrane (SiN) are not coated with Al and the only reflection from the surface comes from the electrode beneath the SiN layer (the first reflection from the SiN is small and the program records only the strongest reflection signal) which is denoted with the green dashed line. Therefore, the difference between between the two layers is an approximate measure of the distance between the membrane and the chip-electrode around that region. Having experimented with dozens of samples, we have typically observed variations on the order of  $0.5 \mu\text{m}$  along the whole sample.

### 3.2.2 Capacitor chips and membranes

#### Capacitor chips

The capacitor chip together with the membrane serves as an element that has a position dependent capacitance. The electrodes of the chip are kept at a dc bias voltage to provide the electrostatic induction of the membrane and an rf voltage is applied on top that can actuate the mechanical resonator via the capacitive force.

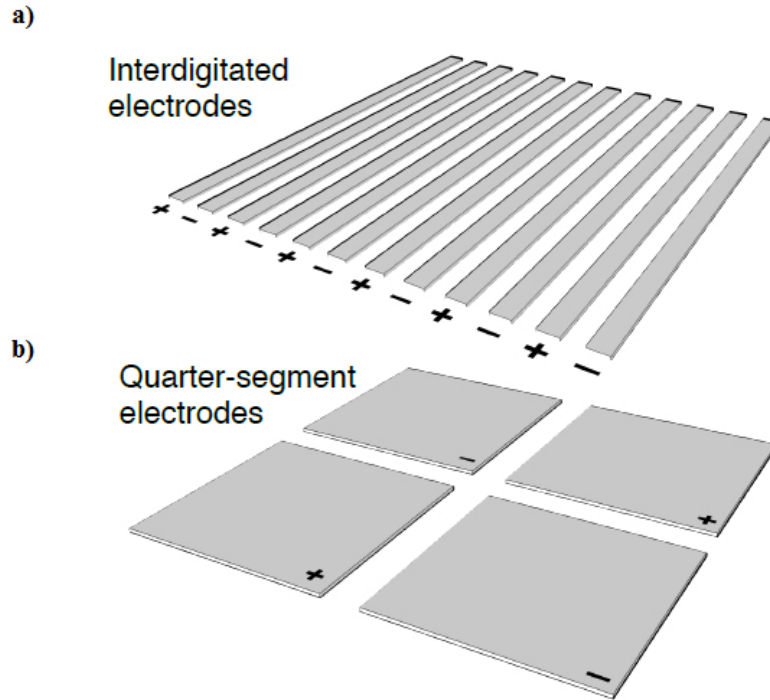


**Figure 3.7** a) Interdigitated chip design for dielectric capacitive actuation. The typical electrode width is  $4 \mu\text{m}$  with a gap of  $2 \mu\text{m}$ . The gap provides the electric field gradient which is necessary for the interaction with a dielectric object through the Kelvin polarization force b) Four-segment electrode structure. The electrodes induce charges on the surface of the metallic membrane and directly interacts with the field lines from the electrodes (reproduced from [41]).

The experiments with the aim of investigating different capacitor chips and membranes span a time period of almost a year in which the fabrication process has been iterated a few times due to the problems realized during characterization (mostly related to the fingers of the interdigitated capacitors). The general procedure for the fabrication of chips is based on standard clean-room processing. Electrodes made of 200 nm thick gold layer are deposited on a substrate (SiN-covered silicon or borosilicate glass) [41]. We have experimented with two types of chips; one with interdigitated fingers and the other with four-segment electrodes to achieve dielectric and metallic type of coupling, respectively, which are depicted in Fig. 3.7. Before starting the fabrication process, simulations have been performed (by S. Schmid) in order to calculate the geometric parameters for reaching suitable capacitance values (aimed to be typically between 0.4 pF - 5 pF).

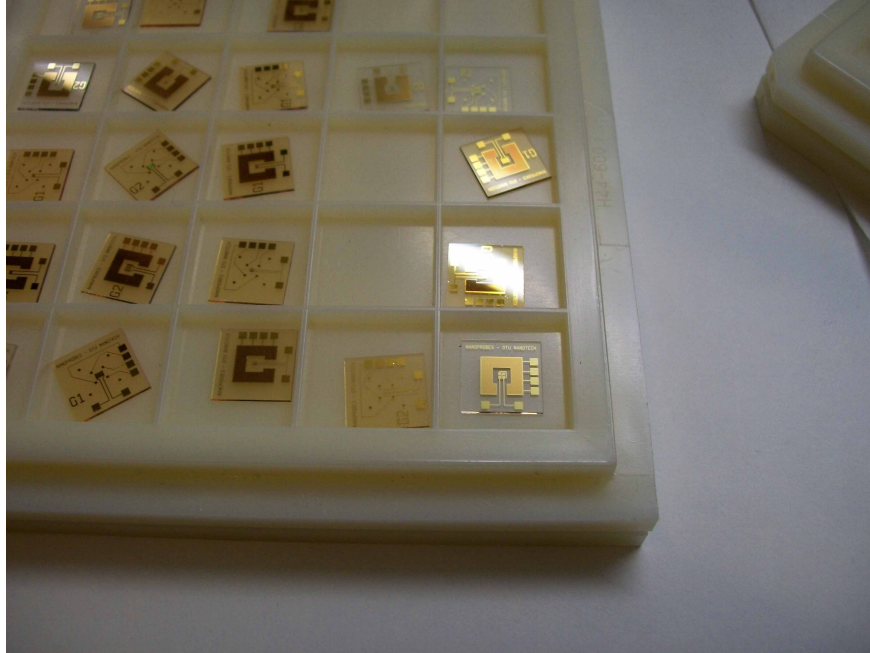


**Figure 3.8** Capacitor chips (with slightly different geometric designs and sizes) fabricated at DTU. The substrate is made of glass and the electrodes deposited on top are made of gold. The upper layer of the chip is covered with a polymer for protection which is removed just before being used in a measurement.

The first fabrication run has been performed with a silicon substrate. Although these substrates work in the sense that capacitive actuation has been observed with the SiN membranes, there have been two crucial problems experienced with that batch of chips. Firstly, the capacitance of the chip itself is measured to be around 250 pF with an LCR meter—much larger than the typically expected values of 5 pF. Secondly, we have realized that the substrate introduces significant loss which is tested by recording the resonance response of an LC circuit with a high-Q inductor. We think both effects presumably come from the free charges in the semiconductor silicon layer. Therefore, we switched to chips with glass substrates for the second generation chips and it has been observed that these effects are eliminated, yielding small capacitance values with low-loss as expected.

### Membranes

The three types of membranes we have used in this project are: 1) Bare SiN membranes 2) Aluminum coated SiN Membranes (SiN-Al) 3) Graphene coated SiN Membranes (SiN-G). **Bare SiN** square membranes (including stoichiometric high stress and low stress samples) are bought from Norcada with typical sizes of 0.5 mm and 1 mm and a thickness of 50 nm. For the fabrication of **SiN-Al** membranes, standard cleanroom processing is used where the Al layer is deposited on top of the whole wafer after the membranes have been released [4]. Along the anchor of the membrane is a rim for the purpose of minimizing damping [33] and in addition a circular Al layer (hole) is removed from the center. Both patterning processes

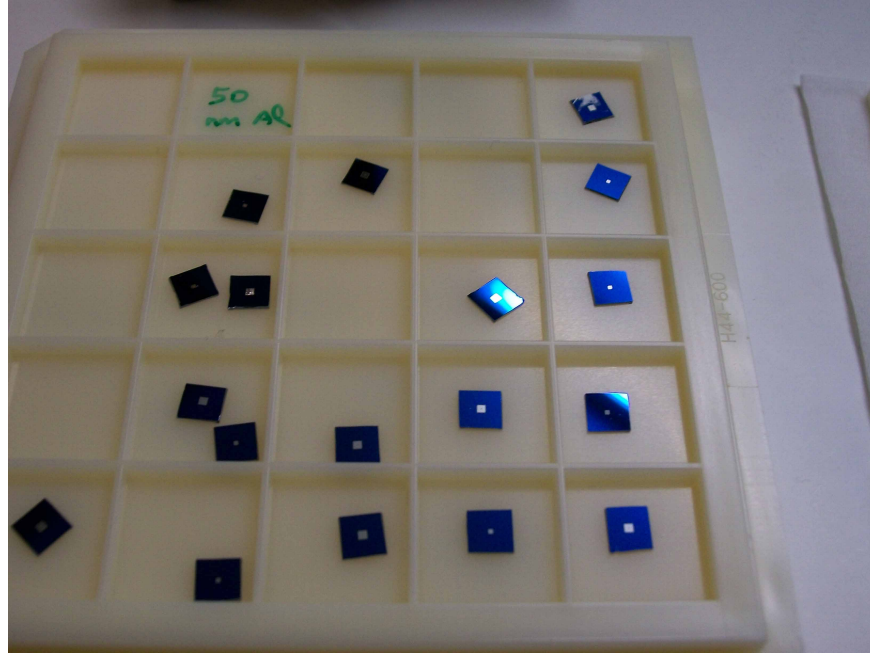


**Figure 3.9** A bunch of aluminum coated SiN membranes fabricated at DTU. Typical sizes for the membranes (windows in the middle) are 0.5 mm and 1 mm. The membranes are surrounded with a thick silicon frame.

are performed via photolithography and chemical etching. For the fabrication of the **SiN-G** membranes, standard CVD (Chemical Vapor Deposition) techniques are used. A single layer graphene is grown on copper foil. After cutting the graphene on copper to size, the copper layer is wet-etched and the graphene is transferred to the surface of the membrane in an aqueous solution. The graphene is supported by a thin PMMA film during the transfer. Acetone vapor is used to remove the PMMA layer in the end [41]. The procedure turned out to be fragile and unfortunately the number of surviving samples after the fabrication process was only a few.

In order to see the quality of the graphene coating and whether it is single layer, Raman spectroscopy is performed (by S.Schmid). The Raman signal is investigated on 22 different points on the membrane. Below in Fig. 3.10, we show the spectra recorded at a point within the coated membrane area. The result indicates a high quality (with probably few defects) graphene as the D-peak at  $1300 - 1400 \text{ cm}^{-1}$  is missing in all the measurements. Overall, we see a typical single layer graphene spectrum with a 2D peak having double the amplitude of the G peak. The G peak in graphene refers to the high-frequency  $E_{2g}$  phonon. The origin of the D peak is the breathing modes of six atom rings and the activation of this peak requires a defect which is found to be absent in our Raman spectra. 2D peak is an overtone of this, however since momentum conservation is satisfied by two phonons with opposite wave vectors, this peak is always present even in the absence of defects [47].

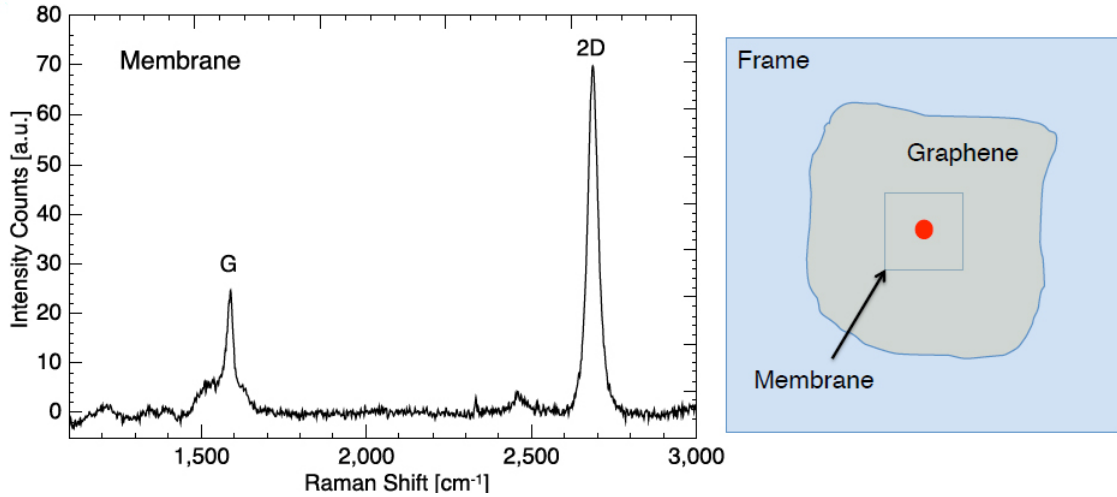


**Figure 3.10** Raman spectrum of a SiN-G chip recorded on a point within the graphene coated membrane area. An optical beam of 10 mW power from a 532 nm laser is used for the measurement with an exposure time of 15 s (reproduced from [41]).

### Assembling the chip and the membrane

Our assembly process is a manual operation performed before investigation of each membrane. A membrane is first cleaned by soaking it in acetone and then in water typically for a minute. The procedure is followed in the same manner for the chip as well. Immediately after soaking in the solution, both the chip and the membrane are blown with high-pressure air gun. Afterwards, the membrane is placed gently (with a tweezer) on the chip surface. The membrane-chip sample is then placed inside a vacuum chamber which sits under the vibrometer head for the measurements. A typical pair of an Al-membrane on four-segment electrodes is shown with the microscope image of the vibrometer in Fig. 3.11. However, this procedure of assembly has yielded varying distances between the membrane and the chip ( $3.5 - 14 \mu\text{m}$ ), significantly larger than the pre-determined pillar heights. This issue is touched upon in section 5.5 together with the second generation membrane (etched) fabrication to tackle this problem.

The electrical connection to the capacitor chip is provided via thin electrodes ending with a pad- which is an extension of the gold electrodes of the interdigitated or four-segment capacitor. For some of our old chips, the capacitor chip is glued on a PCB and the electrode pads are wirebonded to the connection lines on the PCB. However, it turned out to be not practical in terms of experimenting with many samples quickly. During the course of time, we switched to a configuration where the glass substrate of the capacitor chip is placed on a rigid mount and the electrode pads are contacted by pressing with contact probes to apply voltage. This has given us the opportunity to directly use the glass chip-membrane sample and change it quickly if another sample is required for testing.

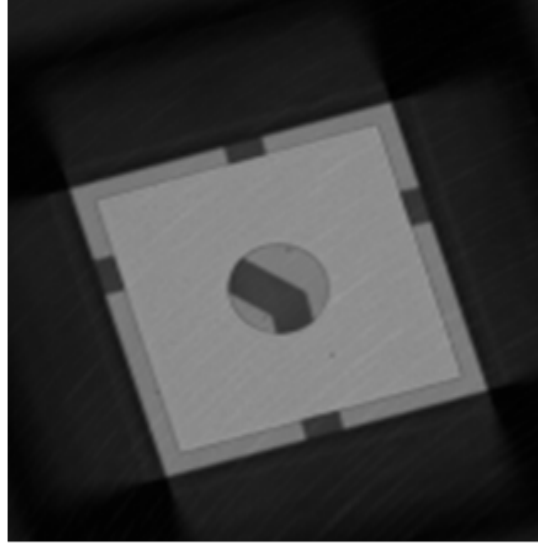


**Figure 3.11** Picture of an Al-coated SiN membrane (under the microscope of the vibrometer) placed on a four-segment electrode chip. For this sample, the electrodes of the chip are bigger than the 0.5 mm membrane. Note that the edges of the membrane do not contain aluminum for mechanical Q-factor considerations. There is a hole in the middle of the aluminum layer for future cavity optomechanics experiments.

### 3.3 Preliminary tests

The preliminary tests involve measurements with several samples in order to test our capacitive actuation/coupling and understand the observed behaviour based on our expectations from the capacitive force. The physics of this type of capacitive coupling can be tracked via measurements like the frequency shift of the mechanical resonator, the static displacement and the mechanical response at resonance due to an applied dc and rf voltage. Starting from the capacitive force equation and taking the case of a dc bias voltage with a small rf modulation on it, the capacitive force takes the form as follows (as shown in Chapter 2)

$$F_c = cAf(d)V^2 = cAf(d)(V_{dc}^2 + 2V_{dc}V_{rf} + V_{rf}^2) \approx cAf(d)(V_{dc}^2 + 2V_{dc}V_{rf}) \quad (3.9)$$

where  $V_{rf}^2$  term is neglected [40]. The first term in the equation brings a static force which is proportional to the square of the dc voltage and the second term brings an ac force that is linearly proportional to the dc voltage.

#### 3.3.1 AC force as a function of the dc bias and rf modulation

For the general case of a broadband rf modulation, the mechanical resonator will feel an ac force term  $F_{rf} = 2cAf(d)V_{dc}V_{rf}$  and exhibit driven vibrations governed by its mechanical susceptibility. For simplicity, we focus on detection of the vibrations at a single frequency which is the fundamental mechanical resonance frequency of the membrane. Keeping the rf modulation amplitude the same, the membrane resonance amplitude is expected to grow linearly with the dc bias voltage as it gets polarized more strongly. Fig. 3.12 a) shows an

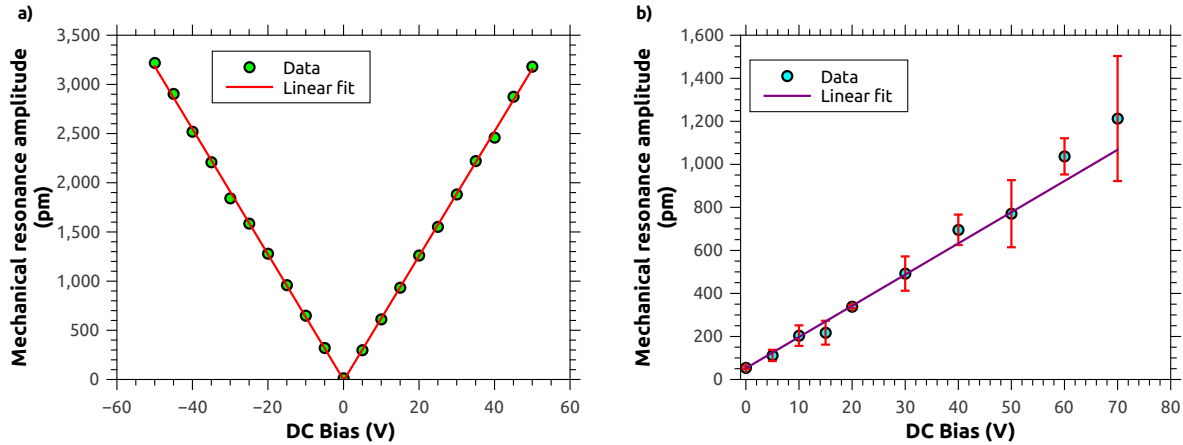


**Figure 3.12** a) A SiN-Al membrane (1 mm) on a four-segment electrode with a gap distance =  $11 \mu\text{m}$  is excited with a fixed rf modulation of 10 mV as the dc bias voltage is varied. The metallic membrane shows a perfectly linear curve as expected with reversed polarity as well. The maximum mechanical excitation amplitude is chosen to be sufficiently far from the nonlinear regime. b) Graphene coated (SiN-G) membrane (0.5 mm) on an interdigitated capacitor with a gap distance =  $6.5 \mu\text{m}$ . Error bars refer to the standard deviation of 3 consecutive measurements.

example recorded with an aluminum coated (50 nm) SiN membrane (100 nm) which has an eigenfrequency of 238 kHz (1 mm size). The mechanical resonator amplitude is tracked on resonance via the FFT of the vibrometer while it is being excited by a periodic chirp rf signal (2 kHz bandwidth) provided from the vibrometer electronics unit. In the first measurement (Fig. 3.12 a), we apply a fixed rf modulation = 10 mV from the signal generator of the vibrometer and vary the bias voltage supplied by a dc source. The mechanical resonance amplitude grows linearly (high quality linear fit) with the dc voltage as expected. Another important test for the nature of the capacitive force is the behaviour with respect to the polarity of the dc source [40]. As seen from the plot, the mechanical amplitude is symmetric with respect to the polarity change and the values are very similar at opposite polarities meaning that a hysteresis or a memory effect is negligible in this case. In panel b, we show the same type of measurement with varying dc bias on a SiN-G membrane. A second type of measurement to test the behaviour of the capacitive force is conducted by keeping the dc bias fixed and varying the rf excitation amplitude. With a dc bias = 1 V, the mechanical resonance amplitude scales linearly (high quality fit) with the rf excitation as expected from the capacitive force expression (Fig. 3.13). Including these sample measurements, our complete set of experiments show that the metal-coated membranes behave in a totally expected manner where additional free charge effects and hysteresis type of behaviour are negligible (also quite similar in graphene-coated membranes) which, however, is not the case with bare SiN membranes as we will see in the discussion regarding free charge and hysteresis effects in subsection 3.3.4.

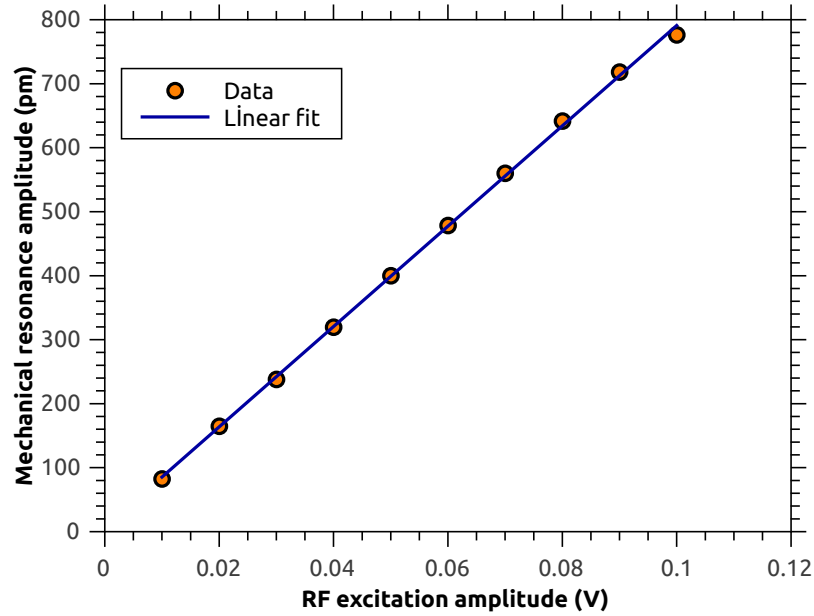


**Figure 3.13** A SiN-Al membrane (the same one as in the previous figure) is excited with a dc bias= 1 V as the rf excitation amplitude is varied. The mechanical amplitude scales linearly with the rf voltage.

### 3.3.2 Static displacement of the membrane

Due to the capacitive force, the mechanical resonator experiences a static force term  $F_s = cAf(d)V_{dc}^2$  which displaces its equilibrium position simply by  $F_s/k_0$  where  $k_0$  is the intrinsic spring constant (under the assumption that the displacement is small compared to the initial gap distance). In our measurements, we also check this dependence by varying the dc bias voltage and looking at the supposedly quadratic behaviour of the static displacement of the membrane. However, the static displacement measurement is not straightforward as it requires reading out a stable dc signal. Therefore, we chose to work under quasi-static conditions which would approximate the static displacement of the membrane under certain conditions. To this end, we typically send a low frequency ac modulation (square waveform) to the capacitor and track the demodulated peak amplitude of the mechanical resonator at this specific frequency (beam position close to the center of the membrane). The modulation frequency (typically a few kHz) is chosen such that it is sufficiently far away from the fundamental resonance frequency of the membrane in order to resemble a static response. In Fig. 3.14, we show a sample measurement which compares the two types of membranes, a) bare SiN membrane and b) SiN-Al membrane. AC modulation of 20 kHz (SiN) and 10 kHz (SiN-Al) is used to quasi-statically excite the membrane and the mechanical amplitude at this frequency is plotted against the amplitude of the dc voltage (quasi-static). As can be seen, the response of the bare SiN membrane does not follow the quadratic behaviour expected from the polarization force. It first grows linearly with the voltage for small values and starts to behave quadratic for large values. We believe this

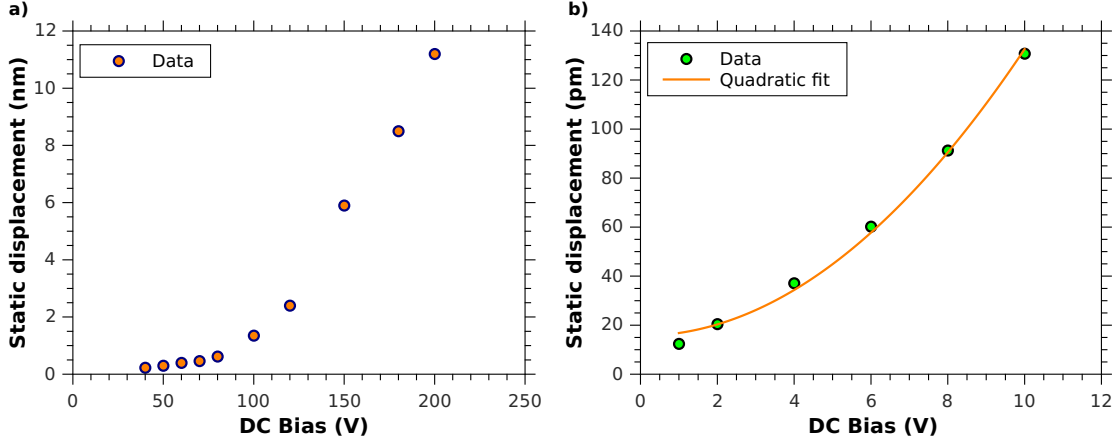


**Figure 3.14** a) Quasi-static response of a bare SiN membrane. It shows a behaviour which is a combination of free charges and induced charge effects, bringing both linear and quadratic terms. b) SiN-Al membrane shows the expected quadratic dependence on the quasi-static voltage. The quadratic fit function is  $f_{\text{fit}} = a_0 + a_1 \times x^2$ .

irregular behaviour is mostly due to the free charges in the SiN layer which has been a problem for MEMS devices [44]. For example, if the free charges on the SiN, the number of which is fixed, dominate the interaction, one would expect a linear behaviour since it is the fixed amount of charge  $q$  that interacts with the varying quasi-static voltage instead of induced charges that would otherwise bring quadratic dependence. On the contrary, we observe a quadratic dependence with the SiN-Al membrane which is expected from the induced voltage behaviour on the metal surface.

### 3.3.3 Frequency shift of the membrane

A well-known property of a capacitively coupled nanomechanical system is the so-called electrostatic spring softening effect [40] due to the capacitive force on the mechanical resonator which leads to a shift in the mechanical resonance frequency. The shift in the resonance frequency appeared within our formal treatment in the theory chapter starting from the coupled Langevin equations of a generic membrane-LC circuit system. The origin of this effect comes from the distance dependent nature of the interaction between the membrane and the capacitor. Following a simple and intuitive approach, the derivative of the capacitive force with respect to displacement can be interpreted as being equivalent to an additional spring constant term ( $k_{el} = -\frac{\partial F_c(x)}{\partial x}$ ). This term (negative in this case) pulls the intrinsic constant  $k_0$  down, resulting in a decrease in the frequency since the frequency is directly linked to the spring constant via  $\Omega_m = \sqrt{\frac{k_0 + k_{el}}{m}}$ . Taking the derivative of the general capacitive force term, one reaches

$$k_{el} = -\frac{\partial F_c(x)}{\partial x} = \frac{1}{2} \frac{\partial^2 C(x)}{\partial x^2} V_{dc}^2 \quad (3.10)$$

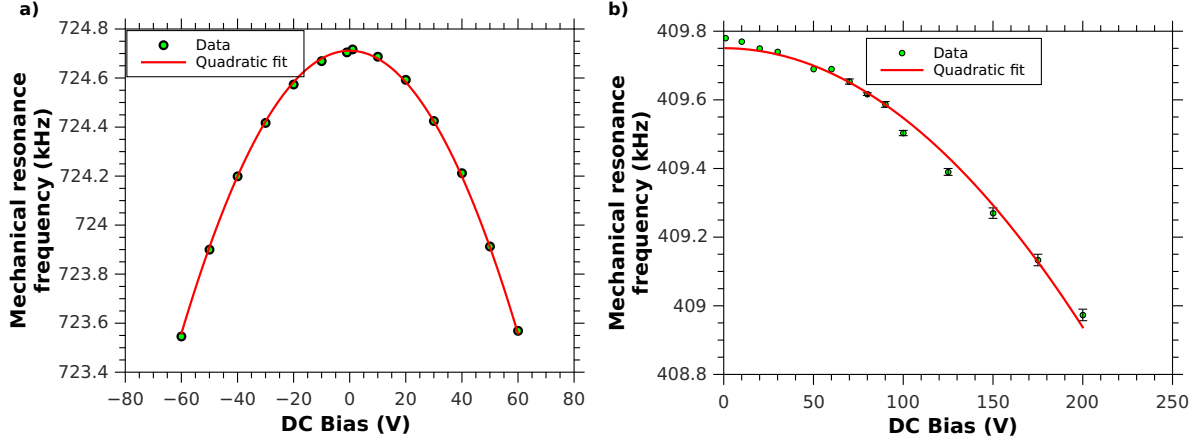


**Figure 3.15** a) Frequency shift of a high-stress SiN-Al membrane as a function of the dc bias voltage. The shift follows perfectly the quadratic behaviour of the capacitive force along with a symmetric response with respect to polarity reversal. b) Frequency shift of a bare SiN membrane.

Keeping only the first order term with the Taylor expansion for small frequency shifts, the modified eigenfrequency of the membrane then becomes [40]

$$\Omega_m \approx \Omega_0 \left( 1 - \frac{aV_{dc}^2}{2k_0} \right) \quad (3.11)$$

where  $a$  is a constant absorbing the second derivative of the capacitance. The end result shows that the effect of the electrostatic interaction can be observed by tracking the membrane resonance frequency and that the frequency shift should scale quadratically with the dc bias voltage. Monitoring the frequency shift provides us a reliable way to extract the electrostatic force factor which will be discussed in section 3.4.

An example for the experimental observation of the frequency shift with respect to dc bias voltage is shown in Fig. 3.15. The SiN-Al membrane follows the expected quadratic curve very closely, whereas the bare SiN membrane shows deviations due to the free charge effect. We note that at each new dc voltage setting, we wait for the membrane frequency to settle to the new shifted value (which takes a few seconds) and once it is stable around this value, we start recording the data. Each data point corresponds a few seconds of averaging for the thermal membrane peak. The resolution of the FFT of the vibrometer is 1 Hz. The error bars for the SiN membrane come from the std (standard deviation) of several measurements. An important test for the frequency shift is the effect of polarity reversal. It is clear from the mathematical form that changing the sign of the voltage source should not have any effect on the results. What matters is the square of the voltage difference between the electrode gaps, therefore it is insensitive to the direction of the field lines. This means that the eigenfrequency of the membrane is always pulled down irrespective of the sign of the voltage, which is shown in Fig. 3.15a for the SiN-Al membrane.

### 3.3.4 Charging and hysteresis effects in bare SiN membranes

As can be seen from the sample figures shown in this chapter and based on the general trend observed for dozens of different membranes we have experimented so far, we can report that bare SiN membranes have exhibited complicated and irregular behaviour such as time-dependent charging and discharging, deviations from the expected curves for dc and ac voltage driving and quite unstable membrane resonance amplitudes along with hysteresis. Although it is difficult to identify the exact origin of all these phenomena, our measurements

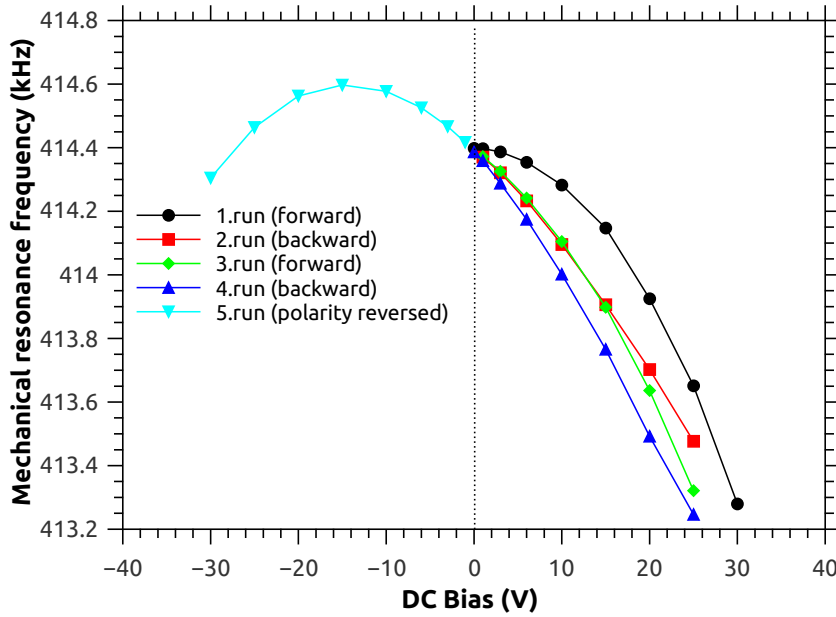


**Figure 3.16** Frequency shift of a bare SiN membrane. First run (black) starts by increasing the voltage up to 30V. After short time (around a minute) it is followed by a second run where the voltage is decreased. Third and fourth runs follow the same procedure. For the fifth run, the voltage polarity is reversed and increased in the negative direction. A hysteresis behaviour (leftover charge) and deviations from quadratic voltage dependence are clearly seen.

indicate that it presumably comes from trapped charges in SiN which has been known by the NEMS world especially in the context of SiN based switches [44]. The origin of these charges is complicated and different mechanisms have been proposed to account for that. For example, silicon and nitrogen dangling bonds can form states that trap holes or electrons [51,52]. Apart from that, it has been shown that silicon and hydrogen have an effect on the amount of trapped charges [44] in SiN. In contrast to the complex and uncontrollable behaviour of bare SiN membranes, almost all the aluminum and graphene coated SiN membranes have shown responses that would be expected from the induced charge mechanisms. In these membranes, the metallic coating layer dominates the free charge effects present on the bare SiN layer. This is a meaningful result also in the context of our future experiments (coupling to the LC circuit) that metal and graphene coated membranes are more suitable

since the mechanism behind coupling is clearly comprehensible and experimentally controllable.

A clear observation of irregularities of the bare SiN membranes related to the charging/discharging and hysteresis effects is solidified in a more systematic measurement shown in Fig. 3.16. Several runs of voltage scan are performed where the voltage is varied in the forward and backward direction. It is observed that the data show quadratic dependence in the beginning and start to deviate from that in the next runs, in the fourth run becoming dominantly linear. This is an indication that the interaction between the free charges in the SiN layer and the biased electrodes start to take over the polarization based interaction. This is consistent with the fact that as time goes by, SiN gets more charged since the free charges are separated more towards the interface. The frequency shift also becomes larger for the same voltage as time passes which suggests a hysteresis effect. Another effect consistent with the free charge domination sets in when the voltage polarity is reversed. Instead of a regular decrease in frequency which is insensitive to polarity, this time the frequency climbs up as the voltage becomes negative. In this case, the charges that are already accumulated can not immediately follow the polarity reversal, thus they carry the same sign of charge resulting in a repulsive interaction which increase the spring constant. Beyond a certain voltage, the polarization mechanism starts to take over again.

### 3.4 Results/Analysis

This section is dedicated to the comparison of bare SiN, SiN-Al and SiN-G membranes in terms of their electrostatic interaction strength (based on the electrostatic force constant) and their mechanical quality factors.

#### 3.4.1 Electrostatic interaction strength with different types of membranes

As we have encountered before, the electrostatic (capacitive) force can most generally be described by

$$F_c = cAf(d)V^2 \quad (3.12)$$

where  $c$  refers to the interaction strength (electrostatic force constant) as  $A$  and  $f(d)$  take care of the geometric parameters. Written in this form, we take  $c$  as the figure of merit when we compare different membrane types on particular electrode configurations. Based on our measurements with several membranes so far, monitoring the frequency shift, which can be performed in a simple experimental setting, provides a reliable way of extracting this number experimentally. Here in this subsection, we represent the frequency shift in a form based on our work [41] as it allows us to write it conveniently in terms of the  $c$  factor and the geometric parameters of the membrane-capacitor pair.

Starting from the equation of motion for the membrane and using the first order Taylor expansion for the capacitive force (where  $V_{dc}$  is the only voltage applied), we have

$$\sigma_0 h \nabla^2 z - \rho h \frac{\partial^2 z}{\partial t^2} + (cV_{dc}^2 f(d) - cV_{dc}^2 f'(d)z) \xi(x, y) = 0 \quad (3.13)$$

where

$$z(x, y, t) = \sum_{n=1}^{\infty} \sum_{m=1}^{\infty} A_{nm} \Phi_{n,m}(x, y) e^{i\Omega_m t} \quad (3.14)$$

denotes the deflection of the membrane with vibrational modes  $\Phi_{n,m}(x, y)$ . As we are only interested in the fundamental mode, we multiply the equation by  $\Phi_{1,1}$  and integrate over the entire membrane area  $A = L_x \times L_y = L \times L$  with thickness  $h$ . We then reach the following for the equation of motion

$$-2 \frac{\pi^2}{L^2} \sigma_0 h \iint_A \Phi_{1,1}^2 dx dy + \rho h \Omega_m^2 \iint_A \Phi_{1,1}^2 dx dy - c V_{dc}^2 f'(d) \iint_A \Phi_{1,1}^2 \xi(x, y) dx dy = 0 \quad (3.15)$$

By using this equation, we can write the square of the modified mechanical frequency as

$$\Omega_m^2 = \underbrace{2\pi^2 \frac{\sigma_0}{\rho} \frac{1}{L^2}}_{\Omega_0^2} + c \frac{V_{dc}^2 f'(d)}{h\rho} \frac{\iint_A \Phi_{1,1}^2 \xi(x, y) dx dy}{\iint_A \Phi_{1,1}^2 dx dy} \quad (3.16)$$

and again using a first order Taylor approximation, the eigenfrequency itself can be written as the sum of the original eigenfrequency  $\Omega_0$  and frequency shift term  $\Delta\Omega$  which comes from the electrostatic force

$$\Omega_m \approx \Omega_0 \left( 1 + \frac{c}{2} \frac{V_{dc}^2 f'(d)}{h\rho\Omega_0^2} \eta_{1,1} \right) \quad (3.17)$$

with  $\eta_{1,1}$ , the correction function due to the spatial overlap between the membrane mode shape and the fixed electrodes where  $\xi(x, y)$  takes into account the mask, hole in the middle and gaps.

$$\eta_{1,1} = \frac{\iint_A \Phi_{1,1}^2 \xi(x, y) dx dy}{\iint_A \Phi_{1,1}^2 dx dy} \quad (3.18)$$

Equation 3.17 shows that given we know the geometrical parameters of the chip and the membrane, we can extract the  $c$  factor by fitting the experimentally measured mechanical frequency to a quadratic function of  $V_{dc}$ . The fit coefficient  $\alpha$  in front of  $V_{dc}^2$ , can then be related to the  $c$  factor via

$$c = 2\alpha[-f'(d)]^{-1} h\rho\Omega_0^2 \eta_{1,1}^{-1} \quad (3.19)$$

To this end, we have performed mechanical frequency vs dc bias measurements on two different types of electrodes. The first type is interdigitated electrodes on which we have placed bare SiN and SiN-G membranes. The second type is the four-segment coplanar electrodes used to compare the performance of SiN-Al and SiN-G membranes.

The distance dependence of the force for interdigitated capacitors can be approximated by

$$f(d) = A_0^{-1} e^{-\kappa d} \quad (3.20)$$

where  $A_0$  is a scaling constant with units of area which for our set of parameters is taken as  $1\mu m^2$ . This exponential dependence comes out of numerical simulations (by Emil Zeuthen) based on the number of interdigitated fingers used in the experiments. Starting from the midpoint of one the fingers and ending at the midpoint of the adjacent finger including the gap between them defines the unit cell for the E field simulation. The boundary condition

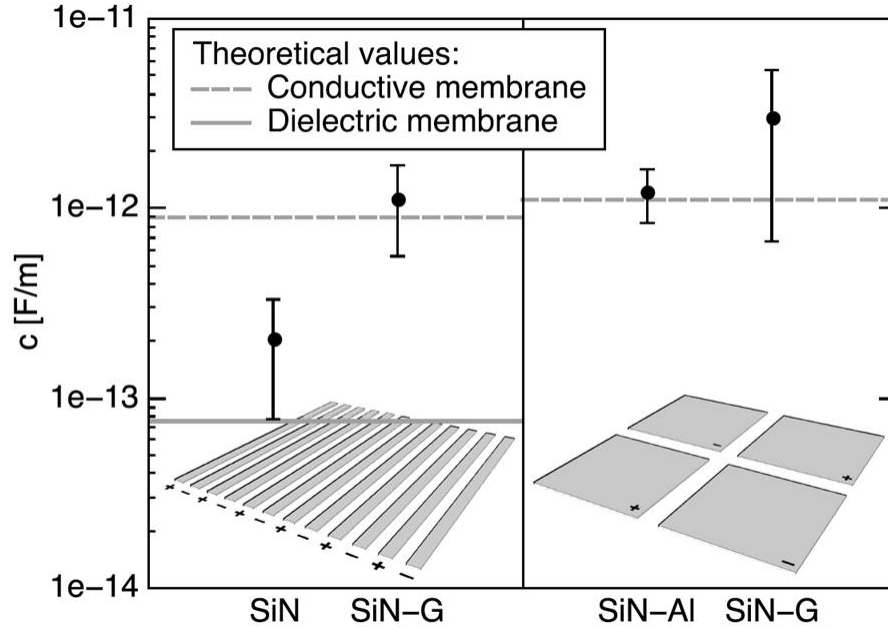


**Figure 3.17** Comparison of force constants  $c$  for different combinations of membranes and electrodes. In the panel to the left, the mean values for SiN (4 samples) and SiN-G (3 samples) are shown where the error bars correspond to the standard deviation. For these experiments, the width of the electrode fingers is  $4 \mu\text{m}$  and the gap between them is  $2 \mu\text{m}$ . In the panel to the right, force constants  $c$  of SiN-Al (3 samples) and SiN-G (4 samples) are shown on four-segment electrodes. The solid and dashed lines refer to the theoretical force constants for the dielectric polarization force and electrostatic force for conductive membranes, respectively (reproduced from [41]).

that the electrical field is zero accounts for the influence of neighbouring cells. The dependence is valid for the distances we are working with, which are comparable to the gap length.  $\kappa$  is numerically determined to be  $1.05\mu\text{m}^{-1}$  for our setup.

The second configuration consists of four-segment electrodes with SiN-Al and SiN-G membranes on, where the membranes serve as the floating electrodes. This configuration follows the simple distance scaling law (essentially coming from the capacitance law between two parallel plates) which is

$$f(d) = 1/d^2 \quad (3.21)$$

The experiments we have performed for the comparison of  $c$  are outlined in Fig. 3.17 where the values are extracted from the experimentally measured frequency shifts by using the general equation 3.19. The distance dependent function is taken with the proper scaling for the interdigitated and four-segment electrodes.

Firstly, we show (on the left) the comparison of bare SiN and SiN-G membranes on the interdigitated capacitors. As can be seen, a single layer of graphene improves the  $c$  factor by 5.5 with respect to the bare SiN membranes. The solid line, which corresponds to the theoretical value, comes from the numerical simulations based on the exponential dependence as

stated previously. Graphene layer added on the SiN membranes is simulated as a perfectly conducting layer where the potential goes to half of the difference between the potentials on the electrode fingers. The dielectric constant of SiN is taken to be 7.6 for the simulations. The experimentally extracted values for the SiN is slightly above the theoretical line which might presumably come from the enhancement due to the free charges on the SiN layer as the distance dependence would be weaker in this case ( $\propto 1/d$ ). The mean value of SiN-G membranes on the other hand agree with the theoretical prediction well within the error bar.

Secondly, we investigate the performance of metallic SiN-Al and SiN-G membranes on four-segment electrodes (on the right). The experimentally extracted values agree with theory within the error bars for both types of membranes showing similar values. Here, the theoretical value is predicted from a simple analytical expression for the capacitance between a floating electrode and two fixed electrodes beneath, which will be discussed in the next subsection. The distance dependence is simply  $1/d^2$  in this case. According to this data, graphene seems to act as a perfect conductor as one would intuitively expect. We note that the large error bars can be attributed to the uncertainties in the distance  $d$  measurements which may be up to  $0.5 \mu\text{m}$ . The lateral misalignment is also predicted to yield up to 20 percent error. We believe that the somewhat larger  $c$  value of the SiN-G membranes can arise due to the excess graphene layer on the frame which is also discussed in the next subsection.

### 3.4.2 Theoretical force constant for four-segment electrodes and effects of the graphene layer

The force constant  $c$  for the four-segment electrodes can be written readily with simple arguments starting from the magnitude of the well-known force between two parallel plates (neglecting fringe field effects)

$$F_c = \frac{1}{2}\epsilon_0 \frac{A}{d^2} V^2 \quad (3.22)$$

If the conducting and floating membrane is placed symmetrically over the fixed electrodes, then the potential on the membrane becomes  $V/2$  which makes the force constant 4 times smaller than the usual two parallel plate case.

$$c_{\text{sym}} = \frac{1}{8}\epsilon_0 \quad (3.23)$$

Another approach to reach the same result is to separate the total capacitance between the two fixed electrodes into its three components - namely the capacitance from the (+) electrode to the membrane ( $C_1$ ), the capacitance within the conducting membrane ( $C_3$ ) which can be assumed to be very small and finally the capacitance from the membrane to the (-) electrode ( $C_2$ ) closing the field line loop between the two fixed electrodes. As these capacitances are in series, the total capacitance then becomes

$$C_T = \frac{1}{\frac{1}{C_1} + \frac{1}{C_2}} \quad (3.24)$$

Since both  $C_1$  and  $C_2$  have half the area  $A$  and they are summed in a parallel configuration, this leads to a decrease of the capacitance by a factor of 4 as compared to the two parallel

plate capacitor configuration. In the end, this yields the same  $c_{\text{sym}}$  we have shown previously. As seen from the data for SiN-G in Fig. 3.17, the  $c$  factor for SiN-G on 4-segment electrodes is relatively larger than the theoretical value. This, we believe, can be explained by some hypothetical effects that take into account the deviation from the symmetric placement of the membrane on the electrodes. This effect of asymmetry might be strongly pronounced since we have the graphene layer extending over the entire membrane frame area as opposed to the aluminum-coated membranes. Assuming an extremely asymmetric case with respect to two polarities due to this excess graphene layer, the force constant for one of the polarities will vanish, whereas it would yield  $c_{\text{asym}} = \frac{1}{2}\epsilon_0$  for the other one, in the end summing up to  $c = \frac{1}{4}\epsilon_0$  for the force constant (a factor of 2 enhancement). This, we think, might to some extent explain the average force constant being above the predicted value by a factor of 2.7 with respect to the case of perfectly symmetrical coupling.

### 3.4.3 Overlap factor as a correction to the force constant

As it has been noted before, the force constant  $c$  we extract from the experimental data takes into account the asymmetry and imperfect overlap of the membrane with the fixed electrodes by introducing the general overlap factor  $\eta_{n,m}$ . This overlap factor accounts for the asymmetry by dividing the capacitance contributions to three ( $C_3$  however is negligible) as shown in the previous subsection and also for the gaps between the segments, edges, a slight asymmetry in the mask and finally a central hole in the Al layer. These corrections have been worked out in detail by Emil Zeuthen. Here, we write down the most general form of the overlap factor (Supp.Info [41])

$$\eta_{n,m} = 4 \left[ \frac{O_+^{(2)}}{\left(1 + \frac{O_+^{(0)}}{O_-^{(0)}}\right)^2} + \frac{O_-^{(2)}}{\left(1 + \frac{O_-^{(0)}}{O_+^{(0)}}\right)^2} - \frac{1}{O_+^{(0)} + O_-^{(0)}} \left( \frac{\frac{O_+^{(1)}}{O_+^{(0)}} - \frac{O_-^{(1)}}{O_-^{(0)}}}{\frac{1}{O_+^{(0)}} + \frac{1}{O_-^{(0)}}} \right)^2 \right], \quad (3.25)$$

where

$$O_i^{(j)} \equiv \frac{\iint_{A_i} \Phi_{n,m}^j \xi(x,y) dx dy}{\left( \iint_A \Phi_{n,m}^2 dx dy \right)^{j/2}}, \quad (3.26)$$

with  $i \in \{+, -\}$  and  $A_i$  being the area of the membrane above electrodes of polarity  $i$  and the term in the denominator simply comes from the normalization of the coordinate. The first (second) term represents the frequency shift contribution from the membrane area above positive (negative) electrodes for fixed potential values. These terms come from the second derivative of the position dependant capacitance where the mode shape of the membrane is taken into account. Thus, the derivatives are calculated in a more general form by using the chain rule which takes the position also as a function of the corresponding mode amplitude. The third term is a minor correction due to the modulations of the membrane potential around the equilibrium value.

### 3.4.4 Mechanical Q-factor comparison

Apart from the electrostatic performance of SiN, SiN-Al and SiN-G membranes, we were also interested in the comparison of the mechanical Q-factors. To this end, we have performed quality factor measurements in two ways; bandwidth determination and ringdown measurements which have shown similar values. The simplified experimental setup for the

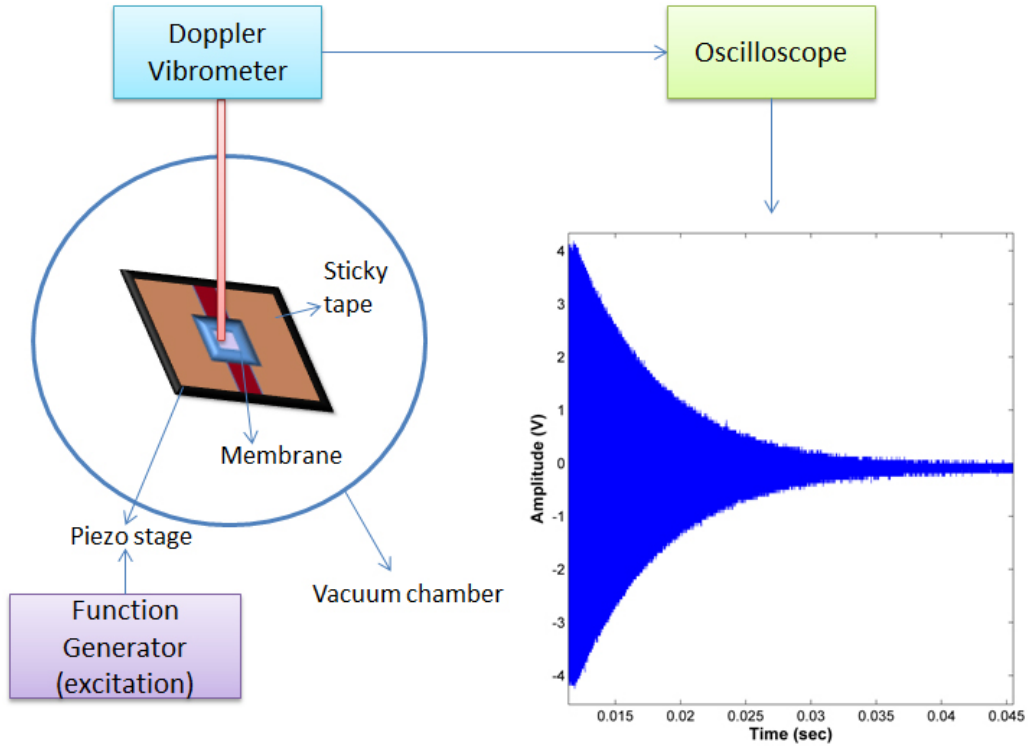


**Figure 3.18** Experimental setup for the ringdown measurements in order to extract the mechanical quality factor of the membranes. The optical interferometric signal from the vibrometer is fed to an oscilloscope. The plot shows an example of the amplitude ringdown of a SiN membrane.

ringdown measurements is shown in Fig. 3.18. We place the membranes on a small frame with a piezo attached and drive them at their eigenmode frequencies. The edges of the membrane frame (lower side) are in contact with a sticky tape on both sides to ensure fixing of the membrane to the stage. We record the vibrations of the membrane via the Doppler Vibrometer. The optical signal from the vibrometer is fed to a fast oscilloscope. The excitation from a function generator is cut off at a proper time to observe the exponential decay which is then fitted to extract the mechanical Q-factors via  $Q = \Omega_m \tau$  where  $\Omega_m$  and  $\tau$  are the mechanical eigenfrequency and the energy decay time, respectively.

The result is shown in Fig. 3.19. For this specific experiment, we have used membranes with the same geometry-  $0.5\text{mm}^2$  area and high-stress stoichiometric SiN layer. We remind that the SiN-Al membranes are patterned such that there is no Al layer in the edges in order not to degrade the Q [33]. Our results suggest that there is no observable difference between the Q-factors of different membranes. The Q-factors are highly mode dependent

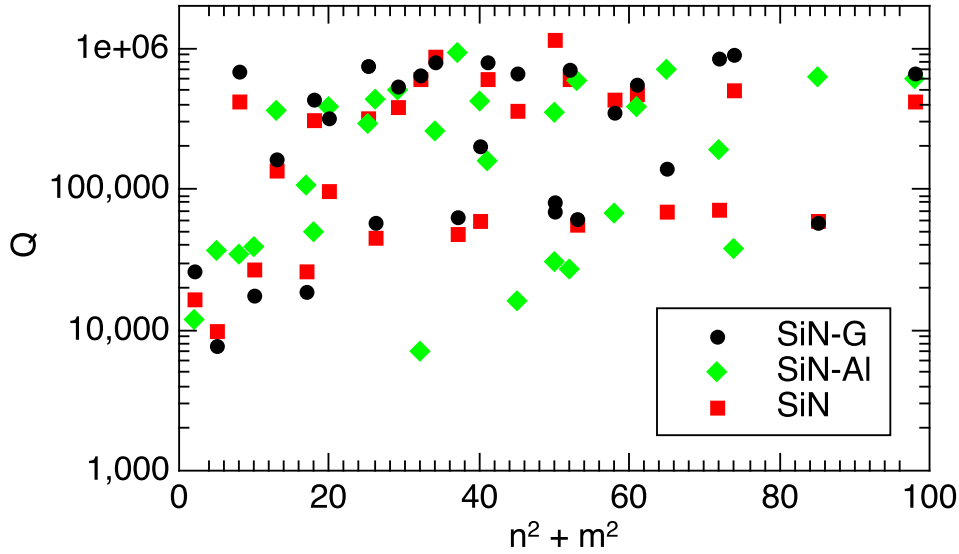


**Figure 3.19** Mechanical quality factors ( $Q$ ) of SiN (red), SiN-Al (green) and SiN-G (black). Several modes with increasing frequencies are measured (reproduced from [41]).

as it would be expected from clamping limited loss (the membrane frame is attached gently to the piezo frame with a double sided tape) in agreement with [33]. A positive result from this measurement is that a single graphene layer (even though it covers the whole frame and is not patterned like Al to avoid the edges) does not degrade the mechanical  $Q$ -factor compared to the bare SiN membranes. We note that a similar experimental study has been made in [32] where it has been found that a single graphene layer brings minimal loss to the  $Q$ -factor, only around 30% on average with respect to the bare SiN membranes. It should be noted, however, that a perfectly one to one comparison between all membrane types is not possible due to the fact that SiN-Al membranes show a frequency that is typically 10 percent lower due to the added mass.

### 3.5 Conclusive remarks

The measurements we have conducted in this chapter contain our first tests with capacitive coupling under different membrane-electrode configurations and the specific measurements we have performed in order to extract the intrinsic electrostatic force constant of different membrane types. Aside from that, these measurements have been relevant and guiding for our goals in the next chapter dealing with membrane-LC circuit coupling, as the capacitive coupling is precisely the same except that there is an additional element, namely the inductor.

In summary, we have experimented with bare SiN, SiN-Al and SiN-G membranes on different electrode configurations. Our results show that graphene coating on SiN membranes significantly improves the intrinsic electrostatic force factor compared to bare SiN on interdigitated electrodes. In addition to that, by comparing the SiN-Al and SiN-G on four-segment electrodes, we have shown that graphene coating behaves like a perfect conductor

following the intuitive expectation and brings similar electrostatic force constant to SiN-Al. The results follow the theoretical predictions based on the simple analytical expressions and numerical simulations when the proper correction factors are taken into account.

Our findings suggest that bare SiN membranes usually yield relatively small electrostatic force constants and also exhibit uncontrollable charging and hysteresis effects presumably coming from trapped charges in the SiN layer. Together with our quantitative comparative analysis, we can argue that addition of a metallic or graphene layer helps in removing these unwanted effects and in addition increases the electrostatic force constant which is critical for achieving high electromechanical coupling strengths. Apart from that, the mechanical Q-factor measurements show that a single layer of graphene does not degrade the mechanical Q-factor and it does not pull the eigenfrequency down due to its almost negligible mass, which is desirable in the context of electromechanical coupling and rf to optical conversion.

## Chapter 4

# Optical/Electrical readout of electromechanical coupling

This chapter deals with the experimental realization of a coupled electromechanical system and the analysis of the results we have obtained with this system. The hybrid system is partitioned into its components (optical interferometry, LC electrical circuit, metal-coated nanomembrane) and explained along with the technical issues. We discuss the methods we have used to characterize the system both optically and electrically. The mechanically induced transparency (MIT) and strong coupling regimes achieved with this electromechanical system are analyzed. Our analysis based on both optical tracking of the membrane and electrical readout of the LC circuit shows very good agreement with our theoretical models which is crucial to characterize the electromechanical coupling strength of the system. The systematic analysis carried out in this chapter forms the basis for the understanding of the opto-electromechanical device as a voltage sensor, which is discussed in Chapter 5. We note that for achieving electromechanical coupling and implementing a hybrid device, we decided to work with aluminum-coated membranes due to the higher yield in fabrication. But overall, based on our measurements in the previous chapter, we expect similar performances from both coated membrane types which is significantly better than bare SiN membranes.

### 4.1 Experimental Setup

In this section, a simplified and a wholistic picture of the setup, including the two different optical interferometers is depicted (Fig. 4.1). We have carried out series of experiments at DTU by using the commercial vibrometer and at NBI by using our home-made Michelson interferometer. Apart from that, the idea of the setup is mainly the same, where we have an LC circuit that is capacitively coupled to a vibrating aluminum-coated membrane. The characteristics of the electromechanical system is analyzed by monitoring the electrical response of the circuit via standard lock-in detection and the mechanical vibrations of the membrane via optical interferometric methods.

A photo of the setup established at NBI is shown in Fig. 4.2. The membrane and the four-segment electrode capacitor are placed inside a vacuum chamber forming the probe arm of the Michelson interferometer. The beam from a Nd:Yag laser (Mephisto-Innolight [54]) is sent onto the membrane in a vertical configuration and the reflected light is back coupled

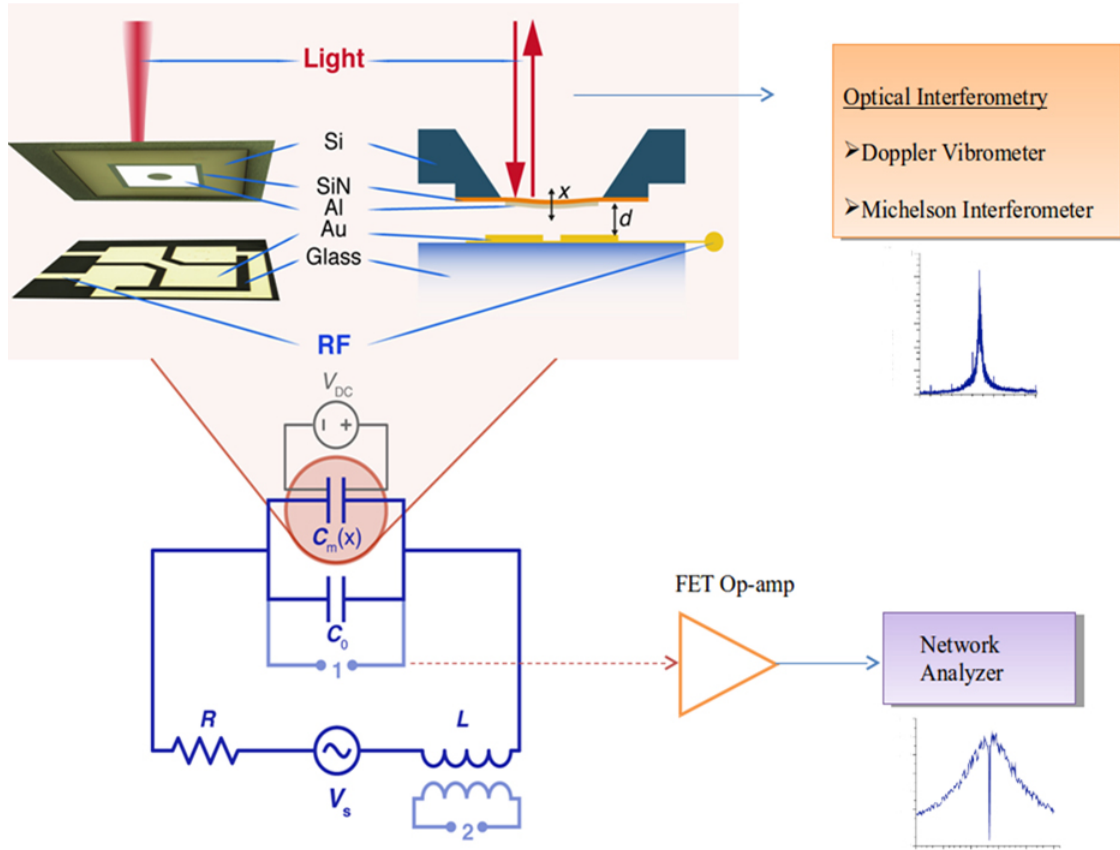


**Figure 4.1** A simplified version of the setup. A SiN-Al membrane is placed on the four-segment coplanar electrode (capacitor) with a spacing  $d$ . Membrane motion is tracked optically with the laser beam via two alternative methods - Doppler Vibrometry and Michelson Interferometry. As the membrane vibrates, it modulates the capacitance of the LC circuit, thereby creating electromechanical coupling, where  $V_{dc}$  acts as a knob for enhancing the coupling. A simplified electrical circuit schematics depicting the LC resonator is shown in the bottom left (for details see section 4.2.1). The two resonators are matched by tuning a trimmer capacitor  $C_0$ . The ferrite inductor ( $L$ ) acts as an antenna inducing rf signals in the circuit. The circuit can be driven inductively through port 2 and the voltage fluctuations on the capacitor are probed by a low noise fast FET (Field Effect Transistor) op-amp (port 1) and then fed to a lock-in amplifier or a spectrum analyzer for noise measurements. The membrane-capacitor is placed in a vacuum chamber ( $< 10^{-5}$  mbar).

to the interferometer via a fiber. All the electronic elements necessary for controlling the electromechanical coupling are contained in the shielded PCB (Printed Circuit Board). The output of the PCB is connected to the electrical feedthrough in the chamber and a short low-capacitance wire inside the chamber extends the connection to the membrane-capacitor chip. The inductor is made of a high-Q ferrite rod material wounded with Litz wires. It is

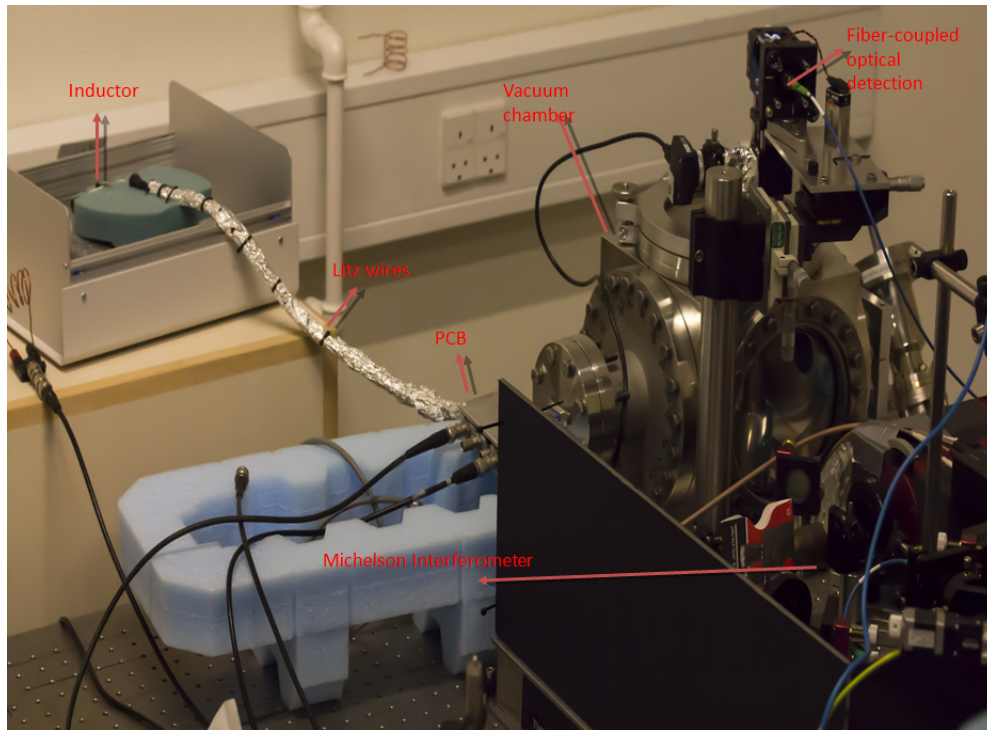


**Figure 4.2** A photo of the setup at NBI. The optical table is occupied with the Michelson Interferometer (partly seen here), the PCB unit (for electromechanical coupling) and the membrane-capacitor chip sitting inside the vacuum chamber (probe arm of the interferometer).

positioned inside a shielding box and connected to the PCB control unit (to form the LC resonator) via shielded Litz wires.

The optical interferometer at DTU is a commercial vibrometer (Polytec MSA-500) which uses the Doppler shift effect to extract the velocity of the mechanical resonator and to deduce the displacement. The operating principle of the device is explained in chapter 3. A large fraction of our experimental data as well as fast, preliminary tests of samples during the first two years of the project have been recorded with this device.

For the sake of more sensitive measurements and the general needs of the Membrane projects at Polzik Lab, our group - during the course of time - has developed a home-made Michelson Interferometer. The operation of the interferometer is also explained in the experimental methods section 4.3.

A vacuum chamber is used in order to prevent air damping of the mechanical resonator and therefore to preserve the high Q-factor of the membrane. Typically a pressure of  $10^{-5}$  mbar is enough to eliminate air damping and we operate around  $10^{-6}$  mbar.

## 4.2 LC circuit

Our resonant LC circuit is composed of a ferrite inductor and a capacitor whose total capacitance ( $\approx 80$  pF) is the sum of a large tuning capacitor, the modulated membrane-

electrode chip capacitance and other small parasitic capacitances. In the following subsections, the key components of the circuit are discussed.

#### 4.2.1 LC Circuit diagram and the PCB

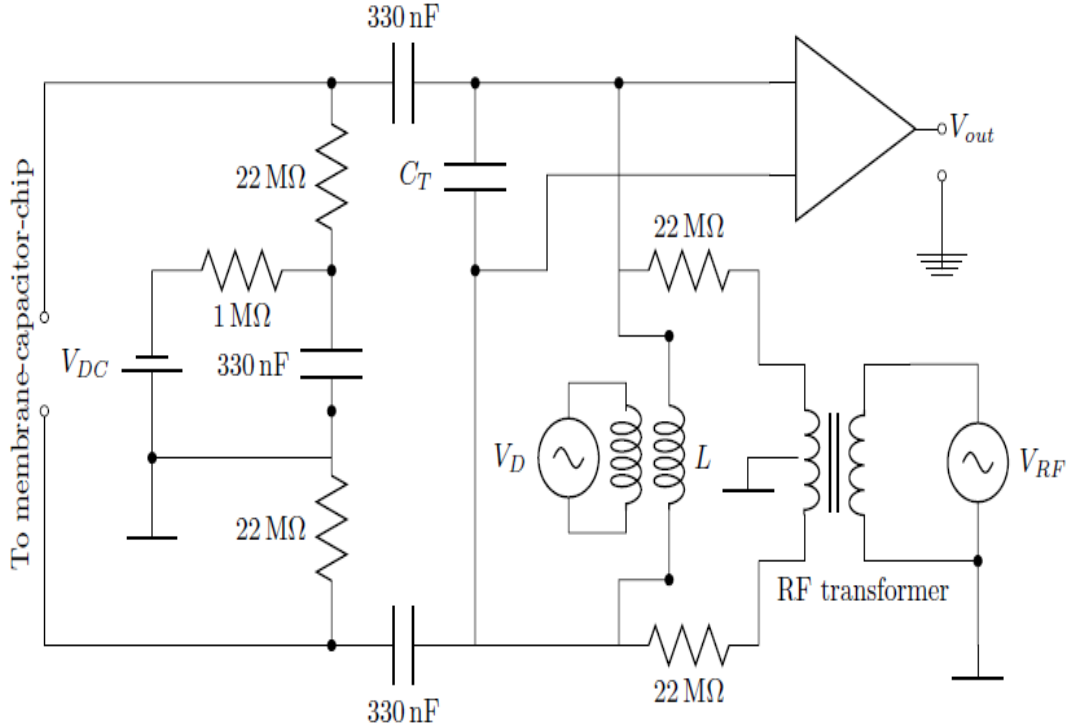


**Figure 4.3** Schematics of the electronics for realizing electromechanical coupling and characterizing the electrical response of the electromechanical system. Reproduced from [4].

The design of the PCB (see Fig. 4.3) takes into account concerns such as keeping the high  $Q$  of the LC resonator, minimizing coupling of unwanted capacitive or inductive noise and keeping parasitic capacitances added by connection lines as low as possible. We soldered these components on a PCB shielded with a metal box.

The dc bias voltage is used to charge the membrane (by electrostatic induction) and therefore to increase the coupling strength.  $V_{RF}$  port on the PCB, which consists of a BNC input and a small 1:1 transformer, is used for the option of exciting the system capacitively. For example, the ringdown measurements at zero coupling (inductor disconnected) was performed by using this port. For the driven LC measurements and exciting the membrane inductively, we placed a coil with a few windings (driven by  $V_D$ ) in the close vicinity of the inductor. In order not to load the LC circuit with the dc and ac drive, two 22 MΩ resistors are used. Short circuiting of the dc bias through the inductor is avoided with the

two 330 nF capacitors. The dc voltage source is low-pass filtered with a 1 M $\Omega$  resistor and a 330 nF capacitor.  $C_T$  is a high Q trimmer capacitor used for frequency tuning of the LC circuit. The voltage fluctuations on the capacitor (therefore on the membrane) are probed by a FET op-amp. The op-amp inputs are protected by 1 k $\Omega$  resistors which are not shown in the diagram. The op-amp component is more involved in reality (actually consisting of two identical op-amps followed by a third) and the total gain is 1000 at our frequency of interest. The power supply for the op-amp is filtered by capacitors and kept constant at 5V by regulators. The detailed schematics for the circuit is provided in Appendix A.

Fig. 4.4 shows how our PCB looks like in practice. It is designed in a compact way such that the parasitic capacitances are eliminated as much as possible. Panel on the left shows the upper side of the PCB that is placed in a shielded metal box. One of the FET op-amps (ADA4817-2) from Analog Devices [58] which can take differential inputs is soldered on this side. The tuning capacitor can be varied with screws to match the resonance frequencies. One connector goes to the inductor that is to be used and the multi-pin connector goes to the feedthroughs of the vacuum chamber in order to have connection to the membrane-capacitor inside. Panel on the right shows the lower side of the PCB where the other op-amp ADA4817-1 is placed.

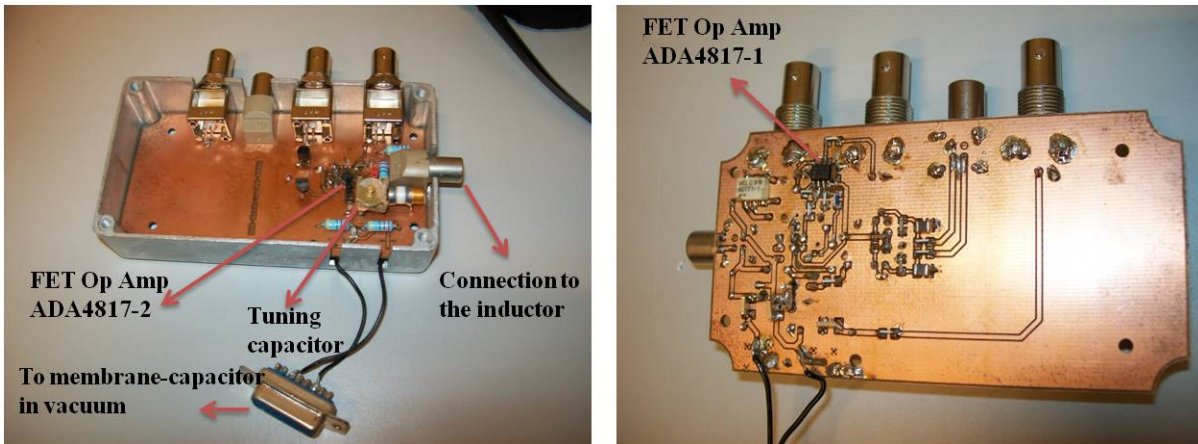


**Figure 4.4** Upper side of the PCB (left). Lower side of the PCB (right).

### 4.2.2 Inductor-The antenna

This subsection is dedicated to the inductor which is a crucial component of our LC circuit. Several tests have been conducted during the initial period of the project in pursuit of making the appropriate inductor for the specific requirements in our experiment. For the reasons as outlined below, it turned out that experimenting with ferrite core inductors (wound with Litz wires) was a promising a solution, especially in terms of getting high Q-factors. As the project was moving forward, we switched to different compact inductor geometries, specifically for low-noise detection considerations which will be discussed in chapter 5.

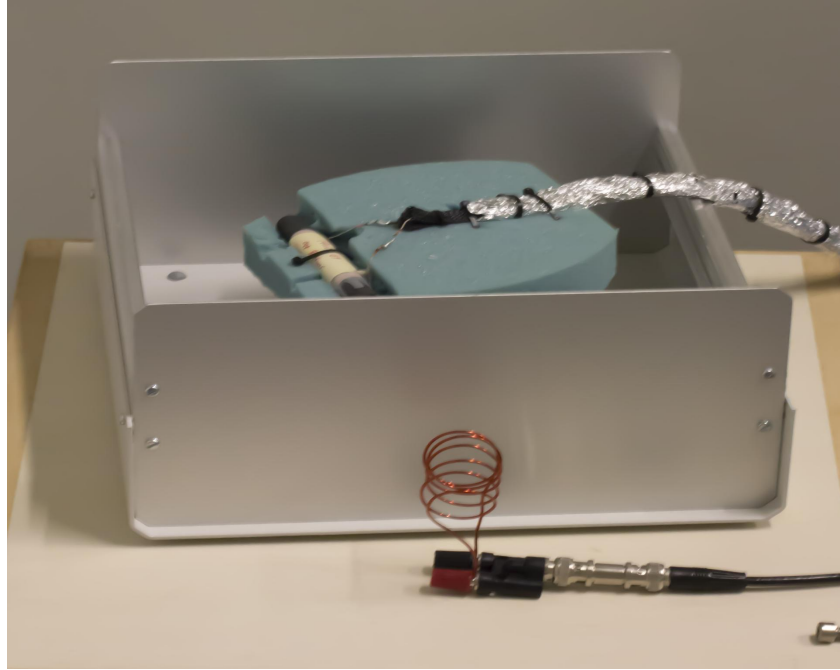


**Figure 4.5** A close-up photo of our ferrite rod inductor placed inside the shielding box. The Litz wires wrapped in aluminum foil (for shielding) connect the inductor to the PCB unit. The coil nearby can be used to drive the inductor.

**Frequency matching of the LC:** As our mechanical resonators typically have frequencies in the range of 700 kHz (for 0.5 mm size), the LC circuit has to be tuned to those frequencies. Taking a realistic approach for the total capacitance we could have in the circuit (a few tens of pF), this means that the inductance should be in the mH range for frequency matching. As this is a relatively high inductance, using a core material is typically necessary to reach those values at small sizes.

**High Q-factor:** In order to demonstrate strong coupling between the nanomebrane and the LC circuit, the coupling rate should exceed both the mechanical and the LC decay rate. The mechanical decay rates are typically very small (meaning quite high Q-factors), however the Q-factor of rf circuits at MHz frequencies is hardly above 100. Known to radio amateurs, ferrite cores (with the proper material and geometric design) provide the best way of getting higher Q-factors [55, 57] and this becomes crucial if the coupling rates are suspected to be small. Also in terms of the voltage sensitivity of our opto-electromechanical device, cooperativity has to be close to its optimum value and this becomes difficult if both the LC circuit and the mechanical resonator are lossy for some samples. Apart from the core material, Litz wires are crucial in eliminating skin effect and proximity effects which are typical loss mechanisms for AC signals [56]. These wires are made of bundles of very thin, individually isolated wires which are in the end connected at the soldering point. Thus the current flows independently in each wire, minimizing ac loss.

**Parasitic capacitance:** The parasitic capacitance added to the circuit should ideally be as small as possible to have higher coupling. Making a big inductor without a core material is usually accompanied by large parasitic capacitance which favors the use of compact core inductors due to their low parasitic capacitance (a few pF).

Driven by these initial motivations and following the common knowledge of radio amateur designers [57], we embarked on a few tests with winding inductors on a ferrite core. Ferrite has large resistivity and is therefore expected to have less eddy current loss. The material we chose for the ferrite core is Ferrite 61 (mixture of Zinc and Nickel) from Amidon as it is known for its suitability at MHz range [55]. These core materials are usually dominated by

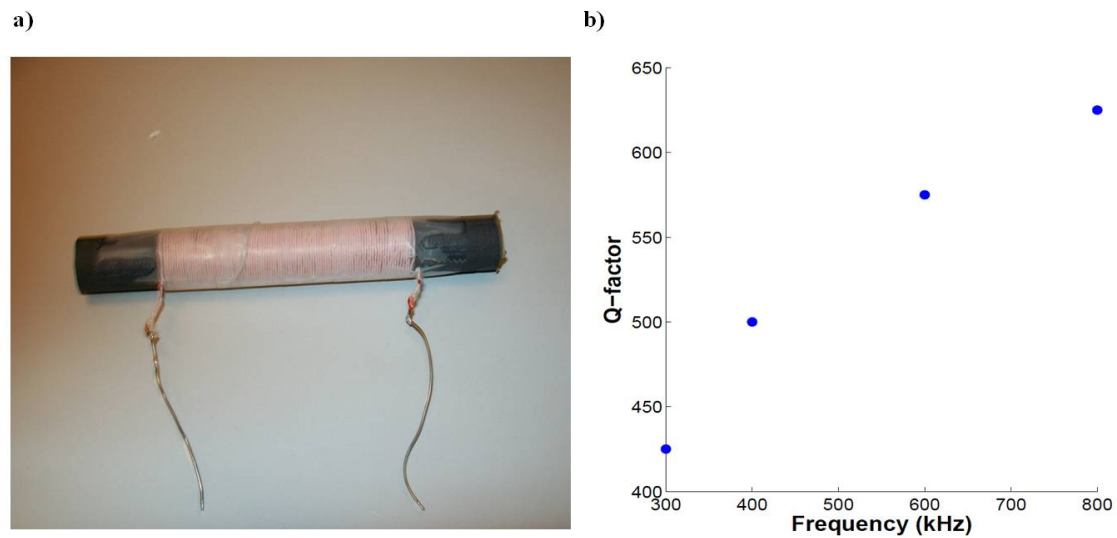


**Figure 4.6** a) One of our ferrite rod inductors wound with Litz wires. b) A sample test of a ferrite rod inductor with respect to operation frequency. The Q-factor is measured with an analog Q-meter.

core losses (hysteresis loss) at high frequencies. Furthermore, the geometry and positioning of the wires is important in determining the Q-factor. Ferrite rods with optimized length and diameter ratio (10 cm long, 1.25 cm diameter) have been purchased for this purpose. Apart from that, commercial Litz wires have been chosen with optimal diameter and bundle number for our specific frequency (20  $\mu\text{m}$  diameter, 50 AWG, 130 strands).

In Fig. 4.6a, we show one of our manually wound (Litz wires) ferrite rod inductor. In panel b, a test performed with a Ferrite 61 rod (83 turns, 1 layer) is shown. Around our frequency of interest (700 kHz), a remarkable Q-factor ( $\approx 600$ ) can be realized with the right range of inductance ( $\approx 500 \mu\text{H}$ ). In the experiments with the systematic analysis of our LC-membrane coupling, we have used a 90 winding inductor with an inductance of 635  $\mu\text{H}$  and a Q-factor of around 500.

### 4.2.3 Membrane-Capacitor chip

The membrane-capacitor chip component used in the LC coupling experiments is in principle the same with the ones explained in the previous chapter. In this chapter, based on the reasons mentioned before, we will be dealing with aluminum-coated membranes. Fig. 4.7 shows a microscope picture of one of our samples.

In panel a, we show a four-segment electrode capacitor. The four circles surrounding the

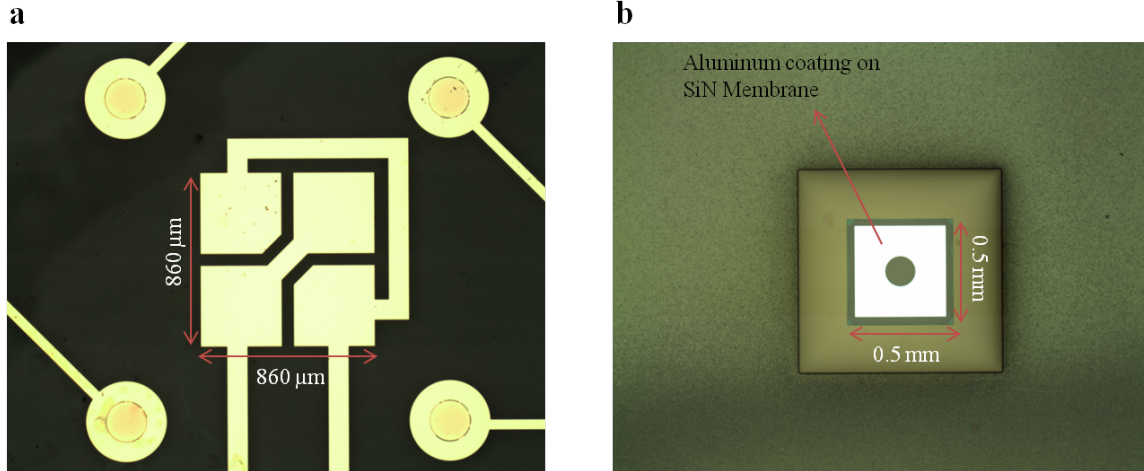


**Figure 4.7** a) Four-segment electrode forming the capacitor. b) An Al-coated SiN membrane. Metal coating on the edges are patterned out for mechanical Q considerations. The hole in the middle is considered for future cavity opto-electromechanics experiments (reproduced from [4]).

electrodes are the pillars that are designed to determine the membrane-electrode distance. In panel b, we show a sample SiN membrane coated with aluminum avoiding the edges. The layer that is surrounding the membrane is a large silicon frame. A photo of a typical combination we have been using, which is a  $860 \times 860 \mu\text{m}$  capacitor chip with a 0.5 mm Al-coated SiN membrane, is shown in Fig. 4.8. Assembly of the membrane and the capacitor chip is a critical task and the procedure is the same as described for the samples discussed in the previous chapter. After the assembly, the samples are inspected under the microscope (as in Fig. 4.7) for the gentle alignment of the membrane with respect to the chip and general inspection of dirt or residual particles. As can be seen in Fig. 4.8, the four-segment electrode is patterned on a transparent glass substrate. The substrate is then placed on a mount inside the vacuum chamber. We use contact probes to press on the electrode pads from above for electrical connection that also helps to immobilize the chip.

### 4.2.4 Loss of the equivalent circuit

The LC decay rate is a determining parameter of the setup. The cooperativity of the system (which effects the sensitivity) is inversely proportional to the LC linewidth and for reaching the strong coupling regime, the coupling rate should be larger than both the LC and the mechanical decay rates. As outlined in the inductor section, we have used a high Q ferrite inductor ( $\approx 500$ ), however the whole circuit including all the parasitic elements has

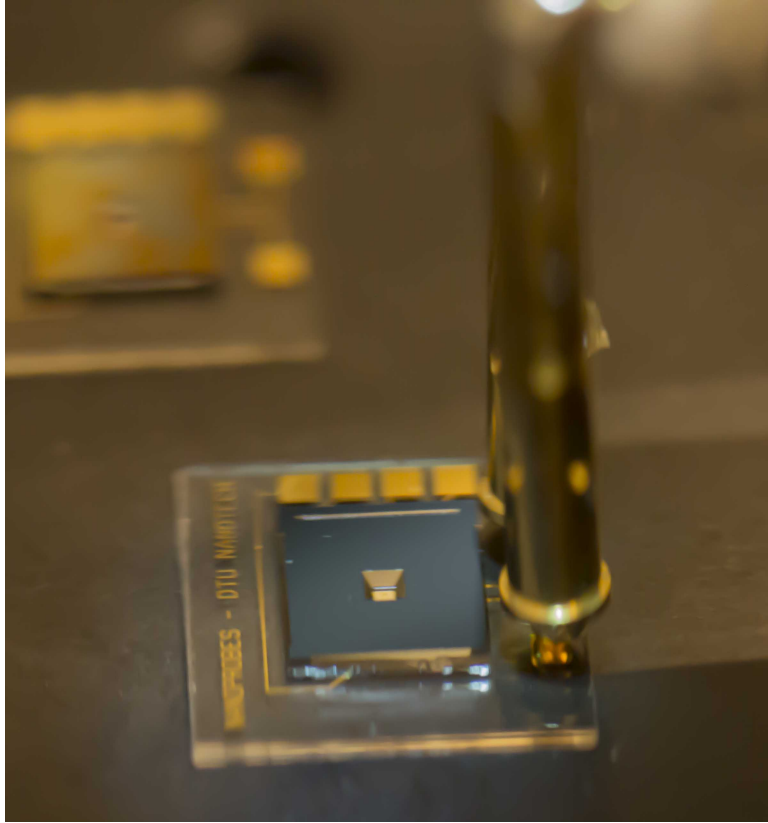


**Figure 4.8** Photo of a SiN-Al membrane placed on a four-segment electrode chip deposited on glass. The chip is connected to the PCB via the gold contact probes shown here.

shown Q-factors of around 130 (confirmed with LC resonant response measurements). Even though this was sufficient for us to observe strong coupling in the end, it would be useful to mention the possible loss mechanisms in the chain. First of all, we suspect that the the PCB introduces some dielectric losses since the connection of the PCB and the inductor only (without the membrane-capacitor chip) already reduces the Q to typically 300. Later on, the inductor is placed in a shielding box which is kept at a certain distance from the optical table. We have realized that at our working distances the optical table and magnetic elements contribute to the reduction of the Q, roughly to around 250. In the last stage, we connect the combined LC circuit to the membrane-chip inside the chamber. In this case, we have consistently observed the Q-factor being reduced to 100-130. In order to investigate whether the membrane or the four-segment electrode chip brings the significant reduction, we have tested the situation with a membrane on chip and a chip only. Even without the membrane, we have still observed similar reductions suggesting that the four-segment electrode is mainly responsible for the decrease in Q. We measured roughly a contact resistance of  $50 \Omega$  for the gold connection lines on the chip at that time and lower than  $10 \Omega$  for our next generation chips with wider electrodes. The origin of the reduction in the loss rate of the combined circuit is not clearly understood, but it is presumably a combination of ohmic and dielectric losses.

### 4.3 Experimental Methods

In this section, we describe the full set of methods we have so far utilized in order to characterize our electromechanical system and extract the crucial parameters. First, the

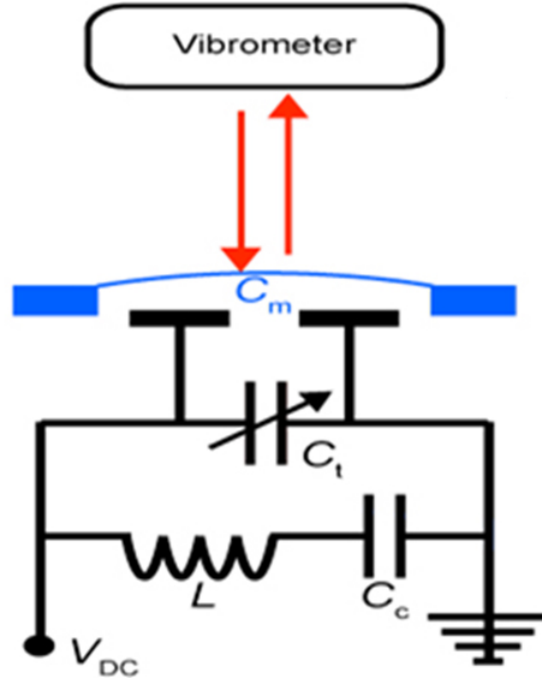


**Figure 4.9** Depiction of the Doppler Vibrometer tracking the mechanical vibrations coupled to the LC circuit (the detailed circuit is the same as depicted in Fig 4.3). Here  $C_c$  in series to the inductor represents the capacitor necessary in order not to short-circuit the dc bias through the inductor (reproduced from [71]).

optical interferometry part is introduced (including the experiments with the vibrometer at DTU and the Michelson Interferometer at NBI) with which the membrane vibrations are tracked. Then, we will describe the electrical measurements where we simply extract the system parameters by recording the spectral response of the LC circuit via lock-in detection or noise measurements of the circuit voltage. Finally, we will explain the calibration methods where we deduce the absolute vibrations of the membrane in units of meters.

#### 4.3.1 Optical Interferometry I- Doppler Vibrometer

Major part of our preliminary experiments and LC coupling results (except for the recent high sensitivity measurements) have been recorded with the Doppler vibrometer. Fig. 4.9 shows in a simplified way how the vibrometer optics is interfaced with the coupled electromechanical system. All the details about the vibrometer are given in Chapter 3, which also applies to the methods of the LC coupling experiments.

## 4.3.2 Optical Interferometry II- Michelson Interferometer

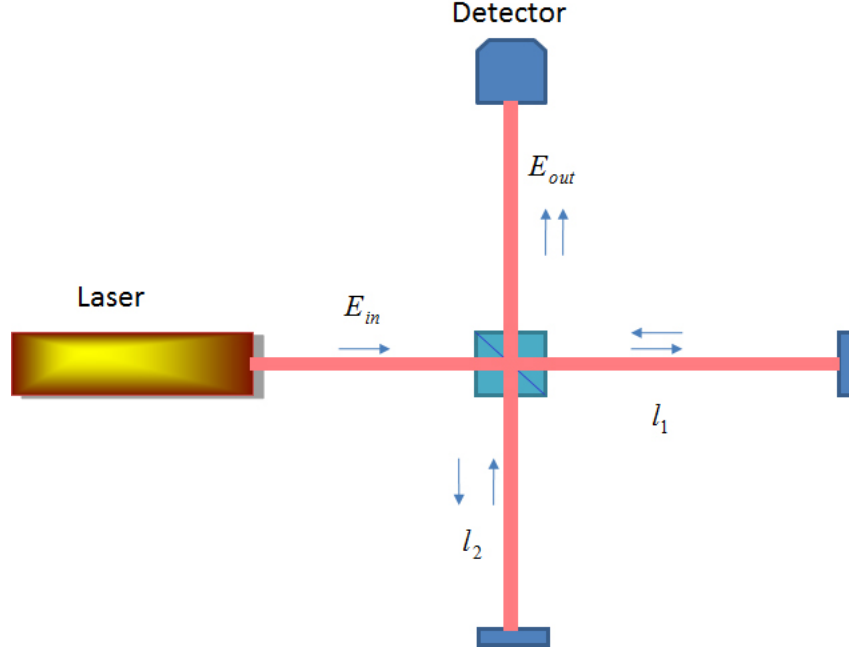


**Figure 4.10** A generic picture of a Michelson Interferometer with a probe and reference arm.  $E_{in}$  is the incoming laser beam and  $E_{out}$  is the output beam which carries the interference pattern of the probe and reference arm.

Michelson interferometry is known to be a well-established technique used to detect minute path length changes [59–61]. Fig. 4.10 depicts a typical Michelson interferometer with a reference and probe arm (Other necessary optical elements are skipped). The main idea is that the beam coming from the laser is split into the two arms via the beam splitter, reflected back and recombined at the detector part. Assuming that the reference arm is stable and not moving, path length changes caused by the motion of the probe arm (a moving mirror etc) can be detected via the interference pattern seen on the detector.

The mathematics behind detection can be grasped in a straightforward manner by writing down the electric field amplitudes summed up at the detector side. Imagine the input beam to be a simple plane wave with frequency  $\omega$ , then the input and the following output fields can be written as follows

$$E_{in} = E_0 e^{i(\omega t - kx)} \quad (4.1)$$

$$E_{out} = \frac{i}{2} E_{in}(2l_1, t) + \frac{i}{2} E_{in}(2l_2, t) \quad (4.2)$$

where  $t = 1/\sqrt{2}$  and  $r = i/\sqrt{2}$  have been used as the complex transmission and reflection coefficients for a 50/50 beam splitter and  $k = 2\pi/\lambda$  is the wave number with  $\lambda$  referring to the wavelength of the laser beam. Following the two equations above, the output field can be written as

$$E_{out} = \frac{i}{2} E_0 e^{i\omega t} (e^{-i2kl_1} + e^{-i2kl_2}) \quad (4.3)$$

yielding

$$E_{out} = iE_0 e^{i(\omega t - k(l_1 + l_2))} \cos(k(l_1 - l_2)) \quad (4.4)$$

We are interested in the power measured by the photodetector, so by taking the square of the field amplitude, one reaches

$$P_{out} = \frac{E_0^2}{2} (1 - \cos(2k\Delta l)) \quad (4.5)$$

At this point, it is useful to define the parameter  $V$  (visibility) that is used to characterize the contrast of interference of the optical system

$$V = \frac{P_{max} - P_{min}}{P_{max} + P_{min}} \quad (4.6)$$

The detailed schematics of our home-built interferometer is depicted in Fig. 4.11. First, the laser beam (fiber coupled to the laser source) is introduced into the common path of the interferometer. The polarization is cleaned with a polarizer right after the fiber output.

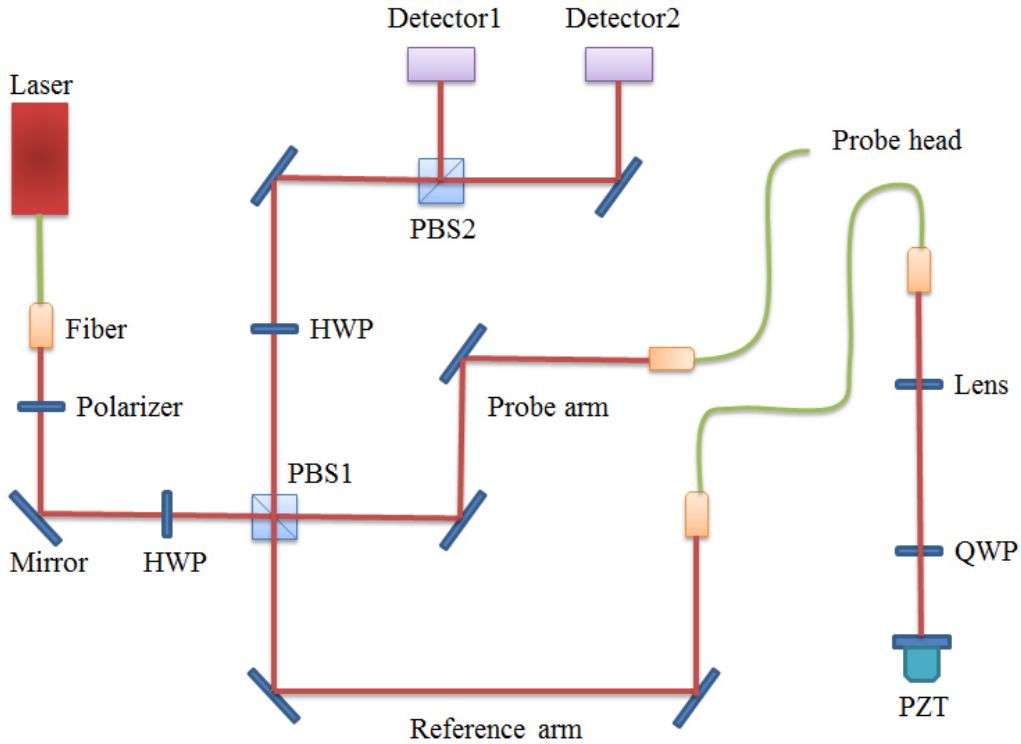


**Figure 4.11** Schematics of the Michelson interferometer with balanced detection (HWP: Half wave plate, QWP: Quarter wave plate, PBS: Polarizing beam splitter, PZT: Piezo tube ).

A  $\lambda/2$  waveplate is used to arrange the amount of light going to the reference and probe arms. Then PBS1 splits the beam into two arms. The beam continuing in the reference arms is fiber coupled and sent onto a piezo mounted mirror to change the path length of

the arm. The piezo is controlled with a servo box to scan the fringe pattern and lock the interferometer at the right operating point.

The beam travelling on the probe arm is also coupled to a fiber and sent on to the membrane in the vacuum chamber with the head (involving a camera to monitor and illumination). A  $\lambda/4$  waveplate is used both in the probe and reference arm to recombine the reflected lights at the first beam splitter. The back reflected beams from the reference and probe arm recombine at PBS1 again and then split at PBS2 for balanced homodyne detection. The waveplate in between can be used to finetune the powers on the two arms reaching the two photodiodes of the detector. The photodetector is a sensitive Thorlabs balanced detector (InGaAs) with 0-75 MHz bandwidth with high common-mode rejection ratio. There are two DC output ports of the photodetector which can be used to monitor the interferometer signal and an rf output which gives the differential signal from the two. The difference of the two DC ports is used to generate an error signal for the lock.

Our home-built interferometer is shown in the photo in Fig. 4.12a. Light from the Mephisto laser (Nd:YAG) at 1064 nm is sent through an isolator and follows the optical paths aimed for different experiments. Part of the optical power is coupled to the fiber that enters the the

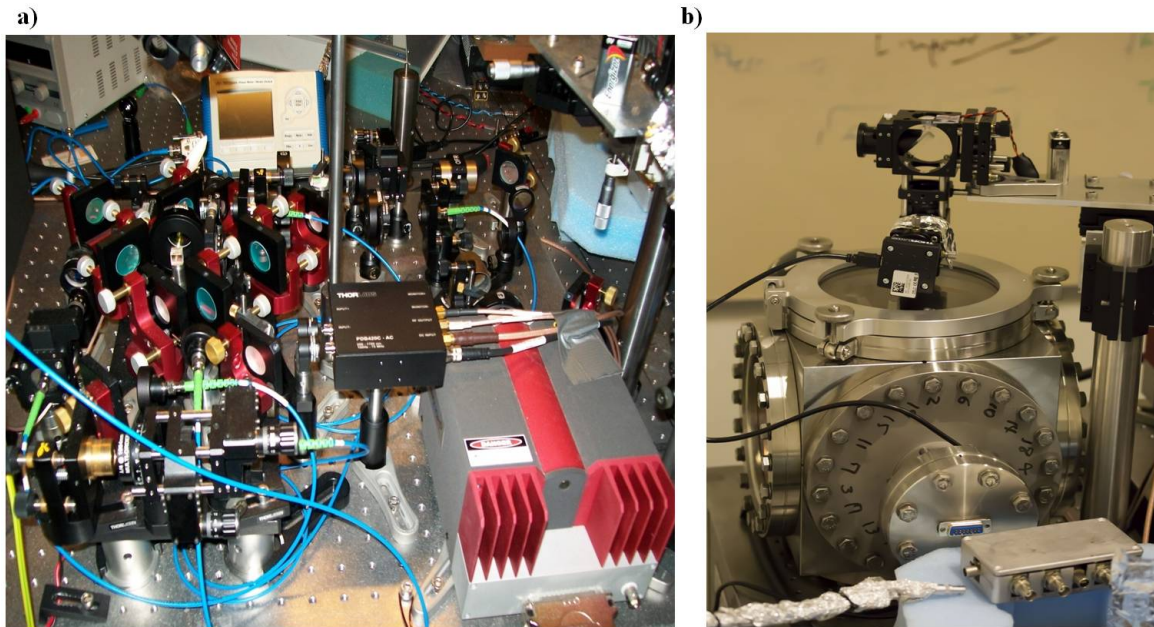


**Figure 4.12** a) Michelson Interferometer setup b) Probe head with the fiber port and the camera on top of the vacuum chamber. The other optical elements are tied together in a cage system.

interferometer arm. As shown in the right (b), the beam in the probe arm is coupled to a fiber and is mounted on the readout head fixed in a cage system (fiber is not connected in the picture). The beam travels inside the cage system and follows a quarter waveplate, a beam splitter and a focusing lens before hitting the membrane. The beam passes through the beam splitter, hits the membrane and some part of the reflected light shines on the vertically positioned camera inside the cage. With some LED illumination, we can see the membrane and the beam position on the membrane as well as the electrodes underneath.

Big portion of the reflected light couples back to the fiber (having passed through the quarter waveplate two times) and goes back to the interferometer with the right polarization for detection.

### 4.3.3 Calibration of the mechanical amplitude

In this subsection, we will describe how we convert our optical signals from membrane vibrations into absolute amplitudes in meters, separately for the Doppler Vibrometer and the Michelson Interferometer.

#### Doppler Vibrometer

The mechanical noise spectrum measurements done with the vibrometer uses the built-in calibrated procedure of the commercial device. As the membrane moves, it gives rise to a Doppler shift proportional to its velocity which is detected interferometrically. The voltage controlled piezo in the reference arm is used for the absolute calibration of the displacement. The velocity information is then processed to yield amplitudes and an FFT is performed to generate the membrane spectrum in units of meters.

However, for the driven membrane measurements with the vibrometer, an additional calibration procedure has to be implemented since the output of the vibrometer is fed to a lock-in amplifier for those measurements. The procedure we have used can be described as follows. The membrane is first excited with a single frequency sine wave of known amplitude from the rf output of the lock-in via a drive coil. This appears as a sharp mechanical response on the FFT analyzer of the vibrometer which is already calibrated in meters. This value is then used to calibrate the wide membrane spectrum while we scan the rf excitation signal and record the driven response of the vibrometer output which is fed to the lock-in amplifier.

#### Michelson Interferometer

The working principles and key equations of the Michelson Interferometer have been explained in the Optical Interferometry-II part. The way we calibrate the mechanical amplitudes in meters rely on the interference fringe equations. In the experimental setup, we have (ideally) two identical voltage measures (except for their signs) coming from the two photodiodes of the balanced detector. The voltage measured by those is proportional to the power of the light impinging, therefore the difference of the two can be written simply as

$$V_{\text{diff}} = A \cos(2k\Delta l) \quad (4.7)$$

where  $A$  quantifies the signal amplitude and the signal is a function of the path length difference as expected. The two voltages and their difference in a typical measurement are depicted in Fig. 4.13 yielding the interference fringe pattern (numerical) as one scans the path length difference. As can be seen, the difference signal oscillates around zero where the intensity fluctuations are cancelled to a large extent. Furthermore  $\lambda/8$  point gives the highest slope, therefore the sensitivity is maximized around this point. For these reasons, we lock our interferometer at this 0V point. The piezo is feedback depending on this differential error signal such that it keeps this level the same. Then, we look at the high frequency signals (1MHz) that carry the mechanical vibrations with the rf part of this error signal. To see how calibration is performed, we need to look at the equations that convert a certain voltage to an absolute displacement. First of all, the differential voltage can be reexpressed

in terms of  $V_{FF}$  the full fringe voltage (peak-to-peak) - maximum and minimum of the interference signal

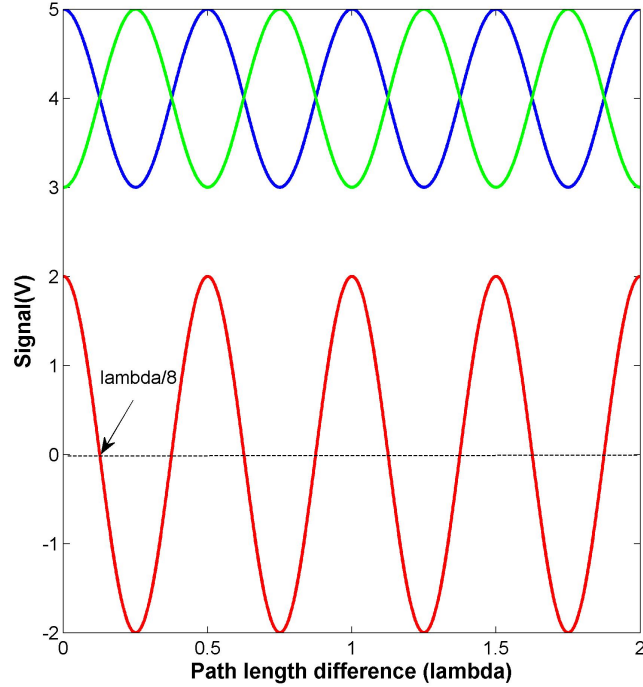


**Figure 4.13** Interference fringe pattern (numerical) for the separate signals from the two photodiodes (green and blue) and their differential signal (red) which produces the error signal for the lock.

$$V_{\text{diff}} = \frac{V_{FF}}{2} \cos(2k\Delta l) \quad (4.8)$$

Assuming that we are operating at the locking position ( $\lambda/8$ ) and we are interested in small vibrations of the mechanical oscillator in the vicinity of this locking point, the detected voltage can be written as follows

$$dV = V_{\text{diff}}(\lambda/8 + dx) = \frac{V_{FF}}{2} \cos\left(\frac{\pi}{2} + 4\pi \frac{dx}{\lambda}\right) = -\frac{V_{FF}}{2} \sin\left(4\pi \frac{dx}{\lambda}\right) \quad (4.9)$$

where  $dV$  and  $dx$  refer to the rms voltage and vibration amplitude, respectively.

As the vibrations are expected to be small, the sin term can be approximated by  $\sin(4\pi dx/\lambda) \approx 4\pi dx/\lambda$ . Thus the conversion equation between voltage and displacement is given by

$$|dx| = \frac{\lambda}{2\pi} \frac{|dV|}{|V_{FF}|} \quad (4.10)$$

This means that for a given voltage detected with this differential signal, we can deduce the absolute displacement if we know the wavelength of light and the full fringe voltage. In the experiment, we realize the calibration procedure using the following methodology. We

first make a fringe measurement where we sweep the piezo with a certain voltage to see the full fringe signal like depicted in Fig. 4.13. We read off a full fringe voltage from the two signals on the scope which will enter in the calibration equation. Then we use a calibration peak, which is itself calibrated with respect to the full fringe measurement by using the fringe equation, to set a reference for the membrane thermal noise measurements. The calibration peak is essentially a small modulation at a frequency close to the mechanical frequency (typically 700 kHz) which is provided by driving the piezo with a certain voltage amplitude. This signal shakes the piezo and the interferometer optical readout sees it as a modulation peak in the spectrum (a sample calibration plot is shown in Fig. 4.14). To

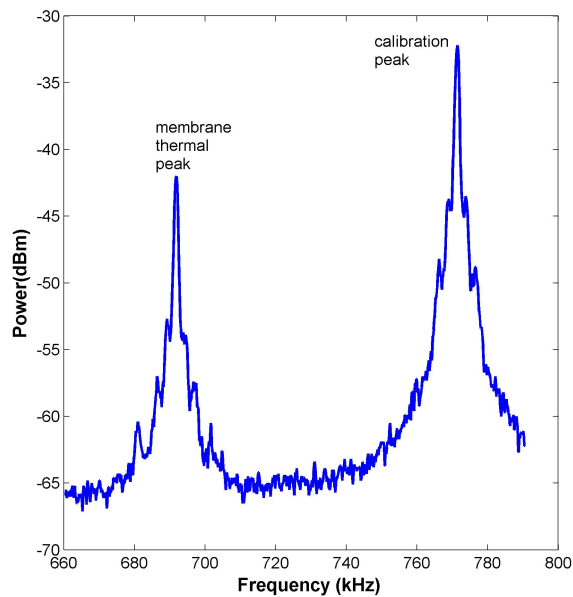


**Figure 4.14** Calibration peak and membrane thermal peak recorded in the same spectrum with a low resolution setting. The peak amplitudes in this setting correspond to rms values that can also be used as a way of calculating the effective mass.

determine this calibration peak amplitude, we measure it with a high impedance setting of a lock-in amplifier which gives the rms voltage at this specific frequency. Once this is done, the calibration peak itself can then be compared to the full fringe voltage and its amplitude in meters can be calculated. Following this procedure, the thermal peak of the membrane can be calibrated by referencing it to the calibration peak. The calibration of the membrane peak with the intermediate step of referencing it to a calibration peak is useful for practical reasons. In case the beam position or light power change or have to be varied for various experiments, it is not necessary to re-do the full fringe measurements from the beginning since no matter what is changing in the system, the calibration peak will automatically adjust itself as the membrane does. Thus the significant quantity to keep track of is the ratio of the two. Depending on the purpose of the experiment, a low resolution or a high resolution spectrum recording might be used for the displacement

calibration and effective mass determination. For example, for quick determination of the mass, it is convenient to use a low resolution spectrum (both wider than the calibration and membrane peak linewidth) as the thermal peak amplitude refers to the rms value and the square of this calibrated rms value gives the integrated  $x^2$  which can be directly inserted in the equipartition theorem,  $\frac{1}{2}kx_{\text{rms}}^2 = \frac{1}{2}k_B T$  as in Fig. 4.14. The temperature  $T$  is assumed to be room temperature (300K) in our case. Alternatively, the narrow membrane spectrum can be recorded with a high resolution setting and then fitted to a Lorentzian in order to extract both the effective mass and the mechanical linewidth  $\Gamma_m$  by using the double-sided thermal spectrum [14, 62]

$$S_{xx}(\Omega) = |\chi_m(\Omega)|^2 S_{FF}(\Omega) = \frac{1}{m^2} \frac{1}{(\Omega_m^2 - \Omega^2)^2 + \Gamma_m^2 \Omega^2} 2m\Gamma_m k_B T_m \quad (4.11)$$

We note that the measured effective mass for our membrane is dependent on the position of the optical readout beam on the membrane. The expected value (referenced to the center of the membrane) is always 1/4 of the physical mass for a square membrane. Therefore, depending on where our laser beam hits (typically slightly off-center with respect to the hole in the middle), the effective mass can show variations from this expected number.

#### 4.3.4 Electrical characterization

##### Driven LC circuit and Noise Measurements

In our setup, we have the advantage of using two non-perturbative probing methods; optical interferometry and electrical probing. As the membrane is coupled to the capacitor (which drives its vibrations) and the capacitor is part of a resonant LC circuit, one can observe the electromechanical coupling and extract crucial parameters by driving the LC circuit and monitoring the voltage on the capacitor with a low-noise detection configuration. Here, we achieve this by incorporating a weakly coupled rf driving (not to load the Q) and a very low-noise amplifier (FET) which detects the voltage on the capacitor, ideally without affecting the system (as it was shown in the detailed circuit diagram). Fig. 4.15a shows an example from a characterization measurement of the coupled electromechanical system. In order to extract the bare properties of the LC circuit such as linewidth, the circuit is driven with a coil in the vicinity of the ferrite inductor. The resonating voltage is then tracked with the op-amp, the output of which is fed to a lock-in amplifier or a spectrum analyzer. The Lorentzian fits give the intrinsic Q (or the linewidth) of the uncoupled LC in the absence of DC voltage. The LC resonance frequency is tracked in this way as well while adjusting the tuning capacitor. When a DC voltage is applied, membrane vibrations couple to the circuit and create voltage fluctuations that dramatically change the LC circuit behavior as seen in the mechanically induced transparency dip of Fig. 4.15b. We make fits coming from our theoretical models to extract coupling related parameters as it will be discussed in the MIT regime later.

Apart from driven LC measurements, we have also performed electrical noise measurements where the electrical spectrum is recorded with a spectrum analyzer or an oscilloscope (FFT). For the measurements performed at DTU, we have worked with a lock-in amplifier from Zurich Instruments (HF2LI) which can be set to work both in FFT spectrum analyzer and lock-in mode. For the measurements performed at NBI, we have used several devices depending on the purpose of the experiment. An ESA Agilent Spectrum Analyzer and an HP

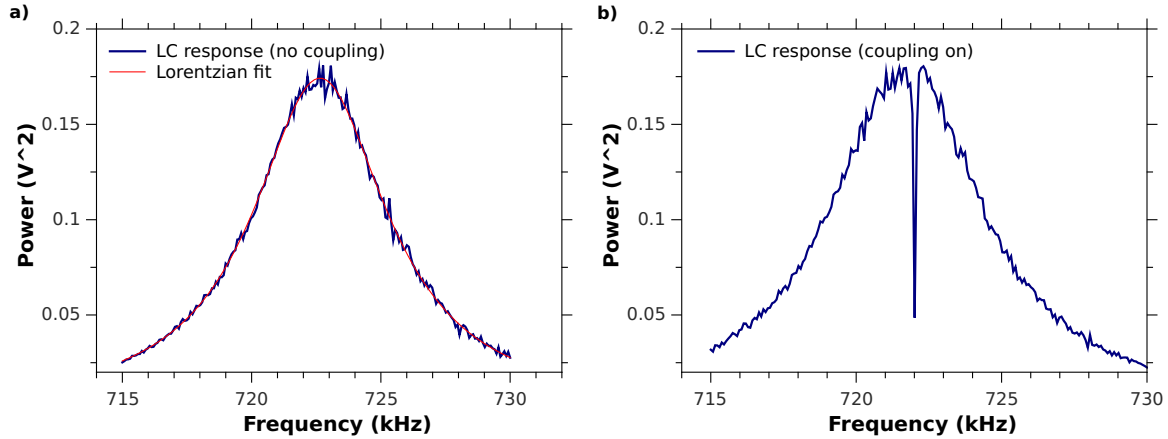


**Figure 4.15** An example from an electrical characterization measurement of the electromechanical system. a) Rf coil driven response of the LC circuit at 0 V dc bias. Without any dc voltage, membrane dynamics is decoupled from the LC circuit and the Q-factor of the bare LC circuit can be determined. b) Rf driven response with dc=25 V. A clear dip (MIT feature) is observed due to coupling to the vibrations of the membrane.

Network analyzer have been utilized for driven response and noise measurements together with a fast Lecroy Oscilloscope for acquiring FFT spectrum data.

### FET Op-amp

In order to read out the voltage across the capacitor, to which the membrane is connected, we have used a low-noise fast FET (Field Effect Transistor) ADA4817 from Analog Devices [58]. The op-amp has a specified voltage noise of  $4 \text{ nV}/\sqrt{\text{Hz}}$  and a current noise of  $2.5 \text{ fA}/\sqrt{\text{Hz}}$  at 100 kHz. The actual bandwidth of the op-amp is 1 GHz, however this gets reduced down to a few MHz in our case depending on the feedback resistors we use for achieving gain. The configuration we utilize in the experiment is a High Speed JFET Input Instrumentation Amplifier mode (with three ADA4817 op-amps) arranged in a way to yield a gain of  $G=1000$ . This Instrumentation Amplifier mode is suitable for our application since it is possible to accept floating inputs from both leads of our capacitor. A more detailed information about our op-amp configuration can be found in Appendix A.

## 4.4 Data analysis and results

One of the immediate goals in our project was to demonstrate coupling between the membrane and the LC circuit by optical means. This would then pave the way for using this system as an efficient transducer to readout rf signals with optics or convert rf photons to optical photons, as well as further possible applications in different coupling regimes. In this section, we will present the results obtained with this electromechanical system and analyze the data in light of our theoretical models. The section is divided into three main parts; MIT regime, strong coupling regime and extraction of the coupling strength.

### 4.4.1 Mechanically induced transparency regime

The fundamental reason behind electromechanical coupling is the distance dependence capacitance of the LC resonator. As the membrane moves, it alters the capacitance, thereby modulating the resonance frequency of the LC circuit. In such an electromechanical system, one can observe the dramatic effect of coupling in both ways (on the membrane and the LC circuit) if the coupling rate is sufficiently large. This dynamics would then give rise to an interesting phenomenon called MIT (Mechanically Induced Transparency) which is an interference effect like the well-known EIT (Electromagnetically Induced Transparency) [64]. Such a phenomenon has been observed with a microwave circuit operating at cryogenic temperatures [21] and named EMIT (Electro-mechanically Induced Transparency). When the coupling microwave tone (together with a probe tone) is injected into the circuit, the mechanical resonator is driven coherently and this in turn causes voltage fluctuations in the circuit which interferes destructively with the incoming probe signal. This results in a dip at resonance which is manifestation of the physics of coupling [68]. This phenomenon has first been observed in an optomechanical system (OMIT- Optomechanically Induced Transparency) with an optical cavity and a mechanical resonator [20]. Slightly different from the setups described, here we observe this phenomenon with a room temperature LC circuit and a membrane by using a DC voltage source for the coupling. In both examples stated above, the microwave and optical cavities are driven at vastly different frequencies than the mechanical resonator which is known as the parametric coupling [65–67], whereas in our case the LC resonator and the mechanical resonator frequencies are matched.

We have experimented with several Al-coated SiN membranes for the preliminary tests on the way to the observation of electromechanical coupling. Those measurements have been performed with the Doppler vibrometer. The handy feature of the vibrometer is that the initial distance between the membrane and the chip can be measured quickly with the White Light Interferometer setting without first placing the sample under vacuum and connecting to a voltage source. This helps us in estimating quickly the possibility of observing high coupling rates with different samples for a realistically applicable voltage. At the same time, the Michelson Interferometer at NBI had been under construction and was not available until our first experiments for low-noise optical detection.

Usually our procedure of observing a coupled system starts with initial frequency shift tests of the membrane with the inductor being disconnected from the PCB (same procedure as stated in the previous chapter). This helps us identify the expected shifted membrane frequency (shift corresponding to  $\Delta\Omega_m \approx -C'''(x)V_{dc}^2/2m\Omega_m$ ) after applying a dc bias voltage. Fig. 4.16 shows the mechanical frequency vs dc bias of a 0.5 mm size SiN-Al membrane tracked with the Doppler Vibrometer in the presence of the LC circuit (inductor connected). In this measurement, the peak frequencies are extracted from Lorentzian fits to the driven membrane spectra (via the drive coil in the vicinity of the inductor). Note that the frequency shift vs dc bias measurement does not require the presence of the inductor (as it has been performed in the capacitive coupling chapter), but it allows observing all features of the coupled system in one and the same setting.

The results we will show in the MIT section refer to a data set taken with this sample which has 50 nm Al coating and a 100 nm SiN layer with a measured effective mass of 30 ng. After having observed the range of the mechanical frequency (how it shifts with the dc bias), we concentrate on the LC response when driven with the coil in order to see the first

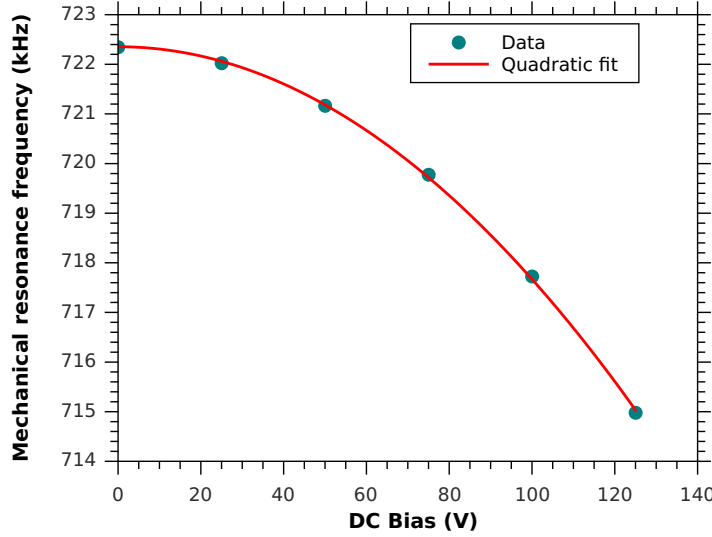


**Figure 4.16** Membrane mechanical resonance frequency tracked with the Doppler Vibrometer. The fit is a quadratic function of the dc bias voltage as expected from our models.

signs of LC-membrane coupling. With the dc bias off, we can tune the capacitor to match the LC to the desired mechanical frequency, known from the previous tests. Then applying a dc bias voltage generates coupling between the membrane and the LC circuit which can be observed with an MIT dip at the mechanical frequency on the driven LC response. Fig. 4.17 shows a sample coupling picture at 25 V dc. The fit function for the electrical response comes from equation 4.12 for the voltage across the capacitor.

As we first see the MIT dip, we also fine tune the position of the dip by slightly changing the dc voltage. In this way, one can position the MIT dip in the center. This should correspond to the maximization of the coupling strength. At the same time, we can monitor the membrane fluctuations by looking at the optical signal from the Doppler Vibrometer. Due to the coupled nature of the system, a dramatic change becomes clear in the spectrum, namely broadening of the membrane linewidth from a few Hz to several kHz increasing with the dc voltage. This can be understood by looking at the Langevin equations of the coupled system we have treated in the theory chapter. An intuitive explanation is that the membrane (the high Q oscillator in this case) couples to a lower Q resonator, therefore dissipating its energy faster than its intrinsic decay rate. The models that we use to fit the data come from the coupled equations of motion that describe the voltage probed on the capacitor and membrane vibrations derived in the theory chapter. It is possible to show that the voltage on the capacitor - assuming that the drive is dominated by the induced voltage on the inductor - can be described by (as shown in section 2.3)

$$\delta V_c(\Omega) = - \left( \frac{1}{C(\bar{x})} - \chi_m(\Omega)G^2 \right) \chi_{LC,eff}(\Omega) \delta V_s(\Omega) \quad (4.12)$$

By inserting the total capacitance measured beforehand (typically  $C(\bar{x}) = 80$  pF) and fitting

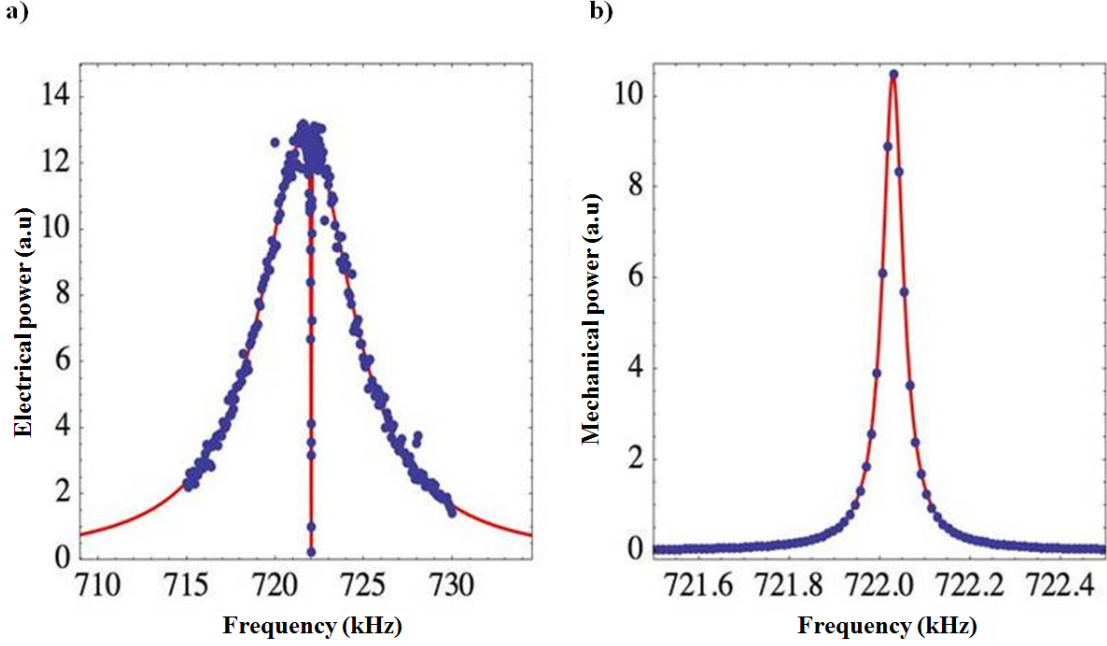


**Figure 4.17** a) MIT dip in the driven electrical response with a model fit at 25 V bias. b) Broadened membrane driven response (at the same bias voltage) tracked optically and fitted to the model for the mechanical resonator.

this function to the measured voltage on the capacitor, we extract the parameters  $\Omega_m$ ,  $\Omega_{LC}$ ,  $\Gamma_{LC}$ ,  $G$  and  $\delta V_s$ . Following the relationship between the optically detected phase fluctuations and the membrane fluctuations

$$\delta\phi(\Omega) = 2k\chi_{m,\text{eff}}(\Omega)G\chi_{LC}(\Omega)\delta V_s(\Omega) \quad (4.13)$$

the membrane spectrum can be described by

$$\delta x(\Omega) = \chi_{m,\text{eff}}(\Omega)G\chi_{LC}(\Omega)\delta V_s(\Omega) \quad (4.14)$$

where again the driving voltage dominates over the thermal noise of the membrane. The system parameters like  $m$  and  $C$  are extracted from independent measurements (uncoupled membrane thermal spectrum for determining  $m$  and LC resonance frequency with a known inductance for determining  $C$ ) and  $\Gamma_{LC}$  is found by fitting the measured voltage on the capacitor with the equation 4.12. The fit function for the mechanical spectrum is then used to extract the parameters  $\Omega_m$ ,  $\Omega_{LC}$ ,  $G$  and  $\delta V_s$  as done for the electrical response.

Another test of the nature of the experimentally observed coupling comes from the detuning of the two resonators. As the LC resonator's frequency is varied by tuning the capacitance, the strength of coupling falls, having a maximum at the zero detuning case (resonant coupling) at a constant dc bias voltage (60 V in this case). This is what we observe in Fig. 4.18 fitted to a Lorentzian function. We note that at the time of this specific measurement, we did not have the FET op-amp, so this was recorded with a pick-up coil and a simple op-amp to detect the driven response.

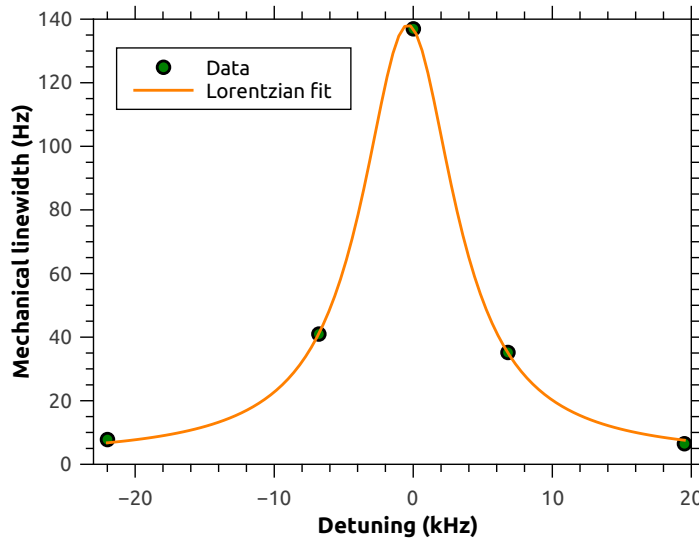


**Figure 4.18** The LC circuit is tuned to a specific frequency for each data point and the circuit is driven with an rf signal. Driven membrane spectrum (optical signal) is recorded to determine the mechanical linewidth at each detuning.

After the preliminary experiments with our membrane-LC circuit and testing different PCB designs, we recorded data with the PCB (now including the FET op-amp) for the systematic analysis of our system. The membrane- electrode distance is around  $5.6 \mu\text{m}$  for this sample

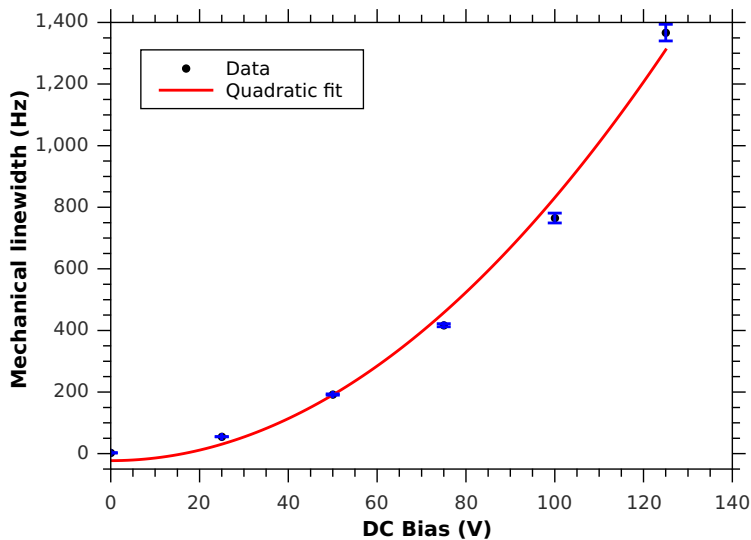


**Figure 4.19** Membrane broadening as a function of the dc voltage exhibiting quadratic behaviour as expected.

and thus requires relatively high dc voltages to achieve measurable coupling strengths. In

the MIT regime, the mechanical resonance linewidth is a good parameter to extract the coupling strength of the system. The broadening of the membrane due to coupling to the LC is described by the simple relation

$$\Gamma_{\text{eff}} = \Gamma_m(1 + \mathcal{C}_{\text{em}}) \quad (4.15)$$

where  $\mathcal{C}_{\text{em}}$  is the cooperativity which has been introduced in the theory section. Since the cooperativity is proportional to  $g_{\text{em}}^2$  and  $g_{\text{em}}$  is a linear function of  $V_{\text{dc}}$ , broadening of the linewidth is expected to scale quadratically with the bias voltage which is seen in Fig. 4.19. Each point comes from a high quality Lorentzian fit to an rf driven membrane response. Error bars come from the uncertainties in the fitted width. A similar phenomenon for the membrane linewidth broadening has been observed in a different system [63] where a nanomembrane is coupled to an ultracold atomic ensemble.

Later on, we embarked on more systematic measurements with this sample in the MIT regime. Fig. 4.20 shows our investigation in a compact way. Panel a and b refer to the driven electrical and mechanical responses, respectively. As we increase the dc bias voltage, membrane linewidth gets broadened as expected from the theory and on top of that, the quadratic frequency shift can be seen (dashed line is a fit to the points corresponding to the dip). We note that for each dc bias voltage measurement, we tune the LC circuit to resonance with the shifted mechanical frequency. Broadening of the membrane is shown in an inset in panel b and analyzed in three ways by model fits to the electrically (circles) and optically (boxes) measured response and Lorentzian fits to the optically measured membrane response (diamond). These three ways show very similar values. Absolute displacement

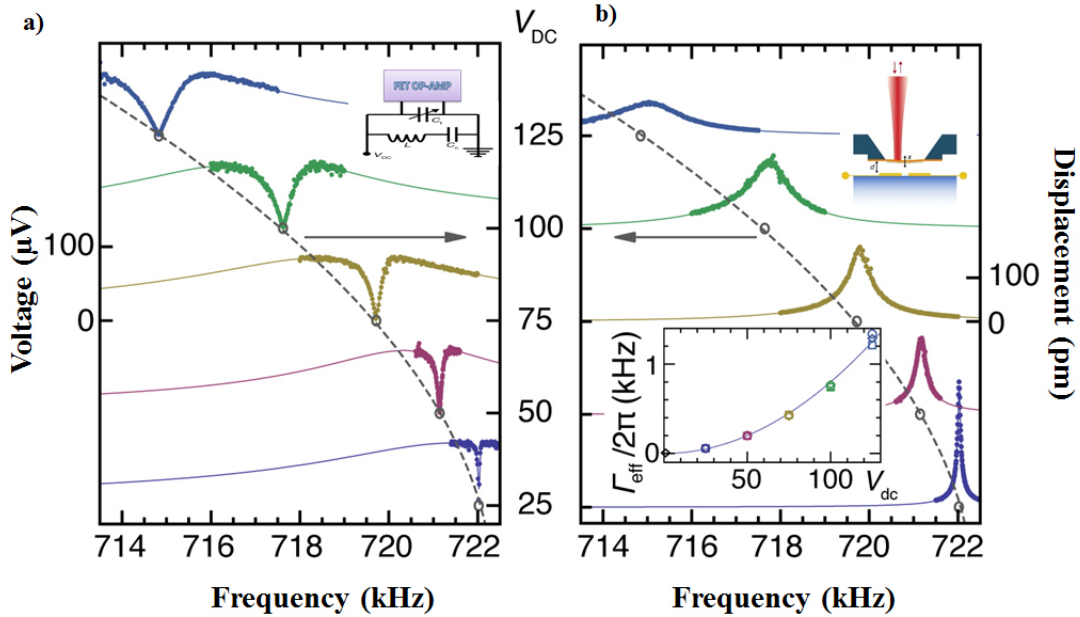


**Figure 4.20** Detailed systematic study of the MIT regime showing both LC circuit (a) and membrane (b) responses. Reproduced from [4].

of the membrane is performed via the methodology described in the calibration discussion

4.3.3. We note that in this figure, the curves for each dc bias voltage are given an offset to match the baseline to the corresponding dc voltage in the y-axis. In panel a, we analyze the corresponding electrical picture (voltage probed with the op-amp) showing the MIT dips of the LC resonance. The width of the MIT dip also broadens and dip depth grows in unison with our theoretical expectations. Our fits to the electrical and optical spectra are based on the theoretical model discussed in the theory chapter. These fits have been used to determine crucial system parameters like  $\Omega_m$ ,  $\Omega_{LC}$ ,  $\Gamma_{LC}$ ,  $G$  and  $V_s$  and the agreement between the two fits (optical and electrical) is fairly good for  $\Omega_m$ ,  $\Omega_{LC}$  and  $G$  - within 1%. In addition to that, we measure the intrinsic mechanical linewidth of the membrane via the thermal noise spectrum recorded with the Doppler vibrometer with high resolution (1Hz). Typically, with a few averaging the mechanical spectrum can be fitted to a Lorentzian and the linewidth can be extracted. Then this calibrated mechanical displacement is integrated to estimate the effective mass ( $\approx 30$  ng) for this membrane which is in very good agreement with the theoretical effective mass deduced from the physical mass divided by four (28 ng). The mechanical linewidth referring to this particular data set is  $\Gamma_m/2\pi = 2.3$  Hz .

#### 4.4.2 Extraction of the coupling parameter ( $G$ ) in different ways

After the systematic measurements in the previous section, we now extract the coupling strength parameter  $G$  for our electromechanical system in this regime.  $G$  is a crucial parameter of the coupled electromechanical system for understanding the physics and is also one of the figure of merits of the system in the context of a sensitive voltage probe. We, therefore, have analyzed it in several ways and confirmed the consistency of the numbers we have extracted. The four independent ways we have used for quantifying the coupling strength comprise;

- 1) Spectral Response - Electrical and Mechanical
- 2) Amplitude ratio - Comparison of the voltage and displacement modulation amplitudes (fits to electrical and optical data)
- 3) Frequency shift - with dc bias.
- 4) Purely theoretical- Estimates starting from the geometry of the transducer

These four independent methods have shown fairly good agreement with each other. The details for each method are given below based on the S.I of our work [4].

##### 1) Spectral Shape

The spectral shape of the voltage fluctuations probed by the op-amp and the membrane vibrations recorded via optical means give us two independent ways of extracting  $G$  from the experimental data and model fits. The expressions governing the voltage and the membrane displacement were given in equations 4.12 and 4.14. By fitting the experimentally recorded spectrum to these functions, we can obtain fit parameters including  $G$  as outlined before where the amplitudes (voltage and displacement) are fit parameters as well. At a dc bias voltage of 125 V for the MIT regime data, this spectral method yields  $G_I = 10.3$  kV/m.

## 2) Amplitude Ratio

Another way of extracting  $G$  is to infer the ratio of the measured voltage fluctuations to the mechanical fluctuations (rms) and then use the fit model. The frequency dependent expression for this ratio is given by

$$\frac{\delta V_c(\Omega)}{\delta x(\Omega)} = \frac{-(\frac{1}{C(x)} - \chi_m(\Omega)G^2)\chi_{LC,eff}(\Omega)\delta V_s(\Omega)}{\chi_{m,eff}(\Omega)G\chi_{LC}(\Omega)\delta V_s(\Omega)} \quad (4.16)$$

A simpler expression can be constructed by choosing a specific frequency, namely the resonance frequency where  $\Omega_{res} = \Omega_{LC} = \Omega_m$  and then the formula is simplified to

$$\left| \frac{\delta V_c(\Omega_{res})}{\delta x(\Omega_{res})} \right| = \sqrt{G^2 + \frac{L^2 m^2 \Gamma_m \Omega_{res}^6}{G^2}} \quad (4.17)$$

We have had several trials for measuring this ratio at resonance, however it turned out to be tedious since we have not been able to extract consistent experimental values. For this method, we first scan the LC resonance (including the MIT dip) with an rf signal and locate the MIT dip point. Then we choose the demodulation frequency of the lock-in exactly at this dip frequency, so that this value can be recorded in a narrow band (high resolution). Afterwards, we perform the same type of lock-in detection for the mechanical resonance by attempting to track the maximum peak height. However, the peak values we extract in this way, are not stable in time and mainly the frequency shift of the membrane with respect to the LC resonance makes it challenging to record reasonable values. Therefore, instead of using only the resonance point, we have decided to rely on the broadband scan of the LC and mechanical resonance and use the frequency dependent fit functions to infer the ratio of the mechanical amplitude to the MIT dip voltage amplitude. This has resulted in more stable values and the value of  $G$  turned out to be within the expected range. At 125 V, we extract  $G_{II} = 8.5 \text{ kV/m}$ .

## 3) Frequency Shift

The electrostatic spring softening effect that brings a shift to the mechanical resonator frequency (that has been discussed several times so far) can also be used as an independent way of inferring the coupling strength  $G$ . The frequency shift is proportional to the second derivative of the reciprocal of the position dependent capacitance. We start by defining  $m^*$  as the physical mass with the correspondingly defined  $x$  coordinate. In order to proceed further from here, we assume a certain distance dependence for the capacitance. For a capacitive system like ours, it is valid to assume a relationship of the form

$$C(x) = C_0 + C_m(x) = C_0 + \frac{a}{d+x} \quad (4.18)$$

since our system can be envisioned as a simple parallel plate capacitor with one end free to move ( $d$  is the equilibrium distance between the plates and  $x$  is a small perturbation of the moving end). Here,  $C_0$  is a large capacitance offset on top of which the small membrane modulation comes. Then the relationship between the first and second derivatives becomes trivial

$$\frac{\partial}{\partial x} \frac{1}{C(x)} = -\frac{\partial^2}{\partial x^2} \frac{1}{C(x)} \cdot \frac{d}{2} \quad (4.19)$$

Following our approach in [4], it is convenient to insert an additional factor to the right hand side of the equation, namely to account for the freedom of choice with regards to the gauge for the oscillator mass. (with  $m$  being the effective mass and  $x$  needs to be scaled suitably as well). This is carried out as follows by writing the membrane displacement around the equilibrium  $\delta x(y, z)$  as an expansion of drum modes  $\Phi_{m,n}(y, z)$  with the canonical coordinates  $\beta_{m,n}$

$$\delta x(y, z) = \sum_{m,n} \beta_{m,n} \Phi_{m,n}(y, z) \quad (4.20)$$

where the modes are normalized in such a way

$$\iint_{A_{\text{mem}}} \Phi^2(y, z) dy dz = \frac{m}{m^*} \quad (4.21)$$

With this coordinate transformation and using the chain rule for the derivatives with respect to the coordinates (switching between  $\beta$  and  $\delta x$ ) one reaches

$$\frac{\partial}{\partial x} \frac{1}{C(x)} = -\frac{\partial^2}{\partial x^2} \frac{1}{C(x)} \cdot \frac{d}{2} \sqrt{m/m^*} \quad (4.22)$$

$G$  is related to the second derivative of the reciprocal of the capacitance (therefore to the frequency shift) as shown in the theory chapter

$$G = \bar{q} \frac{\partial}{\partial x} \frac{1}{C(x)} = -\bar{q} \frac{d}{2} \sqrt{m/m^*} \frac{\partial^2}{\partial x^2} \frac{1}{C(x)} = -\frac{2\sqrt{mm^*} \Omega_m d}{C(\bar{x}) V_{\text{dc}}} \Delta \Omega_m \quad (4.23)$$

As can be seen,  $G$  is now a function of independently measurable parameters and can be deduced for a given dc voltage. For the MIT data, we find  $G_{III} = 14.4 \text{ kV}/m$  at 125 V bias voltage. Here,  $m = 30 \text{ ng}$  is the experimentally measured effective mass,  $m^* = 110 \text{ ng}$  is the physical mass from the dimensions calculated by using the mass densities  $\rho_{\text{SiN}} = 3.0 \text{ g}/\text{cm}^3$  and  $\rho_{\text{Al}} = 2.7 \text{ g}/\text{cm}^3$ . The total capacitance  $C(x) = 76 \text{ pF}$  is measured independently via the experimentally determined resonance frequency and inductance.  $d = 5.5 \text{ }\mu\text{m}$  is the initial distance measured with the white light interferometry before the experimental run.

#### 4) Theoretical - Geometry

The coupling strength  $G$  can in principle be calculated based on a purely analytical approach where the geometric parameters pertaining to the capacitive system are provided as inputs. This has been carried out in detail by Emil Zeuthen by taking into account the membrane mode shape, the electrode mask and their relative alignment as well. Here, we neglect edge effects for the capacitance and also take the membrane to be locally flat as it is small compared to the large initial distance between the membrane and electrodes. Following the coordinate definitions and transformation stated in the third method (frequency shift) and writing  $G$  as

$$G = \bar{q} \frac{\partial}{\partial \beta} \frac{1}{C[\delta x(y, z)]} \quad (4.24)$$

Also taking into account the specific geometry of our capacitor design (four-segment electrodes), we can write the total capacitance as the series combination of  $C_+$ ,  $C_-$  and  $C_0$

which denote the capacitance from the positive and negative electrodes and the total tuning capacitor, respectively

$$C = C_0 + \frac{1}{\frac{1}{C_+} + \frac{1}{C_-}}, \quad (4.25)$$

The end result for  $G$  is then found to be

$$G = \frac{V_{\text{dc}}\epsilon_0 L^2}{C^{(\text{eq})}d^2} \sqrt{\frac{m}{m^*}} \left[ \frac{\frac{O_+^{(1)}}{[O_+^{(0)}]^2} + \frac{O_-^{(1)}}{[O_-^{(0)}]^2}}{\left(\frac{1}{O_+^{(0)}} + \frac{1}{O_-^{(0)}}\right)^2} \right], \quad (4.26)$$

where  $L$  is the membrane side length and the overlap factors are defined in the following way

$$O_i^{(j)} \equiv \frac{\iint_{A_i} \Phi^j(y, z) \xi(y, z) dy dz}{\left( \iint_{A_{\text{mem}}} \Phi^2(y, z) dy dz \right)^{j/2}} \quad (4.27)$$

with  $i \in \{+, -\}$  and  $A_i$  being the area of the membrane above electrodes of polarity  $i$ ;  $\xi(y, z)$  is the Heaviside function that takes into account the electrode gaps and the hole in the membrane metalization just as stated within the treatment in the previous chapter. For the value of the overlap factor, we used the mean value taking into account the typical 25 % lateral misalignment. With the parameters of our device, we find  $G/V_{\text{dc}} = 66\text{m}^{-1}$ . For  $V_{\text{dc}} = 125\text{ V}$  we find a value of  $G_{\text{iv}} = 8.2\text{ kV/m}$ .

### 4.4.3 Strong coupling regime

In this part, we will concentrate on the strong coupling regime which is of interest in any kind of physical system as it refers to the energy exchange at a considerable rate between two resonators. The very general description of the strong coupling regime is that the coupling rate between the two coupled systems exceeds the dissipation rates of the two individual systems [69], thus allowing transfer of excitations between the two before they die out. More formally, it corresponds to the condition  $2g$  (splitting)  $> \Gamma_1, \Gamma_2$  where  $g$  is the coupling rate and  $\Gamma_1$  and  $\Gamma_2$  are the dissipation rates of the two independent systems. In the context of optomechanics and microwave electromechanics, strong coupling has been observed in several setups [9–11, 70]. In that case, a mechanical resonator is coupled strongly either to an optical field in an optical cavity or a microwave field resonating in an LC circuit. The resulting dynamics is intriguing since it allows coherent manipulation of signals between mechanics and microwave or optical fields. It may also serve for interfacing microwave and optical systems for coherent state transfer via mechanics in this case. Here, we should note that quantum strong coupling regime has more strict requirements in the opto-electromechanics context - that the coupling rate should be larger than  $\Gamma_m n$ , namely the mechanical decay rate multiplied by the thermal occupation number which is typically quite large at room temperature. Therefore, it becomes possible at the expense of a formidable task of having very high-Q mechanical resonators and starting from very low

base temperatures. This has recently been achieved in [9,11].

The strongly coupled system shows distinct features with qualitatively observable changes when the system is probed. The onset of strong coupling is characterized by a phenomenon called normal mode splitting, where the coupled system shows splitting into two peaks in the frequency domain [69,70]. In this regime, the two individual systems can no longer be treated separately, but they have instead truly hybridized into a common mode. Based on the Hamiltonian introduced in [19]

$$H = \frac{\phi^2}{2L} + \frac{q^2}{2C} + \frac{p_m^2}{2m} + \frac{m\Omega_m^2 x_m^2}{2} + \frac{g_{em}}{q_0 x_0} (q x_m) \quad (4.28)$$

and applying the resonance condition ( $\Omega = \Omega_m = \Omega_{LC}$ ), the usual canonical variables referring to charge and displacement can be rewritten in the language of normal mode solutions  $Y_+, Y_-, P_+, P_-$  [19] where

$$x_m = (Y_+ + Y_-)/\sqrt{2m}, \quad q = (Y_+ - Y_-)/\sqrt{2L} \quad (4.29)$$

$$p_m = (P_+ + P_-)\sqrt{m/2}, \quad \phi = (P_+ - P_-)\sqrt{L/2} \quad (4.30)$$

and the two modes have separated frequencies depending on the strength of the coupling rate as follows

$$\Omega_{\pm} = \Omega\sqrt{1 \pm g_{em}/\Omega} \quad (4.31)$$

From a practical point of view, although strong coupling (observation of the splitting)

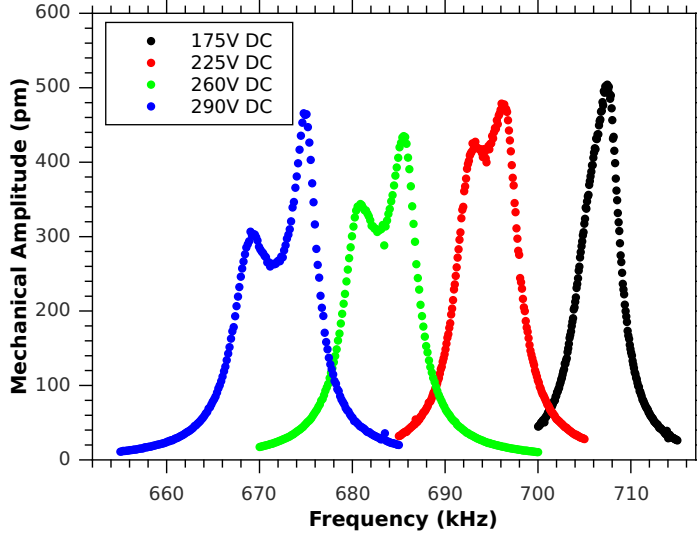


**Figure 4.21** Optical detection of the membrane vibrations and gradual observation of the strong coupling regime. At 175 V, the mechanical peak starts to get asymmetric and splitting becomes clearer with increasing bias voltage.

is not necessarily the best condition for reaching high voltage sensitivities for the opto-electromechanical device (considering the optimization for  $C_{em}$  discussed in the following

chapter), it is important to see the limits of the coupling rate when considering the bandwidth of the device. For example, it might first be desirable to show as high coupling rate as possible and then the LC linewidth may be deteriorated (loaded manually etc.) until the device is optimized for both bandwidth and cooperativity. Other than that, an interesting opportunity would arise if one can incorporate the strongly coupled electromechanical system inside a high finesse cavity and cool the normal modes of the LC-membrane system via radiation pressure cooling of the membrane as proposed in [19].

In our experiments, we have tested several membrane-chip samples in the beginning to reach the strong coupling regime. Pushing the coupling rate up in order to overcome the LC decay rate (which is typically 5 kHz) has been challenging due to the large membrane-capacitor distances. In addition to that, our PCB has a margin of 280 V DC due to the capacitive elements used in the circuit and going above that can damage the circuit. In the end, we managed to observe the onset of strong coupling (normal mode splitting) for the first time with the sample investigated in the MIT section, at a distance of  $5.5 \mu\text{m}$  with a high dc voltage  $V_{dc} > 250 \text{ V}$ . Fig. 4.21 shows the data where we gradually monitor the appearance

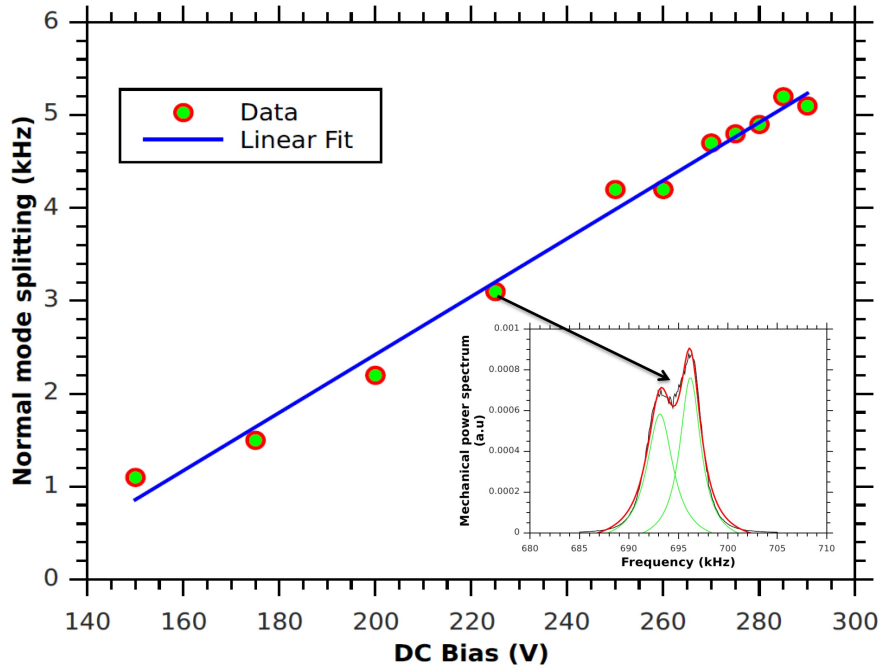


**Figure 4.22** Linear dependence of the normal mode splitting ( $2g_{em}/2\pi$ ) on the dc bias voltage. At each dc bias voltage, the splitting is extracted from a two-peak Lorentzian fit to the mechanical spectrum.

of strong coupling (mode splitting) with increasing bias voltage. The membrane amplitude tracked by the vibrometer decreases as the coupling strength is increased and the mechanical frequency shifts to lower values as expected.

After the first indication of strong coupling, we started analyzing this regime more systematically to extract some parameters and confirm the normal mode splitting with our

theoretical predictions. We first study the dependence of the coupling rate  $2g_{em}/2\pi$  on the dc bias voltage in a different experimental run. According to our models, the coupling rate should scale linearly with the applied voltage as follows

$$g_{em} = V_{dc} \frac{C'}{C} \frac{1}{\sqrt{2m\Omega_m} \sqrt{2L\Omega_{LC}}} \quad (4.32)$$

We observe this linear scaling as can be seen in Fig. 4.22. The bias voltage is increased starting from the onset of normal mode splitting up to 290 V where  $2g_{em}$  safely exceeds the LC decay rate for this experimental run. Each data point corresponds to the splitting ( $2g_{em}/2\pi$ ) that is extracted from the frequency spacing of the two-peak Lorentzian function fitted to the mechanical spectrum (at the resonant coupling condition). We note that even though our sample is the same, we have observed slight changes of the dc bias voltage for the onset of normal splitting as small misalignments and gap distance changes between different runs (on different days) might alter the coupling strength.

In addition, we have observed and analyzed the phenomenon of avoided crossing in another experimental run, which can be seen in Fig. 4.23. We note that these data are recorded

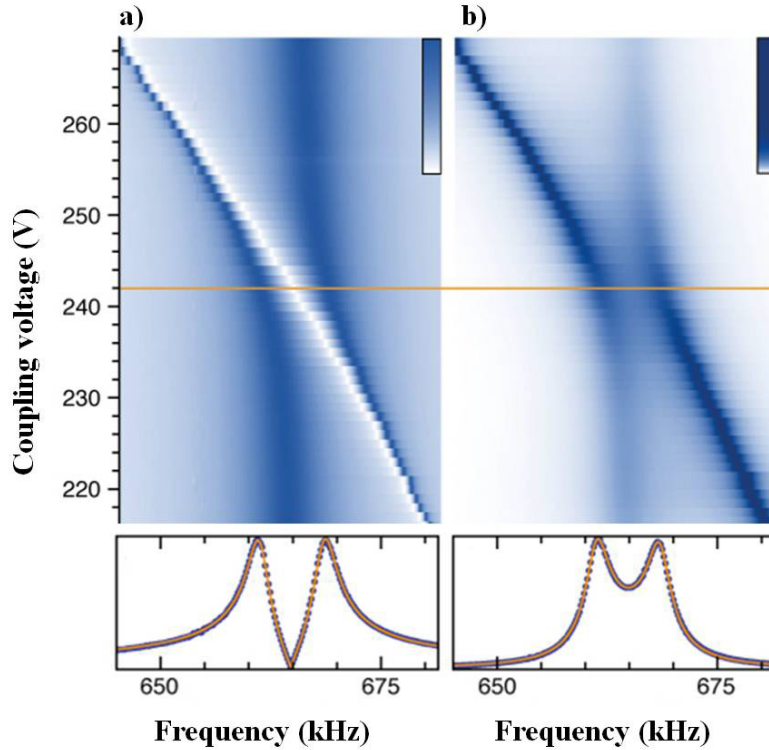


**Figure 4.23** Avoided crossing as a typical feature of the strongly coupled system. a) Electrical response of the LC circuit. b) Optical detection of membrane displacement. Reproduced from [4].

with a smaller distance of  $4.5 \mu m$ . Panel a shows the electrical response tracked with the op-amp and panel b corresponds to the mechanical response recorded with the vibrometer. The circuit (and consequently the membrane) is driven inductively to clearly demonstrate

the phenomenon. In the mechanical response, normal mode splitting becomes clear for a dc voltage of 242 V (corresponding to the orange line). We also show the model fits on the electrical and mechanical spectrum based on our coupled set of equations. The parameters we extract from the fits are in excellent agreement with the predictions and the coupling strength values (extracted by using the link between  $g$  and  $G$ ) from the two independent measurements are very close. For this specific condition, we have achieved a cooperativity of  $\mathcal{C}_{em} = 3800$  with parameters  $m_{\text{eff}} = 24$  ng and  $\Gamma_m/2\pi = 3.1$  Hz deduced independently from thermal noise spectra of the membrane.

Avoided crossing is clearly observed with the system in both responses. The large dc bias voltage is scanned in small steps in order to tune the LC resonator and the membrane (by exploiting the frequency shift of the membrane due to the electrostatic spring softening) and the colored graphs in Fig. 4.23 map out the detected probe voltage and membrane displacement with respect to a certain dc voltage and frequency. As can be seen, when the two resonators approach the resonance condition, they exhibit avoided crossing which is  $2g_{em}$  apart in frequency space. The small steps in the dc bias also changes the coupling strength, however over this small scan range and on top of the large dc bias, this effect turned out to be negligible.

After the fabrication of the second generation membranes (etched) to tackle the gap distance problem mentioned earlier, measurements have been performed with membrane-chip distances getting closer to the designed pillar heights. Fig. 4.24 shows the highest normal mode splitting recorded with such an etched membrane-chip sample. Y-axis is the mechan-

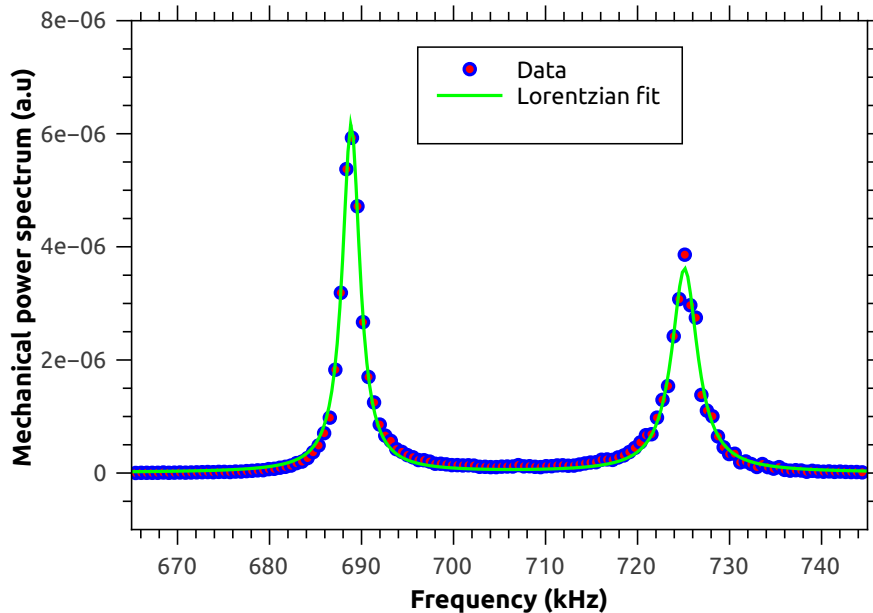


**Figure 4.24** Largest splitting achieved with a small gap distance ( $\approx 1$   $\mu\text{m}$ ).

ical spectrum (arbitrary units) tracked via the vibrometer. The spectrum is fitted to a two-peak Lorentzian function (green). The gap distance is around 1  $\mu\text{m}$  in this case and only a dc voltage of 16 V is enough to see a splitting of  $\approx 35$  kHz which is almost six times

larger than the typical linewidth of the LC circuit. However, one problematic issue with this sample (and many others we have experimented with) is that the mechanical linewidths are usually much worse than the intrinsic linewidth of the membranes which will be discussed in section 5.5. We note that this membrane collapsed on the chip after taking this data upon increasing the dc bias slightly more, suggesting that it was very close to the instability limit due to the pull-in voltage discussed in section 2.6.

## 4.5 Conclusive remarks

In this chapter, we have shown the experimental details of our coupled system consisting of the mechanical resonator and the electrical LC circuit. We have characterized and studied systematically the electromechanical coupling (characterized by  $G$ ) and explained the physics behind with a well-understood theoretical modelling. The electromechanical system is investigated both electrically and optically together with the observation of mechanically induced transparency and strong coupling physics. Mode splitting of around 35 kHz, which is several times higher than the LC linewidth, has been achieved. The results and the characterization of the system presented here lay the foundations for the next chapter where the device is investigated as an opto-electromechanical voltage sensor.

## Chapter 5

# An opto-electromechanical sensor for detection of rf waves

Having investigated the experimental observation of electromechanical coupling, we continue with our recent experiments in that direction, which in summary, support the use of this coupled system as a sensitive room temperature device for optical detection of radio waves via a mechanical interface. The outstanding noise performance of the device (achieved with the NBI interferometer) will be discussed in detail along with the limitations and current problems to be investigated. Apart from sensitive voltage detection, photon conversion from rf to optical domain will shortly be discussed with possible future directions. Towards the end, we will touch upon the issue of extension of this voltage sensor to microwave frequencies ( $\approx$  GHz) with improved bandwidth together with future prospects for an integrated and compact opto-electromechanical sensor.

### 5.1 Voltage sensitivity under ambient rf noise

#### 5.1.1 First noise tests with the Michelson interferometer

In parallel to the characterization measurements at DTU, a Michelson Interferometer has been developed at NBI with the hope of improved optical readout for highly sensitive voltage measurements. In June 2013, the interferometer was ready for operation. We then established the same electromechanical setup and put it under investigation with the new optical interferometry. It turned out that the Michelson interferometer performed considerably better (with the possibility of higher optical powers and flexibility of optimizing the readout in a custom manner as opposed to the commercial vibrometer at DTU). In the end, a shot-noise limited resolution of around  $1.5 \text{ fm}/\sqrt{\text{Hz}}$  has been reached.

Details of the experimental setup can be found in the previous chapter. The results discussed here have been recorded with the experimental configuration corresponding to the Michelson interferometer section 4.3.2. In Fig. 5.1, we show a compact depiction of the setup in the language of input/output ports. Briefly put, the opto-electromechanical system can be thought as an amplifier/receiver that takes an rf input signal and converts it to an optical output with the help of a mechanical resonator.

To continue our experiments in that direction, we first started experimenting with the

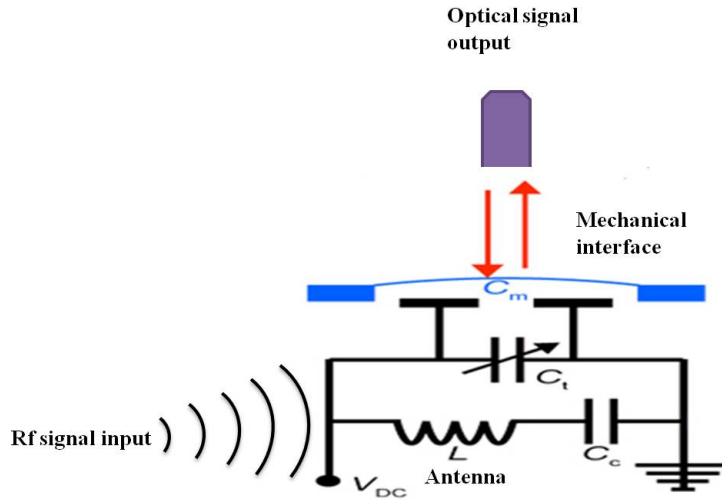


**Figure 5.1** Depiction of our opto-electromechanical device based on a mechanical interface. Typically, an rf signal is injected as an input through the receiver coil and converted into mechanical vibrations. These vibrations then introduce a phase shift of the reflected optical beam, which carries the signal through a fiber to an interferometric detection route.

etched Al-coated membranes to ensure that the distance between the electrodes and the membrane was sufficiently small so as to achieve high coupling rates at small dc voltages. The initial measurements have been performed with a membrane-capacitor sample with a gap distance of  $\approx 1\mu\text{m}$  (inferred from the frequency shift) and a mechanical linewidth of  $\approx 20\text{ Hz}$  also confirmed with the ringdown method which we have used for some of our samples.

The measurement procedure for the ringdown is carried out as follows: First, we apply a certain dc voltage (the coupling voltage that we aim to operate at) and on top of that, we apply an rf signal at the membrane-capacitor connection lines to excite the membrane via the capacitive force. For this, the rf drive port inside the PCB (shown in the detailed circuit diagram in Fig. 4.3) is used as the inductor should be disconnected for the intrinsic (no coupling) linewidth measurement. The excitation signal coming from the generator is gated such that during the excitation time a sinusoidal waveform at the mechanical frequency is applied and during the dead time there is no signal. In this way, ringdown of the membrane is readily observed with the Michelson interferometer optical signal that is fed to a fast oscilloscope. Fig. 5.2 shows an example of a high-Q membrane measured with the ringdown method.

Apart from the investigation of mechanical properties of the membrane, we have optimized the interferometer for low optical readout noise. As a general procedure, we first maximize the back reflection (probe arm fiber) from the membrane by fine tuning the optical head alignment for a given beam position on the membrane. We then adjust the input power with polarizing elements such that the recombined beams coming from the probe arm and the reference arm are balanced to a large extent. Additional waveplates are used to fine

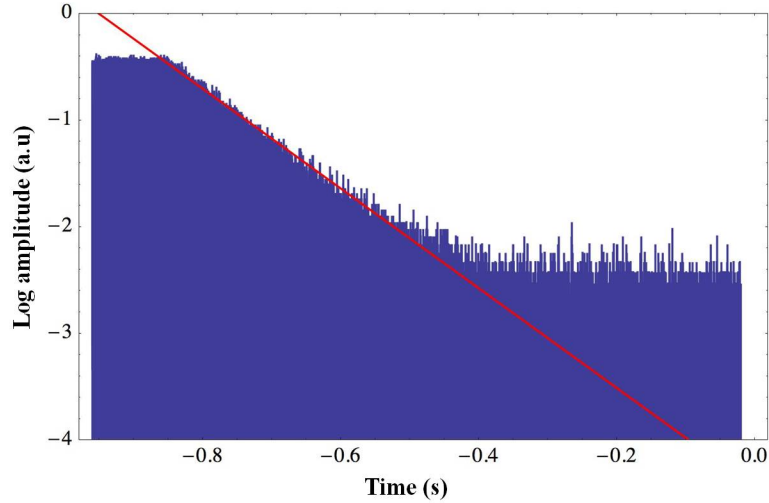


**Figure 5.2** Optical interferometric signal encoding the decay of the mechanical vibrations of the Al-coated membrane. Y-axis is the natural logarithm of the absolute value of the voltage signal with a ringdown time of 0.21 s and a linewidth of 1.5 Hz (reproduced from [4]).

tune the balancing of the homodyne detection path - the light hitting on the two detectors. Based on these short optimization procedures, an optical noise background of a few  $\text{fm}/\sqrt{\text{Hz}}$  has been reproduced consistently over time. Finally, the offset of the locking position is adjusted which helps in increasing the sensitivity slightly.

After having settled on a particular membrane-chip sample for the systematic measurement series, we started recording noise traces. All the procedures (such as tuning the LC and the membrane) are the same as explained before in the previous chapter. In Fig. 5.3, one can see (a) the undriven membrane response (power) which is strongly coupled to the LC circuit at 21 V dc bias voltage, where the membrane frequency is around 700 kHz (shifted due to electrostatic spring softening). The peak at 770 kHz is used for calibration. The signal is the optical interferometric signal coming from the vibrations of the membrane around the locking point of the interferometer. Strong coupling (splitting) is clearly visible in the mechanical response (log scale). For this specific noise measurement, we have used 0.8 mW light (1064 nm Nd:YAG) returned from the membrane. The effective mass of this particular membrane (50 nm Al coated on 180 nm SiN) is measured to be 140 ng, higher than expected from the dimensions of the membrane (44 ng). Later on, we noticed that this was due to the off-center beam position resulting in a smaller amplitude, therefore a bigger mass compared to the center.

In panel b, we show the electrical noise power of the LC circuit (measured with the op-amp on the capacitor) at 21 V coupling voltage. The two pictures (a-b) are equivalent in the sense that the antenna pick-up noise in the environment which can be seen in the noisy MIT trace of the non-driven LC circuit (b) is actually the noise responsible for the high membrane mechanical noise that is optically tracked (a). The origin of the noise and how it fits our model is discussed in the next subsection. However, a qualitative hint can already be noticed from the comparative figure here that the narrow peaks picked up by the inductor

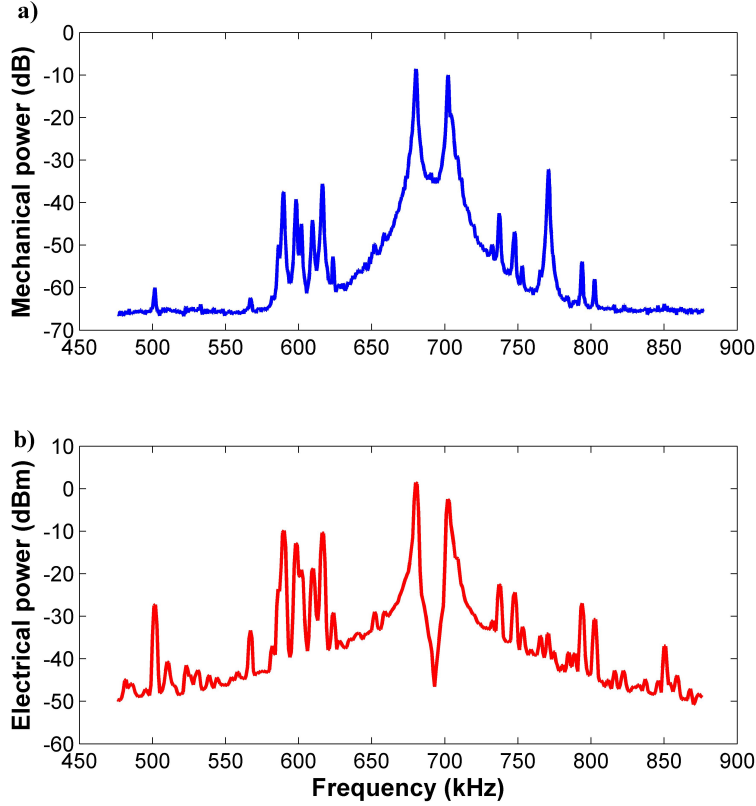


**Figure 5.3** a) Membrane displacement noise power via optical interferometry at 21 V dc bias (The large peak at 770 kHz is used for calibration). b) Corresponding voltage on the capacitor measured with the op-amp at 21 V dc with a broad dip due to the electromechanical coupling. The pick-up noise peaks (especially pronounced around 600 kHz) show up in both pictures.

in the LC response are also present in the membrane response, indicating their correlated nature through the electromechanical coupling.

### 5.1.2 Experimental noise performance, model fits and discussion

In this section, we discuss in detail the noise performance of our device and the sensitivity achieved at certain experimental settings. Our theoretical model describing the underlying physics of coupling so far can be extended further to predict the rf voltage detection sensitivity via optical interferometry. The optical readout signal is essentially a phase shift due to the fluctuations of the membrane which is given by,  $\delta\phi_{mem} = 2k\delta x$ . By using the Langevin equations of motion, one can find an expression for the displacement fluctuations and thus the phase fluctuations (derived in the theory chapter). The final result is a spectral density for the phase fluctuations as follows

$$S_{\phi\phi}^{\text{tot}}(\Omega) = (2k)^2 |\chi_{m,\text{eff}}(\Omega)|^2 \left( |G_{\chi LC}(\Omega)|^2 S_{VV}(\Omega) + S_{FF}^{\text{th}}(\Omega) \right) + S_{\phi\phi}^{\text{im}}(\Omega) \quad (5.1)$$

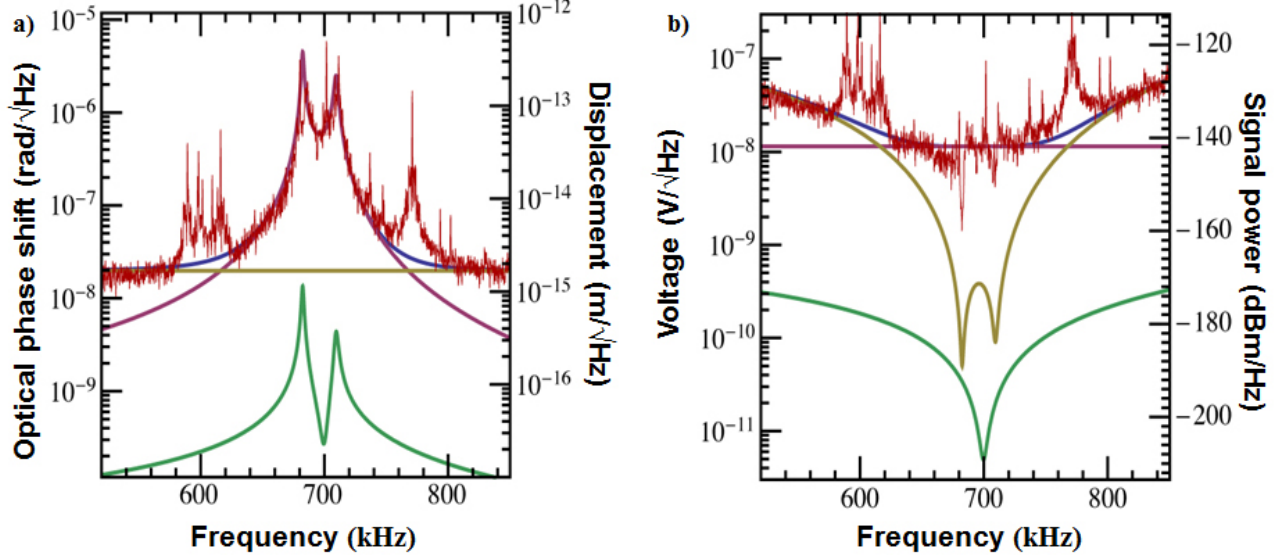


**Figure 5.4** a) Phase and displacement spectral density of the membrane recorded via optical interferometry at 21 V dc bias with strong coupling in the presence of high ambient rf noise. Red points represent the measured noise. Blue curve corresponds to the total optically measured noise based on our theoretical model. The other curves; violet, yellow and green refer to the Johnson noise of the LC, optical detection noise (quantum) and membrane noise, respectively. b) The same values represented as a voltage noise with respect to the input resistance of the circuit, by using the transfer function of the interface (reproduced from [4]).

where  $S_{\phi\phi}^{\text{im}}(\Omega)$  is a term denoting the optical readout imprecision. Optical readout noise limited voltage sensitivity could then be written as

$$S_{VV}^{\text{im}}(\Omega) = \frac{S_{\phi\phi}^{\text{im}}(\Omega)}{|2k\chi_{\text{m,eff}}(\Omega)G\chi_{LC}(\Omega)|^2} = \frac{S_{xx}^{\text{im}}(\Omega)}{|\chi_{\text{m,eff}}(\Omega)G\chi_{LC}(\Omega)|^2} \quad (5.2)$$

By using the equation above, an experimentally realized optical displacement readout sensitivity can be converted to an equivalent voltage sensitivity for our opto-electromechanical transducer.

Fig. 5.4 shows a detailed analysis from one of our measurements performed in order to demonstrate the noise performance of our device. In panel a and b, we present the optical phase/displacement spectral densities and the corresponding voltage noise, respectively. The voltage noise/sensitivity is determined by dividing the values and curves in panel a by the total transfer function of our system  $\chi^{\text{tot}} \equiv 2k\chi_{\text{m,eff}}G\chi_{LC}$ . We note that all the voltage values refer to the resistance of the circuit at the antenna input ( $R$ ). The total noise (blue curve) consists of high ambient rf radiation (violet curve) and the optical readout noise (yellow curve) together with the membrane noise (green curve). For the data set presented here, we have achieved an interferometric imprecision level of  $1.7 \text{ fm}/\sqrt{\text{Hz}}$  and dividing this

constant value by the transfer function, one reaches the frequency dependent yellow curve shown in panel b. On resonance the optical noise contribution is around  $500 \text{ pV}/\sqrt{\text{Hz}}$ . We note that by using more optical power (with some modification of our detection setup) or going to a high-finesse cavity, this optical readout sensitivity can be improved significantly. The second source of noise that can limit the voltage sensitivity is the membrane thermal fluctuations at room temperature. However, in our system, we have the advantage that this noise contribution is strongly suppressed due to the presence of the high electromechanical cooperativity. A simple expression for the membrane noise limited sensitivity (on resonance where  $\Omega_m = \Omega_{LC}$ ) is, in the theory chapter, found to be

$$S_{VV}^{\text{mem}} = 2k_B \frac{T_m}{\mathcal{C}_{\text{em}}} R \quad (5.3)$$

where  $R$  is the resistive loss of the circuit. As can be seen, the effective noise temperature is reduced by the cooperativity of the system and can be made significantly smaller with high coupling strengths as achieved here. For the data of Fig. 5.4, a bias voltage of  $V_{\text{dc}} = 21 \text{ V}$  yields a cooperativity of  $\mathcal{C}_{\text{em}} = 6800$  which brings the voltage sensitivity to a level as low as  $5 \text{ pV}/\sqrt{\text{Hz}}$  over a bandwidth of  $\Gamma_{LC}$  (green curve in Fig. 5.4b). This corresponds to an added noise of only 40 mK. The sensitivity here can further be slightly increased by pushing the voltage to the maximum allowable voltage due to the instability effect which will be discussed in subsection 5.5.3.

Although, with the presented experimental parameters, very low voltage sensitivities can be inferred for the optical and membrane noise, the actual performance of our device in this case is limited by high ambient rf pick-up noise which is represented with the violet curve in Fig. 5.4. The equivalent voltage sensitivity is in the range of  $10 \text{ nV}/\sqrt{\text{Hz}}$ . This also agrees with the independent electrical noise measurements, where we have measured the ambient noise picked up with the LC circuit by probing the voltage on the capacitor via the low noise op-amp. Although the Q-factor of the inductor is high and this enables us to easily observe strong coupling (splitting), the ferrite inductor, at the same time, serves as a very sensitive antenna that picks up the ambient radiation and hinders us from realizing the actual transducer noise. Despite our efforts to shield the inductor with an aluminum box, the noise level was still high. Considering the frequency range we are working at ( $\approx 1 \text{ MHz}$ ), it is not unlikely that ambient noise levels can be dramatically high for typical radio receivers. For example, references can be found in CCIR 322 report (Consultative Comitee on International Radio) that has tracked the noise variations from 1960-1980 [72]. There are typically three noise contributions; atmospheric noise stemming from natural atmospheric processes mainly caused by lightning discharges, man-made electronic noise from various devices [74] and galactic noise (Sun, Milky Way etc) [73, 75]. Lightning discharges from distant locations can cause white noise, whereas closer ones can cause pulsed noise. We believe in our case, where the operation frequency is around 700 kHz, it is likely that we observe a combination of atmospheric and man-made noise.

Apart from the spectral response of the noise we have observed with the ferrite rod inductors, we have also investigated its dc voltage dependence to compare it to our expectations from our model. As can be seen in Fig. 5.5, the theoretical curve that is derived from the equations for a signal coupled from the inductor port well describes the evolution of the mechanical peak amplitudes with respect to the dc bias voltage. For this measurement, we detect the ambient noise-driven mechanical vibration amplitudes of the membrane with

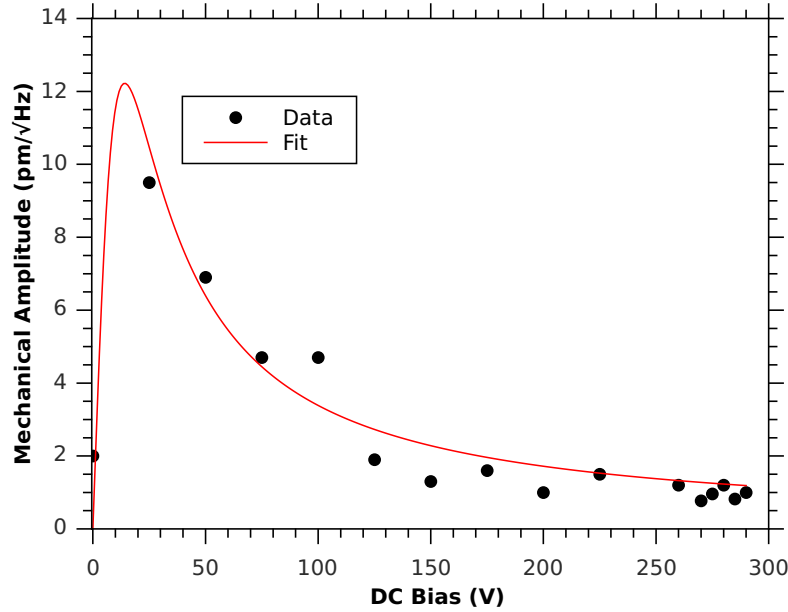


**Figure 5.5** Mechanical amplitude as a function of the dc bias voltage in the case of high ambient rf pick-up. The curve is a theoretical line derived from the coupled equations relating the induced voltage and membrane fluctuations (reproduced from [4]).

the Doppler vibrometer. Peak amplitudes are extracted from Lorentzian fits to the spectral data. The points up to 150 V cover the MIT regime where the amplitude corresponds to a single resonance peak. As we start to see splitting beyond 150 V due to the onset of strong coupling, we use the amplitude in the plateau between the two split-peaks for this regime. The function used for the fit is given by  $f = \frac{\alpha V_{dc} V_s}{(\alpha^2 V_{dc}^2 + Lm\Gamma_{LC}\Gamma_m\Omega^2)}$  where  $\alpha$  is a constant absorbing the parameters for the linear dependence of the coupling parameter on the voltage ( $G = \alpha V_{dc}$ ). We note that this treatment is valid for resonant driving ( $\Omega = \Omega_m = \Omega_{LC}$ ) assuming white ambient noise ( $V_s$ ) throughout the relevant frequency range.

## 5.2 Johnson noise-limited performance with shielded inductors

### 5.2.1 Reducing the noise

In order to improve the noise performance of the device that is limited by the high ambient rf noise, we have attempted to try different types of inductors that are less susceptible to ambient noise. During the course of time, we have experimented with toroidal and compact commercial inductors which have showed noise performances much better than the ferrite inductors - getting close to the Johnson noise limit [77]. However, their Q values were usually small, in the end reducing our cooperativites. Fig. 5.6 shows a compact com-

pilation of our efforts to have a better understanding of how the inductor pick-up noise affects the membrane noise temperature. Panel a and b refer to data recorded with a ferrite

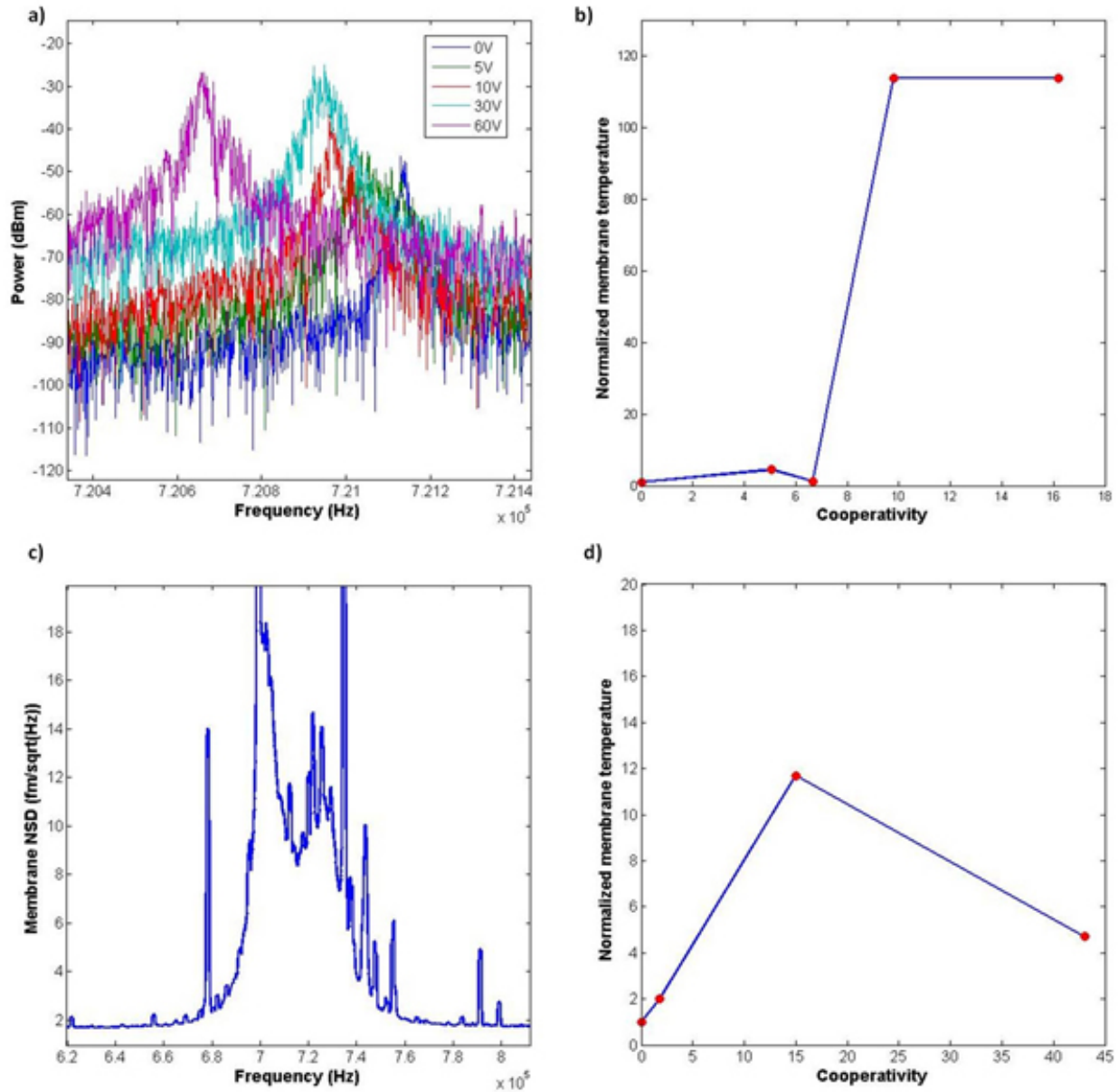


**Figure 5.6** a) Optically detected mechanical noise power of the membrane connected to a ferrite inductor with varying dc bias. b) Normalized noise temperature of the membrane with respect to cooperativity extracted from Lorentzian fits. c) Calibrated mechanical noise spectral density (NSD) of the membrane coupled to a compact commercial inductor (1 mH). d) Normalized noise temperature of the membrane with the same type of compact inductor (470  $\mu$ H).

inductor connected to the setup. As the dc voltage is increased, we observe an increase in

the mechanical power spectrum (optical interferometry) which is a typical sign of excess pick-up noise, as otherwise 300 K membrane temperature should stay constant. In b, we show the normalized noise temperature of the membrane extracted from the area under the Lorentzian fits to the mechanical spectra. X-axis refers to the cooperativity values which are extracted from broadened Lorentzian-shaped membrane spectra. Normalization is referenced to the membrane temperature at 0 V (300 K). Data shown for panels c and d, refer to a compact commercial inductor (1 mH and 470  $\mu$ H, respectively). The noise performance is significantly improved compared to the ferrite inductor although it is still above being Johnson-noise limited. In panel c, the membrane is biased at 83 V and the calibrated amplitude goes down to as low as tens of fm which we have never been able to achieve with the ferrite inductors. In the end, through our searches, we have found a compact commercial ferrite inductor (Pico electronics [76]) which has magnetic shielding and exhibits Q-factors that are tolerable for our parameter set (roughly ranging between 30 and 80).

For the analysis of the specific Johnson-noise limited measurements, we continue with our experiments performed with the home-made Michelson interferometer. The optical power returned from the membrane is  $\approx 1$  mW. Precharacterization of the membrane yields an effective mass of 64 ng deduced from thermal noise measurements and the equipartition theorem and we extract an intrinsic linewidth of  $\Gamma_m/2\pi = 20$  Hz. For this measurement, a SiN-Al membrane-with a coating of 100 nm Al on 50 nm SiN- is used. The initial distance of this sample is estimated from the observed frequency shift (26 kHz at 88 V) by using the relation  $d^3 = \frac{cV_{DC}^2 C}{\Delta\Omega 2h\rho\Omega_0}$  yielding  $d = 2.3 \mu\text{m}$ . We note that in order to extract the correct cooperativity for a given dc coupling voltage, one should refer to the intrinsic mechanical linewidth at this specific voltage, since as stated before, we have observed dc voltage dependent intrinsic linewidth broadening. This is done, as usual, by disconnecting the inductor (no coupling) at a dc bias voltage and recording the membrane linewidth. Q of the LC circuit with the new shielded inductor ( $L = 700 \mu\text{H}$ ) is found to be 47 from LC response measurements.

Before recording the Johnson-noise limited membrane spectrum, we have implemented quick tests in order to see whether the transducer operates close to that noise limit or has some extra noise. This becomes necessary to check, because each time the inductor is connected to the membrane through the pcb, the other parts of the circuit become critical if they pickup extra noise (through ground loops, cables etc). In order to achieve a low noise performance, a big aluminum shield is used to cover the shielded pcb unit and the inductor attached to that. This has helped substantially in terms of reducing the inductive and capacitive pickup.

Though several methods have been tested to quickly confirm whether the membrane is LC Johnson-noise limited or not, one of them has proven to be fast and reliable. The method uses the same principle to extract the effective mass (which is explained in the previous chapter). The procedure is carried out as follows: We first start with 0V dc bias case which corresponds to the condition that coupling to the LC circuit is off. At this condition, the membrane integrated area should correspond to 300 K (which actually yields the same values when all the electrical connections are disconnected from the membrane). We take this as a reference and we monitor the behaviour of the membrane noise area as the dc bias voltage is increased. If there is no extra pick-up noise, this value should stay constant. In

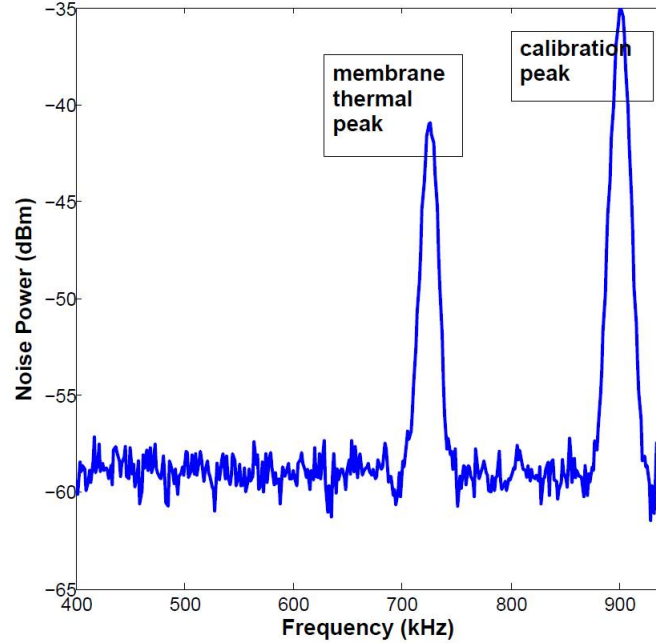


**Figure 5.7** A sample measurement to deduce the membrane noise temperature. The spectrum is recorded with a big resolution bandwidth (10kHz) with typically an averaging of 30. Calibration peak is always present so as to infer the membrane noise referenced to the calibrated signal.

order to do this in a fast and convenient way, we record the power spectrum including the calibration peak and the membrane thermal peak with a Spectrum Analyzer (SA) using a much broader resolution bandwidth - RBW (10 kHz) than the two peaks. This ensures that the square of the rms peak values tracked by the SA are actually proportional to the integrated area (or the temperature). It is important to normalize the thermal peak to the calibration peak for each measurement, since this takes into account any changes in the interferometric detection (power fluctuations, fringe variation etc). We then compare the normalized values for 0V and the coupling voltage to conclude whether the performance is close to the Johnson-noise limit within the uncertainty of our measurement scheme. The method is summarized in a sample measurement shown in Fig.5.7. We note that this method has been improved significantly (in terms of data recording) for the following experiments with the cooled resistor, especially in order to reduce the error bars.

### 5.2.2 Adjusting the optimum cooperativity

For this measurement, we operate close to the optimum cooperativity  $\mathcal{C}_{\text{opt}}$  which we estimate by following our model and equations for the total noise of the system we have developed in the theory chapter. The thermal rms amplitude (at resonance) of the membrane is given

by

$$x_{\text{res}} = \sqrt{\frac{2k_B T}{m\Omega_m^2 \Gamma_m}} \quad (5.4)$$

whereas this amplitude is reduced by a factor of  $\sqrt{\mathcal{C}_{\text{em}}}$  when it is not strongly coupled to the LC circuit leading to the coupled amplitude  $x_c$  (where  $\mathcal{C}_{\text{em}} \gg 1$ )

$$x_c = \sqrt{\frac{2k_B T}{m\Omega_m^2 \Gamma_m \mathcal{C}_{\text{em}}}} \quad (5.5)$$

Following this, we can assign an equivalent noise temperature for the optical detection sensitivity. Replacing this coupled  $x_c$  by  $x_L$  to denote the optical (laser) sensitivity and taking the square of  $x_L^2$  to calculate  $S_{xx}^{\text{im}}$ , we reach the following equation

$$S_{xx}^{\text{im}} = \frac{2k_B T_L}{m\Omega_m^2 \Gamma_m \mathcal{C}_{\text{em}}} \quad (5.6)$$

and the noise temperature from the optical detection becomes

$$k_B T_L = \frac{1}{2} \mathcal{C}_{\text{em}} m\Omega_m^2 \Gamma_m S_{xx}^{\text{im}} \quad (5.7)$$

The added membrane noise for our transducer is suppressed by the cooperativity giving  $\frac{T_m}{\mathcal{C}_{\text{em}}}$  thus making the total noise temperature  $T_T$  (optical, membrane and LC Johnson noise)

$$k_B T_T = \frac{1}{2} \mathcal{C}_{\text{em}} m\Omega_m^2 \Gamma_m S_{xx}^{\text{im}} + \frac{k_B T_m}{\mathcal{C}_{\text{em}}} + k_B T_R \quad (5.8)$$

where the term  $k_B T_R$  - LC Johnson noise - is referenced to the resistive loss of the LC circuit. The sum of the first two terms that is a function of the cooperativity can be minimized at the optimal cooperativity which is found to be

$$\mathcal{C}_{\text{opt}} = \sqrt{\frac{x_{\text{res}}^2}{S_{xx}^{\text{im}}}} \quad (5.9)$$

The expression has a form that can be readily tracked experimentally.  $S_{xx}^{\text{im}}$  is the optical measurement imprecision which is the background noise in the membrane spectrum measurements with the SA and its absolute value (typically on the order of 1-2 fm<sup>2</sup>/Hz) is known since we compare it to the calibration peak.  $x_{\text{res}}$  is the thermal peak amplitude of the membrane (rms) when it is decoupled from the LC circuit which we also measure with the inductor disconnected. Having done these preliminary measurements, we estimate our optimal cooperativity  $\mathcal{C}_{\text{opt}}$  to be around 150 for our present settings. We then increase our dc voltage up to a point where we get close to this cooperativity value (this is checked by looking at the broadening of the membrane at this voltage and estimating  $\mathcal{C}_{\text{em}}$  from that). For this experiment, we operate around 88 V bias voltage to reach this optimal cooperativity. As can be seen in Fig. 5.8, the optically measured membrane spectrum data indicates that the extra ambient rf noise in our previous measurements (Fig. 5.4) is now eliminated due to the shielded inductor (almost 20 dB improvement) and that our total noise is dominated by the Johnson noise of the LC circuit (violet curve). The experimental data is also

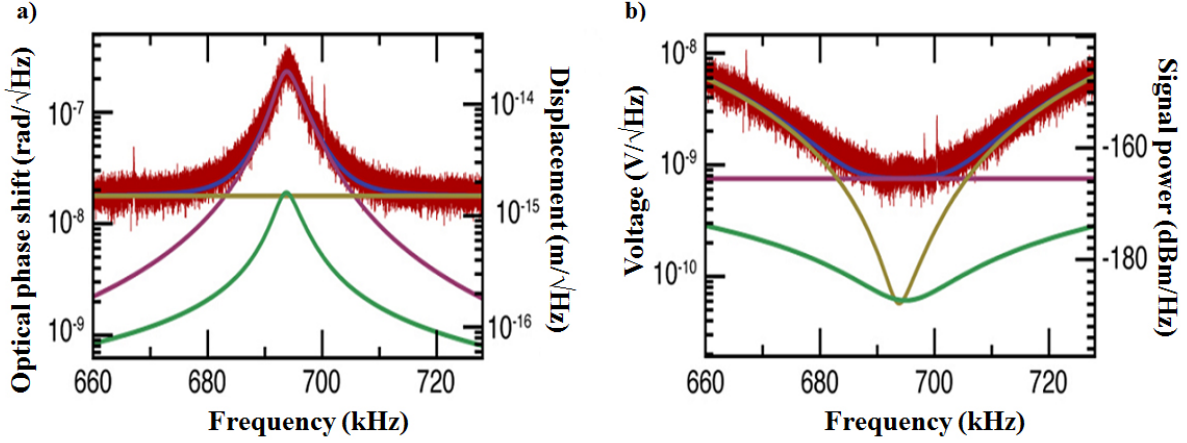


**Figure 5.8** a) Spectral density of the optical phase shift/membrane displacement at  $C_{\text{opt}} = 150$  measured with the interferometer (red points). Blue curve corresponds to the total optically measured noise based on our theoretical model. Violet, yellow and green curves refer to the Johnson noise of the LC, optical detection noise (quantum) and membrane noise, respectively. b) The red points and curves refer to the same noise contributions now represented as equivalent voltage noise by dividing the displacement noise by the transducer transfer function (reproduced from [4]).

very well-described by our model regarding the total noise of the system (blue curve). As has been done before, the total transducer noise is broken into its components which are the LC Johnson noise (violet), optical quantum noise (yellow) and membrane noise (green). The Johnson noise voltage estimated from the LC parameters for the present resistive loss is  $\sqrt{2k_BTR} = 734 \text{ pV}/\sqrt{\text{Hz}}$  is in agreement with the measured value of  $\approx 800 \text{ pV}/\sqrt{\text{Hz}}$ . At this optimum cooperativity, the sum of the optical measurement noise and membrane noise is minimized and has equal contributions coming from each. In panel b, we again have curves translated into voltage noise by using the transducer transfer function. In terms of voltage noise, both membrane and optical readout noise contribute with  $60 \text{ pV}/\sqrt{\text{Hz}}$  at resonance (inferred from the theoretical curves). Bandwidth of the detection is determined by the broadened linewidth of the membrane, which in this case, is approximately  $\Gamma_m/2\pi \times C_{\text{opt}} \approx 3 \text{ kHz}$  where  $\Gamma_m/2\pi = 20 \text{ Hz}$  is the intrinsic mechanical linewidth. We note that the mechanical response is also significantly cleaner than our previous measurements, where several narrow peaks coming from rf pick-up in the environment have been observed. Being an already important result in itself, this Johnson noise-limited measurement provides the stage for the next measurement run, where we have made an attempt to show the sub-Johnson noise contributions of our nanomechanical transducer backed up with more systematic analysis.

## 5.3 Noise measurements with a cold resistor

### 5.3.1 Noise temperature and the Y-factor method

As seen in the previous section, the real noise of the transducer (membrane and optical readout noise) is still buried in the Johnson noise of the LC circuit. In order to be able show experimentally that the real noise performance of our transducer can be smaller, we have implemented a well-known technique in the field of low noise operational amplifiers. The technique is named Y-factor method [29, 78] and aims at deducing the added noise of an amplifier by linear extrapolation of measured outputs at two different temperatures. A generic picture to depict the procedure is shown in Fig. 5.9. This can be achieved by

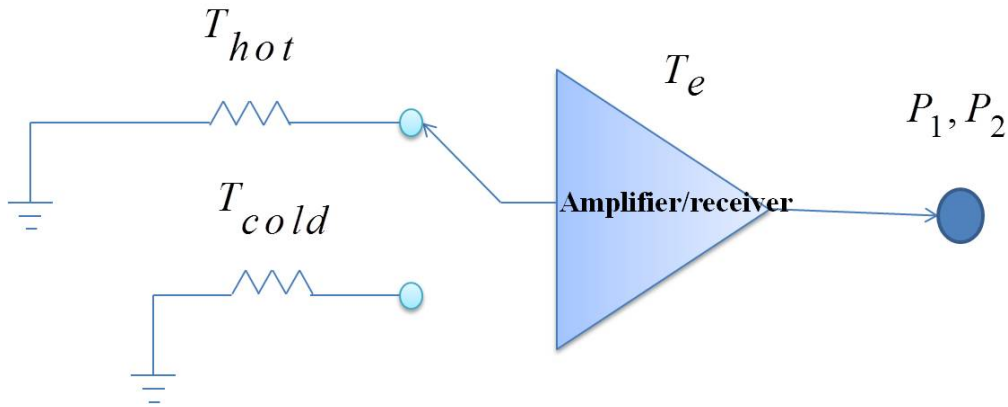


**Figure 5.9** Typical procedure for a Y-factor measurement.  $T_{hot}$  and  $T_{cold}$  refer to the physical temperatures of the two resistors. The amplifier/receiver has an equivalent noise temperature  $T_e$ . The output powers ( $P_1$  and  $P_2$ ) corresponding to  $T_{cold}$  and  $T_{hot}$  are measured to extract  $T_e$ .

connecting a source resistance  $R_s$  to the input of the amplifier and measuring the output noise of the amplifier at two different source resistor temperatures,  $T_{hot}$  and  $T_{cold}$ . The equations for the output noise in the two cases are given as follows

$$\begin{aligned} T_{cold} + T_e &= P_1 \\ T_{hot} + T_e &= P_2 \end{aligned}$$

where  $P_1$  and  $P_2$  refer to the measured output powers and  $T_e$  is the equivalent noise temperature added by the amplifier. Defining  $P_2/P_1$  as the Y-factor and solving for  $T_e$ ,

$$T_e = \frac{T_{hot} - Y T_{cold}}{Y - 1} \quad (5.10)$$

This expression is equivalent to measuring the output power (in arbitrary units) at two different temperatures and extrapolating the noise temperature to the zero value of the y-axis (intersecting the x-axis at a negative source temperature). The result is a 'negative' noise temperature representing the added noise of the amplifier.

In order to relate this equivalent noise temperature to the noise of our specific transducer, we write down the individual noise contributions of our device. This has been shown step

by step in the theory chapter, therefore we note the end result which is referenced to the source resistor and encodes the total noise of our transducer corresponding to  $T_e$  defined within the concept of the Y-factor measurement.

$$T_n = \left( \frac{1}{\eta_e} - 1 \right) T_R + \frac{1}{\eta_e} \left( \frac{T_m}{C_{em}} + \frac{(1 + C_{em})^2}{C_{em}} T_L \right) \quad (5.11)$$

Here  $\eta_e = \frac{R_s}{R_s + R}$  is the degree of loading the intrinsic resistance of the LC circuit with the external source resistance and  $T_L = n^{im} \hbar \Omega_r$ . The first term is the Johnson noise contribution of the LC circuit which is modified due to the loading with a colder resistor. The term with  $T_m$  refers to the membrane noise that is suppressed by the cooperativity (note that cooperativity is reduced with the external loading) and the last term being the quantum shot noise of optical detection. Thus by measuring the total noise temperature with the Y-factor method, the measured noise can then be decomposed into its components and we can apply our model by using equation 5.11 in order to identify the individual contributions.

### 5.3.2 Preliminary measurements with liquid nitrogen

We have performed several experimental runs in order deduce the noise temperature of our transducer with the Y-factor method. To this end, we attach a source resistor to our compact inductor (Pico electronics) as shown in Fig. 5.10 and physically cool this resistor by dipping it in a styrofoam box filled with liquid nitrogen. The resistor is specifically chosen



**Figure 5.10** The ultra-high precision resistors (with jumpers on the back side to vary the total resistance) connected to the compact inductor with a shielded coaxial cable.

to be an ultra-high precision cryogenic resistor (from Vishay [79]) which ensures that the resistance value is unchanged at cryogenic temperatures and the added noise and capacitance are minimized with proper fabrication methods (Appendix D). The source resistor is connected to the inductor- pcb unit (in a big rf shield) with a 10-20 cm length of cable. The setup for the liquid nitrogen cooling experiments is depicted in Fig. 5.11.

We have realized throughout the experimental runs that it is challenging to achieve first of all a Johnson-noise limited setting as we have shown before in Fig. 5.8. This task becomes crucial since any extra noise added by the additional circuit elements would show up when

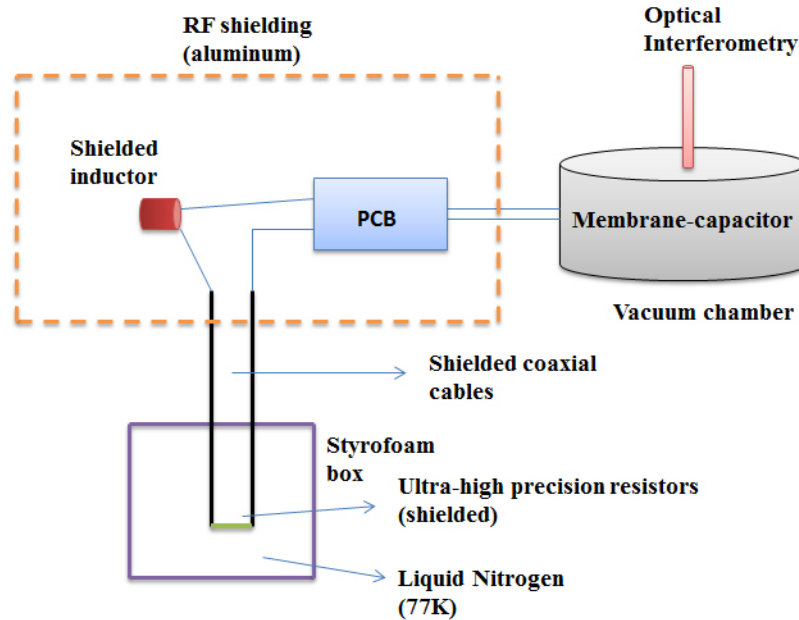


**Figure 5.11** Optical noise thermometry setup with reduced Johnson-noise. A high-precision resistor placed in liquid nitrogen is connected to the inductor in series, providing a cold bath that reduces the effective LC circuit temperature. In this way, a Y-factor measurement is performed with the resistor at two different temperatures; 77 K and 300 K to determine the actual noise of our opto-electromechanical transducer.

we start to cool the circuit with liquid nitrogen. Practically, it took us considerable amount of time with many iterations of measurements to get down to the level we have aimed at. Briefly put, we have observed that shielding of the added cable to the resistor as well as the resistor itself, meticulous grounding of several circuit elements extended over the optical table and finding a quiet frequency band become critical in order to reach the optimal noise performance. Furthermore, the op-amp together with its power supply, has to be disconnected from the pcb as it has been observed that large amount of noise can couple to the membrane when the op-amp has gain instability issues from time to time. The cable to the source resistor is chosen to be a well-shielded coaxial cable with the shield properly grounded. The proper cable has helped significantly in reducing the capacitive pick-up. Finally, shielding the resistor dipped in liquid nitrogen has improved our performance considerably. To summarize all our efforts in the direction of achieving low noise, we discuss briefly the output of our intermediate measurements - including the ones exhibiting excess noise. This, I believe, would be meaningful in terms of testing our model and interpreting the possible extra noise terms coupling to our transducer.

In Fig. 5.12, we show our first attempt to cool the resistor and measure the corresponding membrane noise temperature via optical interferometry. The membrane noise is (as mentioned before) measured with 10 kHz resolution bandwidth (sufficiently broader than the

thermal peak) and is always referenced to a calibration peak at 900 kHz (in other words, the ratio of the thermal and calibration peak is used to assign a temperature). Each data point refers to five averaged spectrum measurement (acquired for 30 seconds each) and the error bars correspond to the standard deviation. 300 K room temperature, in our case, is

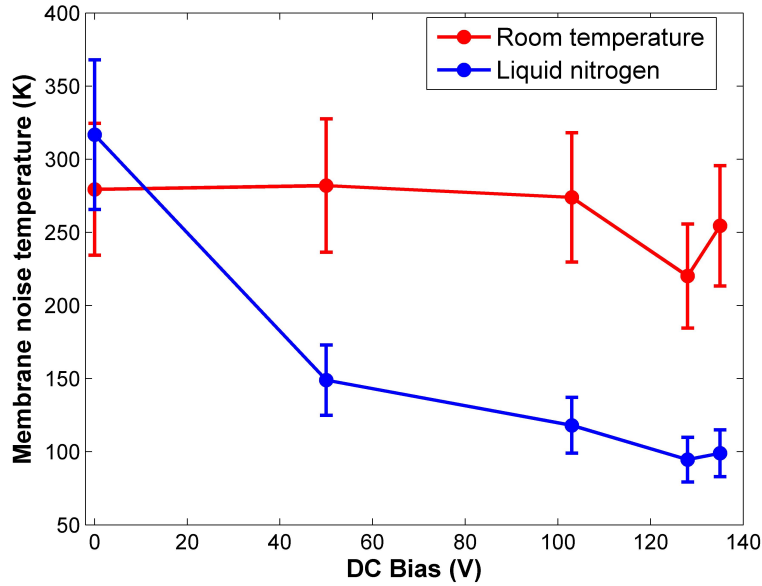


**Figure 5.12** Noise thermometry via optical detection of the membrane noise. First run is performed with the source resistor at room temperature and the second run in the same manner at liquid nitrogen temperature.

referenced to many averages recorded at 0 V corresponding to no coupling (therefore the bare membrane at room temperature). We note that the temperatures deduced from the measured spectra and the equipartition theorem, are corrected for frequency shift due to the dc bias. The dc voltage is first scanned at room temperature behaving as expected (relatively constant) except for a small dip at 128 V. We note that beyond 140 V, we see a large increase in the noise temperature since at those specific dc voltages, the corresponding membrane frequency coincides with a noisy spectral region (possibly pickup from the environment). After the measurements at room temperature, we pour liquid nitrogen on the resistor until it is fully dipped and start recording the membrane noise at the corresponding dc voltages. We have observed a clear effect of cooling of the membrane through the cooled resistor, showing that the mechanism is actually working. However, the analysis of noise contributions shows that we have excess noise on the membrane on top of our predicted noise floor. For the best data point (at 128 V) with the highest cooperativity, we deduce a total transducer noise of 92 K (from extrapolation/Y-factor at 128 V). 10 K of this total noise comes from the membrane estimated at a cooperativity of 28. We note that although the estimation for the suppressed membrane noise  $T_m/C_{em}$  is valid on resonance, our measurement within the 10 kHz bandwidth is still a good approximation as it will also be shown in our final noise data. 30 K comes from the Johnson noise of the LC (which is reduced from 300 K by a factor of 10 due to the loading resistor that is cooled). Light noise is shown to be

negligible at these experimental settings and thus we end up with an extra noise of  $\approx 50$  K. The inductor for this particular experiment is a shielded inductor with  $Q=20$  corresponding to  $\approx R = 200 \Omega$  and the cooled source resistor is  $2 \text{ k}\Omega$ . Since the loaded LC circuit  $Q$  is around 2 and the width is large, tuning of the capacitor each time at a different dc voltage is not necessary.

We deduce the estimated membrane noise contribution by extracting the cooperativity from the broadened membrane linewidths. As can be seen in Fig. 5.13,  $\mathcal{C}_{\text{em}}$  does not necessarily increase with the dc bias since the intrinsic linewidth degrades due to an unknown effect. However, the thermal membrane noise we estimate from the cooperativities still can not explain the discrepancy in our total noise since the membrane contribution is found to be only  $\approx 10$  K. Therefore, it is highly likely that the noise comes from extra pick-up, presumably from the cable-resistor line which was not shielded at that time.

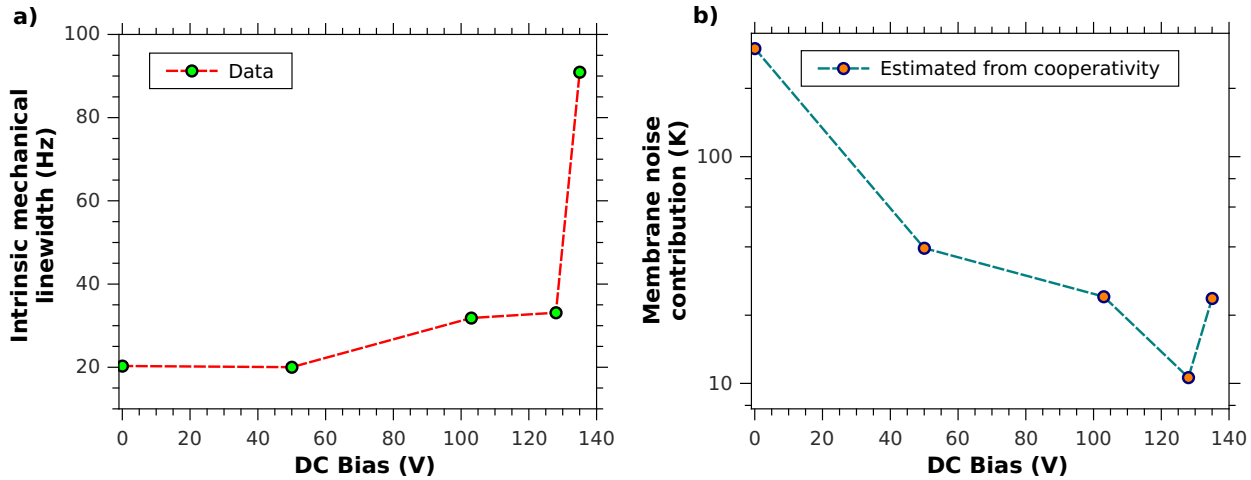


**Figure 5.13** a) Investigation of the intrinsic membrane linewidth change with respect to the dc bias voltage. The inductor is disconnected (no electrical coupling) and the membrane spectrum is recorded at each voltage. The linewidths are extracted from Lorentzian fits to the thermal traces. b) Estimated membrane thermal noise contribution due to suppression by the cooperativity.

After this measurement, we proceeded with slightly different settings, namely with a new inductor (again from Picoelectronics) to reach higher cooperativities. The inductor has a higher  $Q \approx 50$  and in this run, it is loaded with a  $500 \Omega$  resistor. Fig. 5.14 shows the extrapolated total noise temperature of the transducer based on the Y-factor method at 125 V and the corresponding membrane noise spectra with the source resistor at an equivalent noise temperature ( $T_e$ ) of 77 K and 300 K. Instead of the 10 kHz broadband detection in the previous measurement, the output noise power (a.u) is determined from the square of the peak height (on resonance) of the membrane. The peak height is extracted from a Lorentzian fit to the spectral response of the membrane (the optical noise background is included). The deduced temperature is 80 K with an error bar of 26 K. Even though the error bar is relatively large due to the propagation of individual error bars at the extrapolation point, there is still a large discrepancy between the model and the data. Subtracting

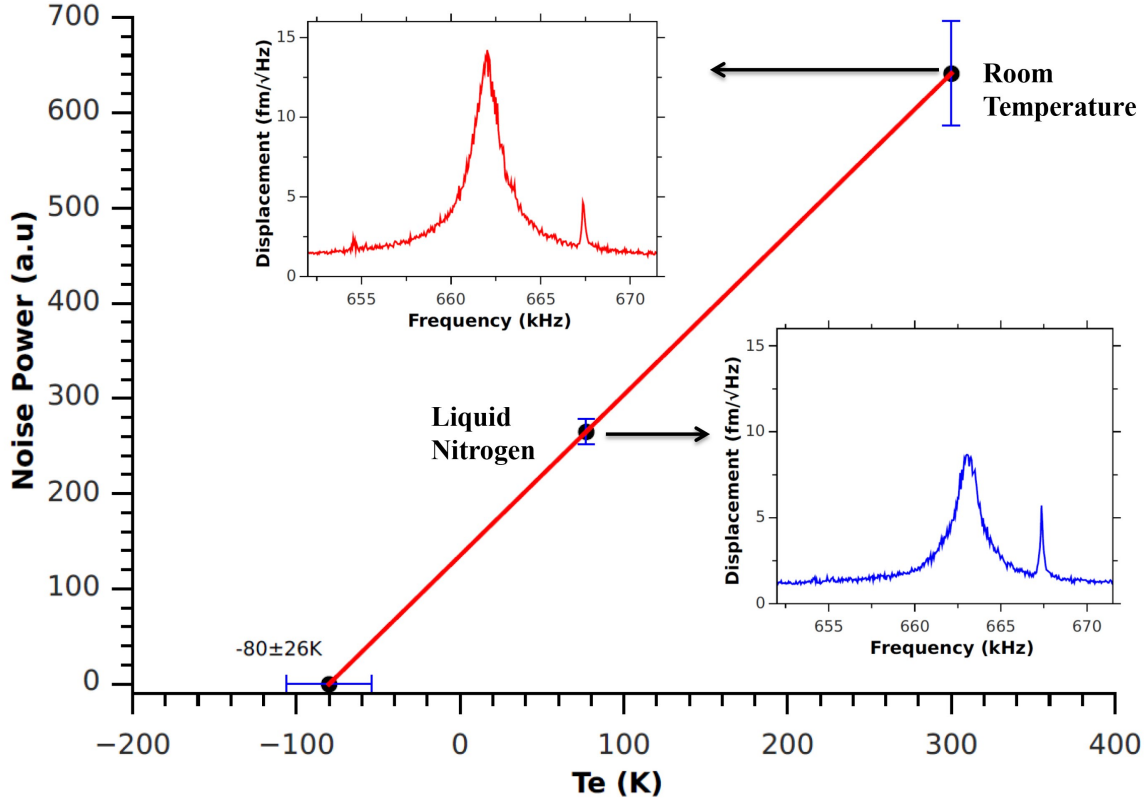


**Figure 5.14** Extraction of the total noise temperature of the transducer via the Y-factor method at 125 V dc bias.  $T_e$  refers to the equivalent noise temperature of the source resistor (77 K and 300 K for the two data points). The insets show the corresponding membrane spectral responses. Error bars come from the standard deviation of five identical measurements.

the Johnson noise and membrane noise contributions for this set of parameters, we end up with  $\approx 40$  K extra noise, still suggesting pick-up from the environment. In order to rule out whether a possible change in the LC circuit response due to cooling with nitrogen is responsible for such a discrepancy, we monitor (Fig.5.15a) the bare LC spectral response with the op-amp when we pour liquid nitrogen on the resistor. As can be seen, the spectral shape does not change and therefore the LC circuit itself does not bring any complication to the noise performance of the device. We have also performed another type of measurement in order to rule out that membrane heating due to the laser beam is responsible for extra noise temperature. For this measurement, the membrane is completely disconnected from the electrical components and we monitor the bare membrane noise temperature (tracked with low RBW=10 kHz method) and vary the laser power hitting on the membrane. The result is shown in Fig. 5.15b indicating that within the typical laser powers we use in our

experiments, there is no observable systematic effect on the membrane noise temperature upon increasing the laser power. Error bars come from the standard deviation of several subsequent recordings.

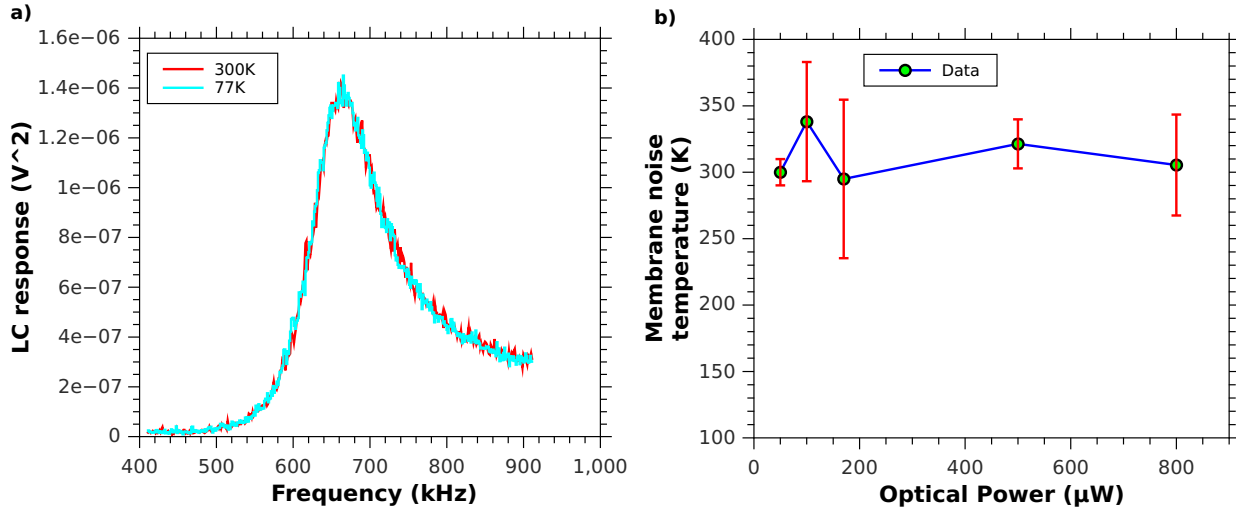


**Figure 5.15** a) LC circuit response without the membrane confirming that the spectral response of the LC circuit is not altered due to cooling with liquid nitrogen. The blue data corresponds to the source resistor ( $500 \Omega$ ) in liquid nitrogen, whereas the red data refers to the source resistor at room temperature. b) Membrane noise temperature with varying laser power. Here x-axis refers to the returned power from the membrane that goes to the interferometer arm.

### Varying the source resistance

Having observed excess noise which is likely to originate from pickup, we proceeded by performing more experimental runs where we varied the source resistor in order to gain a better understanding. The source resistors (in steps of  $50 \Omega$ ) are soldered on a small pcb with jumpers on each to be able to vary the resistor in liquid nitrogen. For this measurement we implement the low resolution bandwidth method in a slightly different way in order to record more data points for the sake of reducing the large noise temperature error bars. The thermal mechanical peak is recorded with an SA with a RBW of 10 kHz and smoothed by VBW (video bandwidth)=30 Hz in order to increase averaging. The calibration peak rms amplitude is separately tracked with a lock-in amplifier with proper time constants and the ratio of the two is used to assign a noise temperature. More averaging is performed by measuring in subsequent time chunks (which is limited by our stability of lock). Fig. 5.16, shows the outcome of such a measurement taken at 125 V dc bias by varying the source resistance at a fixed liquid nitrogen temperature in this case. We note that here we plot the total membrane temperature that is optically tracked. 300 K is referenced to the membrane noise temperature when the inductor is disconnected. The cooperativity without any external load resistance is  $\mathcal{C}_{em} = 222$  found from the broadened linewidth of 6700 Hz and an intrinsic linewidth of 30 Hz at this specific voltage. Insight on the noise performance

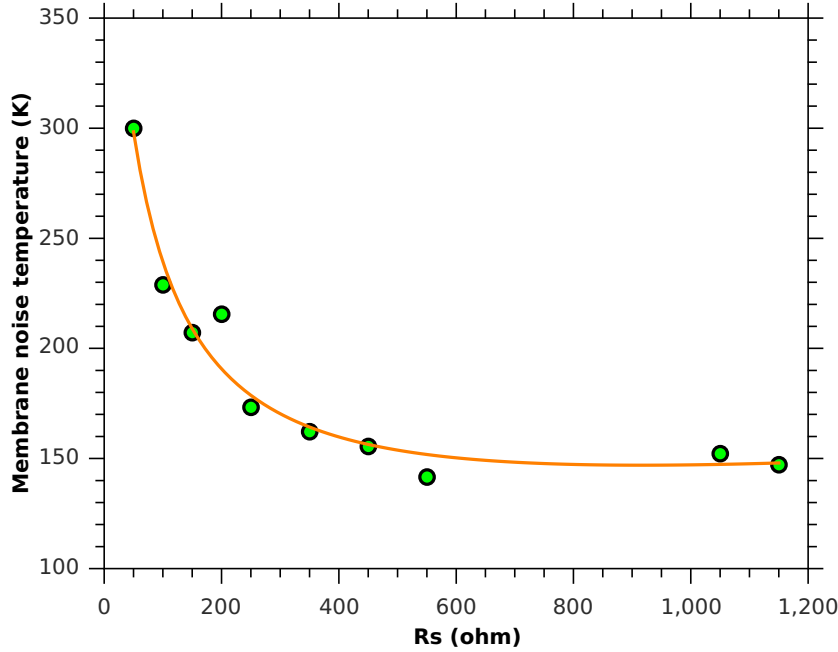


**Figure 5.16** Membrane noise temperature (optically tracked) with increasing source resistance ( $R_s$ ) kept at liquid nitrogen temperature. The fit function (orange line) which includes different extra noise contributions is used to explain the higher membrane noise temperature.

can be gained by fitting the data points to the expected total membrane noise temperature based on the following function

$$T_{\text{total}} = \frac{R_s}{R + R_s}(77 + n) + \frac{R}{R + R_s}(300 + e) + a \frac{R_s + R}{R} \quad (5.12)$$

where  $R = 60 \Omega$ . The individual terms are based on a possible scenario of noise terms coupling through different ports. The first term comes from the source resistance with a hypothetically added extra noise temperature denoted by  $n$  on top of 77 K. The second term is the Johnson noise contribution from the LC circuit which is suppressed by the source resistor.  $e$  represents a hypothetical noise source coupling through the pickup of the inductor. The last term is the membrane thermal noise contribution scaled by the degrading cooperativity with added source resistance. Optical readout noise is negligible in this case. Here  $a$  refers explicitly to  $T_m/C_{\text{em}}$ , physical temperature of the membrane (300 K) divided by the cooperativity at  $R_s = 0$ . The fit parameters yield,  $n=26.5$  K for the excess source resistance temperature and  $e=156$  K for the excess noise of the inductor indicating that extra noise coupling through different channels might explain the higher total added noise appearing in the optically detected membrane noise. Remarkably, the fit parameter  $a=1.33$  K is in very good agreement with the predicted value of 1.35 K independently extracted from the cooperativity of 222 (inferred from the measured linewidth).

### 5.3.3 Sub-300 K transducer noise temperature without excess noise

As shown in the previous sections, it has proven to be tricky to get down to low noise temperatures mainly due to excess pickup from different channels. After several trials with grounding of the elements (such as the cables) on the optical table and also incorporating a metallic shield for the cryogenic resistors in liquid nitrogen, the excess pickup noise has finally been eliminated. This is indicated in a separate experimental run shown in Fig. 5.17

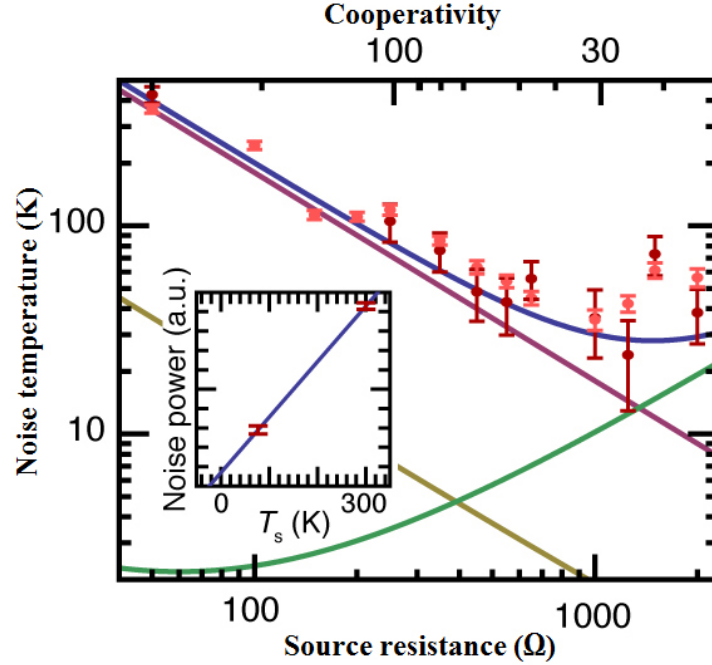


**Figure 5.17** Noise temperature of the opto-electromechanical receiver/amplifier as a function of the source resistance. The temperatures are determined via the Y-factor measurements (as shown in the inset for  $R_s = 1250 \Omega$ ), where the noise powers are measured at the resonance frequency (dark red points) and within a 10 kHz bandwidth (light red points). Blue curve (theoretical total noise) is the sum of the violet (Johnson noise), yellow (optical readout) and green (membrane) curves from our model. Error bars come from the standard deviation of identical measurements (reproduced from [4]).

and the analysis is carried out in the same manner based on the noise temperature equation 5.11 and the Y-factor method. The inductor is the same shielded commercial inductor with resistance  $R = 60 \Omega$ . The intrinsic cooperativity  $C$  is 550 at  $R_s = 0$  and scales accordingly as we start to load the circuit with the cooled external resistor ( $R_s$ ). Each data point is deduced from the Y-factor method (the extrapolation is shown as an inset for  $R_s = 1250 \Omega$ ) by measuring the output noise power of the membrane optically, at 300 K and 77 K with a fixed source resistance. Dark red points refer to the measurements on resonance, where the noise power is deduced from the square of the resonance amplitude extracted from the Lorentzian fits to the spectral shape. Light red points refer to the low RBW method within 10 kHz bandwidth where the noise power is referenced to the square of the peak amplitude.

The two methods show fairly good agreement with relatively small error bars compared to our previous measurements. The source resistance is then varied in discrete steps and the output noise measurements are performed for each resistance value. In the end, we see a behaviour consistent with our noise model based on the equation 5.11 represented by the blue curve. Violet curve refers to the Johnson-noise contribution from the LC circuit which is suppressed as the source resistance in liquid nitrogen is increased. Green curve is the membrane noise which, in this case, increases as the cooperativity gets smaller due to the increased source resistance. Yellow curve is the optical readout noise (quantum) which is expected to fall with larger resistance. As can be seen, the sum of the noise contributions from the membrane and the optical readout can be minimized at the optimal cooperativity corresponding to  $\mathcal{C}_{\text{opt}} = 70$  in this case. Subtracting the Johnson noise from the measured total noise (we rely on the blue curve), we infer that the membrane noise and the optical readout noise each contribute with 4 K noise temperature or equivalently with  $210 \text{ pV}/\sqrt{\text{Hz}}$  voltage noise referenced to the input. With this measurement, we have a more controlled way of monitoring the output noise by varying the source resistance which we analyze by using our model. We show that the Johnson noise contribution can indeed be reduced by coupling to a cold resistor and sub-300 K temperatures for the transducer can be shown experimentally (we observe a total noise of 24 K for the best data point). This measurement therefore makes our claims stronger for the Johnson-noise limited measurement in Fig. 5.8 where we had inferred our best sensitivity to be  $60 \text{ pV}/\sqrt{\text{Hz}}$  for both the membrane and the optical readout noise.

## 5.4 Performance comparison

It is interesting to compare the noise performance of our opto-electromechanical transducer with commercially available low-noise voltage sensors. For highly sensitive measurements, operational amplifiers (op-amp) typically made of bipolar junction transistors or field effect transistors are used with preferably high input impedance and low input capacitance. Gain-bandwidth products of 1 GHz is usually achievable. In a more general sense, both input voltage noise and current noise of the op-amp have to be taken into account for a specific source impedance

$$S_{VV}^{\text{oa,tot}}(\Omega) = S_{VV}^{\text{oa,in}}(\Omega) + R^2 S_{II}^{\text{oa,in}}(\Omega) \quad (5.13)$$

where  $S_{II}^{\text{oa,in}}(\Omega)$  is introduced as the current noise spectral density. For low source impedance applications, bipolar transistors can provide the best performance due to their very low voltage noise (as low as  $0.85 \text{ nV}/\sqrt{\text{Hz}}$  with a commercially available LT1028 [80]) even though the current noise is relatively high ( $\approx 1 \text{ pA}/\sqrt{\text{Hz}}$ ). However, for high source impedance applications, FET transistors are preferable [29] as they can reach current noise levels as low as a few  $\text{fA}/\sqrt{\text{Hz}}$ .

So far we have considered detection over a large bandwidth as many commercial amplifiers can achieve. However, an LC resonator can be used to enhance the sensitivity (by Q-factor) furthermore at the expense of narrowing the bandwidth of the device. Following the simple circuit equations at resonance and assuming  $Q_{LC} \gg 1$ , one reaches for the total noise,

$$S_{VV}^{\text{oa,tot}}(\Omega_{LC}) = \frac{S_{VV}^{\text{oa,in}}(\Omega_{LC})}{Q_{LC}^2} + R^2 Q_{LC}^2 S_{II}^{\text{oa,in}}(\Omega_{LC}) \quad (5.14)$$

For our measurements, we have used an ADA4817 op-amp cascade operating at  $G=1000$  and ended up with  $S_{VV}^{\text{oa,tot}(\Omega_{LC})} = (130 \text{ pV})^2/\text{Hz}$  by taking into account the resonant enhancement of the LC circuit which is comparable to our opto-electromechanical transducer's current performance. In principle, amplifiers specified with  $1 \text{ nV}/\sqrt{\text{Hz}}$  and  $\sim 50 \text{ fA}/\sqrt{\text{Hz}}$  voltage and current input noise [91] can be used however their performance is also similar for the parameters  $Q_{LC} = 45$  and  $R = 60 \Omega$  in our current setup. We note that within this comparative treatment, the commercial amplifiers also operate in a very narrow bandwidth due to the resonant LC enhancement. In terms of impedance performance, commercial amplifiers can typically have very high values ( $\approx G\Omega$ ) whereas our device has a coupling dependent impedance given by  $Z_{\text{em}}(\Omega_m) = \frac{1}{j\Omega_m C_m(x=0)} + \frac{G^2}{m\Gamma_m\Omega_m^2}$  at the mechanical resonance. By increasing the coupling parameter  $G$ , the impedance of our device can be tuned higher on demand. Apart from those commercial amplifiers, it is worth noting an interesting nanomechanical device made of a carbon nanotube that acts as an integrated, compact radio receiver [83]. However, the performance of the device is limited by the thermal noise of the mechanical resonator to  $1 \text{ V}/\text{m}/\sqrt{\text{Hz}}$  which is far above our noise limit.

As can be seen, it is not trivial to reach very low-noise performance even with the state-of-the-art electronic amplifiers. For example in radio astronomy, it is required to cool the low noise amplifiers to achieve a level needed for a specific task. Recently, SiGe transistors operating at a physical temperature of 15 K have demonstrated 5 K noise temperature [86] (without LC enhancement). For much more demanding detection tasks, it becomes a necessity to use very expensive amplifiers [12] that have to be operated at cryogenic conditions, like HEMT (High Electron Mobility Transistor) and JPA (Josephson Parametric Amplifier). For example, a HEMT microwave amplifier has been used to detect nanomechanical motion with only an added noise quanta of 30 [81]. Detection with added noise of less than half a quanta has been demonstrated with a JPA [82].

## 5.5 Limitations of the setup

### 5.5.1 Gap distance

Throughout the whole project, we have experimented with several membranes at varying electrode-membrane distances. In specific experiments where the coupling has to be relatively large (especially for demonstrating strong coupling) or where reaching a sufficient cooperativity is critical, achieving a smaller gap is crucial as the electromechanical coupling strongly depends on the distance given by

$$g_{em} \propto V_{dc} \frac{1}{d^2} \quad (5.15)$$

During our first experiments with the LC-membrane coupling, we have worked with samples (first generation) having large gap distances (ranging between 3-14  $\mu\text{m}$ ). This made it difficult to see a large splitting or more importantly achieve large cooperativities for noise measurements. Through our investigations with optical microscopy, we have come to the conclusion that residual particles both on the membrane frame and chip surface have had an effect on the larger than expected distance (pillar height) between the membrane and the chip. This typically originates from either fabrication residuals or dust picked up from the environment during the assembly process. In order to solve this problem, a second

fabrication step has been taken with the SiN-Al membranes where most of the frame area is etched away (50  $\mu\text{m}$  thick layer) with the idea of reducing the possibility of contamination. Our trials with several samples have shown that this method works and we have been able to confirm distances typically between 1-3  $\mu\text{m}$ . So the coupling strengths with these samples are typically higher and this has allowed us to reach the desired cooperativities at relatively smaller dc voltages. However, for most of the samples, it has brought another negative effect which reduces the cooperativity due to the increased mechanical linewidth. This issue is summarized in the following subsection.

### 5.5.2 Mechanical damping

For the set of membranes we have been working with (bare SiN, SiN-Al and SiN-G), the typical mechanical linewidth (without connection to any electrical element) is 1-2 Hz. This is confirmed by mechanical spectrum and ringdown measurements. When the membrane and chip are assembled and the gap distance between them is around 4-5  $\mu\text{m}$ , it has been observed that the mechanical linewidth stays around the same value also in the presence of a dc bias voltage. As discussed in the previous subsection, smaller distances ( $\approx$  1-3  $\mu\text{m}$ ) have been achieved by using etched SiN-Al membranes. However, cooperativity has suffered from this due to a yet unexplained decrease in the mechanical linewidth at these small distances. The effect becomes more clear upon increasing the dc voltage. An example of this behaviour is investigated in Fig. 5.13, which limits our cooperativity. We have tracked more dramatic linewidth broadening with other samples. It has been observed that the linewidth degraded day by day, broadening up to  $\approx$  200 Hz which in the end made the cooperativity too small for further measurements. The origin of this effect is not clear at the moment and requires further investigation. Possible explanations for this effect might be surface charge interactions starting to dominate at a certain distance creating another dissipation channel for the membrane or residual particles getting close to the membrane surface as the membrane is deflected towards the electrodes with the dc bias voltage.

### 5.5.3 Sensitivity limit due to instability

The instability issue due to the spring softening with the applied dc voltage has been discussed in section 2.6. Based on that treatment, we can estimate the improved cooperativity we can achieve with the experimental parameters for the data presented in Fig. 5.4 with  $C_{\text{em}} = 6800$ . As the instability occurs at the condition when the displacement is one third of the initial distance or in other words the frequency shift is one third of the bare membrane frequency, this yields a maximum allowable frequency shift of  $\Delta f_{\text{max}} = 260$  kHz for our membrane (bare frequency is 780 kHz at 0V dc bias). At a dc bias voltage 21 V, we observe a frequency shift of 88 kHz at a distance of 1  $\mu\text{m}$ . Using the frequency shift scaling with dc voltage ( $\propto V_{\text{dc}}^2$ ), we can argue that the dc voltage can be increased by a factor of  $\sqrt{260/88}$  leading to an increased cooperativity by a factor of 3 ( $C_{36\text{V}} = 20000$ ). This would mean that the membrane noise limited voltage sensitivity can be improved down to 2.9 pV/ $\sqrt{\text{Hz}}$ .

## 5.6 RF to optical photon conversion in practice

In this section, the concept of rf-to-optical photon conversion and the preliminary results we have realized so far with our system will be discussed. The main idea behind conversion is that an input voltage  $V_s$  injected through the inductor port causes driven motion of the membrane which in turn results in a phase modulation of the light that is reflected from the membrane. Following the treatment in the theory chapter, we have reached for  $V_\pi$  (a figure of merit for conversion) at the optimal cooperativity condition  $\mathcal{C}_{em} = 1$  (on resonance)

$$V_\pi = \frac{1}{2} \sqrt{mL\Gamma_m\Gamma_{LC}} \lambda \Omega_r \approx 140 \mu\text{V} \quad (5.16)$$

which is much smaller than microwave photonic devices such as [92, 93]. The experimental parameters are based on our data set for Fig. 4.20. The theoretical quantum efficiency for our system has been shown to be (in section 2.7)

$$\eta_{eo} = 4(kx_{zpf})^2 \frac{\Phi_{car}}{\Gamma_m}. \quad (5.17)$$

Now we extract our experimental conversion efficiency based on the data for the MIT regime. At the highest cooperativity at 125 V (in contrast to  $V_\pi$ , high cooperativity is better for making  $\eta_{eo}$  large), we can directly reach the efficiency by using

$$\eta_{eo} = \frac{\Phi_{sb}}{\Phi_{rf}} = \frac{P_{sb}/\hbar\Omega_{opt}}{P_{rf}/\hbar\Omega_{rf}} \quad (5.18)$$

Here the modulated optical power  $P_{sb}$  and the rf power  $P_{rf}$  are given by  $P_{sb} = P_{opt}2(\phi/2)^2$  and  $P_{rf} = \frac{V_s^2}{r_s(1+\mathcal{C}_{em})}$  where  $\phi = 2(2\pi/\lambda)x_{rms}$  and the incident light on the membrane  $P_{in} = 250\mu\text{W}$  for this specific experiment. Note that since the beam hits the aluminum part, the reflection is assumed to be unity. Inserting our experimental parameters and the independently measured rf voltage and optical phase modulation at this specific bias voltage, we end up with a conversion efficiency of 0.8%. Note that this efficiency is limited by the optical power of the Doppler Vibrometer. We have afterwards tested sending 20 mW optical power on the membrane with the NBI interferometer and confirmed that the mechanical properties are unaffected. Thus by using the theoretically expected efficiency in equation 5.17 and inserting typical parameters  $m = 30$  ng,  $\Omega_m/2\pi = 690$  kHz,  $\Gamma_m/2\pi = 2$  Hz,  $\Phi_{car}hc/\lambda = 20$  mW, we find a projected conversion efficiency of  $\eta_{eo} = 48\%$ . We note that a thorough investigation of rf to optical conversion efficiency in a cryogenic opto-electromechanical setup has been tackled in [85] and classical efficiencies on the order of 10 % has been demonstrated.

## 5.7 Conclusive remarks

The experimental results shown in this chapter demonstrate that our opto-electromechanical device can be used as a very sensitive tool in order to detect faint classical rf signals by optical means. The nanomechanical resonator, utilized in a novel approach, acts as a transducer and a link between the rf signal and the optical signal. This makes the device potentially a universal, versatile tool for sensing purposes without using cryogenics. In summary, we

have demonstrated an actual noise floor that is limited by Johnson-noise of the LC circuit at room temperature, equivalent to  $\approx 800 \text{ pV}/\sqrt{\text{Hz}}$ . Beyond this Johnson noise, we infer our limiting noise to be  $60 \text{ pV}/\sqrt{\text{Hz}}$  from the membrane thermal noise and the optical readout noise (quantum) each, at the optimal cooperativity  $C_{em} = 150$ . Our claims are furthermore supported by our subsequent Y-factor noise figure measurements, where we reduce the effective membrane temperature with a cold resistor at 77 K and extract noise temperatures for the transducer with also varying source resistance. The performance of our device is overall on par with the best commercial op-amps taking into account both their voltage and current noise. Further development in sensitivity of electronic amplifiers requires involvement of cryogenics which is expensive. Our device is completely cryogenic free and its current performance can be pushed further by operating at a higher cooperativity along with a reduced optical readout noise, for example, by incorporating an optical cavity. Apart from that, the device can also be used for rf to optical photon conversion which requires slightly different optimization conditions. Preliminary experimental tests so far without an optimized design have shown conversion efficiencies in the range of  $\approx 1\%$ .

## 5.8 Future prospects and outlook

Our current opto-electromechanical device operates at MHz frequency range and considering the usual rf and microwave applications, a natural way of improving the device would be to extend its operation to GHz frequency range. In addition to specific applications, a GHz version of this setup would necessarily imply a compact design which is expected to help in reducing extra noise effects and parasitic capacitive elements. Furthermore, if our device is coupled to a cold transmission line (for example cold sky at GHz), the ambient noise level would be a few Kelvin which is in comparison with the current noise level of our device, therefore making it interesting for highly sensitive astrophysical applications. For a high frequency version of this device, parametric coupling can be implemented where the LC resonator (GHz) is driven at a frequency vastly different from the mechanical frequency (MHz) which is  $\Omega_{LC} - \Omega_m$ . This type of coupling (beam splitter Hamiltonian) has been realized with different microwave electromechanical and opto-electromechanical systems together with strong coupling and sideband cooling even to the quantum ground state [11] and it has shortly been discussed in the theory chapter.

Along with the idea of extension to high frequencies, it becomes a necessity to realize a compact device. To that end, our near future plans include an integrated design where the mechanical resonator is patterned on top of the capacitor electrodes. This would mean that the manual assembly process that we have gone through so far, would no longer be necessary which is a big practical improvement. Furthermore, either an optical cavity can be used to encapsulate the electromechanical resonator or an etalon can be formed between the membrane and the chip electrodes to allow for integrated optical detection as well. With the incorporation of a high-finesse optical cavity, it would in principle be possible to reach even lower optical detection noise. Apart from that it would be possible to cool the coupled membrane-LC resonator system via radiation pressure cooling which has been proposed in [19]. Using the Hamiltonian and the annihilation operators  $a$  and  $b$  for the membrane displacement fluctuations and the LC circuit charge fluctuations introduced in [19], it is

found that the evolution of the charge operator follows the Heisenberg-Langevin equation

$$\dot{b} \approx -(\gamma + \Gamma)b + \sqrt{2\gamma}b_{in} - i\frac{g_{em}}{2\Gamma_m}\sqrt{2\gamma_m}a_{in} \quad (5.19)$$

for the strong damping limit  $\Gamma_m > g_{em}$  where  $\gamma$  is the LC damping rate,  $\gamma_m$  is the intrinsic mechanical damping rate prior to cooling and  $\Gamma_m$  is the optical cooling induced damping.  $\Gamma = g_{em}^2/4\Gamma_m$  denotes the cooling rate of the charge fluctuations ( $b$ ) that is induced by the optical field interacting with the hybridized electromechanical mode. In the end the thermal occupation number is given by

$$\langle b^\dagger b \rangle \approx \frac{\gamma}{\Gamma + \gamma}n_b + \frac{2\gamma_m}{g_{em}}n_a \quad (5.20)$$

Given high mechanical Q-factors are expected for the membrane, the second term can be made small and the first term dominates the final number. This treatment shows that light can not only be used as a probe for the electromechanical system, but also can manipulate the thermal occupation number acting independently on the hybridized mechanical and electrical modes.

We believe with some crucial improvements like increasing the currently small bandwidth and operating resonance frequency as well as optimizing the impedance for a specific task, our proof-of-principle device can be utilized for highly sensitive applications in fields such as Nuclear Magnetic Resonance (NMR) Spectroscopy and astrophysics. Achieving high signal to noise ratio in NMR is of paramount importance since typical magnetic resonance signals are not so powerful. NMR probes usually consist of high-Q coils that pick up rf waves from the sample. SNR is given by [87]

$$\frac{S}{N} \propto \frac{B_1/I_{\text{coil}}}{\sqrt{4k_B\Delta f(R_c(T_c + T_a) - R_s(T_s + T_a))}} \quad (5.21)$$

where  $B_1$  is the rf magnetic field,  $I_{\text{coil}}$  is the current induced in the coil.  $R_c$  and  $T_c$  refer to the coil resistance and temperature, whereas  $R_s$  and  $T_s$  denote the sample resistance and temperature.  $T_a$  is the preamplifier noise temperature. The noise, in this case, will be determined by the Johnson noise of the coil circuit. In order to reduce this noise, the coil has to be cryogenically cooled. However, this is not sufficient to reach low noise levels, since the preamplifier that is between the cold receiver coil and the ambient temperature electronics should also be cooled as it adds excess noise otherwise. Considering this, our room temperature transducer/amplifier (membrane) can replace cryogenically cooled amplifiers for such applications.

Besides NMR, detection of radio waves is crucial for the study of astrophysical systems. Typical setups to detect galactic signals include large dish antennae picking up signals and transmitting them through a lossy transmission line to a cascade receiver with several amplifiers [28]. First of all, ambient ground noise ( $\approx 300$  K) is avoided by using a narrow antenna at high altitudes in order to detect sub-300 K noise sources. For example, for an antenna looking at the cold sky at 10 GHz frequency, the ambient noise is around 6 K [78,90]. More general behaviour of sky noise with respect to frequency can be found in [88,89]. Another noise channel is the lossy elements in the transmission line. For a loss factor of  $L$  and a physical temperature of  $T_l$  for the lossy channel (for example cable) and  $T_s$  for the source,

the total noise temperature becomes [78]

$$T_{s1} = T_s/L + ((L - 1)/L)T_l \quad (5.22)$$

On top of that, there is finally the receiver/amplifier temperature. This is usually done in a cascaded way where the first preamplifier is followed by several amplifier stages. The total noise added in this case is [78]

$$T_t = T_{e1} + T_{e2}/G_1 + T_{e3}/(G_1G_2)\dots + T_{eN}/(G_1G_2G_3\dots G_{N-1}) \quad (5.23)$$

As can be seen, if the gain  $G_1$  of the preamplifier is high, the other terms are small and it is clear that the low noise performance of the preamplifier is very critical. In order to achieve low noise temperatures for demanding tasks, the amplifier stages are kept in cryogenic coolers to start from low physical temperatures [86]. Considering the current performance of our nanomechanical transducer and given that it can be coupled to a cold transmission line, it brings only a few K added noise when the transducer itself is physically kept at room temperature. Improvements in optical readout sensitivity and increasing the cooperativity will further push this number down. Therefore, we think that our device, with some engineering and optimization, has a big potential in astrophysical applications and can in principle replace cryogenic preamplifiers.

## Chapter 6

# Optical cavity cooling with GaAs membranes

One of the independent experimental projects performed at Polzik group was dedicated to optomechanics with semiconductor - Gallium Arsenide (GaAs) membranes. This project started roughly four years ago (as the main work of Koji Usami and Andreas Næsby) and the author has also been involved in this project before focusing on the main work of this thesis (opto-electromechanics). The author has worked on the initial phase of the development of the experimental setup and helped with several measurements, particularly for the identification of the cooling mechanism. The GaAs project has been worked out in detail in Andreas Næsby's thesis [94] and has resulted in two experimental papers where the author of this thesis is a co-author. In this chapter, we aim at giving a compact overview of the measurements we have performed along with the key results [96, 99]. The details and involved calculations can be found in these references. The main outcome of the GaAs experiment is that we have demonstrated a novel optical cavity cooling mechanism of a semiconductor membrane which stems from electron-hole pair generation and cavity assisted photothermal cooling.

### 6.1 GaAs membranes - Fabrication and characterization

We start by describing the GaAs membranes we have worked with throughout this project. The initial interest was to optomechanically characterize and explore a semiconductor membrane which could have potential use for prospective (quantum) optics experiments that might bring together opto-electronics and nanomechanics. The GaAs membranes were fabricated by Lodahl group (at DTU at that time). During the optomechanical characterizations in a Fabry-Perot cavity at NBI (mainly for the mechanical Q-factor of the membrane), we have realized (with the initial discovery of Koji Usami) that the cavity showed interesting behaviour which would later on be demonstrated to be an optical cooling effect of the GaAs membrane thanks to its semiconductor properties.

### Fabrication procedure

GaAs has been a subject of investigation as a popular material with its direct band-gap semiconductor properties. It also provides a ground for merging opto-electronics with nanomechanics [97]. The considerable effect of its piezoelectricity has been utilized for carrier mediated optomechanical coupling and actuation [98]. Fabricating GaAs based microresonators with good mechanical quality has attracted attention [95], however these structures have usually exhibited considerable mechanical loss. Therefore, fabrication and characterization of GaAs nanomembranes with high mechanical Q-factors is one of the initial motivations of this project.

The fabrication procedure of our GaAs membranes is described in detail in [96]. In order to fabricate the GaAs membrane, a GaAs/AlGaAs heterostructure wafer is used. The substrate is a (100) oriented GaAs substrate of thickness  $350\ \mu\text{m}$ . A  $1\ \mu\text{m}$  thick  $\text{Al}_{0.85}\text{Ga}_{0.15}\text{As}$  layer is used as an etch stop layer. The actual membrane is a  $160\ \text{nm}$  thick layer of GaAs on the same heterostructure. The membrane is a macroscopic structure in the lateral dimensions ( $1.91 \times 1.36\ \text{mm}$ ). The picture of the fabricated membrane with its layers and the real SEM microscope image are shown in Fig. 6.1. In order to remove the substrate, selec-

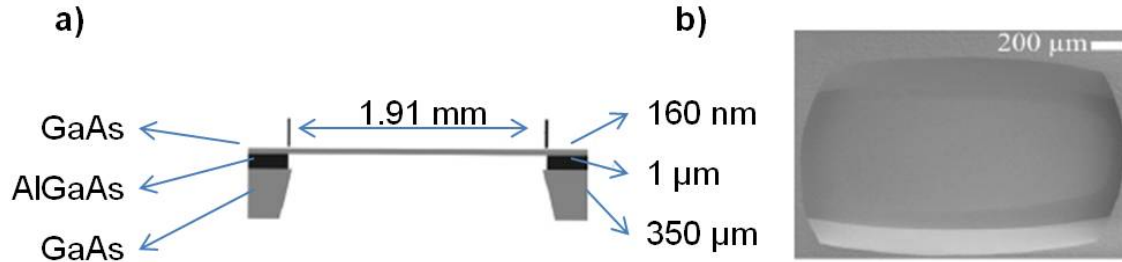


**Figure 6.1** a) Depiction of the layers of the GaAs membrane. After selective etching, the actual mechanical resonator appears as a thin GaAs membrane that is optically accessible from both sides. b) SEM image of the membrane after cleaning (reproduced from [96]).

tive wet-etching with citric acid is used where the AlGaAs acts as an etch stop layer. The next step is to use hydrofluoric acid (HF) for selective wet-etching of the sacrificial AlGaAs layer. Additionally, oxygen plasma and potassium hydroxide (KOH) solution is applied to the membrane for the cleaning process. We note that the shapes of the membranes are not exactly rectangular due to the different etch rates for different crystallographic planes of GaAs. The membranes are also intrinsically bent in a certain direction.

### Mechanical characterization

The mechanical properties of the GaAs membranes have been characterized at NBI in a cavity optomechanical setup with which we have also observed the novel optical cooling mechanism. A macroscopic concave mirror and the GaAs membrane constitute the end mirrors of a Fabry-Perot cavity. We monitor the mechanical vibrations of the membrane by looking at the optical cavity transmission with a photodetector. The rf detector signal is then directly fed to a spectrum analyzer to record the mechanical peaks in the spectrum. The setup used for these measurements is the same with the cooling setup, so it will be

shown in the cooling section. The vibrational modes of the GaAs membrane, that are in-

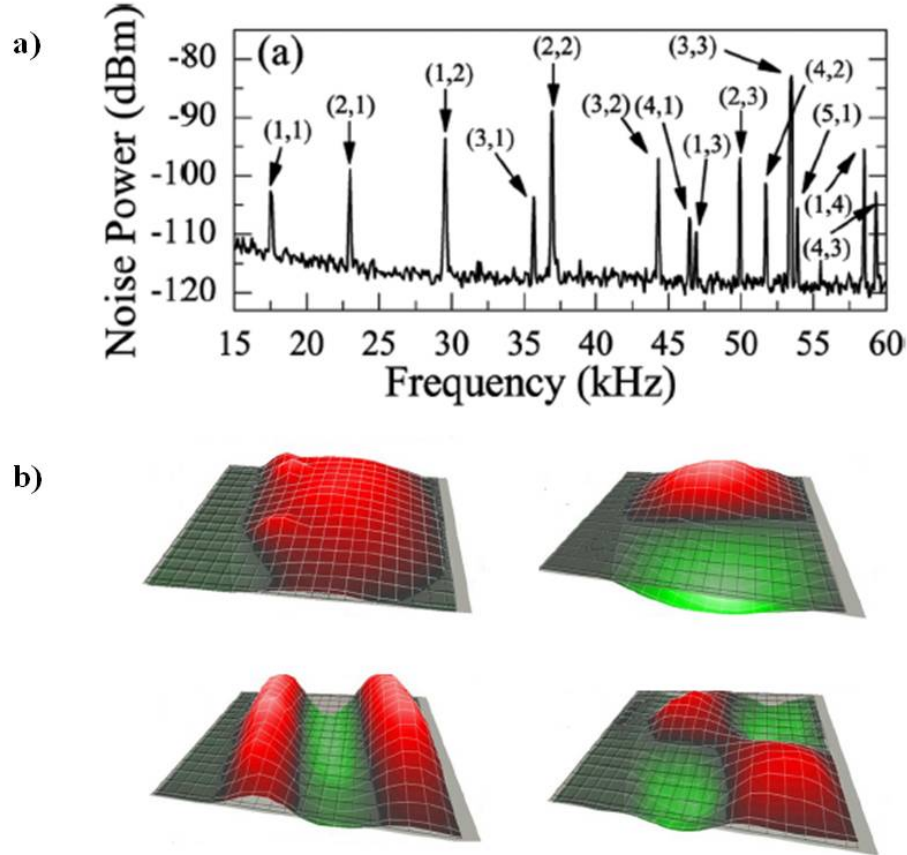


**Figure 6.2** a) Mechanical spectrum of the membrane tracked via the cavity transmission signal. b) Snapshots from Doppler Vibrometry images for a similar GaAs sample showing the (1,1), (2,1), (1,3), (2,2) vibrational modes (reproduced from [96]).

vestigated via cavity transmission spectroscopy, are shown in Fig.6.2a. In order to match to the fundamental mode, tensile stress is used as a fit parameter since it was not known prior to the measurements. The rest of the modes follow in agreement with the rectangular drum mode model. In Fig. 6.2b, scanning vibrometry images (recorded at DTU) are shown for a similar membrane. We have furthermore performed mechanical ringdown measurements in order to extract the Q-factors of several modes. To this end, the cavity field is modulated with an AOM (acousto-optic modulator) for excitation and shut off properly so that the mechanical signal is recorded as a ringdown decay. The mechanical signal for the ringdown is monitored with a split photodiode which is then fed to a lock-in amplifier to look at the mechanical resonance component (Fig. 6.3). However, since we have observed optical power dependent linewidth broadening due to cooling, the intrinsic mechanical decay rates are extracted via extrapolation to zero optical power. Below is a table showing the Q-factors of some mechanical modes. The results we have obtained are unexpectedly high.

A remarkably high  $Q$  is observed with (4,3) mode reaching  $2.3 \times 10^6$  at an eigenfrequency of  $\approx 60\text{kHz}$  that yields a  $Q \times \nu$  product of  $1.4 \times 10^{11}$ . These are the first findings that hint the promising mechanical properties of GaAs membranes.

Mode	Frequency	Q factor
(2,1)	23.4 kHz	$0.50 \times 10^6$
(3,2)	45.5 kHz	$0.56 \times 10^6$
(4,1)	47.5 kHz	$0.53 \times 10^6$
(4,3)	59.5 kHz	$2.3 \times 10^6$

## 6.2 Setup for characterization and cooling of GaAs membranes

The experimental setup we have used throughout this project is outlined in Fig. 6.3. The setup basically serves for two purposes - monitoring the mechanical characteristics of the membrane and cooling the vibrations via light.

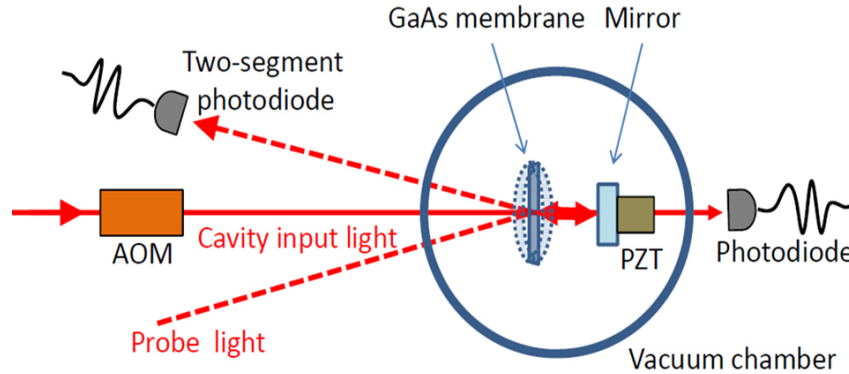


**Figure 6.3** Simplified picture of the experimental setup for the mechanical characterization and optical cavity cooling of GaAs membranes. The Fabry-Perot cavity, composed of a membrane and a piezo-mounted mirror, is contained in a vacuum chamber (reproduced from [99]).

A GaAs membrane (with reflectivity %62) and a concave mirror (with reflectivity %96) are mounted on a stage which is kept in a vacuum chamber ( $10^{-5}$  Pa) to form a Fabry-Perot cavity of length  $\approx 29$  mm. The finesse is measured to be roughly 10. A piezo is attached to the mirror to be able to scan the cavity. Cavity input light is generated from a Ti:Sapph laser (810-880nm) and is used to monitor the mechanical spectrum (with a photodiode), cool or excite vibrations depending on the purpose. For probing, cavity is locked at the slope of the cavity resonance with a slow signal and fast modulations are monitored with a photodiode that is fed to an SA. In order to get a better SNR, the cavity input signal (separated with a BS which is also used for intensity stabilization) is subtracted from the cavity transmission signal. Intensity modulation for mechanical excitation and intensity stabilization are carried out via an AOM. An additional beam from a diode laser (975 nm)

is directed with an angle and used for probing the mechanical ringdown with a split diode photodetector. We excite the membrane by adding a frequency modulation to the rf driver for the AOM (close to the mechanical frequency) and the AOM is switched off with a proper circuit to cut off the excitation. The exponential decay gives the Q-factor of the membrane.

### 6.3 Cooling mechanism

Here we will describe briefly the main mechanism behind cooling of the GaAs membrane. The first sign of this physically interesting phenomenon appeared in our cavity transmission measurements. We have observed unexpected fluctuations in the cavity resonance even though the finesse was so low to expect any kind of radiation pressure induced cooling or heating. Fig. 6.4 shows a snapshot from such a cavity response recording. The input optical

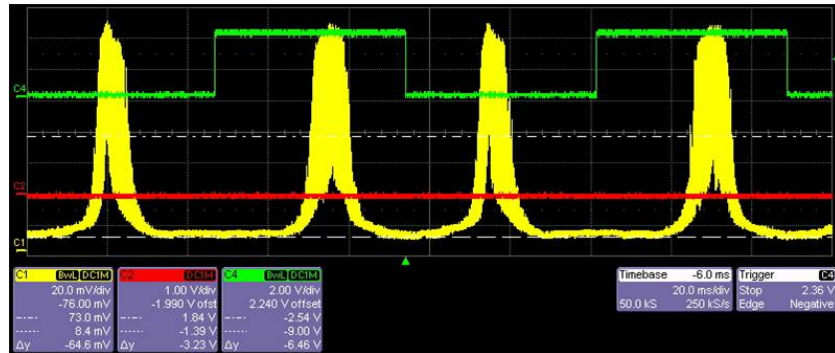


**Figure 6.4** A snapshot from the oscilloscope exhibiting an unexpected response (yellow) in the cavity transmission (with above band-gap light) which was the first hint for semiconductor physics coupled to cavity degrees of freedom. The cavity response is asymmetric and carries fluctuations on both sides stemming from the complex dynamics.

power is around  $500 \mu\text{W}$  and the wavelength of the laser beam is  $810 \text{ nm}$ . It turned out that both the asymmetry that is associated with the static bending of the membrane due to the photo-induced force and the fluctuations we observe come from a complex physical mechanism that combines semiconductor physics with cavity optomechanics. Throughout several experimental runs and confirmations, we have realized that cooling of the mechanical modes originates from the intrinsic semiconductor properties of the GaAs membrane which is subsequently assisted with the cavity. The mechanism is depicted in Fig. 6.5. Vibrational cooling of the GaAs membrane can be summarized as follows. First, a laser beam which has energy larger than the bandgap energy of GaAs, couples in and circulates inside the Fabry-Perot cavity. The energy of the photons absorbed by the GaAs membrane is sufficient to excite electron-hole pairs inside the semiconductor material. These electron-hole pairs recombine non-radiatively leading to heating and thermal stress which in turn deflects the membrane. As the cavity length now changes with the deflection of the membrane, the number of photons inside also change. This leads to a cavity-assisted feedback on the membrane with a position dependent photothermal force, together with a time delay

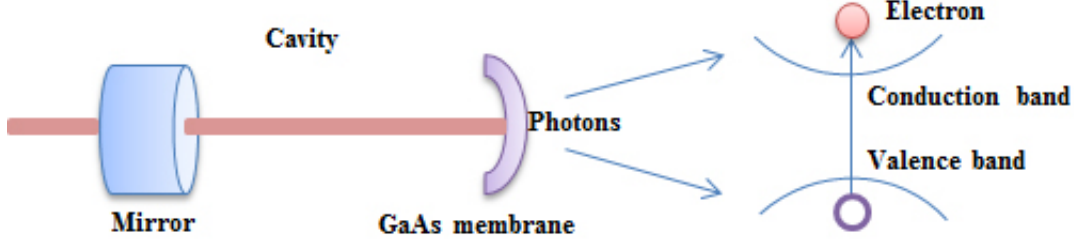


**Figure 6.5** Pictorial description of the internal semiconductor dynamics of the GaAs membrane which is the primary source of optically induced cooling in our experiment. Cavity feedback and thermal stress released by the non-radiative decay of optically excited charge carriers govern the dynamics of cooling.

coming from the thermal diffusion process. This complex coupling mechanism leads to the rich dynamics and the cooling effect on the membrane when certain conditions are satisfied. The origin of the cooling mechanism has been identified and analyzed with several experiments which will be discussed briefly. But before that, it would be useful to give a short theoretical background for the dynamic back-action. No matter how complicated and indirect the structure of the coupling mechanism is, a generic treatment with a position dependent photo-induced force including a time delay is sufficient to understand the core dynamics of the interaction. This has been treated in [14], so we will follow the main formulae derived in this paper. In the presence of thermal force and a photo-induced force  $F$  with a Laplace-transformed time-delay function  $h_\Omega = \frac{1}{i\Omega(1+i\Omega\tau)}$  where  $\tau$  is the time delay originating from the relevant timescale of the mechanism, the equation of motion for the membrane becomes as follows

$$-m\Omega^2 z_\Omega + i\Omega m\Gamma_0 z_\Omega + k_0 z_\Omega = F_{th}(\Omega) + \nabla F i\Omega z_\Omega h_\Omega \quad (6.1)$$

and  $\nabla F$  refers to the spatial derivative of the photo-induced force. Following and rearranging the equation of motion, the effective mechanical decay rate is given by

$$\Gamma_{\text{eff}} = \Gamma_0 \left( 1 + Q \frac{\Omega_0 \tau}{1 + \Omega^2 \tau^2} \frac{\nabla F}{k_0} \right) \quad (6.2)$$

and the effective spring constant is

$$k_{\text{eff}} = k_0 \left( 1 - \frac{1}{1 + \Omega^2 \tau^2} \frac{\nabla F}{k_0} \right) \quad (6.3)$$

which then makes the effective frequency

$$\Omega_{\text{eff}}^2 = \Omega_0^2 \left( 1 - \frac{1}{1 + \Omega^2 \tau^2} \frac{\nabla F}{k_0} \right) \quad (6.4)$$

where  $\Omega_0, k_0$  and  $\Gamma_0$  are the intrinsic resonance frequency, spring constant and mechanical decay rate, respectively. Furthermore, by using the equipartition theorem and the noise spectral densities, one reaches a crucial and simple expression

$$T_{\text{eff}} = T \frac{\Gamma_0}{\Gamma_{\text{eff}}} \quad (6.5)$$

which gives the final temperature depending on the initial temperature ( $T$ ) and the ratio of the intrinsic and effective dampings. Experimentally, this means that by measuring the mechanical dissipation rate with a ringdown measurement, one can quantify the amount of cooling (appearing as an additional damping on the membrane). More explicitly, it can be formulated by

$$T_{\text{eff}} = T \frac{1}{1 + Q \frac{\Omega_0 \tau}{1 + \Omega^2 \tau^2} \frac{\nabla F}{k_0}} \quad (6.6)$$

where the cooling rate is optimized for  $\Omega_0 \tau = 1$ . Here, we have kept the fourier frequency  $\Omega$ , but typically we are interested in the response around the resonance frequency  $\Omega \approx \Omega_0$ .

## 6.4 Vibrational cooling results

We have performed several experiments in order to confirm that the vibrational modes of the GaAs is indeed cooled. First, we look at the cavity transmission signal that reveals the Brownian peak of the (2,1) mode of the membrane. As we increase the optical power from 13  $\mu\text{W}$  to 26  $\mu\text{W}$ , we observe a decrease in the integrated membrane area as a first indication of vibrational cooling (Fig. 6.6a). In addition to that, we measure the effective mechanical damping rate which is modified due to the cooling force (Fig. 6.6b). Mechanical ringdown times are measured at varying optical powers with the ringdown method outlined before and damping rates are extracted from that. At the same time, mechanical eigenfrequencies can be easily tracked. As expected, we see an increase in the effective damping linear in optical power and a decrease in the egenfrequency also linear in optical power, which in our case, is due to heating and released tensile stress.

We further confirm our cooling results by comparison of the mode temperatures extracted from two different methods in Fig. 6.6c. The purple points come from the average of 5 identical measurements of the mechanical power spectrum and the red points come from the average of 5 identical measurements of the ringdown time. We see good agreement between the two methods and the mode temperatures extracted from the ringdown time follow the curve with  $1/\tau$  with respect the cavity input power. This is because the damping time  $\tau$  is a linear function of the input power. Wavelength of the laser is 870 nm for this experiment. We note that we have done most of the systematic analysis for the cooling with the (2,1) mode, however the best cooling performance is achieved with the (4,3) mode as it has a remarkably higher mechanical Q-factor, which is a crucial parameter for the cooling performance. For this specific mode, we have achieved a cooling factor of 75 (confirmed with the ringdown results) which allows us to reach 4 K mode temperature starting from room temperature with a cavity input power of 50  $\mu\text{W}$  and finesse of 10. The cooling performance of our setup is limited by the instability that stems from the static deformation of the membrane due to photothermal stress, setting in around 50  $\mu\text{W}$  optical power.

Another experimental run is performed by changing the wavelength of the laser thanks to the tunability range of the Ti-Sapph laser as shown in Fig. 6.7. The result indicates possibly the most dramatic consequence of electron-hole pair generation in the GaAs membrane. The cooling rate is calculated by measuring the effective damping rate and the intrinsic damping rate of the membrane and plotted as a function of the photon energy. As can be seen, before reaching the bandgap energy ( $E_g \approx 870$  nm), the cooling rate is very small and it quickly rises up close to the bandgap edge. Beyond the bandgap energy, it stays more or

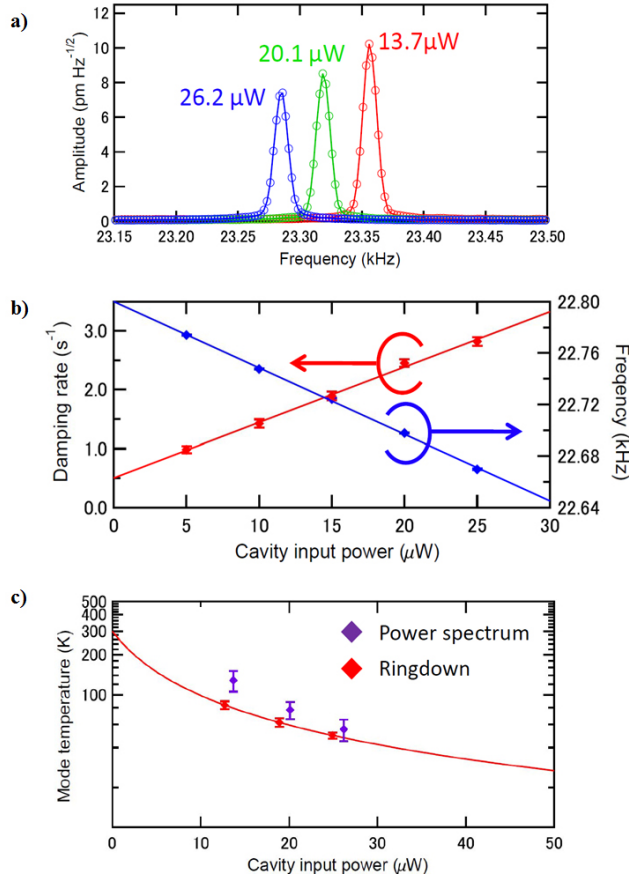


**Figure 6.6** a) Calibrated Brownian vibration spectrum (with Lorentzian fits) of the (2,1) mode of the GaAs membrane with varying cavity input power. The thermal peak area decreases as the optical power for the cooling light increases. b) Mechanical damping rate and mechanical resonance frequency as a linear function of the input power. c) Comparison of the mode temperature with the ringdown and power spectrum methods. Error bars come from the standard deviation of five measurements (reproduced from [99])

less constant with some bumps which have to be investigated further. The overall picture is consistent with the excitonic absorption spectrum [100]. This measurement yields one of the strongest evidences that cooling of the membrane is related to the electron-hole pair formation within the semiconductor structure.

Apart from that, detuning dependence of the cooling is also interesting to note since it shows some deviances from a typical Fabry-Perot cavity. This comes from the complex interference picture that shows up inside the cavity due to the finite thickness of the GaAs membrane. Therefore, it becomes necessary to solve the electric field equations for the coupled cavity and then calculate the intra-membrane photon number (and its spatial derivative) which is crucial in determining the cooling behaviour. This problem has been tackled in detail in the Supplementary Info. of [99]. The outcome is that the transmission, reflection and absorption of such a coupled cavity shows a shifted detuning picture with

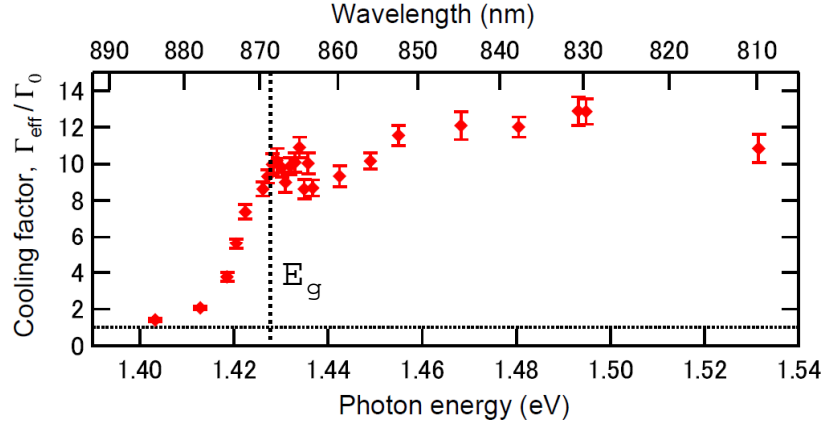


**Figure 6.7** Cooling factor extracted from  $\Gamma_{\text{eff}}/\Gamma_0$  as a function of the wavelength (or energy) of the cooling beam (reproduced from [99]).

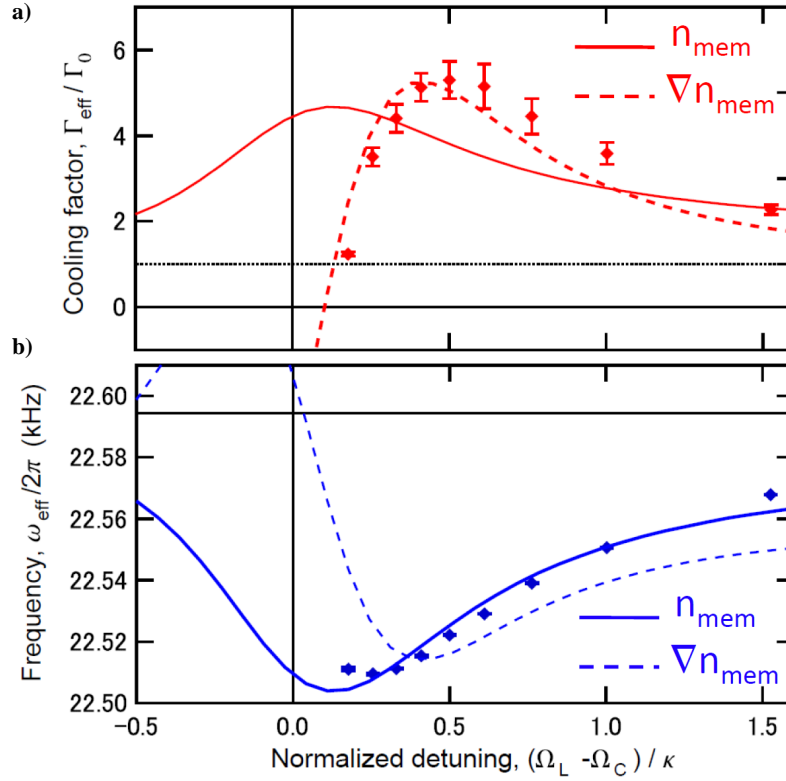


**Figure 6.8** a) The cooling factor as a function of the normalized detuning with respect to the cavity resonance. b) Mechanical resonance frequency as a function of normalized cavity detuning (reproduced from [99]).

asymmetric features in contrast to normal Fabry-Perot cavities. Consequently,  $n_{\text{mem}}$  - the number of photons inside the membrane - follows this modified absorption profile. In Fig. 6.8, we show our experimental results revealing the peculiar detuning dependence of cooling

in our coupled cavity system. In panel a, the cooling factor with respect to the detuning of the cooling light is shown. The cooling factor follows the shifted curve calculated for the spatial derivative of the intra-membrane photon number ( $\nabla n_{\text{mem}}$ ) instead of the intra-membrane photon number itself ( $n_{\text{mem}}$ ) as expected since  $\Gamma_{\text{eff}}/\Gamma_0 - 1 \propto \nabla F \propto \nabla n$ . The mechanical resonance frequency, however, follows directly  $n_{\text{mem}}$  as shown in panel b due to the fact that the dominant effect in our case is the photothermal stress instead of the dynamic backaction which would follow  $\nabla n_{\text{mem}}$ . Error bars come from the standard deviation of subsequent measurements.

## 6.5 Investigation of the cooling mechanism

Gathering the experimental results outlined in the previous section, we have had strong evidence that the primary source of the cooling mechanism was related to electron-hole pair generation as the wavelength dependent cooling factor data also supports this. Furthermore, the effect of radiation pressure cooling is estimated to be very small with our moderate finesse of 10. In addition to that, the opposite side of detuning for cooling and heating does not comply with conventional radiation pressure cooling. It turned out that this effect actually comes from the initially bent (towards the cavity mirror in this experiment) structure of the GaAs membranes. However, it was not experimentally clear which mechanism was responsible for the deflection and cooling dynamics with its characteristic timescale after the generation of charge carriers in GaAs. There might be two typical mechanisms for such a membrane: first one being the electronic stress due to radiative recombination of the pairs and the second one being the thermal stress due to non-radiative recombination. From a simple intuitive argument, the total electronic and thermal stress can be estimated by  $\sigma_{\text{el}}\delta n_{\text{mem}}\tau_{\text{el}}$  and  $\sigma_{\text{th}}\delta n_{\text{mem}}\tau_{\text{th}}$  where  $\sigma_{\text{el}}$  is the electronic stress with a timescale  $\tau_{\text{el}}$  and  $\sigma_{\text{th}}$  is the thermal stress with a timescale  $\tau_{\text{th}}$  where  $\delta n_{\text{mem}}$  is the number of photons absorbed per unit time. And for our case, thermal stress dominates due to the huge timescale difference ( $\tau_{\text{el}}/\tau_{\text{th}} \leq 5 \times 10^{-9}$ ).

In order to demonstrate the thermal stress related dynamics, we have performed a measurement where the timescale of the mechanism behind cooling could be addressed. For this measurement, a pump laser (853 nm) is used to excite electron-hole pairs in the GaAs membrane and a cavity probe laser (884 nm) is used to monitor the membrane displacement. As the pump is switched on and off, the photodetector signal is recorded to measure the relaxation timescale. For both cases, we find an exponential behaviour yielding a timescale of 10 ms (Fig. 6.9a). This is in good agreement with an estimated heat diffusion time of  $l^2/2D = 20$  ms where  $l \approx 1$ mm is the lateral dimensions and  $D = 0.25\text{cm}^2/\text{s}$  is the thermal diffusivity constant of GaAs.

For further confirmation, we have performed a spectral type of measurement where we measure the imaginary part of the mechanical response for slow modulations of the photo-induced force (cavity input light) [14]. The imaginary part of the lock-in response in this case is given by

$$\text{Im}[z_{\Omega}] \approx -\frac{F_{\text{ph}}\epsilon_{\Omega}}{m\Omega_{\text{eff}}}\frac{1}{\Omega_{\text{eff}}\tau}\frac{\Omega}{\Omega^2 + (1/\tau)^2} \quad (6.7)$$

where  $\epsilon_{\Omega}$  is the modulation depth.

The experimental result is shown in Fig. 6.9b. The data points follow the expected curve

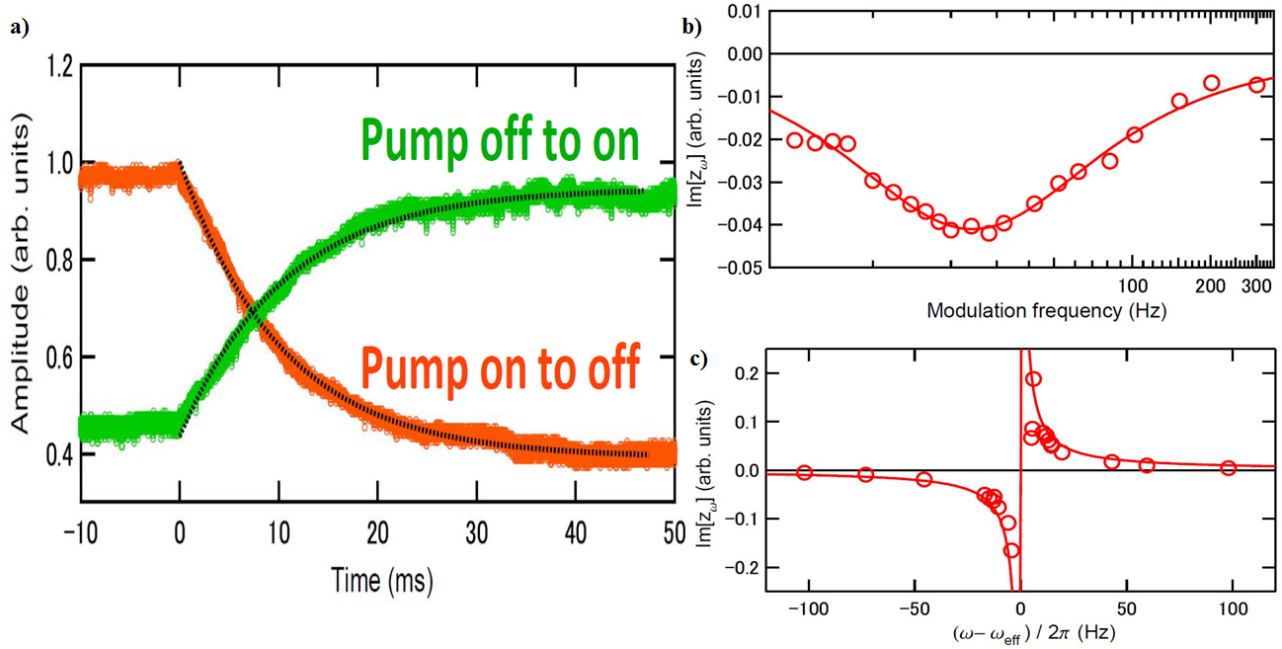


**Figure 6.9** a) Cavity transmission signal when the pump is on (green) and when the pump is off (orange). b) Imaginary part of the lock-in response of the membrane position fluctuations when driven with a modulated (lower than mechanical resonance frequency) cavity beam c) The response in the vicinity of the mechanical resonance (reproduced from [99]).

and has a minimum around 30 Hz corresponding to an extracted time constant  $\tau$  of 6.6 ms as a fit parameter (along with  $F_{\text{ph}}$ ) which is in agreement with the time domain measurement. As a last measurement, the response around (2,1) mechanical mode is recorded and fitted to the model which is expected to show a dispersion like behaviour (Fig. 6.9c). This time the parameters from the previous measurement ( $\tau = 6.6$  ms and  $F_{\text{ph}}$ ) are used to plot the fit function. All these measurements confirm our supposedly dominant thermal stress related dynamics in the cooling process, ruling out the deformation potential effect which is expected to take place with a much faster time constant.

## 6.6 Conclusive remarks and outlook

In conclusion, we have realized a novel cooling mechanism with a GaAs membrane by exploiting the internal degrees of freedom (electron-hole pair generation) and the cavity assisted photothermal effect. The GaAs membrane has a remarkably high mechanical Q-factors for several modes with an exceptional value of  $\approx 2 \times 10^6$  for (4,3) mode) for which we achieve a mode temperature of 4 K. We have performed several systematic measurements to figure out the underlying mechanism behind the cooling. We confirm that the primary source is the electron-hole pair generation upon excitation with an above band-gap laser beam and the cooling dynamics is then governed by the cavity assisted photothermal stress

on the membrane. However, it would be an interesting direction to search for the conditions of making the other mechanism- electronic pressure- dominant as the thermal stress mechanism currently limits the cooling rate due to the thermal expansion related instability. This can in principle be achieved by increasing the time constant of the electronic pressure coupling mechanism by, for example, engineering quantum well structures to increase the radiative recombination time. This is one of the initiatives started in the group in collaboration with Imamoglu group at ETH Zurich and Lodahl group at NBI. The idea is to tune the lifetime of GaAs quantum well structures by applying voltage at the contacts and tests are ongoing at the moment. One other possible way is to start the base temperature from 12 K or 50 K since the thermal expansion of GaAs goes to zero and the thermal stress related mechanism is expected to diminish. Along with the experiments, a theoretical work in [101] has been carried out in order to understand the electron-hole pair dynamics and the electronic pressure coupling better for future applications. We believe that this experimental work presented here might pave the way for interesting photonics experiments with semiconductors where their unique intrinsic electronic properties are coupled to the mechanical degrees of freedom in an optical cavity.

## Chapter 7

# Summary and conclusion

In the beginning of the PhD study (within the first year), the author first contributed to an optomechanics experiment with a GaAs membrane. After the characterization measurements, the surprisingly high mechanical quality factors of the membranes were reported in Liu *et al* [96]. Later on, we performed systematic studies on a novel optical cavity cooling mechanism. We have shown that above bandgap light generates electron-hole pairs which results in thermal stress in the semiconductor membrane due to non-radiative recombination. Along with cavity feedback, this photothermal mechanism is responsible for cooling the mechanical modes of the membrane. These findings were published in our work by Usami *et al* [99] and treated in detail in Andreas Næsby's thesis [94].

The author then concentrated on the main project of the PhD thesis which deals with the demonstration of an opto-electromechanical device for low-noise radio signal detection. In the first phase of the project, capacitive coupling has been explored via optical interferometry for different membrane types - bare SiN, aluminum and graphene coated SiN membranes. The advantage of metal and graphene coatings over the bare SiN membranes has been demonstrated with regard to the electrostatic interaction strength. Our findings show good agreement with the expected capacitive force behaviour. Furthermore, single layer graphene -with negligible added mass- does not bring an observable systematic effect on the excellent mechanical properties of SiN membranes. The results of this comparative study, which have also been illuminating for our following experiments in the project, are presented in our work [41] by Schmid *et al*.

In the second phase of the project, we have worked on the capacitive coupling of an Al-coated membrane to an LC circuit. The rich resonance dynamics stemming from the electromechanical coupling (including mechanically induced transparency and strong coupling) has been investigated and analyzed via both optical interferometry and electrical means, showing excellent agreement with our theoretical models. Electromechanical cooperativities as high as  $\approx 7000$  have been achieved. We then show with our room-temperature opto-electromechanical transducer highly sensitive optical detection of radio waves via use of Michelson interferometry. Beyond the actual Johnson noise limited sensitivity of our device, we infer a total noise contribution (at the optimal cooperativity) on the order of a few Kelvin for the membrane and optical readout noise (quantum shot noise) that is in competition with the state of the art op-amps operating at room temperature. Y-factor noise figure measurements with a cold resistor supplement our findings. Apart from that, rf-to-

optical photon conversion performance of the device (currently  $\approx 1\%$ ) has been discussed. The measurements demonstrating the optical detection of electromechanical coupling and the characterization of the noise performance of our device are presented in our work [4] by Bagci *et al.* The current noise performance of the device can be further improved by reducing the optical readout noise - at the same time allowing for higher cooperativities in order to suppress the membrane noise floor significantly.

We expect that our opto-electromechanical device - with its improved bandwidth and extension to higher frequencies - will find place in demanding sensing applications like NMR imaging and astrophysics. In such applications, the currently limiting Johnson noise of the LC circuit is expected to be suppressed to a large extent as our transducer will be coupled to a cold signal line. The total noise of the transducer in this case will fundamentally be dominated by the membrane noise and the optical readout imprecision. Thus we expect that our room-temperature transducer can potentially replace the expensive cryogenic amplifiers used for ultra-sensitive applications.

# Appendix A

## Detailed schematics for the electrical circuit

Here we give a more detailed schematics of the pcb we have used for controlling the electrical detection, coupling and excitation of our electro-mechanical system (Fig.A.1). Although

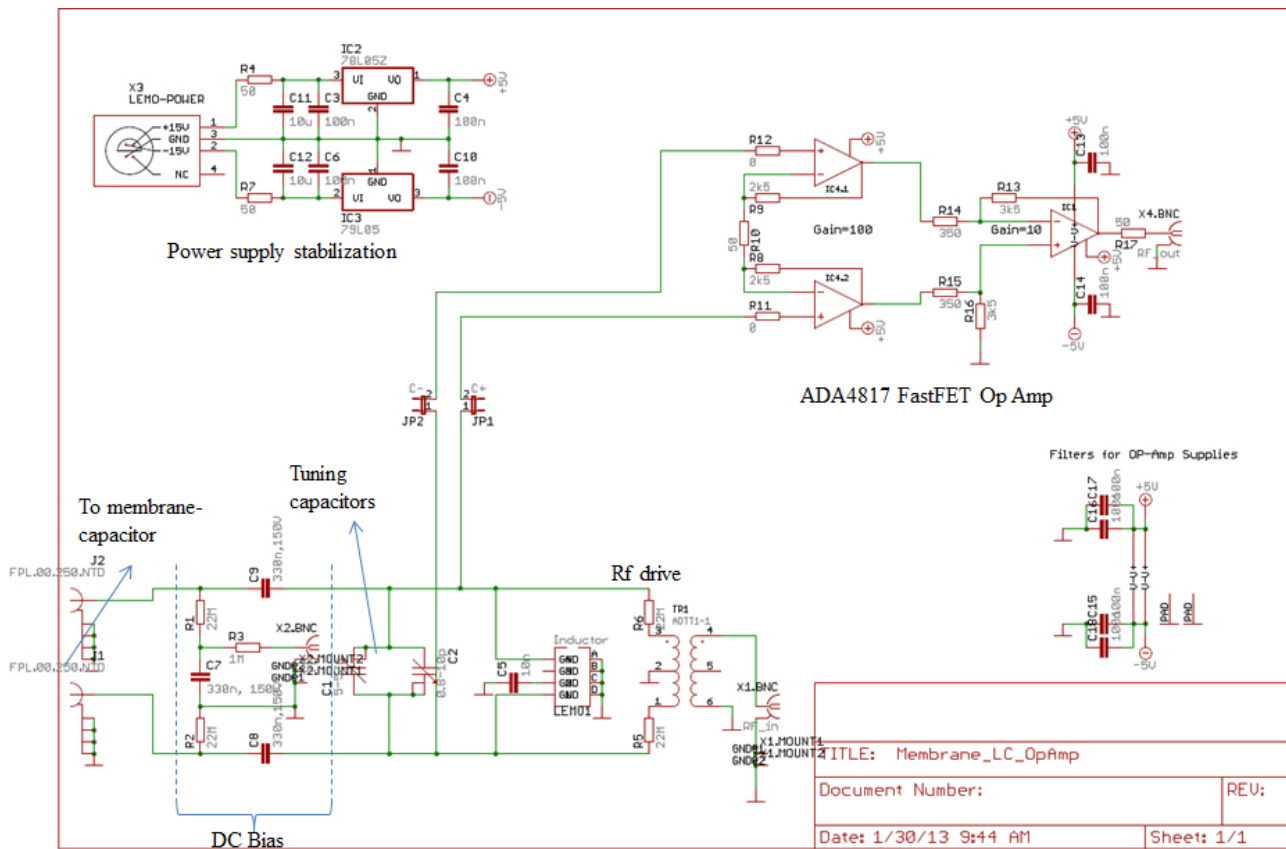


Figure A.1 The detailed schematics of the PCB with the op-amp.

during the course of the experiments, we made small modifications on the circuit, this

picture represents the main idea and elements behind the circuit design. The LC circuit part is connected via jumpers to the fast FET op-amp used for the detection of the capacitor voltage in a non-perturbative way. The LC circuit is also connected to the membrane-capacitor system inside the vacuum chamber via short cables not shown here. The op-amps are powered from a 15V Lemo line which is stabilized and filtered by a set of resistors and capacitors before they reach the op-amps (here the power supply stabilization and filtering are not connected to the op-amps in order to keep the picture simple). We use three low-noise ADA4817 fast FET op-amps which are operated in a JFET input instrumentation amplifier configuration. The first two symmetrically set amplifiers (ADA4817-2) receive input voltages from the LC circuit (both floating) and the third amplifier (ADA4817-1) carries out the differential detection with common-mode noise rejection. The total gain of the amplifier in the differential mode ( $V_N$  and  $V_P$  are the voltages going to the first amplifier and the second amplifier, respectively) is given by [58]

$$V_{out} = (V_N - V_P) \left( 1 + \frac{2R_F}{R_G} \right) \quad (\text{A.1})$$

In our case, the values of  $R_8, R_9$  and  $R_{10}$  are chosen such that we yield a gain  $G=100$ . On top of that, the third amplifier brings gain  $G=10$ . In total, we end up with a gain of 1000. This of course significantly reduces the original bandwidth of 1 GHz for unity gain. However, we still have a bandwidth of around 4 MHz estimated from

$$BWD = (f_{CR} \times R_G) / (2 \times R_F) \quad (\text{A.2})$$

where  $f_{CR}$  is the corner frequency which is 400 MHz for our op-amp. The achieved bandwidth is sufficient for our application since our operation frequency is around 700 kHz.

## Appendix B

# FET Op-amp for the electrical measurements

Some of the specifications (from [58]) of the fast FET op-amp (1GHz) we have used:

**High speed**

3 dB bandwidth (G=1, RL=100): 1050 MHz

**Low input bias current:** 2 pA

**Low input capacitance:**

Common-mode capacitance: 1.3 pF

Differential-mode capacitance: 0.1 pF

**Low noise**

Input voltage noise: 4 nV/Hz @ 100 kHz

Input current noise: 2.5 fA/Hz @ 100 kHz

**Common mode noise rejection:** 90 dB (typical)

**Low distortion:** 90 dBc @ 10 MHz (G=1, RL=1 k)

**Offset voltage:** 2 mV maximum

**Input resistance:** 500 G $\Omega$



## Appendix C

# Mechanical endurance of the membranes

Throughout the experimental runs related to this project, we have experimented with numerous membrane samples. The membranes have thicknesses varying from 50 nm-180 nm which makes them mechanically fragile to external perturbations. During our trials, we have lost several membranes due to various reasons. First of all, the current assembly process - namely placing the membrane on the capacitor chip in a reasonably well-aligned way - becomes, from time to time, tricky as it might be necessary to move the membrane around when it stands on the chip. Several times, this has caused the membranes break most probably due to residual elements on the chip-membrane surface. We have experienced breaking of the membranes which can be attributed to electrical effects as well. If the grounding of the whole setup is problematic, the membrane might break when a dc voltage is applied, presumably due to the high current leaking through the membrane-capacitor path. Furthermore, when an ac drive is applied to excite the LC circuit, the membrane can be excited to high vibration amplitudes which might be above the nonlinearity threshold causing instability and eventual breaking of the membrane. Therefore, attention must be paid to stay typically below 1 nm amplitude range even though it might compromise signal to noise ratio in some cases. Also for small distance samples, we have experienced that tuning the capacitor manually is destructive when a dc voltage is on (most probably due to the increased sensitivity to static charges coupling to the membrane at these small distances). From then on, we first tuned the capacitor (dc coupling off) and only then applied the dc voltage, which solved this problem.



## Appendix D

# Ultra-high precision resistors for the Y-factor measurement

In our measurements of the Y-factor, we have used ultra-high precision Vishay foil resistors as it is crucial, for such cryogenic measurements, to have a practically unaltered resistance value due to temperature changes together with immunity to noise. We chose to work with SMR1DZ/SMR3DZ resistors which are compact Z-foil molded surface mount resistors. The special design of these resistors allow for very low TCR (Temperature Coefficient of Resistance), very low PCR (Power Coefficient Temperature) and low noise performance. For foil resistors, ambient temperature variations cause negligibly small changes in resistance which are reversible. Typical reported values are [79] :

Temperature Coefficient of Resistance (TCR):

0.05 ppm/°C typical (0 °C to + 60 °C)

0.2 ppm/°C typical (- 55 °C to + 125 °C,+ 25 °C)

and

Power Coefficient of Resistance (PCR):

$\Delta R$  due to self heating: 5 ppm at Rated Power

Since TCR and PCR values are not specified for temperatures as low as 77K, we have checked the resistance change with an ohmmeter when the resistors were immersed in liquid nitrogen. As we could not see a measurable change in the resistance, we concluded to proceed to the measurements with these resistors. Apart from temperature stability and noise considerations, the special Z-foil design minimizes the parasitic capacitance and inductance of the resistor. The interloop capacitance is reduced due to series capacitance and the mutual inductance is reduced due to change in the current direction with the zigzag structure.



## Appendix E

# Shot noise limited optical detection

For the highly sensitive optical interferometry measurements at NBI, we have utilized an Innolight Mephisto Laser (Nd:YAG) as a light source and balanced homodyne detection with a fast Thorlabs InGaAs photodetector. The noise behaviour of the optical detection has been investigated with optical power dependence measurements. It was observed that

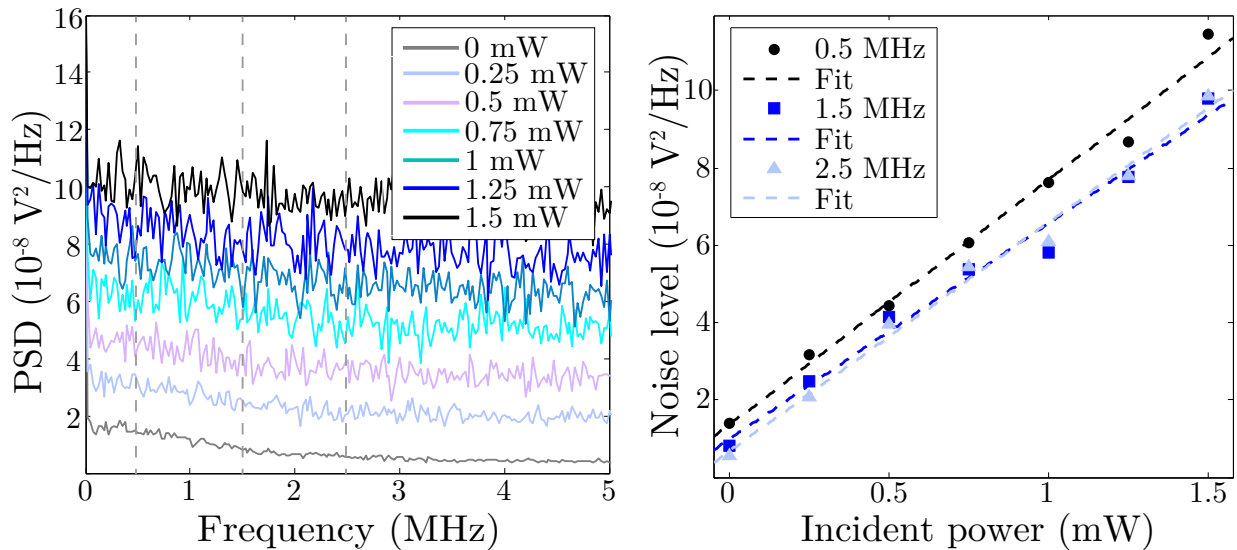


**Figure E.1** PSD (Power Spectral Density) of detected light noise with respect to the frequency (left). The optical power is increased from 0 mW up to 1.5 mW in small steps. Noise level (right) plotted with respect to the optical power at three different frequencies with linear fits for each data set (Courtesy of Andreas Barg).

around 1 MHz the laser shows relaxation oscillations when the interferometer operates at the unbalanced condition and the noise scales quadratically with optical power as it would be expected for classical noise. However, this relaxation noise peak is strongly suppressed when the interferometer is operated at the balanced condition allowing us to see the linear power dependence as an indication of shot noise limited sensitivity. (shown in Fig.E.1).



## Appendix F

# Effective mass

In our experiments, we have worked with square membrane mechanical resonators and looked at their vibrational modes which can be treated as drum modes and this has been studied in the theory chapter. It is convenient to treat the thin 2D membrane as a one dimensional harmonic oscillator with a certain amplitude along that direction and use this approach when we write down the equations of motion. However, since all the points on the 2D membrane surface vibrate with a certain amplitude governed by the modal shape and contribute with a different kinetic energy, it becomes necessary to assign an effective mass consistent with a proper coordinate definition. There is furthermore another factor involved as one also needs to take into account the optical beam overlap that samples the mechanical mode. However, as the beam size is relatively small with the respect to the membrane size, this can be neglected in our case. We start by writing down the deflection for a single point depending on the vibrational mode

$$u(x, y, z, t) = \sum_{m=1}^{\infty} a_m \Phi_m(x, y, z) \quad (\text{F.1})$$

Summing over all infinitesimal elements on the membrane and using the equipartition theorem, the total average kinetic energy for mode  $k$  can be written as

$$\langle E_k \rangle = \langle a_k \rangle^2 \Omega_k^2 \underbrace{\int_V \rho(x, y, z) |\Phi_k(x, y, z)|^2 dV}_{m_{eff}} = k_B T \quad (\text{F.2})$$

where  $\rho(x, y, z)$  is the density of the membrane. The term in underbrace can be recognized as the effective mass where the physical mass is given by  $m_{phys} = \int_V \rho(x, y, z) dV$ . The choice of the amplitude  $a_k$  is indeed arbitrary, however a convenient approach would be to define it as the maximum displacement of the antinode of the corresponding mode. For our square membranes with dimensions  $L \times L$  and thickness  $h$ , we have shown that the vibrational modes are given by

$$\Phi_{ij}(x, y, z) = \sin\left(\frac{i\pi x}{L}\right) \sin\left(\frac{j\pi y}{L}\right) \quad (\text{F.3})$$

therefore the effective mass referring to mode  $ij$  becomes

$$m_{ij} = \rho h \int_0^L \int_0^L \sin^2\left(\frac{i\pi x}{L}\right) \sin^2\left(\frac{j\pi y}{L}\right) dx dy = \frac{1}{4} m_{phys} \quad (\text{F.4})$$

We end up with the conclusion that for our square membranes, all the vibrational modes have an effective mass equal to 1/4 of the physical mass.

# Bibliography

- [1] D. J. Wilson, C. A. Regal, S. B. Papp and H. J. Kimble. Cavity optomechanics with stoichiometric SiN films. *Physical Review Letters* 103(20), 207204 (2009).
- [2] B. M. Zwickl, W. E. Shanks, A. M. Jayich, C. Yang, A. C. Bleszynski Jayich, J. D. Thompson and J. G. E. Harris. High quality mechanical and optical properties of commercial silicon nitride membranes. *Applied Physics Letters* 92,103125 (2008).
- [3] O. Arcizet, P-F. Cohadon, T. Briant, M. Pinard, A. Heidmann, J-M. Mackowski, C. Michel, L. Pinard, O. François, L. Rousseau. High-Sensitivity optical monitoring of a micromechanical resonator with a quantum-limited optomechanical sensor. *Physical Review Letters* 97,133601 (2006).
- [4] T. Bagci, A. Simonsen, S. Schmid, L. G. Villanueva, E. Zeuthen, J. Appel, J. M. Taylor, A. Sørensen, K. Usami, A. Schliesser, E. S. Polzik. Optical detection of radio waves through a nanomechanical transducer (Accepted to *Nature* - 2014). Preliminary version arXiv:1307.3467 (2013).
- [5] L. D. Landau and E. M. Lifshitz. *Theory of Elasticity - Course of Theoretical Physics*. 3rd edition, Volume 7. Pergamon Books Ltd (1986).
- [6] <http://mathworld.wolfram.com/WaveEquationRectangle.html>
- [7] J. D. Thompson, B. M. Zwickl, A. M. Jayich, Florian Marquardt, S. M. Girvin and J. G. E. Harris. Strong dispersive coupling of a high-finesse cavity to a micromechanical membrane. *Nature* 452, 72-75 (2008).
- [8] J. Chan, T. P. Alegre, A. H. Safavi-Naeini, J. T. Hill, A. Krause, S. Gröblacher, M. Aspelmeyer and O. Painter. Laser cooling of a nanomechanical oscillator into its quantum ground state. *Nature* 478, 89-92 (2011).
- [9] E. Verhagen, S. Deléglise, S. Weis, A. Schliesser and T.J. Kippenberg. Quantum-coherent coupling of a mechanical oscillator to an optical cavity mode. *Nature* 482, 63-67 (2012).
- [10] S. Gröblacher, K. Hammerer, M. R. Vanner and M. Aspelmeyer. Observation of strong coupling between a micromechanical resonator and an optical cavity field. *Nature* 460, 724-727 (2009).

- [11] J. D. Teufel, T. Donner, Dale Li, J. W. Harlow, M. S. Allman, K. Cicak, A. J. Sirois, J. D. Whittaker, K. W. Lehnert and R. W. Simmonds. Sideband cooling of micromechanical motion to the quantum ground state. *Nature* 475, 359-363 (2011).
- [12] C. A. Regal and K. W. Lehnert. From cavity electromechanics to cavity optomechanics. *Journal of Physics: Conference Series* 264, 012025 (2011).
- [13] Sh. Barzanjeh, M. Abdi, G. J. Milburn, P. Tombesi and D. Vitali. Reversible Optical-to-Microwave Quantum Interface . *Physical Review Letters* 109, 130503 (2012).
- [14] C. Metzger, I. Favero, A. Ortlieb and K. Karrai. Optical self cooling of a deformable Fabry-Perot cavity in the classical limit. *Physical Review B* 78, 035309 (2008).
- [15] T. Briant, P. F. Cohadon, A. Heidmann and M. Pinard. Optomechanical characterization of acoustic modes in a mirror. *Physical Review A* 68, 033823 (2003).
- [16] [www.kaajakari.net](http://www.kaajakari.net)
- [17] T. Mattila, J. Kiihamaki, T. Lamminmaki, O. Jaakkola, P. Rantakari, A. Oja, H. Seppä, H. Kattelus and I. Tittonen. A 12 MHz micromechanical bulk acoustic mode oscillator. *Sensors and Actuators A* 101, no. 1-2, pp. 1-9 (2002).
- [18] M. A. Sillanpää, J. Sarkar, J. Sulkko, J. Muhonen and P. J. Hakonen. Accessing nanomechanical resonators via a fast microwave circuit. *Applied Physics Letters* 95 , 011909 (2009)
- [19] J. M. Taylor, A. S. Sørensen , C. M. Marcus and E. S. Polzik. Laser cooling and optical detection of excitations in a lc electrical circuit. *Physical Review Letters* 107, 273601 (2011) .
- [20] S. Weis, R. Rivière, S. Deléglise, E. Gavartin, O. Arcizet, A. Schliesser, T. J. Kippenberg. Optomechanically induced transparency. *Science* 330, 1520-1523 (2010).
- [21] X. Zhou, F. Hocke, A. Schliesser, A. Marx, H. Huebl, R. Gross and T. J. Kippenberg. Slowing, advancing and switching of microwave signals using circuit nanoelectromechanics. *Nature Physics* 9, 179-184 (2013).
- [22] T. A. Palomaki, J. W. Harlow, J. D. Teufel, R. W. Simmonds and K. W. Lehnert. Coherent state transfer between itinerant microwave fields and a mechanical oscillator. *Nature* 495, 210-214 (2013).
- [23] D. Rugar, R. Budakian, H. J. Mamin and B. W. Chui. Single spin detection by magnetic resonance force microscopy. *Nature* 430, 329-332 (2004).
- [24] H. J. Mamin and D. Rugar. Sub-attoneutron force detection at millikelvin temperatures. *Applied Physics Letters* 79, 3358 (2001).
- [25] P. Rabl, S. J. Kolkowitz, F. H. L. Koppens, J. G. E. Harris, P. Zoller and M. D. Lukin. A quantum spin transducer based on nanoelectromechanical resonator arrays. *Nature Physics* 6, 602 (2010).

- [26] T. Larsen, S. Schmid and A. Boisen. Micro string resonators as temperature sensors. A I P Conference Proceedings Series (ISSN: 0094-243X), vol: 1552, pages: 931-936 (2013).
- [27] J. Chaste, A. Eichler, J. Moser, G. Ceballos, R. Rurali and A. Bachtold. A nanomechanical mass sensor with yoctogram resolution. *Nature Nanotechnology* 7, 301-304 (2012).
- [28] [educyclopedia.karadimov.info/library/sysnoise.pdf](http://educyclopedia.karadimov.info/library/sysnoise.pdf)
- [29] P. Horowitz Hill and W. Hill. *The art of electronics*. Cambridge University Press. 2nd edition (1989).
- [30] S. Chowdhury, M. Ahmadi and W. C. Miller. A closed-form model for the pull-in voltage of electrostatically actuated cantilever beams. *Journal of Micromechanics and Microengineering* 15, 756-763 (2005).
- [31] C.B. Aiken. *Proceedings of the Institute of Radio Engineers*, Volume:25 , Issue:2, 230-272 (1937).
- [32] S. Lee, V. P. Adiga, R. A. Barton, A. M. van der Zande, G. Lee, B. R. Ilic, A. Gondarenko, J. M. Parpia, H. G. Craighead and J. Hone. Graphene Metallization of High-Stress Silicon Nitride Resonators for Electrical Integration. *Nano Letters*, 13 (9), pp 4275-4279 (2013).
- [33] P.L. Yu, T. P. Purdy, and C. A. Regal. *Physical Review Letters* 108, 083603 (2012)
- [34] D. Antonio, H. Pastoriza, P. Julian and P. Mandolesi. Cryogenic transimpedance amplifier for micromechanical capacitive sensors. *Review of Scientific Instruments* 79, 084703 (2008)
- [35] F. L. Hampton and J. R. Cricchi. Steadystate electron and hole space charge distribution in LPCVD silicon nitride films. *Applied Physics Letters*. 35, 802 (1979)
- [36] J. Wibbeler, G. Pfeifer, M. Hietschold. Parasitic charging of dielectric surfaces in capacitive microelectromechanical systems (MEMS). *Sensors and Actuators A* 71, 74-80 (1998).
- [37] J.U. Jeon and T. Higuchi. Electrostatic Suspension of Dielectrics. *IEEE Transactions on Industrial Electronics* 45, No. 6 (1998).
- [38] P. A. Truitt, J. B. Hertzberg, C. C. Huang, K. L. Ekinici and K. C. Schwab. Efficient and sensitive capacitive readout of nanomechanical resonator arrays. *Nano Letters* 7, 120-126 (2007)
- [39] T. Faust, P. Krenn, S. Manus, J.P. Kotthaus and E.M. Weig. Microwave cavity-enhanced transduction for plug and play nanomechanics at room temperature. *Nature Communications* 3, Article number: 728 (2012).
- [40] Q. P. Unterreithmeier, E. M. Weig and J. P. Kotthaus. Universal transduction scheme for nanomechanical systems based on dielectric forces. *Nature* 458, 1001-1004 (2009).

- [41] S. Schmid, T. Bagci, E. Zeuthen, J. M. Taylor, P. K. Herring, M. C. Cassidy, C. M. Marcus, L. G. Villanueva, B. Amato, A. Boisen, Y. C. Shin, J. Kong, A. S. Sørensen, K. Usami and E. S. Polzik. Single-layer graphene on silicon nitride micromembrane resonators. *Journal of Applied Physics* 115, 054513 (2014).
- [42] S. Schmid, C. Hierold and A. Boisen. Modeling the Kelvin polarization force actuation of micro- and nanomechanical systems. *Journal of Applied Physics* 107, 054510 (2010).
- [43] B. Pillans, G. Rebeiz, and J.-B. Lee. *Advances in RF MEMS Technology*. IEEE MTT-GaAs Dig. Int., 17-20 (2003)
- [44] A. Dogan. The reliability of the silicon nitride dielectric in capacitive MEMS switches. Master thesis in Materials Science and Engineering. The Pennsylvania State University (2005).
- [45] K. S. Novoselov, V. I. Falko, L. Colombo, P. R. Gellert, M. G. Schwab and K. Kim. *Nature* 490, 192 (2012).
- [46] D. G-Sanchez, A. M. van der Zande, A. S. Paulo, B. Lassagne, P. L. McEuen and A. Bachtold. Imaging mechanical vibrations in suspended graphene sheets. *Nano Letters* 8, no:5, 1399-1403 (2008)
- [47] A. C. Ferrari and D. M. Basko. Raman spectroscopy as a versatile tool for studying the properties of graphene. *Nature Nanotechnology* 8, 235-246 (2013).
- [48] H. A. Pohl. *Dielectrophoresis*. Cambridge University Press, Cambridge, 1978.
- [49] Polytec-MSA 500 Micro System Analyzer
- [50] <http://www.norcada.com/>
- [51] G. Dupont, H. Caquineau, B. Despax, R. Berjoan, and A. Dollet. Structural Properties of N-rich a-SiN:H films with a low electron-trapping rate. *J. Phys. D: Appl. Phys.*, 30 1064-76 (1997).
- [52] C.T. Kirk. Valence alternation pair model of charge storage in MNOS memory Devices. *Journal of Applied Physics*, 50 [6] 4190-95 (1979).
- [53] Peter R. Saulson. *Fundamentals of interferometric gravitational wave detectors*. World Scientific Publishing, USA (1994).
- [54] Innolight, Mephisto, Ultrastable single frequency cw laser. Technical Data.
- [55] <http://www.amidoncorp.com/61-material-ferrite-rods/>
- [56] C. R. Sullivan. Optimal choice for number of strands in a Litz-Wire transformer winding. *IEEE Transactions on Power Electronics*, vol. 14, no. 2, 283-291 (1999).
- [57] <http://www.bentongue.com/xtalset/29MxQFL/29MxQFL.html>
- [58] Analog Devices, ADA4817, Technical Data Sheet.

- [59] <http://www.ligo.org/science/GW-IFO.php>
- [60] A. Abramovici *et al.* LIGO: The Laser Interferometer Gravitational-Wave Observatory Science, vol.256, no. 5055, pp. 325-333 (1992).
- [61] Carlton M. Caves. Quantum-mechanical noise in an interferometer. Physical Review D 23, 1693 (1981)
- [62] M. Pinard, P. F. Cohadon, T. Briant and A. Heidmann. Full mechanical characterization of a cold damped mirror. Physical Review A 63, 013808 (2000).
- [63] S. Camerer, M. Korppi, A. Jöckel, D. Hunger, T. W. Hänsch and P. Treutlein. Realization of an optomechanical interface between ultracold atoms and a membrane. Physical Review Letters 107, 223001 (2011).
- [64] S. E. Harris, J. E. Field and A. Imamoglu. Nonlinear optical processes using electromagnetically induced transparency. Physical Review Letters 64, 1107 (1990).
- [65] E. Gavartin, P. Verlot and T. J. Kippenberg. A hybrid on-chip opto-mechanical transducer for ultra-sensitive force measurements. Nature Nanotechnology 7, 509-514 (2012)
- [66] G. Anetsberger, O. Arcizet, Q. P. Unterreithmeier, R. Rivière, A. Schliesser, E. M. Weig, J. P. Kotthaus and T. J. Kippenberg. Near-field cavity optomechanics with nanomechanical oscillators. Nature Physics 5, 909 (2009).
- [67] J. M. Dobrindt, I. Wilson-Rae and T. J. Kippenberg. Parametric normal-mode splitting in cavity optomechanics. Physical Review Letters. 101, 263602 (2008).
- [68] C. L. Garrido Alzar, M. A. G. Martinez and P. Nussenzveig. Classical analog of electromagnetically induced transparency. American Journal of Physics 70, 37 (2002).
- [69] L. Novotny. Strong coupling, energy splitting, and level crossings: A classical perspective. American Journal of Physics 78, 1199 (2010).
- [70] J. D. Teufel, Dale Li, M. S. Allman, K. Cicak, A. J. Sirois, J. D. Whittaker and R. W. Simmonds. Circuit cavity electromechanics in the strong-coupling regime. Nature 471, 208 (2011).
- [71] T. Bagci, A. Simonsen, E. Zeuthen, J. M. Taylor, L.G.Villanueva, S. Schmid, A. Sørensen, A. Schliesser, K. Usami and E.S. Polzik. Optical readout of coupling between a nanomembrane and an LC circuit at room temperature. CLEO Europe (2013).
- [72] CCIR (Consultative Comitee on International Radio) Report 322.
- [73] J. Carr. Microwave and Wireless Communications Technology. Butterworth-Heinemann (1996).
- [74] E. N. Skomal. Man-Made Radio Noise. Van Nostrand Reinhold (1978).
- [75] J. D. Kraus. Radio Astronomy. McGraw (1966).

- [76] <http://www.picoelectronics.com/>
- [77] R. C. Li. RF Circuit Design. John Wiley and Sons. 2nd edition (2012).
- [78] <http://www.w1ghz.org/noise/noise99.pdf>
- [79] Vishay, Ultra-high precision resistors SMRxDZ, Data Sheet.
- [80] T. H. O'Dell. Circuits for electronic instrumentation. Press Syndicate of the University of Cambridge (1991).
- [81] C. A. Regal, J. D. Teufel and K. W. Lehnert. Measuring nanomechanical motion with a resonant microwave interferometer. *Nature Physics*, 4, 555 (2008).
- [82] M. A. Castellanos-Beltran, K. D. Irwin, G. C. Hilton, L. R. Vale and K. W. Lehnert. *Nature Physics* 4, 929 (2008).
- [83] K. Jensen, J. Weldon, H. Garcia and A. Zettl. Nanotube radio. *Nano Letters* 7, 3508-3511 (2007).
- [84] J. Bochmann, A. Vainsencher, D. D. Awschalom and A. N. Cleland. Nanomechanical coupling between microwave and optical photons. *Nature Physics* 9, 712-716 (2013).
- [85] R. W. Andrews, R. W. Peterson, T. P. Purdy, K. Cicak, R. W. Simmonds, C. A. Regal and K. W. Lehnert. Reversible and efficient conversion between microwave and optical light. [arXiv:1310.5276](https://arxiv.org/abs/1310.5276) (2013).
- [86] S. Weinreb, J. Bardin, H. Mani and G. Jones. Matched wideband low-noise amplifiers for radio astronomy. *Review of Scientific Instruments* 80, 044702 (2009).
- [87] H. Kovacs, D. Moskau and M. Spraul. Cryogenically cooled probes - a leap in NMR technology. *Progress in Nuclear Magnetic Resonance Spectroscopy* 46, 131-155 (2005).
- [88] D. Pozar. *Microwave and RF Design of Wireless Systems*. J. Wiley, pg. 127 (2001).
- [89] B. Sklar. *Digital Communications*, Prentice Hall, pg. 194 (1988).
- [90] M.B. Graves, WRØI. Computerized Radio Star Calibration Program. Proceedings of the 27th Conference of the Central States VHF Society, ARRL, pp. 19-25 (1993).
- [91] F. Resmer, H. C. Seton and J. M. Hutchison. Cryogenic receive coil and low noise preamplifier for MRI at 0.01T. *Journal of Magnetic Resonance* 203, 57-65 (2010).
- [92] V. S. Ilchenko, A. B. Matsko, I. Solomatine, A. A. Savchenkov, D. Seidel and L. Maleki. ka-band all-resonant photonic microwave receiver. *IEEE Photonics Technology Letters* 20, 1600-1612 (2008).
- [93] M. Hossein-Zadeh and A. Levi. Ring resonator-based photonic microwave receiver modulator with picowatt sensitivity. *IET Optoelectronics* 5, 36 (2011).
- [94] A. Naesby Rasmussen. Optomechanics with semiconductor nanomembranes. PhD Thesis. QUANTOP, Niels Bohr Institute. Faculty of Science, University of Copenhagen (2013).

- 
- [95] G. D. Cole, S. Gröblacher, K. Gugler, S. Gigan and M. Aspelmeyer. Monocrystalline  $Al_xGa_{1-x}As$  heterostructures for high-reflectivity high-Q micromechanical resonators in the megahertz regime *Applied Physics Letters* 92, 261108 (2008).
- [96] J. Liu, K. Usami, A. Naesby, T. Bagci, E. S. Polzik, P. Lodahl and S. Stobbe. High-Q optomechanical GaAs nanomembranes. *Applied Physics Letters* 99 , 243102 (2011).
- [97] H. Ukita, Y. Uenishi and H. Tanaka. A photomicrodynamic system with a mechanical resonator monolithically integrated with laser diodes on Gallium Arsenide. *Science* 260, 786 (1993).
- [98] H. Okamoto, D. Ito, T. Watanabe, K. Onomitsu, H. Sanada, H. Gotoh, T. Sogawa and H. Yamaguchi. Carrier-mediated optomechanical coupling in GaAs cantilevers. *Physical Review B* 84, 014305 (2011).
- [99] K. Usami, A. Naesby, T. Bagci, B. M. Nielsen, J. Liu, S. Stobbe, P. Lodahl and E. S. Polzik. Optical cavity cooling of mechanical modes of a semiconductor nanomembrane. *Nature Physics* 8, 168-172 (2012).
- [100] A. M. Fox. *Optical Properties of Solids*. Oxford University Press (2001).
- [101] A. Xuereb, K. Usami, A. Naesby, E. S. Polzik and K. Hammerer. Exciton-mediated photothermal cooling in GaAs membranes. *New Journal of Physics*. 14 085024 (2012).